Highly-functional Poly(amino acids) for Controlled Therapeutic Drug Delivery

Benjamin Francis Coyne

Supervised by Dr. Paul Thornton

Co-Supervisor: Prof. Bruce Turnbull

Submitted in accordance with the requirements for the degree of Doctor of Philosophy

School of Chemistry, University of Leeds

November 2025

The candidate confirms that the work submitted is his own and that appropriate credit has been given within the thesis where reference has been made to the work of others.

Acknowledgements

I would first like to thank my supervisors, Dr. Paul Thornton and Prof. Bruce Turnbull for their guidance and patience over the years. Without you, this achievement would not have been possible.

I would also like to thank the Thornton group and Lab 3.14 for their continuous kindness, support and encouragement during the highs and lows of PhD life. Special thanks to Patrick Wall for the motivation and drive he has given me, and to Anna Morrell for being a resolute source of advice, coffee and gossip. Thank you to Jeanine Williams for her tireless technical support with LC-MS, DLS and the dreaded APC. Thank you also to Mohammed Asaf for his support with FTIR and warm conversation. Thank you to all at the School of Chemistry stores for your cheerful welcome and to Richard Roper, I wish I'd known you better. Thank you to Richard England and the team at AstraZeneca in Macclesfield. The time spent learning from you was some of my favourite, and I feel privileged to have worked with you.

Thank you also to the staff and students of the SOFII CDT, especially my brethren from cohort 7. It seems a lifetime ago since we were quarantined in St. Mary's, a memory I look back on with a strange fondness. The skills I have developed within my PhD were matched and more by what I have learned as a member of SOFII, and it is a connection I will cherish.

To my family and friends, this thank you has been a long time coming. I couldn't have survived my PhD and the life I lived alongside it without the continued presence and love that has sustained me. Thank you Johnny, Olivia, Alan and Holly. Thank you to my mother, Lucy and my brother, Matthew – my two musketeers. To my father, Neil and to Imogene, fellow compatriots of the secret six. To Grandma and Grandad, always at the end of the phone and always so proud. To Papa and Grandma, just as proud. I wish you were here to see this. Jacob, Harriet, Clare, Neil and the whole Brown family, Sunday at 4pm will always be my favourite time of the week. And to my family to be, Richard, Sharon and Emily, thank you for your love, trust, and for enough free food to sustain a small village.

And finally, thank you to Nicole. My fiancée, my rock, my best friend. Thank for sticking by me in the hardest moments, for believing in me when I couldn't, for encouraging me when all I wanted was to give up, and for showing me that I have time, that I'm not alone, and that I can do this. Wise words that I will take forward into our life together. I love you.

Abstract

Synthesising delivery platforms for poorly soluble, cytotoxic chemotherapeutics remains a crucial challenge in modern medicine. Biomimetic polymer nanocarriers combine biocompatibility, biodegradability and structural tenability, making them ideal for stable transport and controlled release. This thesis investigates the synthesis and optimisation of functional poly(amino acid) and poly(hydroxy acid) systems for the encapsulation and conjugation of therapeutics, producing well-defined polymeric platforms capable of self-assembly and of controlled release of their respective payload.

Monomer synthesis was addressed through preparation of a library of N- and O-carboxyanhydrides (NCA, OCA) including Fmoc-, Z- and Boc-protected lysine NCAs and mandelic acid OCA. Traditional phosgene-activated synthetic strategies were evaluated against modern phosgene-free alternatives, revealing distinct differences in safety, purity and robustness to undesirable side reactions. From these monomers, *via* ring-opening polymerisation (ROP), were synthesised two complementary amphiphilic block copolymer platforms. In the first, mPEG-*b*-poly(mandelic acid) copolymers were synthesised under systematically varied reaction conditions. The products exhibited narrow molecular weight distributions and self-assembled into sub-200 nm nanoparticles with low polydispersity. These platforms were capable of encapsulating doxorubicin with high efficiency and demonstrated slow, pH-responsive release behaviour with no unwanted burst release and limited leakage at physiological pH. This highlighting the potential of the PMA backbone for pH-sensitive drug delivery.

The second system utilised mPEG-*b*-PLys block copolymers, synthesised under extensive kinetic and mechanistic investigation including *in-situ* FTIR monitoring. Challenges with the Fmoc- and Z-protected systems were addressed, with Boc-protected championed for its robust synthesis and rapid, simple deprotection. Subsequent post-polymerisation modification introduced oligo(ethylene glycol) grafts to relieve steric congestion around lysine pendant amines, enabling efficient carbamate conjugation to SN38. The resulting conjugates formed uniform nanoparticles that exhibited excellent stability and sustained release under physiologically relevant conditions.

Table of Contents

List of Figures

List of Tables

List of Schemes

List of Abbreviations

APC	Advanced Polymer Chromatography	**APD**	Avalanche Photodiode Detector
API	Active Pharmaceutical Ingredient	**ATR**	Attenuated Total Reflection
BBO	Broadband Observe NMR Probe	**BCP**	Block Copolymer
Boc	*tert*-Butyloxycarbonyl protecting group	**DCM**	Dichloromethane
DIPEA	N,N-diisopropylethylamine	**DMAP**	4-Dimethylaminopyridine
DMF	Dimethylformamide	**DLS**	Dynamic Light Scattering
DOX	Doxorubicin	**DOSY**	Diffusion-Ordered Spectroscopy
DP	Degree of Polymerisation	**Đ**	Dispersity
Fmoc	Fluorenylmethoxycarbonyl protecting group	**FTIR**	Fourier Transform Infrared Spectroscopy
GPC	Gel Permeation Chromatography	**HA**	Hydroxy Acid
HPLC	High-Performance Liquid Chromatography	**LC-MS**	Liquid Chromatography–Mass Spectrometry
MALDI-TOF MS	Matrix-Assisted Laser Desorption/Ionisation Time-of-Flight MS	**MD-SEC**	Multi-Detector Size-Exclusion Chromatography
mPEG	Methoxy-Poly(ethylene glycol)	**MS**	Mass Spectrometry
MWCO	Molecular Weight Cut-Off	**NCA**	N-Carboxyanhydride
NMR	Nuclear Magnetic Resonance	**OCA**	O-Carboxyanhydride
OPUS	OPUS Spectroscopy Software	**PBS**	Phosphate Buffered Saline
PDI	Polydispersity Index	**PEG**	Poly(ethylene glycol)

PLys	Poly(lysine)	**PMA**	Poly(mandelic acid)
PyBOP	Benzotriazol-1-yloxytripyrrolidinophosphonium Hexafluorophosphate	**ROP**	Ring-Opening Polymerisation
SEC	Size-Exclusion Chromatography	**SN38**	7-Ethyl-10-hydroxycamptothecin
T3P	Propylphosphonic Anhydride	**TBME**	*tert*-Butyl Methyl Ether
TEM	Transmission Electron Microscopy	**TFA**	Trifluoroacetic Acid
TMS	Tetramethylsilane	**UPLC**	Ultra-Performance Liquid Chromatography
UV-Vis	Ultraviolet–Visible Spectroscopy	**WinUV**	Cary UV-Vis Analysis Software
Z	Benzyloxycarbonyl protecting group	**ZSP**	Zetasizer Nano ZSP

Chapter 1: Introduction

1.1 Drug Delivery

Since the earliest implementation of controlled-release mechanisms by Smith-Kline and French in 1952, research into the delivery of pharmaceutical therapeutics has been on an upward trajectory.[1] In 2019, the global drug delivery market size exceeded 26 billion USD and is projected to reach 45 billion USD by 2027.[2] Conversely, the development of new drugs in recent years has declined, and it is estimated that around 90 % of drugs currently in development consist of molecules that are poorly soluble under aqueous, physiological conditions.[3] Of primary significance to this report are the adverse side effects of cytotoxic drugs, such as those employed in the chemotherapy of cancers. Reported side effects of these medications, including vomiting, chronic pain, diarrhoea and fatigue, affect approximately 75 % of patients, with 60 % of patients incurring a serious side effect.[4] The modern development of drug delivery vehicles is a vital solution to these effects, as these materials can greatly increase the efficiency and decrease the detrimental impact of such cytotoxic treatments within the body.

When it comes to medical applications, drug delivery vehicles may suffer from one of several physiological limitations. This can include poor biodegradation, poor bioavailability and instability during circulation and potential cytotoxic effects of their own.[5] Biomimetic materials pose a potential solution to this complication, as they are characterised by their bioavailability, biocompatibility, and biodegradability. Two prominent examples of such materials are poly(amino acid)s and polyesters, the general repeat unit structures for which are shown in **Figure 1** below.

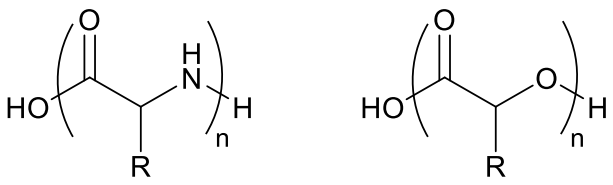

Poly(amino acid) **Polyester**

Figure 1.1: Generalised structure of a poly(amino acid) and a polyester.

The route from amino acid (AA) and hydroxy acid (HA) raw materials to functional polymer products is detailed within this report. This includes the cyclisation of AA and HA molecules bearing hydrophobic pendant chain functionalities into reactive 5-membered heterocycles, followed by their polymerisation. By using nucleophile-terminated hydrophilic macromolecules such as polyethylene glycol methyl ether (mPEG) to initiate ring-opening polymerisation (ROP), it is then possible to develop block-copolymer products with amphiphilic properties. These functional materials are then capable of self-assembly, resulting in the formation of the encapsulant nanoparticles that can carry therapeutic payloads to their destination. To understand this process in greater detail, the mechanistic background for the synthesis and preparation of these block-copolymer amphiphilic nanoparticles has been recounted within this chapter.

1.1.1 Amphiphilic Block Copolymers

Polymers consist of a covalently-linked sequence of monomer building units (repeat units) and can be classified depending on the number and arrangement of these units. Polymers composed of a single type of repeat unit, such as PEG, are referred to as *homopolymers*. Homopolymer physicochemical properties remain consistent throughout the chain and are often similar to those of the constituent monomer.[6] This is exemplified by the hydrophilicity of PEG, owed to the significant quantity of hydrogen-bond donating oxygen atoms within the polymer backbone. Polymers with two or more repeat units are referred to as *copolymers*, and exhibit physichochemical properties intermediate to those of their constituent monomers, depending on their relative sequencing.[7] Differing classifications of copolymer are outlined in **Figure 1.2** below.

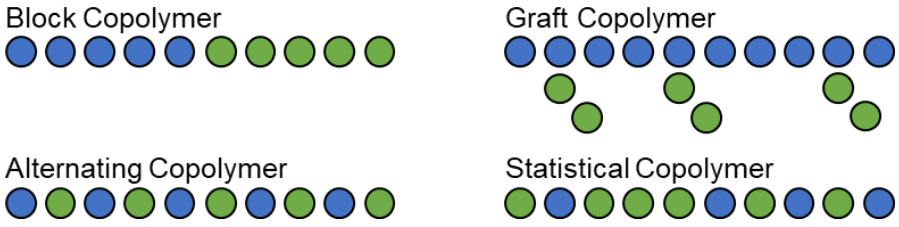

Figure 1.2: Graphical representations of differing copolymer classifications

Block copolymer sequences are often exploited in drug delivery science as building blocks for nanoparticles. Combining the hydrophilic properties of a polymer such as PEG, covalently linked to a block with hydrophobic properties, creates a single chain with *amphiphilic* properties, leading to self-assembly into a particle under aqueous conditions by inter-chain association of multiple hydrophobic blocks into a core, surrounded and compatibilised by a corona of external hydrophilic blocks. Block copolymerisation can be achieved by either covalent linkage of two existing blocks together, sequential monomer addition during polymerisation from a small-molecule initiator, or by using one polymer block as a *macroinitiator*, propagating the next block from this reaction. There is theoretically no limit to the number of blocks that can be added to a polymer system.

PEG is widely utilised in the synthesis of hybrid block copolymers suitable for biomedical applications, due to in part to its commercial viability, but also to its high biocompatibility, hydrophilicity and pharmacokinetic properties.[8-10] The end-groups of the PEG chain can undergo a wide variety of functional modifications, allowing a broad assortment of linkages and chain terminals to be made from the homopolymer framework. Specifically, substitution of the hydroxyl terminals of one PEG chain, one for a methyl and one an amine group, affords a single-terminal functionalised nucleophilic macroinitiator, shown in **Figure 1.3** below.

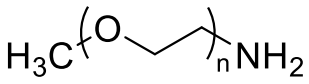

Figure 1.3: Structure of methoxy-poly(ethylene glycol)-NH_2.

According to a review by Knop *et al*, all marketed polymer therapeutics brought to the market up to 2010 contained PEG-functionalised therapeutics, with no other synthetic polymer having reaching that status.[11] This readily exemplifies the benefits that PEG macromolecules provide within the development of polymeric drug delivery platforms in general and, importantly for this work, for self-assembled amphiphilic block copolymers systems.

1.1.2 Block Copolymer Self Assembly

The utilisation of block copolymer (BCP) self-assembly into functionally diverse nanoparticles has been widely explored in the literature. One factor of significant importance to the medical industry is the small size of these nanoparticles, which allows for unique physicochemical properties, such as passage across the blood-brain barrier.[12] Of importance to the work in this report is the self-assembly of polymer nanoparticles in solution, though this is also possible in bulk. Self-assembly in solution occurs once the molarity of BCP has exceeded the critical micelle concentration (CMC), as a result of thermodynamically unfavourable interactions between the solvent and one block of the copolymer. These interactions are limited by the action of self-assembly, which can be interpreted physically as a minimization of the free energy of interaction between the polymer blocks **A** and **B**, as well as that of their interaction with the solvent (χ_{AB}, χ_{AS} and χ_{BS}, respectively).[13]

A range of morphologies are accessible to these nanoparticles, including spherical micelles, cylindrical (worm- and rod-like) micelles and vesicles. The tendency of a nanoparticle system to assembly under one of these morphologies can be crudely characterised by the dimensionless packing parameter ***p***, first introduced by Israelachvili.[14] ***p*** is defined in **Equation 1** below, within which is also found the volume and length of the solvophobic block, ***v*** and $\boldsymbol{l_c}$, as well as the effective interfacial area of the BCP, $\boldsymbol{a_0}$.

$$p = \frac{v}{a_0 l_c}$$

Values of *p* below 0.33 correspond to spherical micelle morphology, while values between 0.33 and 0.5 correspond to cylindrical micelles, and values between 0.5 and 1 correspond to vesicles and polymersomes.[15,16] Investigations by Eisenberg *et al.* into polystyrene-*b*-poly(acrylic acid) (PS-*b*-PAA) in water revealed that block copolymer morphologies were related to the length of the hydrophilic PAA block.[17] With larger lengths of PAA, polymers formed spherical micelles, followed by cylindrical micelles, vesicles and finally inverse micelles. Analysis of the shortest length PAA block copolymers also revealed larger lamellar structures in some cases as well.

Further research by Eisenberg continued to reveal potential morphologies available to these polymer systems, including very long worm-like micelles, and rod-like aggregate species. This research highlights the vast array of potential morphologies available to block copolymer systems, for which there may be a plethora of untapped applications.

1.1.3 Optimisation of Nanoparticles

The properties of block copolymer amphiphiles as platforms for drug encapsulation and controlled release can be altered by fine-tuning both the constituent functional domains and chemistries of the constituent blocks, as well as by varying the method of self-assembly those polymers undertake during nanoprecipitation. Relative block size (degree of polymerisation), solubility and inter-chain interactions have significant impact upon the resultant drug loading, stability and controlled release of the delivery platform.

With increasing nanoparticle drug loading, fewer nanoparticles are required to deliver the necessary dosing of active pharmaceutical ingredient (API) to the target site.[18] API's as a component of therapeutics typically represent the greatest investment of time, resource and cost in the preparation of such materials, and hence higher drug loading offers greater value to the manufacturer, practitioner and patient.[19] This was exemplified by Sabatelle *et al*. who used ultra-high-drug-loaded (UHDL) paclitaxel nanoparticles to increase sustained drug levels in the peritoneal cavity compared to those treated with the low drug-loading formulation (PTX-C/E), and to increase median survival rate from 53 days in the PTX-C/E group to 81 days after a single UHDL dose, and to 122 days after 2 doses.[20] However, research by Chu *et al*. disputes this narrative, wherein mice treated with 9 wt% docetaxel-NP (D-NP) formulation experienced reduced docetaxel exposure in the organs of the mononuclear phagocyte system (MPS), and an increased plasma/tumour docetaxel concentration when compared to those that received 20 wt% D-NP, resulting in increased therapeutic efficiency.[18] These contrasting results highlight the complex physicochemical balance that is faced when tuning high- and low-drug-loading during payload development, between increased dosage efficiency and improved pharmacokinetic profile.

Nanoparticle stability is paramount to the synthesis, storage, intravenous introduction, plasma transport and controlled delivery of therapeutic payloads by amphiphilic block copolymer systems. Particularly as synthesis and nanoprecipitation are scaled to meet industrial manufacture capacity, poor uniformity of the polymer product (Đ) and nanoparticle assembly (PDI) can lead to particle inhomogeneity, which increases the risk both burst release upon exposure to blood plasma and payload leakage during either storage or transport, negating the purpose of controlled release.[21] These effects are of specific interest to this report, which investigates the controlled release of SN38, a potent topoisomerase I inhibitor with poor physiological solubility and limited therapeutic capability in its native form. Spiking concentrations (C_{max}) of native SN38 upon intravenous delivery or burst release leads to dose-limiting toxicities such as myelosuppression and gastrointestinal damage, as well as promoting rapid glucoronidation, which expedites drug clearance and elimination from the plasma.[22-24] Nanoparticle stability is therefore of paramount importance to this work.

Sensitivity of nanoparticle systems to physiological stimuli plays a key role in the selectively-triggered release mechanism of many delivery payloads. Selected stimuli include temperature, enzymatic activation, redox potential and the presence of biomarkers on affected cells, such as receptors and glycoproteins.[25-28] Of specific interest to this research is the pH-sensitivity of ester linkages within drug delivery platforms, the hydrolysis of which is acid-catalysed.[29] This makes them viable for triggered release under the acidic conditions of both the extracellular tumour microenvironment (pH 6.0 – 6.8) and the intracellular conditions of endosomes and lysosomes (pH 5.0 – 5.5).[22]

Finally, size represents a potential limiter for the application of nanoparticle delivery systems to specific sites around the body. The diffusion of these platforms across biological membranes and barriers is vital and requires that the self-assembled nanoparticles fall below specific thresholds. For instance, there is a ca. 100 nm diameter cut-off for nanoparticle to diffuse across the blood-brain barrier. A summary of potential routes for nanoparticle-therapeutic administration within different size thresholds is provided in **Table 1.1**, adapted from Danaei *et al*.[12]

Table 1.1: Required particle sizes for distribution within the body *via* several different administration and dosage routes. Adapted from [12].

Route of Administration / Dosage Form	Particle Size Range
Long-circulating carriers (brain, tumours)	50 – 200 nm
Transdermal	10 – 600 nm
Intravenous / intramuscular	200 – 2000 nm
Ocular	100 – 3000 nm
Aerosol	1 – 10 µm
Nasal	8 – 20 µm
Lymphatic (Reticuloendothelial System)	10 – 50 nm

1.2 Poly(amino acids) for Drug Delivery

In recent years, drug delivery science has benefited from the implementation of biomimetic materials in the development of its encapsulant nanoparticles. Biomimetic materials combine chemistry, biology and engineering in an effort to emulate natural materials, mechanisms and systems in order to tackle human problems. This appropriately describes the role that poly(amino acids) can play as biomimetic drug delivery materials. The ability to self-assemble into complex, biocompatible conformations, makes these materials promising candidates for the targeted delivery of anti-cancer therapeutics.[30]

1.2.1 Amino Acids

Amino acids are the constituent building blocks of two vital groups of macromolecules in the human body. These include peptides, such as insulin and oxytocin, and proteins, such as trypsin. These polymeric structures occur naturally in the body in unique combinations, specific to the role of the molecule. This is made possible by the highly functional nature of the amino acids, which enables them to leverage intramolecular folding interactions to self-assemble into externally hydrophilic nanoparticles, thereby improving intestinal uptake and overall biocompatibility.

In addition, poly(amino acid) macromolecules are biodegradable under homeostatic conditions, subsequently reforming amino acid molecules which are easily metabolised. This combination of improved vehicle uptake and disposal makes poly(amino acid) based nanomaterials an enticing opportunity for pharmaceutical and biomedical applications, specifically as biomaterial scaffolds for controlled drug delivery and tissue engineering.[31,32]

Furthermore, the commercial production of amino acids for poly(amino acid) synthesis obtained via enzymatic biosynthesis is attractive from an environmental sustainability standpoint.[33] The majority of amino acids are biosynthesised by proliferating microorganism cultures, via the fermentation of simple sugar syrups obtained from grains or molasses.[34] This use of a renewable raw material, processed by cultured microorganisms that can be grown to scale, is a great benefit in the case of using poly(amino acid) materials over more economically linear, petrochemical-sourced polymer alternatives.

The generalised structure of an (α-)amino acid is illustrated in **Figure 1.4** below. Bonded to the α-carbon are an amino acid and a carboxylic acid terminal, as well as a pendant side chain group which can bear a multitude of functional domains. These include hydrophobic, hydrophilic, acidic, basic, polar and non-polar domains. Furthermore, amino acids produced by biosynthesis are usually of the S-configuration (or L- by latin nomenclature).

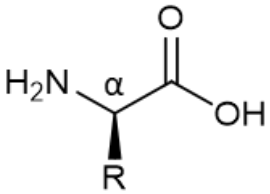

Figure 1.4: A generalised amino acid molecule

For a nanoparticle to be capable of both encapsulating a drug molecule, as well as exhibiting biocompatibility within the body, it is necessary that the constituent polymer materials of those nanoparticles are amphiphilic in nature. By exploiting the wide functional diversity of the available amino acid monomers, it is possible to influence the physicochemical properties of the subsequent poly(amino acid) materials so as to achieve this criterion.[35] **Table 1** below illustrates the 20 proteogenic amino acids commonly found within the body, with the functional varieties of their respective side chain groups highlighted.

Table 1.2: The 20 proteogenic amino acids.

Glycine (Gly)	**Alanine (Ala)**	**Tryptophan (Trp)**
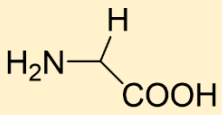	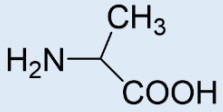	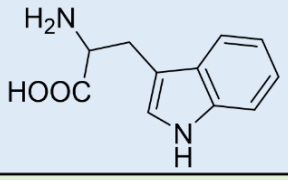
Cysteine (Cys)	**Valine (Val)**	**Lysine (Lys)**
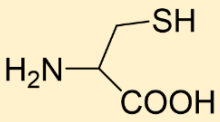	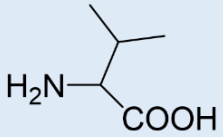	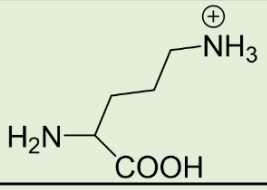
Proline (Pro)	**Isoleucine (Iso)**	**Arginine (Arg)**
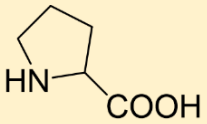	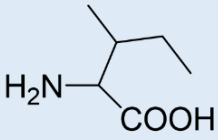	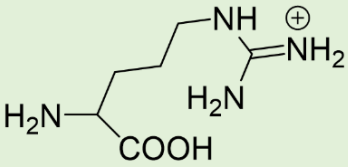
Serine (Ser)	**Leucine (Leu)**	**Histidine (His)**
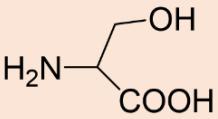	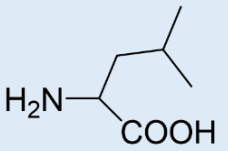	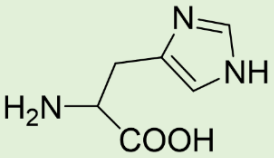
Threonine (Thr)	**Methionine (Met)**	**Aspartic Acid (Asn)**
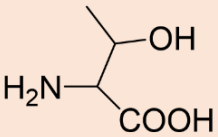	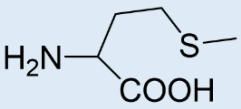	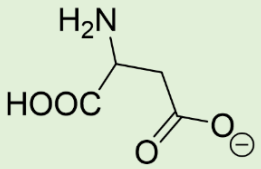
Asparagine (Asn)	**Phenylalanine (Phe)**	**Glutamic Acid (Glu)**
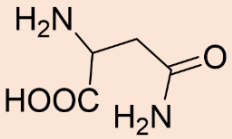	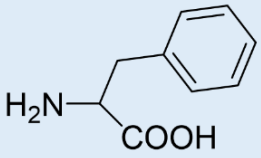	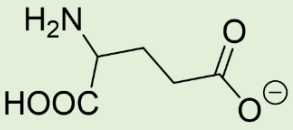
Glutamine (Gln)	**Tyrosine (Tyr)**	Polar (Hydrophilic)
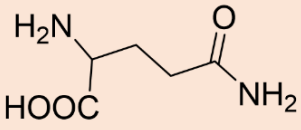	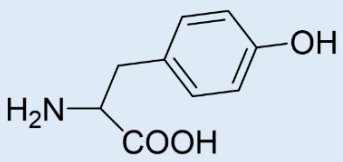	Hydrophobic
		Ionic

In **Table 1.2**, the wide range of exploitable functionality available to amino acids and to consequent poly(amino acid) materials can be visualised. In the literature, the applicability of these amino acids as repeat units in amphiphilic copolymers has been investigated already, with the conjugation of hydrophilic poly(glutamic acid) to polybutadiene by Kukula,[36] and the self-assembly of poly(ethylene glycol)-*b*-poly(phenylalanine) copolymer by Castelletto.[37] The mechanism for this self-assembly is owed to the same biological processes by which polypeptides synthesised within cells undergo folding into discrete and complex shapes, specific to their function.[38] These levels of folding and some specific polypeptide and protein conformations that demonstrate them can be seen in **Figure 1.5** below.

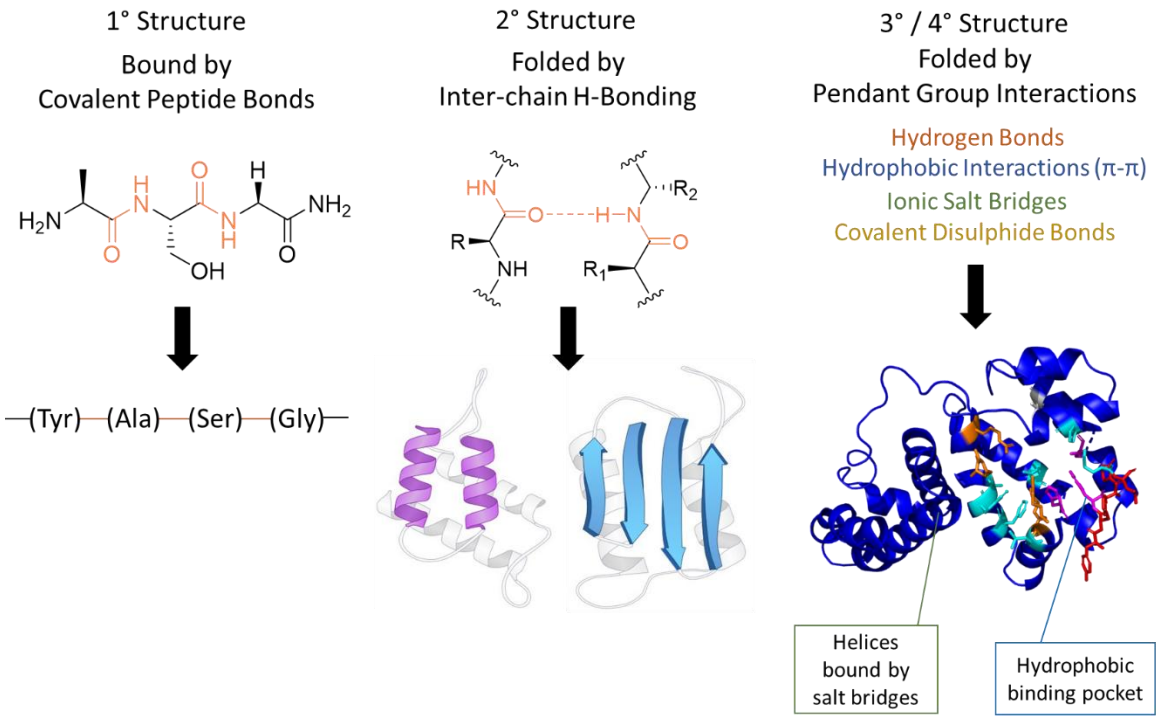

Figure 1.5: The primary, secondary, tertiary, and quaternary structures of polypeptides.

Importantly for the work conducted within this report, key secondary structure folding interactions in polypeptides can be translated to the self-assembly of stable conformations in poly(amino acids). In polypeptides, the formation of conformational domains such as the α-helices in **Figure 1.5** allow for hydrophobic residues in the chain to be internally directed, stabilising them under aqueous conditions.[39]

This is achieved via hydrogen bonding interactions between the core-chain N-H donor and C=O acceptor pairs, situated within each of the amide bonds connecting adjacent amino acid monomers.

For poly(amino acid) amphiphiles, the internalisation of non-polar aliphatic and aromatic residues is imperative, in order for the polymers to encapsulate bulky, hydrophobic-cored molecules, such as therapeutic drug compounds.[40] These interactions stabilise the nanoparticle, improving both stability during storage and during bodily transit, thereby increasing the efficiency of drug molecule delivery to target cells under biological conditions.[41]

Further to this secondary folding, as exemplified in part III of **Figure 1.5**, vital tertiary interactions within the folded polypeptide structure can also be transposed into the bonding interactions involved in the incorporation of drugs into polymer nanoparticles.[42] Specifically, this may relate to the hydrophobic interactions that can occur between hydrophobic residues such as leucine, isoleucine, in their entropically-favourable exclusion of water molecules from a folded pocket, into which an external molecule may be consolidated. This could also relate to intermolecular 'π-π' interactions that occur between quadrupoles, such as the aromatic centres in the side chains of phenylalanine and tryptophan residues and the large, aromatic cores of drug molecules such as doxorubicin.

In addition to the hydrophobic tertiary interactions exhibited above, polypeptides leverage the charged and neutral amino acid residues outlined in **Table 1.2** to further anchor their structural motifs and increase stability.[42] Specifically, ion salt bridges between charged residues such as arginine and histidine, as well as disulphide interactions between cysteine residues, add significant stabilisation to tertiary folding and to the binding of functionalised external molecules. This is extremely relevant to the research of functionalised poly(amino acids) for the design of present and future drug delivery vehicles, through the deployment of post polymerisation modification strategies. Recent examples of this technology include work by Byrne *et al.* who, through the strategic protection and deprotection of lysine side chain functional groups, were able to synthesise well-defined star-shaped polymers for use as gene-delivery vectors.[43]

Another example is the work of Resetco *et al.* in their use of thiol-ene chemistry, wherein cysteine residues on poly(amino acids) were bound via sulphur-to-alkene bonds to a number of components, to improve their sustainability and performance in coating formulations.[44] Clearly, the use of highly-functionalised poly(amino acid) materials in the pursuit of drug delivery vehicles presents a variety of avenues to develop and optimise an effective solution.

However, it is important to first discuss the synthesis of these materials, starting from the cyclisation of amino acids into highly reactive monomer materials known as N-Carboxyanhydrides (NCAs).

1.2.2 N-Carboxyanhydrides (NCAs)

The general structure of an NCA is depicted in **Figure 1.6**. Cyclisation of amino acids by the methods outlined in the subsections below produces a strained 5-membered heterocycle, bearing an anhydride functional group and an NH functionality.

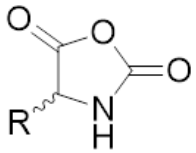

Figure 1.6: A generalised structure of an N-Carboxyanhydride molecule.

In addition, the pendant side chain of the precursor amino acid is conserved, bound to the ring. By cyclising trifunctional amino acids such as lysine and aspartic acid, functionality can subsequently be imparted to the resulting polymer following ring-opening polymerisation of the molecule. This in turn necessitates the careful application of protecting species, such as fluorenylmethoxycarbonyl (Fmoc) and tert-butoxycarbonyl (Boc) esters, to prevent unwanted side-reaction during polymerisation. These protecting groups are illustrated as appendages to the side chain of lysine NCA in **Figure 1.7** below.

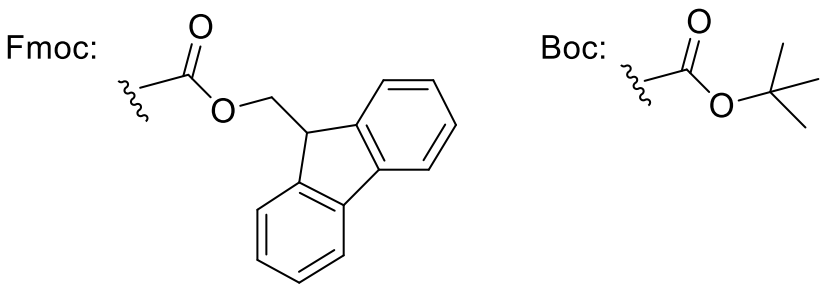

Figure 1.7: Structure of Fmoc and Boc protecting groups.

Polymerisation from N-Carboxyanhydrides also represents a promising alternative to solid-phase peptide synthesis (SPPS), which is currently utilised to manufacture small-scale, short-chain peptides in a highly controlled manner in the present literature.[45,46]

This is because SPPS is achieved by the sequential addition of amino acid molecules, via their α-amine groups, to the unprotected C-terminals of growing peptide chains, immobilised on an inert support material.[47] This process is lengthy and laborious, as each addition of a new amino acid monomer must be followed by a subsequent wash of any unreacted material, as well as deprotection step for the newly-bound peptide C-terminals, before the next intended amino acid monomer can be added to the surrounding solution phase. Furthermore, it was noted by Deming that with an increase in the number of added amino acids, the likelihood of sequence errors in the chains increases exponentially, due to unavoidable deletions and truncations that occur as a result of the failure of these coupling and deprotection reactions.[48] As a result of this, and of the high expense in using a specialist technique such as SPPS, it is avoided in industry for the large-scale production of poly(amino acid) materials over 100 repeat units.

N-Carboxyanhydrides were first synthesised by Hermann Leuchs in 1906, by heating *N*-ethoxycarbonyl or *N*-methoxycarbonyl amino acid chlorides under vacuum between 50 °C and 70 °C.[48-50] The mechanism of this cyclisation reaction is illustrated below in **Scheme 1.1**.

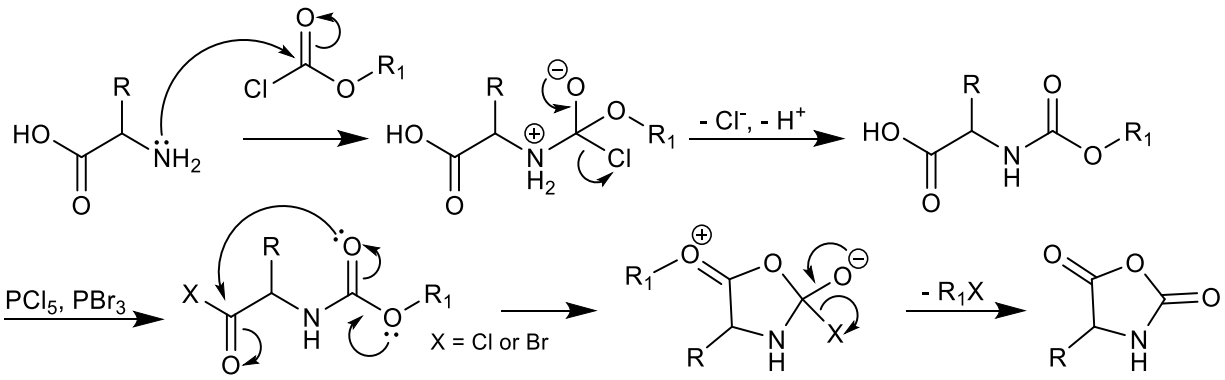

Scheme 4.1: Mechanism of Leuchs carbonylation between an amino acid and a chloroformate molecule, followed by phosphorous pentachloride to form an acid chloride. This is then followed by cyclisation. R – amino acid side chain, R_1 – typically Ph.

This method was not very effective, however, resulting in low yields and impure products. This was because the architecture of the NCAs was fragile and, under the high temperature conditions in the presence of moisture, they underwent ring-opening hydrolysis back to the original amino acid.[51,52]

It should be noted that this ring-opening reaction is entropically favourable for the NCA molecule. This is partly due to the release of ring strain upon opening, as well as the release of a molecule of carbon dioxide during the process. Whilst this process is detrimental for NCA preparation, the positive entropy change is what makes N-Carboxyanhydrides desirable for well controlled ring-opening polymerisation, even under mild conditions.

In 1922, Fuchs published a report on NCA synthesis, whereby an amino acid was coupled to phosgene *in situ* in order to activate it towards ring closure, which greatly simplified and cheapened the preparation of the NCA.[53,54] The Fuchs-Farthing method removed the two-step preparation process of the Leuchs method, shown in **Scheme 1.2**, whereby benzyl chloroformate and thionyl chloride were conjugated to the amino acid to promote cyclisation. This was beneficial both to cost and to purity, as the benzyl chloroformate adduct could not be purified by distillation, resulting in the formation of impurities in the final NCA product. In addition, the use of benzyl chloroformate resulted in the side production of benzyl chloride, more material that had to be removed via increasingly expensive purification strategies.

The Fuchs-Farthing method eliminated these impurities, with the only side product from phosgene being two molecules of HCl per molecule of NCA. Clearly, this method was the more efficient in both cost and resources, and so it is still used in modern NCA syntheses. However, several improvements have been made to the Fuchs-Farthing method over the course of the 20th century, most significantly being the application of liquid diphosgene and solid triphosgene in the place of phosgene gas.[53] This was done to avoid hazards when handling the materials, due to the toxicity of phosgene, which will be discussed.

Scheme 1.2 details the mechanism of the Fuchs-Farthing method, with generalisations for the amino acid used, and structures for the phosgene derivatives, diphosgene and triphosgene, provided.

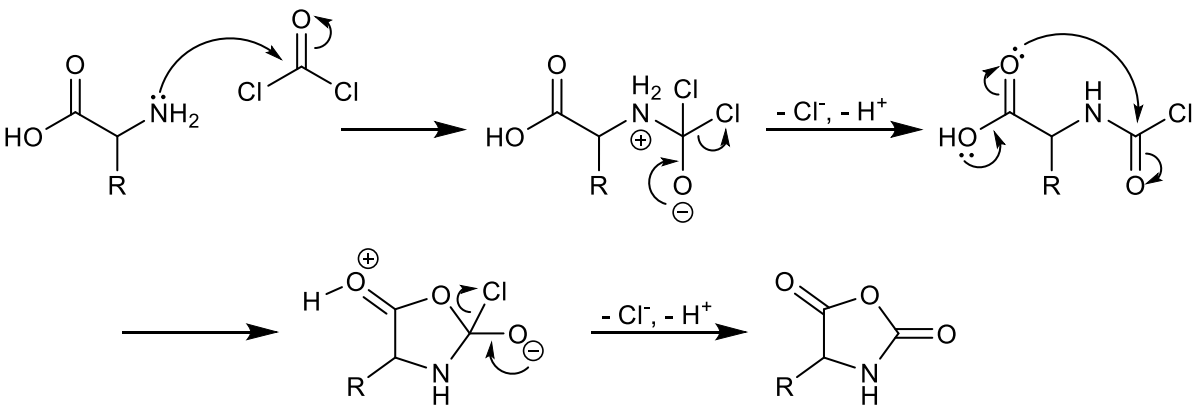

Scheme 1.5: Mechanism for the Fuchs Farthing carbonylation reaction of an amino acid with a phosgene derivative, here shown as a post-derivative-degradation phosgene molecule.

The use of phosgene-derived reagents in the Fuchs-Farthing method, as shown in **Scheme 1.2**, presents a number of obstacles for the operator, especially in the interest of industrial-level scale-up. Phosgene in the gaseous form is extremely toxic and used in the First World War as a chemical weapon. Its weaponisation is attributed with the deaths of around 85,000 people.[55,56] For this reason, crystalline solid triphosgene and liquid diphosgene, which undergo degradation pathways to phosgene gas under reflux conditions, are used *in situ* instead.[33,34] These derivatives are effective at reducing the exposure of operators to phosgene gas to safe levels, less than 2 ppm in air, as defined by the National Institute for Occupational Safety and Health (NIOSH).[59]

Use of these derivates does not, however, reduce the negative impact of the two molecules of HCl generated *in situ* during the synthesis of one molecule of NCA. The presence of HCl in high concentration during this reaction can be detrimental not only for the scale-up of NCA synthesis, but also for the purification of the products and in their subsequent utilisation in ring-opening polymerisation.[60] According to Smeets *et al.*, scale-up of the Fuchs-Farthing procedure slows the liquid-to-gas mass transfer of the HCl molecules.[61] This results in a build-up in the concentration of the HCl molecules, which can then protonate the free amine functional groups of the unreacted amino acid, reducing their nucleophilicity and thereby retarding the rate of reaction.

Furthermore, the increased concentration of HCl molecules increases the probability of their interaction with the newly formed NCA product molecules, resulting in the degradation reaction shown in **Scheme 1.3**, and the subsequent generation of amino acid chloride molecules.[61] These molecules can further react with phosgene or the NCA to produce a wide range of by-products, driving down the yield and overall purity of the reaction.

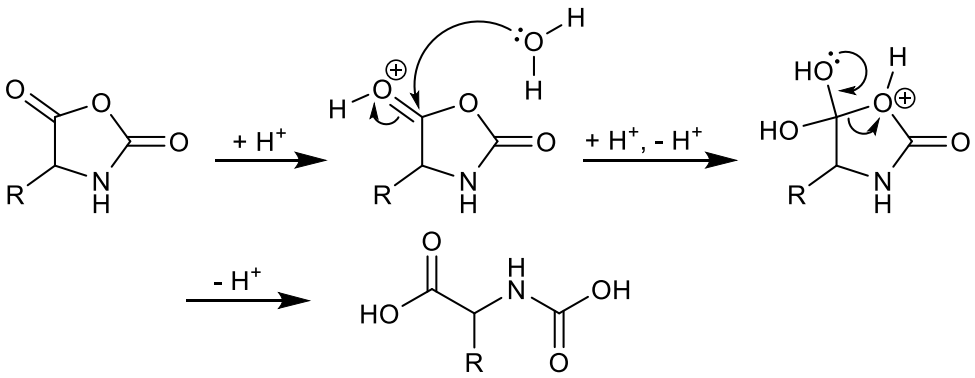

Scheme 1.6: Mechanism for the hydrolysis of an NCA molecule under acidic conditions.

In order to mitigate the effects of high HCl concentration, it is necessary to employ a radical scavenger such as α-pinene or limonene. These are monoterpene molecules that are capable of binding to free HCl in solution during reaction, preventing their disassociation into protons and chloride ions and effectively removing them from the system. This action both reduces the effective proton concentration in solution, vastly reducing the potential for acid-catalysed hydrolysis reactions, as well as relieving the mass transfer traffic of the reaction vessel to allow more HCl molecules to enter the gaseous phase and be removed.

Overall, this results in a notable decrease in the probability of side-reactions during NCA synthesis, thereby improving the purity of the product.

In addition to the health and safety risks associated with phosgene-derived reagents, the harshly acidic conditions of Fuchs-Farthing carbonylation limit its application in the presence of acid-labile functional groups, such as the *tert*-butoxycarbonyl (Boc) protecting group. Pertinent to this research, protected Lys(ε-Boc) is incompatible with this method, highlighting the practical need to explore safer, phosgene-free alternatives.[62]

In 2021, Laconde *et al*. published research on carbonylation reactions using propylphosphonic anhydride (T3P), providing a phosgene-free route to NCAs.[63] Using an amino acid with a Boc group protecting the α-amine, the mechanism of action for this process varies dependent on the method of activation for the T3P. Generalised outlines for each of these methods are illustrated in **Scheme 1.4** below.

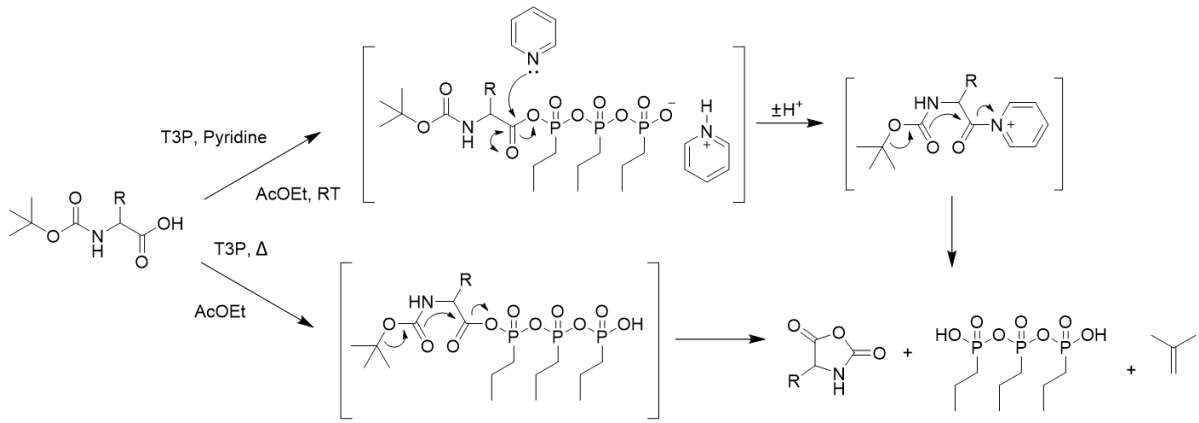

Scheme 1.4: Base and thermal activated routes for T3P cyclisation of amino acids into NCAs.

This method provides a high-yielding, high-purity and phosgene-free alternative to the Fuchs-Farthing carbonylation reactions typically employed in the synthesis of NCAs. With significant reduction in personal and environmental safety ramifications, this method is also far more suitable for scale-up and use in an industrial context for the production of NCA monomer materials within similar timescales.

1.2.3 N-Carboxyanhydride Ring-Opening Polymerisation (NCA ROP)

N-Carboxyanhydrides are converted to poly(amino acids) via a chain-growth, ring-opening polymerisation (ROP) reaction. The reaction features an initiation step, in which an active

molecule is generated by one of two reaction routes. This activated molecule then proceeds to attack the NCA rings in a propagation step, opening them and generating active chain ends, which can undergo further propagation, extending the chain. ROP reactions can be initiated using a variety of activated species, including radicals, anions and cations. In the case of NCA polymerisation, literature sources have traditionally utilised nucleophilic and basic functional groups such as primary amines and alkoxide ions as initiators.[64,65] This is no different for the preparation of amphiphilic block copolymers for nanoparticle self-assembly. Block copolymer syntheses can also utilise macroinitiator species instead of small molecule initiators, allowing for expedient synthesis and facile control over the relative sizes of each block.

In the late 1980s, Hans R. Kricheldorf defined two synthetic pathways for the polymerisation of NCAs.[61,64] The first of these, known as the 'normal amine' (NA) mechanism, is shown in **Scheme 1.5** below, and involves nucleophilic attack by the initiator species into the more electrophilic carbonyl carbon of the NCA ring, which sits opposite the nitrogen atom. Following this addition-elimination reaction at the carbonyl carbon, the NCA ring opens and undergoes proton transfer to yield an unstable carbamic acid intermediate. This is quickly ensued by the elimination of a molecule of carbon dioxide from the terminal of the chain, exposing a terminal primary amine group, which is capable of further nucleophilic attack, propagating polymerisation.

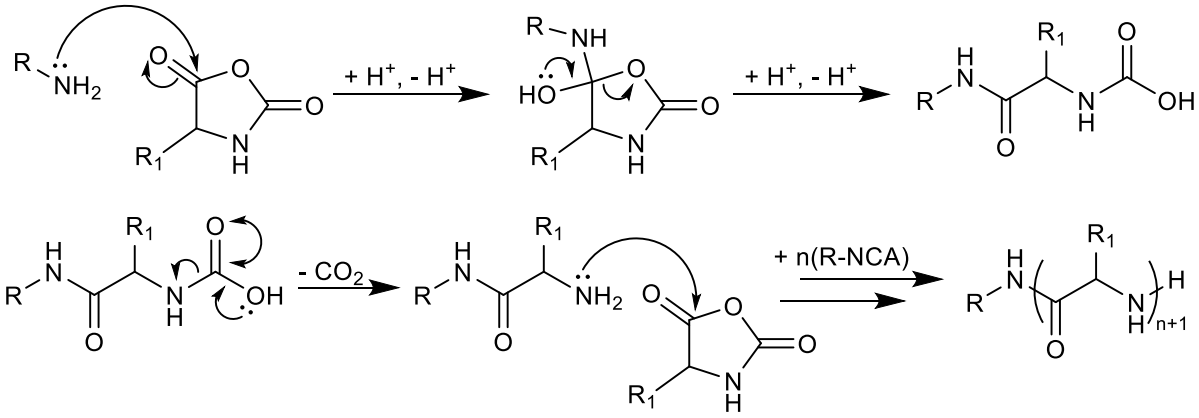

Scheme 1.5: Mechanism for the normal amine route of NCA ROP.

Due to the nucleophilic nature of the initial attack of the NAM route, this mechanism is favoured by primary amine initiators and, conversely, the effective rate of initiation is

determined by the nucleophilicity of the incident functional group.[62] The rate of initiation for the NAM route is in fact higher than that of propagation, though this reportedly does not adversely affect the dispersity of the product polymer chains.

The second mechanistic pathway, referred to as the 'activated monomer' (AM) route, describes a basic role of the initiator, deprotonating an NCA to generate the nucleophile that initiates chain growth. The AM mechanism is illustrated in **Scheme 1.6**. This route is particularly preferable for tertiary amine initiators, although it would be more apt to describe their role as catalytic here.[50]

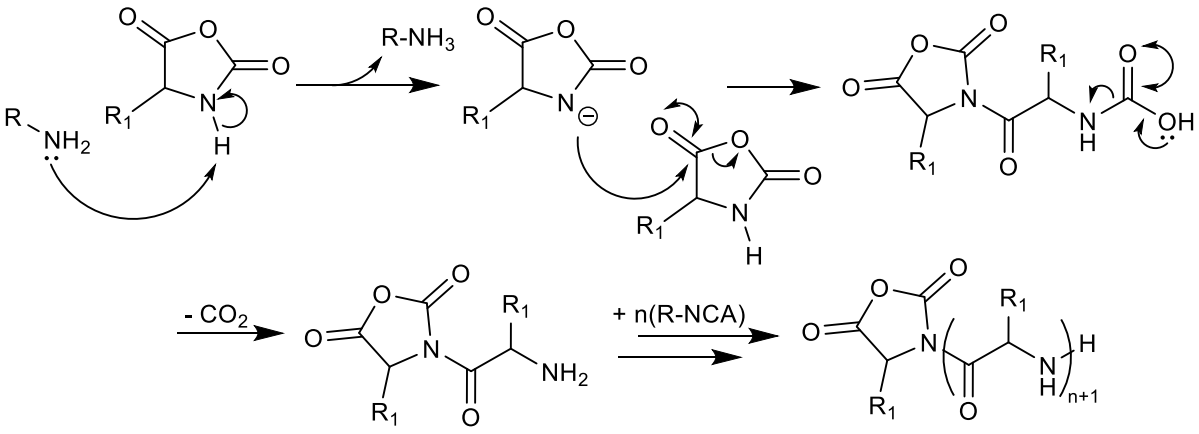

Scheme 1.6: Mechanism for the activated monomer route of NCA ROP.

According to Deming *et al*., the two mechanisms presented above are side reactions of one another and a given system is capable of switching between the two modes multiple times over the course of a reaction. This represents a challenge in the synthesis of block copolymers using NCA monomers, with product structures varying significantly from monomer feed compositions and considerable levels of homopolymer contamination.[50] Pertinent to the research conducted for this report, this may prove detrimental in the synthesis of poly(amino acids) via ROP of NCAs from macroinitiator species, if the AM route proves to be prevalent. Additionally, it should be noted that the rate of initiation (or more accurately deprotonation) of the NCA molecules by tertiary amine initiators is much slower than the rate of propagation, likely owing to the high steric bulk of such initiator species.

As such, products of the AM route have higher molecular weights, but suffer from broad dispersity values, a quality that limits the efficacy of this reaction mechanism in the pursuit of highly regular nanoparticle structures.[50,62]

Another inherent hindrance in conventional NCA polymerisation is the lack of control over the reactivity of the active chain end during reaction. Once the initiator has reacted with an NCA monomer the resulting primary amine, carbamate ion or NCA anion is free to undergo a number of undesirable side reactions. Furthermore, low purity of the NCA monomers can also be a considerable problem. Impurities include traces of acid from improper HCl scavenging during phosgenation and ring closure of the parent amino acid, as well as acid chlorides and isocyanates. These impurities are capable of quenching the propagating chain, limiting molecular weight control and resulting in high dispersity values, which is detrimental to their ability to form effective nanoparticles for drug delivery. Finally, the presence of other adventitious impurities, such as water, can damage polymerisation by acting as chain transfer agents, as well as engaging in acid-catalysed hydrolysis of the product poly(amino acid) chain, yielding oligomeric homopolymer contaminants.[45]

A number of synthetic strategies are available to improve monomer conversion, increase polymer molecular weight, and narrow polymer dispersity values when undergoing ROP of NCA monomers. One example of such optimisation procedures is to work under high vacuum, used to remove contaminating species such as water, carbon dioxide and volatile carbamates from the reaction mixture.[63] Another example is the use of low temperatures during ROP reaction. According to the literature, the degree of polymerisation decreases as higher reaction temperatures are reached, which suggests a dominance in the rate of propagation at low reaction temperatures, and the increased prevalence of chain transfer and termination reactions as temperature increases.[66,67]

1.3 Poly(hydroxyacids) for Drug Delivery

Poly(hydroxy acids) pose an exciting alternative to poly(amino acid) materials for biomedical applications, personal care products, and therapeutics. In the therapeutic landscape, these materials are extensively exploited for drug delivery, gene therapy and tissue engineering.[68]

This is again due to the biomimetic behaviour of polyester materials, as well as their ability to undergo enhanced degradation of main-chain ester linkages in the presence of pH and enzymatic stimuli, which makes them excellent conveyors for anticancer therapeutics.[69] However, synthetic complications in the pursuit of these materials have left an opening in the literature for further developments to be made.

There are three major methods for the synthesis of aliphatic polyesters. The first is conventional direct polycondensation of a diol and a diacid, expelling water as a condensate.[70] Due to the wide availability of difunctional starting materials, this technique offers a range of functionally versatile polyester products, which would suggest that it is a suitable source for therapeutic polyesters. However, the step-growth polymerisation mechanism used to combine these difunctional reagents poses significant drawbacks. Firstly, these reactions are incapable of exceeding low values for the degree of polymerisation prior to achieving 99 % reaction completion, which can result in low molecular weight polymers.[71,72] Additionally, the required combination of large polymer chains late in the reaction can have significant adverse effects on the final dispersity values of the product polymer. This lack of control could render most step-growth polymerisation products unsuitable for the purposes drug delivery, due to the very specific size requirement put upon materials crossing the digestive membranes of the body. Furthermore, the mechanism of step growth polymerisation requires two bifunctional monomer units to be combined in an alternating pattern to build the chain, removing the possibility of synthesising amphiphilic block copolymers for drug delivery using this method.

The second method of polyester synthesis is to utilise enzymatic polymerisation methods, avoiding the need for harsh reaction conditions and toxic reagents in lieu of a specialised and (occasionally) recoverable biological catalyst.[73] Furthermore, the stereo- and regioselectivity of the enzyme affords the opportunity for direct synthesis of functional polyesters and block polyesters without the need for orthogonal protecting groups or their incumbent deprotection procedures.[74] However, enzymatic reactions also suffer from a somewhat major flaw, in that they also produce polymers with such low molecular weights that they may not be suitable for use in nanoparticle formation and drug molecule encapsulation.[70] The third

method, which must be further investigated, is the use of ring-opening polymerisation techniques from the cyclisation products of hydroxyacid (HA) starting materials.

1.3.1 Hydroxy Acids

The general structure of a hydroxy acid is presented in **Figure 1.8** below. Similar to amino acids, the tri-substituted α-carbon is flanked by an adjacent carboxylic acid functional group. However, on the opposite terminal, hydroxy acids bear a tertiary alcohol group instead of an amine.

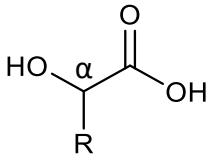

Figure 1.8: A generalised hydroxyl-acid molecule.

Whilst fewer hydroxy acids have been investigated as potential monomers for amphiphilic block copolymer synthesis, there are a number that have some precedence in the existing literature. Illustrated in the **Figure 1.9** below are examples of the hydroxy acids that have been used in the production of such copolymers including lactic acid, mandelic acid, and malic acid.[76-80]

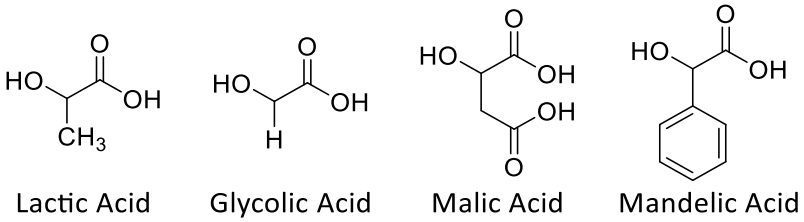

Figure 1.9: Structures of the prominent hydroxy acid monomers in recent literature.

Notably, the first three of these examples are direct analogues of the amino acids alanine, glycine and aspartic acid, with mandelic acid closely resembling phenylalanine. The lack in functionality of lactic acid and glycolic acid made them the ideal starting points for the initial attempts to synthesise polyesters by Kricheldorf in the 1980s.[61] Whilst later forays conducted by Dove *et al.* in 2010 using O-Bn protected malic acid were less successful,[80] efforts by Buchard *et al.* derived poly(mandelic acid) from O-Carboxyanhydride (OCA) molecules.[79,81]

Despite their visual similarities to NCAs, the technology behind OCAs was not pioneered until around 50 years later As such, a wide range of opportunity is still available for the application of hydroxy acids in the field of therapeutic drug delivery.

Prior to the implementation of OCA techniques, initial methods of developing polyesters involved the formation of cyclic diester molecules from low-functionality hydroxy acids such as lactic and glycolic acid.[81-84] This process is outlined in **Scheme 1.7** below.

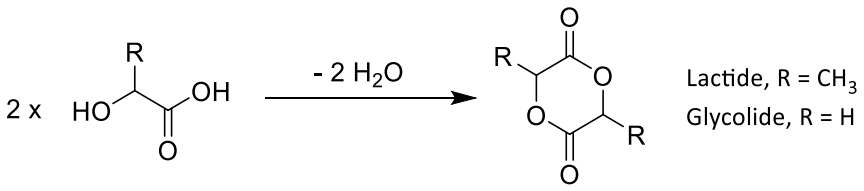

Scheme 1.7: Combination of two hydroxy acid molecules into a cyclic ester molecule.

Whilst this method was effective for the preparation of low-functionality monomers for polyester synthesis, the introduction of functional groups proved to be a significant challenge for prior investigators. It was found by Dove *et al.* that, during the synthesis of the cyclic ester of L-malic acid, the yield of dimerisation of the corresponding α-hydroxy acids catalysed by *p*-tolunesulfonic acid under reflux was only 30 %.[80] According to the authors, this was due to the formation of undesired oligomer by-products via trans-esterification reactions. Attempts were made to mediate these side-reactions using high dilution techniques, without success. As a result, more recent literature has avoided the use of these cyclic esters, instead applying O-carboxyanhydride technologies to greater success.

1.3.2 O-Carboxyanhydrides (OCA)

The first synthetic preparation of O-carboxyanhydrides was demonstrated by Davies in 1951 who, in a similar fashion to Leuchs, reacted an α-hydroxy acid with phosgene to form a cyclic anhydride.[85] The general structure of an OCA is illustrated in **Figure 1.10.**

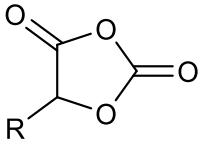

Figure 1.10: The generalised structure of an OCA molecule.

The preparation of a generalised OCA molecule is presented in **Scheme 1.8** below. This method also bears similarities to the Fuchs-Farthing method, utilised to synthesise NCA molecules.

A notable difference in the technique used, however, is that OCA synthesis generally occurs under ambient conditions. For this reason, triphosgene is not used in the synthesis of OCAs as its breakdown to phosgene under ambient conditions would be too time-consuming. As a result, the dimer diphosgene is used instead alongside activated charcoal.

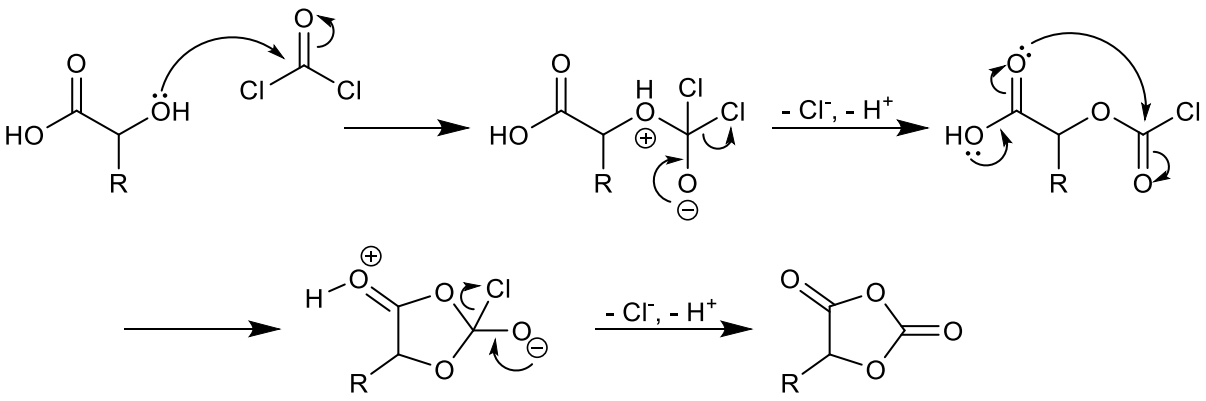

Scheme 1.8: The Fuchs-Farthing mechanism for OCA synthesis.

1.3.3 O-Carboxyanhydride Ring-Opening Polymerisation (OCA ROP)

Similar to NCAs, ROP of OCA monomers occurs either *via* the 'normal amine' mechanism or the 'activated monomer mechanism'. As was noted previously, the activated monomer mechanism is not useful for the formation of amphiphilic block copolymers and increases the risk of homopolymer contamination within the product. However, this can be mitigated by using a nucleophilic initiator species, and through a range of catalyst options, with specific examples discussed below for their relevance to this research.

As for NCA ROP molecules, the driving force behind OCA ROP is the loss of a molecule of CO_2, following the opening of the OCA ring. The loss of gaseous CO_2 following this elimination step prevents the possible (although unlikely) re-cyclisation reaction, meaning reformation of the OCA is not possible, and the only available forward step in the reaction is to attack another OCA molecule.

This is a simple exploitation of Le-Chetalier's principle of equilibrium, but the implications for the ROP reaction of OCA molecules is vast, when compared with the reaction of lactide and glycolide cyclic esters. In 2015, it was demonstrated by Bourissou *et al*. that the ring-opening process of the lactic acid OCA molecule is thermodynamically more favourable than that of the lactide cyclic ester.[77] This was determined computationally using density functional theory (DFT), which modelled the reactions of both of the cyclic lactic acid derivatives. This thermodynamic penalty to the opening of lactide is another supporting argument for the use of OCA molecules for synthesising polyester materials, as they can undergo ROP reactions under mild conditions. However, this does not mean that catalyst options are not available for the ROP of OCAs.

The most common example of an organocatalyst for the ROP of OCAs is 4-dimthylaminopyridine (DMAP). DMAP is a well-known catalyst for acylation and transesterification reactions, and was used in the pioneering work of Hedrick *et al*. in 2001 in the ROP of lactide without metal contaminants.[86] Another piece of prominent research in this field is the work of Bonduelle *et al.* who, in 2008, developed a computational model for the mechanism of action of DMAP within the ROP reaction of lactic acid OCA.[87] It was found by Bonduelle *et al*. that two competing mechanistic options were possible for DMAP. It could act either as a nucleophile, attacking the carbonyl group adjacent to the OCA pendant chain and forming an acylpyridinium intermediate before being substituted for the attacking alcohol, or via basic activation of the initiating/propagating alcohol, facilitating its attack of the OCA ring. The detailed computational study performed by Bourissou *et al.* upon these possible mechanisms determined not only that a slight energetic preference existed for the basic route, but also that DMAP was capable of simultaneous activation of both the incident alcohol and the target carbonyl of the OCA molecule, via a weak nonclassical H-bonding between the ester carbonyl of the OCA and an *ortho* H of DMAP.[87] This bifunctional basic activation route by DMAP, with concomitant activation of the propagating chain end and the monomer is illustrated in **Scheme 1.9** below.

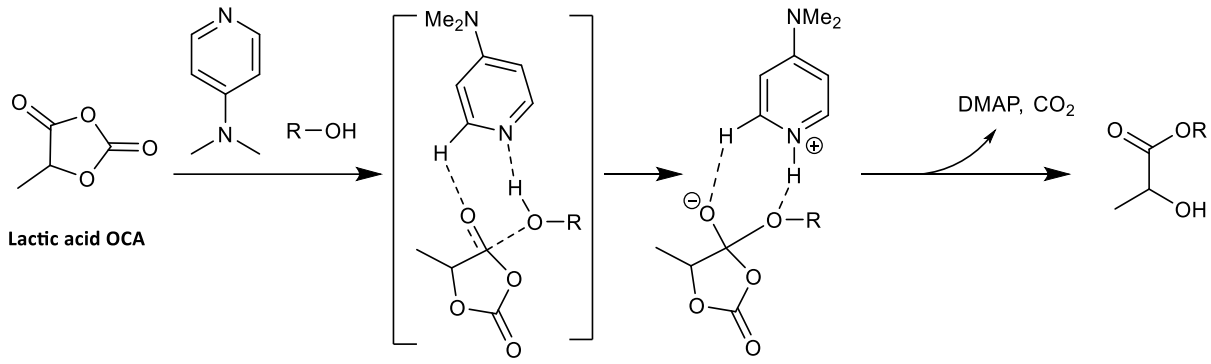

Scheme 1.9: Reaction scheme for the bifunctional catalysis of OCA ring opening by DMAP.

Other recent developments in the literature for OCA ROP organocatalyst options include N-heterocyclic carbenes (NHCs) and thiourea-based organocatalysts, as well as acid/base adducts of OCA molecules.[79] While the work of Li *et al.* in NHC catalysis did yield promising results, producing polymers with dispersity values between 1.10 and 1.16 and achieving degrees of polymerisation as high as 200. This was because of the stereochemical control achieved by these reactions. In 2014, Buchard *et al.* found that crystalline adducts of mandelic acid OCA (manOCA)and pyridine were capable of both catalysing the ROP of manOCA monomers, as well as suppressing the epimerisation of these OCA molecules that could be expected from DMAP catalysis.[79] This yielded higher isotacticity in the product polymers.

1.4 Complex Polymer Architectures for Drug Delivery

The utilisation of complex polymer architectures to enhance the encapsulation, stability and selectivity of therapeutic delivery platforms remains a burgeoning area of development in the current literature.[88-90] Such topologies are achieved *via* the employment of multifunctional motifs during polymer design to create branch points, from which more than one chain can extend.[91] This can significantly vary the resultant product, depending on when this motif is deployed during multi-stage synthesis. Examples of this architectural variety, achievable with only 2 distinct blocks, is illustrated in **Figure 1.11** below.

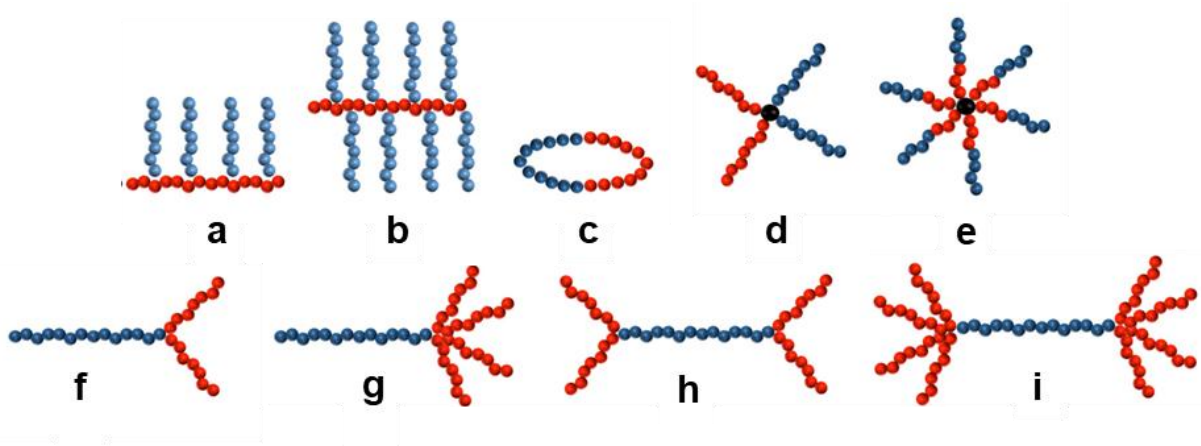

Figure 1.11: Examples of complex architectures, including (a) graft; (b) brush or comb; (c) ring; (d) star; (e) star-block; (f) AB_2 star; (g) palm tree; (h) dumb-bell; and (i) H-shaped. Adapted from Gregory and Stenzel [9]

Compared to linear polymers, complex architectures such as branched, hyperbranched and dendrimeric polymers offer advantageous properties for the encapsulation and delivery of small-molecule payloads. This includes a high density of surface-active functional groups key to biomimicry and compatibilisation *in vivo*, as well as an extensive void space within the branched architecture to house guest molecules.[92-94] Early success of highly complex encapsulation systems was demonstrated by Jansen *et al*. in 1993, wherein DAB(PA)64, a fifth-generation dendrimer of poly(propylene imine) was utilised as a "dendritic box" to house a range of small dye molecules, with marked improvement over linear equivalents.[95] Upon dye encapsulation, variations of bulky amino acid residues (Boc-Phe, Boc-Tyr, Boc-Trp) were attached to the terminal amine groups of the dendrimer *via* NHS-activated ester amidation. According to the authors, this locked the encapsulated dye molecules into place within a dense shell with solid-phase characteristics, demonstrating markedly improved retention versus non systems. Diffusion of dye molecules was deemed "unmeasurably slow", even after weeks in solution and after extensive washing and solvent exchange. This pioneering system laid the groundwork for subsequent developments in branched polymer architecture, utilising complex topologies for encapsulation of small molecules and extending this practice to therapeutic payloads.

1.4.1 Branched and Hyperbranched Polymers

Branching in polymer synthesis can be introduced at several stages, depending on when and how the multifunctional groups are incorporated into the chain. For NCA ROP, the use of multifunctional initiators such as poly(ethyleneimine), PAMAM dendrimers or derivatives of pentaerythritol allows for several simultaneous sites of propagation, yielding star-branched poly(amino acid)s with well-defined arm numbers.[96-98] A notable example of such star-branched polymers applied to therapeutic applications in the literature was reported by Walsh *et al*., who synthesised bio-inspired star-PLL *via* NCA-ROP from PAMAM dendrimers.[98] Deprotection of the product generated cationic primary amine termini for nucleic-acid complexation, with the goal of improved transfection (non-viral delivery) of DNA to mesenchymal stem cells (MSCs), in comparison to both linear PLL and branched PEI (a prominent but cytotoxic industry standard).

Within these MSCs, star-PLL achieved ca. 50 % transfection efficiency, greatly surpassing the ca. 10 % efficiency of the linear PLL, and achieved a ca. 40 % improvement in cell viability versus the PEI benchmark, indicating significantly reduced cytotoxicity. This system highlighted not only the improved biocompatibility of poly(amino acid) polymer systems, but the significant increase in functional density that can be afforded by application of branched polymer architectures for therapeutic complexation and encapsulation. Conversely, branching can also arise during propagation when the monomer itself bears a latent nucleophilic group, as in the polymerisation of Nε-allyloxycarbonyl-L-lysine NCAs, wherein pendant amine groups initiate secondary ROP to yield hyperbranched architectures.[99] A prominent therapeutic example from the literature is the work of Kadlecová *et al*., who synthesised hyperbranched poly(L-lysine) (hb-PLL) *via* NCA-ROP of ε-carbobenzyloxy-L-lysine N-carboxyanhydride (Lys(Z)-NCA). After partial deprotection, pendant ε-amines then underwent re-initiation, producing a hyperbranched topology, which was then evaluated against commercial linear PLL and PAMAM dendrimers of similar charge density for the complexation and transfection of enhanced green fluorescent protein (EGFP) into CHO DG44 cells (a well-established mammalian model for gene-delivery). At similar molecular weights to the linear PLL, but with significantly higher branching density, hb-PLL formed smaller and more stable polyplexes, translating to an 8-fold increase in transfection efficiency.

This was comparable to the branched PEI alternative, which was again improved upon by the increased cell viability (ca. 35 %) of the biomimetic hb-PLL.

Despite the clear functional benefits presented by branched and hyperbranched poly(amino acid)s, several challenges are presented in their synthesis, stemming from an intrinsic lack of control over their topology. For uncontrolled, branching NCA ROP, initiation and propagation can occur irregularly across the available nucleophilic amine sites, creating a greater risk of molecular weight broadening and inconsistent branch density, which in turn harm the reproducibility of the final product.[100] This contrasts with linear NCA ROP, where all chains initiate simultaneously from a fixed number of initiator molecules. For hyperbranched systems, stochastic initiation throughout the reaction duration continuously alters the growth population, reducing uniformity (Đ = 1.5-2.0) and structural homogeneity.

In contrast, the synthesis of dendrimers occurs *via* stepwise generational growth, wherein branching and termination are more closely controlled, yielding monodisperse macromolecules with uniform size and functionality.[101]

1.4.2 Dendrimers and Telodendrimers

Dendrimers represent the pinnacle of control in branched polymer architecture, synthesised through stepwise, generational addition of defined branch points and terminal groups, to yield monodisperse, globular macromolecules with predictable molecular weight, diameter, and surface functionality. In divergent dendrimer synthesis, a multifunctional initiator is utilised at the core, followed by an iterative process of attaching protected blocks *via* coupling reactions, deprotecting and repeating to layer additions of the growing chain.[102] This allows stoichiometric control of chain growth, as well as temporal control of branch location and frequency. The generational growth and notable architectural domains of a generic dendrimer is provided in **Figure 1.12** below.

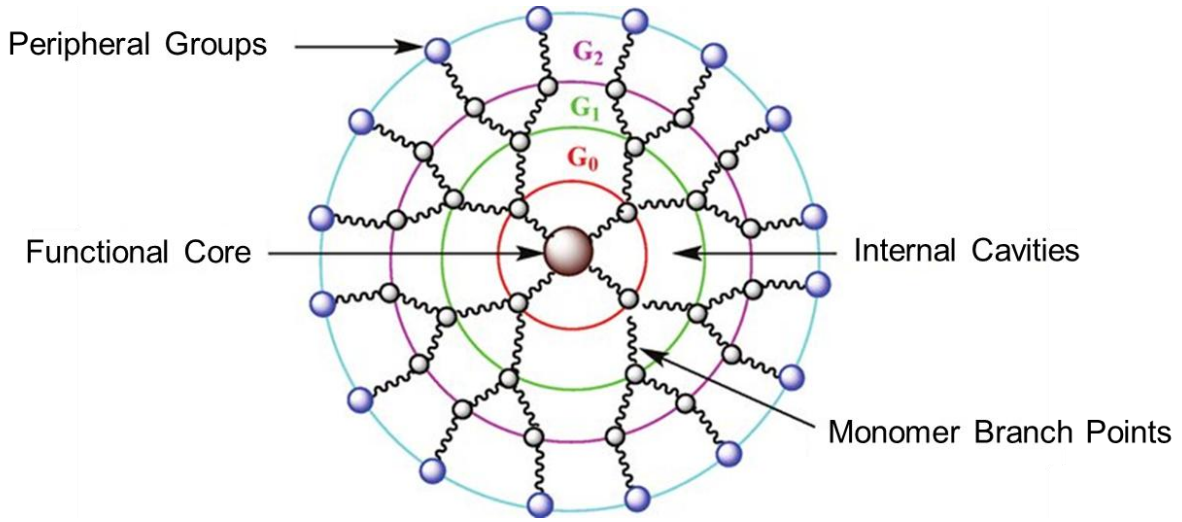

Figure 1.12: Structural features of a generic dendrimer.

The internal cavities and peripheral functional groups of the dendrimer can be furnished independently, providing distinct domains for encapsulation, conjugation, or targeted ligand display.[95,103,104] This functional and spatial organisation allows dendrimers to act as unimolecular nanocarriers, with their respective drug loading capacity, release rate and biological interaction tuneable through architectural design.[105,106]

Recent developments in therapeutic applications of dendrimer technologies have employed poly(amino acid)-based dendrimers and telodendrimers, which combine a dendritic head with a linear or amphiphilic tail for enhanced self-assembly and assisted biocompatibility.[107,108] These systems leverage the functional density and compartmentalisation of dendrimers, whilst improving physiological stability and scalability for therapeutic use. A recent example of this is the work of Luo and Lam, who synthesised PEG-oligo(cholic acid) telodendrimers for the encapsulation of gambogic acid (broad-spectrum anticancer therapeutic) contrasted against linear PEG-vitamin E (PEG5k-VE_4) and TPGS (PEG1k-VE).[107] During encapsulation, the linear controls aggregated when loaded (GA/polymer = 1:10 w/w), whereas the optimised telodendrimers formed stable, monodisperse nanoparticles with high drug loading (GA/VET = 3:10, w/w ≈ 23 wt%). They also reported high loadings of paclitaxel, up to 36.5 wt%, which exceeded typical linear PEG-PDLLA micelles (ca. 25 wt%) and remained stable for far longer than the linear benchmark (ca. 24 h).[109]

Complementing this is the work of Khandare *et al*., who developed poly(L-lysine) dendrimer-PEG conjugates for doxorubicin delivery, in which the payload was covalently and non-covalently associated within the PEGylated dendritic carrier.[110] The resulting formulation showed a >10-fold increase in solubility over free DOX and a marked improvement over the linear PLL control, which showed poorer drug incorporation and "failed to solubilise DOX effectively". Furthermore, acute toxicity was substantially reduced, with ca. 2x dosage tolerated in comparison to linear PLL-DOX formulations, and significantly reduced body-weight losses for mice receiving the formulation. Circulation half-life was also improved markedly, showing over 3-fold increase over the linear alternative. Finally, bio-distribution studies evidenced that the dendrimer-PEG-DOX system achieved ca. 2x higher tumour accumulation at 24 h relative to the linear carriers, attributed to the more compact and biocompatible scaffold of the dendritic system. These examples demonstrated how precise, generational control of dendrimers enables a level of structural definition and functional tuning unattainable within linear and hyperbranched architectures.

However, dendritic delivery systems are not without drawbacks. The highly-controlled, multistep nature of their synthesis presents a significant challenge to industrial translation and large-scale manufacture.

Each generation of growth typically requires iterative protection-deprotection and coupling cycles, with near-quantitative conversion, making the process labour-intensive, time-consuming and reagent-demanding, relative to linear or hyperbranched polymers.[111] This also contributes to high production costs, as the risks of incomplete reaction, purification losses and defect removal accumulate with increasing generation number.[102] Furthermore, the requirement of tight reaction control and successive chromatographic purification steps limits scalability also, restricting dendrimer synthesis to specialised facilities with small batch sizes.[113] These synthetic and operational limitations present a significant real-world obstacle, preventing widespread commercial deployment of dendrimer-based therapeutics.

1.4.3 Graft Copolymers

Graft copolymers represent a broad class of products in which functional pendant side chains, the same utilised for branching in hyperbranch and dendrimer syntheses, are exploited to introduce additional functionality and topological features.[114] This architecture sits conceptually between linear amphiphilic systems and the highly branched and complex architectures described above, both in terms of customisability, synthetic complexity and resource requirement.[115] The modularity of these systems allows for properties such as hydrophilicity, sensitivity to stimuli and drug loading to be independently tuned, through the choice and density of grafted segments. This culminates in a platform that is versatile, and yet simplified compared to hyperbranched and dendritic systems.

A prominent example of graft copolymerisation for therapeutic applications is the work of Lim *et al*., in which hydrazone-functionalised side chains were grafted onto a poly(aspartamide) derivative (PASPAM), for the subsequent, pH-sensitive conjugation of DOX.[116,117] The authors found that the pH-sensitive PASPAM released substantially more DOX content at pH 5.0 (55% - 70%) than at physiological pH (10% - 15%), contrasting with the non-cleavable controls which achieved minimal pH discrimination, with higher baseline leakage at physiological pH. In addition, the non-grafted PASPAM saw poor self-assembly, lower drug association and significant aggregation in serum-containing conditions, versus the stable and uniformly sized nanocarriers achieved through grafting. These properties culminated in an overall 2 to 4-fold increase in cytotoxic potency vs. non-cleavable conjugates highlighting the significant benefits available through architectural fine-tuning.

Whilst this example represents only one potential application of graft copolymer technology, it illustrates how significant therapeutic benefits can be achieved through the installation of functional moieties onto the side chains of multifunctional monomer units. This mirrors the principles behind dendritic systems, whilst reducing synthetic complexity and greatly improving the scalability of the resultant product for large-scale manufacture. In practice, grafting techniques make up one part of the wider scope of post-polymerisation modification (PPM), in which pre-formed polymer backbones such as those of poly(amino acids) are diversified through chemical alteration, rather than through pre-determined architectural design.

A more complete discussion is therefore better situated within the broader context of PPM, where protection-deprotection strategies, side-chain enhancements and polymer-drug conjugation underpin the modularity exploited in modern poly(amino acid) therapeutics.

1.5 Post-Polymerisation Modification

Instead of relying on complex architectural design during NCA ROP (or alternative polymer synthesis methodologies), PPM enables precise tuning of polymer functionalisation and spatial arrangement through chemoselective transformations on existing side chains, reducing the burdens on labour and resource during synthesis. The approach of PPM underpin many of the recent advances in stimuli-responsive delivery, bio-orthogonal conjugation and architectural refinement in PLys-containing systems.[118-120] For their relevance in this investigation, specific categorisation has been provided below to detail functional group protection strategies, chain extension and architectural modification, and polymer-drug conjugation.

1.5.1 Functional Group Protection Strategies

A central requirement in post-polymerisation modification of poly(amino acids), particularly within the application of multifunctional monomers, is the ability to temporarily mask functional domains from participating in reaction with other functional groups. Lysine-based systems, in particular, present a densely packed arrangement of primary amine groups capable of nucleophilic attack, risking uncontrolled branching, acylation, alkylation or crosslinking pathways during NCA-ROP.

By selecting protecting groups with distinct stabilities against specific reaction conditions (acid-labile, base-labile, redox-sensitive), polymer uniformity during navigation of multi-step modification schemes controlled. Orthogonal protection is also enabled by blending synthesis and protection strategies, a key tool used in SPPS that is adapted in the asymmetric functionalisation of PLys block copolymers, as demonstrated by Deming *et al*.[120] An example of such protection strategies is provided in **Section 1.2.2** (**Figure 1.7**), which details the structure of the Fmoc and Boc protecting groups. Synthetic profiles for the protection and deprotection of these group, as well as for the benzyloxy carbonyl protecting group (Z), are illustrated in **Figure 1.13** below.

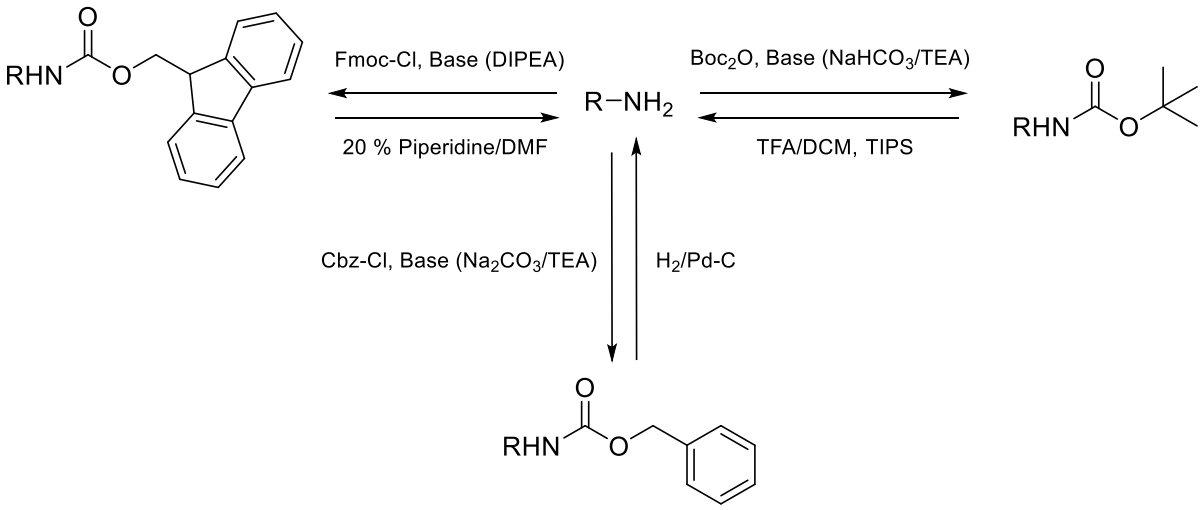

Figure 1.13: Synthetic strategies for protection and deprotection of a primary amine with Fmoc, Boc and Cbz (Z) protecting groups.

The necessity of functional group protection has already been demonstrated within this chapter, in both the T3P-mediated synthesis of NCA molecules and in the NCA-ROP of multifunctional monomers. Likewise, sequential dendrimer synthesis, as outlined in **Section 1.4.2**, required orthogonal protection to achieve generational coupling within crosslinking or loss of fidelity. This same principle underlies more recent research in the literature, such as the work of Athanasiou *et al*., in the synthesis of orthogonally protected lysine block copolymer, $PLys_{78}$-*b*-($PLys_{10}$-g-$PHis_{15}$) *via* block copolymerisation of Nε-Boc-L-Lys-NCA and Nε-Fmoc-L-Lys-NCA.[122] With subsequent base-labile Fmoc deprotection, the freshly-exposed ε-amines were then used to initiation NCA ROP of N_{im}-Trt-L-His-NCA, a protected NCA of histidine. Histidine residues were then deprotected under basic conditions, yielding pH-

buffering Phis grafts, and finally Boc deprotection was performed under acidic conditions to yield cationic PLys features. The resulting architecture presented a versatile gene/drug delivery platform with responsive buffering and complexation functionality, enabled by conscious protection/deprotection design. These examples highlight the vital selectivity that protection strategies provide, enabling complex post-polymerisation workflows. From this foundation it is possible to synthesise practicable alternatives to complex, multi-generational dendrimer architectures *via* the spatial modification of polymer side chains, using grafted chain extender molecules such as those discussed below.

1.5.2 Chain Extension and Architectural Modification

By appending short, well-defined segments onto the deprotected side chains of a pre-polymerised poly(amino acid) backbone, it is possible to tune both the functional and spatial architecture of the resultant amphiphile, thereby influencing downstream conjugation, self-assembly and triggered-release behaviours. Alongside the installation of stimulus-responsive and cationically-binding functional domains, it is also possible for these segments to provide spatial extension to the pendant side chain, thereby increasing conformational freedom around active residues and correspondingly reducing their steric occlusion. Such chain extension has been used previously to relieve steric congestion for the conjugation of fluorophores, with remarkable success (ca. 90 % labelling efficiency).[123] A number of distinct extender classes are prominent in the surrounding literature, each providing a functional or spatial enhancement to the backbones of their respective polymer chains.

Already discussed above by Athanasiou *et al*. is the use of histidine-based extenders. These imidazole-containing residues are introduced to impart pH-responsive buffering, whilst avoiding high densities of charge loading that which cause toxicity in the bloodstream.[122] Histidine is uniquely relevant to drug delivery, in that protonation under low-pH environments, attracts counter ions that in turn increase osmotic swelling and rupture endosomal membranes, expediting endosomal escape, a crucial step in the cytosolic delivery pathway.[122] Another family of chain extenders is derived from glutamic acid, with γ-carboxylate-containing units that enhance solvation and drug interaction (through either increased hydrophilicity or increased opportunity for conjugation).

This technology was previously employed by Sui *et al.* in the preparation of poly(L-glutamic acid) based polypeptides, conjugated to DOX *via* short γ-glutamyl spacers, which increased local hydrophilicity and conformational flexibility around the conjuigation.[124] This subsequently reduced steric hindrance and increased drug loading by controlled access for installing pH-labile hydrazone linkers. Aromatic amino acid-derived extenders, including short PPhe and PTyr segments, offer a contrasting effect by increasing the rigidity of their respective block through π-π stacking interactions. These stacking also acts to increase hydrophopbic drug association and modulate nanostructure packing.[125]

Beyond amino-acid mimicking spacers, zwitterionic spacers such as carboxybetaines and sulfobetaines have emerged as highly effective chain extenders for modifying the interfacial properties of poly(amino acid) systems. These extenders generate robust hydration shells through electrostatically-driven water structuring, which increases local solvation and softens packing density around adjacent residues, thereby diminishing aggregation.[126] This is especially relevant for serum-containing environments, where nonspecific adsorption can compromise colloidal stability. In addition to this antifouling behaviour, zwitterioninc extension also increases conformation flexibility along the polymer chain, reducing electrostatic self-interactions within cationic segments such as PLys. Sun *et al*. utilised this technology in the application of sulfobetaine chain extenders on polypeptides to markedly decrease nonspecific protein binding and maintain narrow size distributions during self-assembly, demonstrating their potential for stabilising nanoformulations under physiological conditions.[126] The final pertinent example of chain-extenders is oligo(ethylene glycol) (OEG) spacers, particularly short chain units such as 2-(2-aminoethoxy)ethoxyacetic acid (AEEA), such as those previously alluded to in the publication by Hnedzko *et al*.[123] OEG spacers are among the most widely used in poly(amino acid) chemistry due to their high flexibility, strong hydrophilicity and excellent steric accessibility around lysine residues. This increase in segmental mobility and accessible reaction volume substantially increases the efficiency of OEG-extended systems in surface modification and drug conjugation. These properties can then be exploited to create tightly-controlled delivery platforms with improved drug loading and colloidal stability versus linear amphiphiles, whilst avoiding the synthetic complexities of comparative dendritic systems.[127]

1.5.3 Polymer-Drug Conjugation

SN38 and doxorubicin are active pharmaceutical ingredients referenced within this chapter and are of primary importance to the research conducted throughout this report. They are each inhibitors of topoisomerase I and II, the enzymes responsible for relieving torsional strain and untangling DNA during transcription.[12] By trapping the enzyme-DNA complex, these drugs induce lethal DNA strand breaks that trigger apoptosis in rapidly dividing cancer cells. The structures of SN38 and doxorubicin are provided in **Figure 1.14** below.

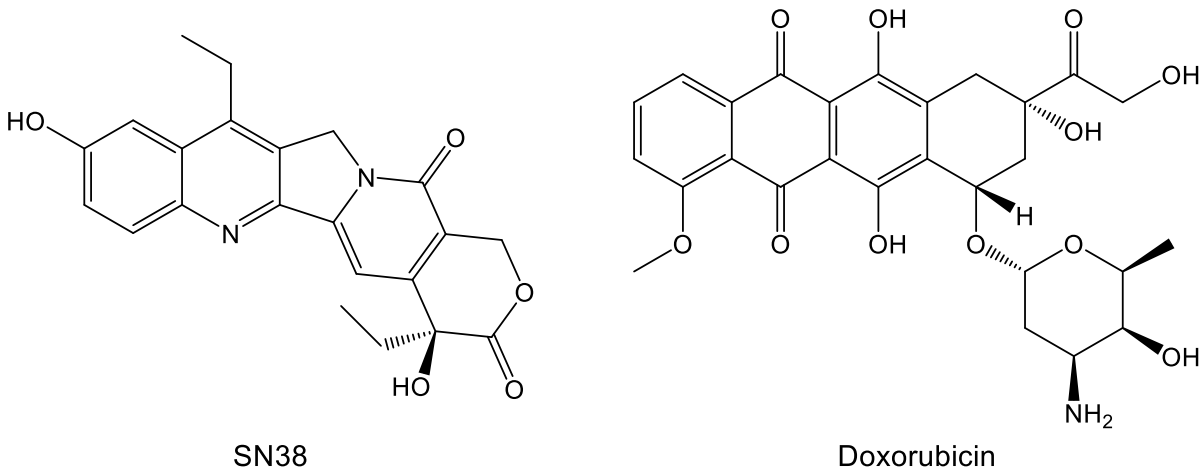

Figure 1.14: Structures of SN38 and Doxorubicin

While potent, these molecules are dose-limited by their poor solubility, rapid clearance from blood plasma and substantial toxicities following IV administration (C_{max}).[22,23] These toxicities lead to symptoms such as gastrointestinal damage and myelosuppression, which are typically associated with chemotherapy. Since its conceptualisation in 1975 by Ringsdorf *et al*., the conjugation of these APIs directly to delivery platforms has been utilised to moderate pharmacokinetics and dynamics, lowering C_{max} and prolonging circulation half-life ($t_{1/2}$) of these chemotherapeutic agents, to improve tumour exposure and reduce systemic injury.[129,130]Compared with supramolecular encapsulation, covalent polymer-drug conjugation provides substantial benefits, guaranteeing minimum drug loading and protecting against burst release and undesired leakage during circulation. In addition, association of the conjugated drug molecules during amphiphilic self-assembly can provide a highly-effective hydrophobic domain for the encapsulation of additional drug molecules, delivering a baseline payload whilst hosting additional non-covalent cargo.

This has been exemplified recently in the literature by the work of England *et al*., who synthesised a poly(sarcosine) and PLL-based telodendrimer system to conjugate fulvestrant, an exemplary drug with extremely poor aqueous solubility.[131] The self-assembled telodendrimer micelles demonstrated good colloidal stability (CMC < 2 μM) and uniformity, were able to solubilise additional fulvestrant to yield an excellent overall drug loading capacity of up to 77 wt% total drug loading, and were tuneable in size between 25-150 nm. This system illustrates the gold standard for polymer-drug conjugation, and a benchmark for the work conducted within this report.

Conjugation relies on linker chemistries to provide a connection between polymer and drug that is stable during storage, administration and circulation, and yet is capable of release at or inside of the target. One prominent example of a stimulus-responsive linker discussed previously is hydrazone, formed by conjugation of a hydrazide with a carbonyl group (typically an aldehyde or ketone).[132,133] Hydrazone hydrolysis is expedited under low-pH conditions, whereby protonation of the imine nitrogen increases carbonyl carbon electrophilicity, making it more susceptible to attack by water. Similarly employed are disulphide linkages, which remain stable under extracellular environments, but are susceptible to reductive cleavage within glutathione-rich cystosol, making them ideal for intracellular delivery strategies such as transfection.[134] Self-immolative spacers (SIS), provide another example of selective release, with examples such as para-aminobenzyloxycarbonyl (PABC) adapted from antibody-drug conjugates intro polymer-based delivery systems over the past two decades.[130] Under exposure to lysosomal enzymes (such as cathepsin B) SISs undergo a 1,6-elimination cascade, yielding the active drug alongside benign elimination by-products. Of specific relevance to this research work is the utilisation of carbamate linkages, as one of a wider carbonyl family (esters, carbonates), in the coupling of SN38 to amine groups. The SN38 10-hydroxyl group is commonly derivatised *via* carbonate activation (e.g. p-nitrophenyl carbonate) and coupled to the amine to furnish carbamates that slowly hydrolyse in circulation, thereby releasing active SN38 over therapeutically useful timescales. Each of these simple linker chemistries was evaluated by Maeda *et al*., utilising them within mPEG-linker-O-SN38 conjugates and evaluating their hydrolysis over time.[135]

Whilst ester linkage achieved controlled release, they exhibited partial premature hydrolysis in serum (ca. 30 % in 12h) which limited their plasma half-life and led to undesired burst release after IV dosing. Subsequent replacement with carbamate demonstrated only ca. 15 % release over 24 h at pH 7.4, versus > 70 % after 48 h under mildly acidic or enzymatic conditions. This resulted in a controlled and predictable hydrolysis half-life of 40-50 h, prolonging systemic circulation, tumour accumulation, and intracellular SN38 concentration by comparison.

In the literature to date, no examples have been reported of PEG-*b*-PLys block copolymers bearing OEG-grafted spacers to sterically relieve ε-amines, conjugated *via* carbamate linkage to SN-38 for controlled delivery. Close neighbours do exist, with PEG-*b*-PGlu-SN38 conjugated systems, linear PEG-SN38 macromolecular prodrugs, PLL-based dendrimer-SN38 conjugates and OEG-tethered SN38 prodrug polymers reported previously.[136-138] The research of such a novel system would fill a gap between simple PEG-SN38 conjugates (good control, limited modularity) and dendritic PLys systems (excellent loading but high synthetic complexity), exploiting OEG chain-extension to improve conjugation efficiency and assembly, whilst retaining linear-BCP scalability.

1.6 Research Aims and Thesis Outline

This research is focused on the creation, development and optimisation of functionalised poly(amino acid) and poly (hydroxyl acid) systems for the encapsulation of (or conjugation to) chemotherapeutic agents with poor aqueous solubility and high toxicity, for the broader end goal of their stable and secure transport and controlled release. Early optimisation of monomer synthesis has been performed *via* evaluation of both traditional Fuchs-Farthing carbonylation and T3P-mediated cyclisation, comparing synthetic complexity, necessary hazard prevention and final product yield and purity. The primary goal of this is to establish a facile and repeatable synthetic protocol for the initiation of mandelic acid OCA ROP (and NCA-ROP of protected lysine NCAs), using methoxy-PEG-based macroinitiators, to produce amphiphilic BCPs with high a degrees of polymerisation and narrow values of Đ. Following this, the research aims to evaluate the resultant BCP platforms for their properties in post-polymerisation modification, self-assembly, and subsequent controlled release.

Chapter 4 includes the synthesis of mPEG-*b*-poly(mandelic acid) (mPEG-*b*-PMA) block copolymers *via* OCA ROP of Man-OCA from mPEG (5000 g mol^{-1}). Polymerisations were conducted under nitrogen atmosphere using DMAP catalyst, with varying catalyst concentration, [M]:[I] ratio, temperature and reaction dilution systematically investigated. Copolymers were synthesised with narrow dispersities (Đ < 1.3), and molecular weight values were determined with good agreement between ^{1}H NMR spectroscopic analysis and APC data. BCPs were self-assembled by nanoprecipitation to form stable nanoparticles (< 200 nm, PDI < 0.2) in PBS buffer, representing the first successful attempt at producing self-assembled nanostructures from the mPEG-*b*-PMA system. Within the one of these samples, DOX free-base was efficiently encapsulated (87 ± 3 wt% encapsulation efficiency, 17.4 ± 1 wt% loading) and its release behaviour was monitored under physiological (pH 7.4) and acidic (pH 5.0) conditions. The nanoparticles demonstrated excellent stability with no burst release, and a significantly increased release rate under low-pH conditions, confirming the acid-labile nature of the PMA backbone's ester linkages and the potential of this polymer system in pH-responsive therapeutic delivery of chemotherapeutic agents.

Chapter 5 includes the ROP of Lys(Fmoc)-NCA and Lys(Z)-NCA, initiated by mPEG (5000 g mol^{-1}) under mild, anhydrous conditions and in the presence of DMAP catalyst.

Products were analysed *via* ^{1}H NMR, DOSY NMR and SEC analysis, and successful deprotection of the benzyloxycarbonyl protecting group was recorded. In the interest of simplifying deprotective purification strategies, attention was shifted to NCA ROP of Lys(Boc)-NCA, initiated by mPEG-NH_2 in DMF under anhydrous conditions, with *in situ* FTIR monitoring utilised to confirm total monomer consumption. A suite of mPEG-*b*-PLys(Boc) BCPs, with systematically varied hydrophobic block lengths, were synthesised and characterised by ^{1}H NMR and SEC analysis, demonstrating successful ROP with well-controlled uniformity (Đ < 1.3). Deprotection of these products was performed using TFA, confirmed by ^{1}H NMR analysis of the products. High-M.W. impurities were detected in the chromatograms of some samples, leading to an investigation into reducing side reactions that may have been the cause. Investigation of THF solvent and low reaction temperatures was performed, highlighting clear reduction in unwanted impurities at low temperatures. These conditions were applied to subsequent NCA ROP for BCP of PLys lengths above 10 repeat units, which were subsequently deprotected.

Reported in chapter 6 is the post-polymerisation modification of mPEG-*b*-PLys[NH_2.TFA]$_n$ block copolymers, investigating the impact of chain extension using OEG spacers on the subsequent conjugation of SN38, nanoparticle self-assembly and controlled release. Protected $OEG_{1\text{-}2}$ chain extenders (O2O-Boc, O2O-O2O-Boc) were attached to the PLys pendant amines *via* amide coupling (PYBOP/DIPEA), with high grafting efficiencies (80 – 97 %) confirmed by ^{1}H NMR spectroscopy and corroborated by SEC. Subsequent TFA protection successfully yielded free amine chain ends on the spacers, again confirmed using ^{1}H NMR and corroborated by SEC. An activated intermediate of SN38 (prepared in 74 % yield) then underwent carbamate coupling to linear, OEG_1 and OEG_2 grafted mPEG-*b*-PLys polymers of systematically varied hydrophobic block lengths, with increases in molecular weight verified with ^{1}H NMR and SEC. Comparison of conjugation efficiencies confirmed improved conjugation for chain-extended systems, lending credence to the steric relief hypothesis. All conjugated samples were then self-assembled *via* nanoprecipitation in PBS buffer, with DLS analysis confirming uniform nanostructures. Subsequent controlled release tests showed sustained SN38 release under simulated physiological conditions, with good stability and no burst release.

1.7 References

1. Park, K., *J. Control. Release*, **2014**, *190*, 3–8.
2. *Drug delivery system market size, share and industry analysis*, https://bit.ly/3lnmnQn (accessed 25/11/2021).
3. Bae, Y.-H.; Park, K., *J. Control. Release*, **2011**, *153*, 198–205.
4. Pearce, A.; Haas, M.; Viney, R.; Pearson, S.-A.; Haywood, P.; Brown, C.; Ward, R., *PLoS One*, **2017**, *12*(10).
5. Senapati, S.; Mahanta, A. K.; Kumar, S.; Maiti, P., *Signal Transduct. Target. Ther.*, **2018**, *3*, 7.
6. Hiemenz, P. C.; Lodge, T. P., *Polymer Chemistry*, 2nd ed.; CRC Press, **2007**, pp. 5–6.
7. Young, R. J.; Lovell, P. A., *Introduction to Polymers*, 3rd ed.; CRC Press, **2011**, pp. 155–160.
8. Cheng, J.; Deming, T., *Top. Curr. Chem.*, **2012**, *310*, 1–26.
9. Li, Y.; Shen, Y.; Wang, S.; Zhu, D.; Du, B.; Jiang, J., *RSC Adv.*, **2015**, *5*, 30380–30388.
10. Iatrou, H.; Frielinghaus, H.; Hanski, S.; Ferderigos, N.; Ruokolainen, J.; Ikkala, O.; Richter, D.; Mays, J.; Hadjichristidis, N., *Biomacromolecules*, **2007**, *8*, 2173–2181.
11. Knop, K.; Hoogenboom, R.; Fischer, D.; Schubert, U. S., *Angew. Chem., Int. Ed.*, **2010**, *49*, 6288–6308.
12. Danaei, M.; Dehghankhold, M.; Ataei, S.; Hasanzadeh Davarani, F.; Javanmard, R.; Dokhani, A.; Khorasani, S.; Mozafari, M. R., *Pharmaceutics*, **2018**, *10*, 1–17.
13. Mai, Y.; Eisenberg, A., *Chem. Soc. Rev.*, **2012**, *41*, 5969–5985.
14. Israelachvili, J. N.; Mitchell, D. J.; Ninham, B. W., *Biochim. Biophys. Acta, Biomembr.*, **1977**, *470*, 185–201.
15. Wang, X.; An, Z., *Macromol. Rapid Commun.*, **2019**, *40*(2), 1800325.
16. Blanazs, A.; Armes, S. P.; Ryan, A. J., *Macromol. Rapid Commun.*, **2009**, *30*(4–5), 267–277.

17. Zhang, L.; Eisenberg, A., *Science*, **1995**, *268*, 1728–1731.

18. Chu, K. S.; Schorzman, A. N.; Finniss, M. C.; Bowerman, C. J.; Peng, L.; Luft, C. J.; Madden, A.; Wang, A. Z.; Zamboni, W. C.; DeSimone, J. M., *Biomaterials*, **2013**, *34*, 8424–8429.

19. Liu, Y.; Yang, G.; Jin, S.; Xu, L.; Zhao, C.-X., *ChemPlusChem*, **2020**, *85*, 2143–2157.

20. Sabatelle, R. C.; Liu, R.; Hung, Y. P.; Bressler, E.; Neal, E. J.; Martin, A.; Ekladious, I.; Grinstaff, M. W.; Colson, Y. L., *Biomaterials*, **2022**, *285*, 121534.

21. Sultana, S.; Alzahrani, N.; Alzahrani, R.; Alshamrani, W.; Aloufi, W.; Ali, A.; Najib, S.; Siddiqui, N. A., *J. Drug Target.*, **2020**, *28*(5), 468–486.

22. Santi, D. V.; Fontaine, S. D.; Wang, Y.; et al., *J. Med. Chem.*, **2014**, *57*, 4979–4989.

23. Haaz, M.; Rivory, L. P.; Robert, J.; et al., *Cancer Chemother. Pharmacol.*, **1997**, *40*, 135–141.

24. Fang, Y.-P.; Chuang, C.-H.; Wu, Y.-J.; Lin, H.-C., *Int. J. Nanomed.* **2018**, *13*, 2789–2802.

25. Karimi, M.; Eslami, M.; Sahandi-Zangabad, P.; Mirab, F.; Farajisafiloo, N.; Shafaei, Z.; Ghosh, D.; Bozorgomid, M.; Dashkhaneh, F.; Hamblin, *Wiley Interdiscip. Rev. Nanomed. Nanobiotechnol.* **2016**, *8*(5), 696–716.

26. M. R.Li, M.; Zhao, G.; Su, W.-K.; et al., *Front. Chem.*, **2020**, *8*, 647.

27. Meng, X.; Shen, Y.; Zhao, H.; et al., *J. Nanobiotechnol.*, **2024**, *22*, 587.

28. Ahmed, S. A.; Abdelrahman, M. M.; Mekhamer, W. K.; Younis, *R. Soc. Open Sci.* **2020**, *7*, 200959.

29. S. A.Versypt, A. N. F.; Pack, D. W.; Braatz, R. D., *J. Control. Release*, **2013**, *165*, 29–37.

30. Hao, G.; Xu, Z. P.; Li, L., *RSC Adv.*, **2018**, *8*, 22182–22192.

31. Deming, T. J., *Nature*, **1997**, *390*, 386–389.

32. Yu, S.; Wu, G.; Gu, X.; Wang, J.; Wang, Y.; Gao, H.; Ma, J., *Colloids Surf., B*, **2013**, *103*, 15–22.

33. Stoimenova, A.; Ivanov, K.; Obreshkova, D.; Saso, L., *Biotechnol. Biotechnol. Equip.*, **2013**, *27*, 3620–3626.

34. *Ajinomoto: Enhancing Life with Amino Acids*, https://bit.ly/31aUXWO (accessed 30/09/2021).

35. Chow, D.; Nunalee, M. L.; Lim, D. W.; Simnick, A. J.; Chilkoti, A., *Mater. Sci. Eng., R*, **2008**, *62*, 125–155.

36. Kukula, H.; Schlaad, H.; Antonietti, M.; Förster, S., *J. Am. Chem. Soc.*, **2002**, *124*, 1658–1663.

37. Castelletto, V.; Hamley, I. W., *Biophys. Chem.*, **2009**, *141*, 169–174.

38. Alberts, B.; Johnson, A.; Lewis, J.; Raff, M.; Roberts, K.; Walter, P. *Molecular Biology of the Cell*, 4th ed.; Garland Science: New York, 2002; **Chapter 3**.

39. Banerjee, J.; Radvar, E.; Azevedo, H. S., *Self-Assembling Peptides and Their Application in Tissue Engineering and Regenerative Medicine*; Elsevier, **2018**.

40. Golla, K.; Reddy, P. S.; Bhaskar, C.; Kondapi, A. K., *Drug Deliv.*, **2013**, *20*, 156–167.

41. Yu, H.; Ingram, N.; Rowley, J. V.; Green, D. C.; Thornton, P. D., *Chem. Eur. J.*, **2020**, *26*, 13352–13358.

42. Berntsson, R.; Thunnissen, A.; Poolman, B.; Slotboom, D., *J. Bacteriol.*, **2011**, *193*, 4254–4256.

43. Byrne, M.; Victory, D.; Hibbitts, A.; Lanigan, M.; Heise, A.; Cryan, S. A., *Biomater. Sci.*, **2013**, *1*, 1223–1234.

44. Resetco, C.; Hendriks, B.; Badi, N.; Du Prez, F., *Mater. Horiz.*, **2017**, *4*, 1041–1053.

45. Merrifield, R. B., *Excerpta Med., I.C.S.*, **1976**, *374*, 29–39.

46. Mitchell, R., *Biopolym., Pept. Sci. Sect.*, **2008**, *90*, 175–184.

47. Palomo, J. M., *RSC Adv.*, **2014**, *4*, 32658–32672.

48. Deming, T. J., *J. Polym. Sci., Part A: Polym. Chem.*, **2000**, *38*, 3011–3018.

49. Leuchs, H. Über die Glycin-carbonsäure. *Ber. Dtsch. Chem. Ges.* **1906**, *39*, 857–861.

50. Cheng, J.; Deming, T., in *Peptide-Based Materials*; Springer, **2012**, Ch. 1, pp. 1–26.

51. Grant, N. H.; Alburn, H. E., *J. Am. Chem. Soc.*, **1964**, *86*, 3870–3873.

52. Lagrille, O.; Danger, G.; Boiteau, L.; Rossi, J. C.; Taillades, J., *Amino Acids*, **2009**, *36*, 341–347.

53. Fuchs, F. Über N-Carbonsäure-anhydride. *Ber. Dtsch. Chem. Ges.* **1922**, *55*, 2943 2943.

54. Farthing, A. C., *J. Chem. Soc.*, **1950**, 3213–3217.

55. Nye, M. J., *Before Big Science*; Harvard University Press, **1999**.

56. *A Brief History of Chemical Weapons*, https://bit.ly/31iq6HG (accessed 28/11/2021).

57. Daly, W. H.; Poché, D., *Tetrahedron Lett.*, **1988**, *29*, 5859.

58. Oya, M.; Katakai, R.; Nakai, H., *Chem. Lett.*, **1973**, 1143.

59. Centers for Disease Control and Prevention, https://bit.ly/3p7vLIU (accessed 20/11/2021).

60. Wilder, R.; Mobashery, S., *J. Org. Chem.*, **1992**, *57*, 2755–2756.

61. Smeets, N. M. B.; Van Der Weide, P. L. J.; Meuldijk, J.; Vekemans, J. A. J. M.; Hulshof, L. A., *Org. Process Res. Dev.*, **2005**, *9*, 757–763.

62. Han, G.; Tamaki, M.; Hruby, V. J., *J. Pept. Res.*, **2001**, *58*, 338–341.

63. Hadjichristidis, N.; Iatrou, H.; Pitsikalis, M.; Sakellariou, G., *Chem. Rev.*, **2009**, *109*, 5528–5578.

64. Kricheldorf, H. R., *α-Aminoacid-N-Carboxyanhydrides and Related Materials*; Springer-Verlag, **1987**.

65. Kricheldorf, H. R., in *Models of Biopolymers by Ring-Opening Polymerization*; CRC Press, **1990**, pp. 160–225.

66. Odian, G., *Principles of Polymerization*, 4th ed.; Wiley, **2004**.

67. Wang, L.; Wu, Y.; Xu, R.; Wu, G.; Yang, W., *Chin. J. Polym. Sci.*, **2008**, *26*, 381–391.

68. Ikada, Y.; Tsuji, H., *Macromol. Rapid Commun.*, **2000**, *21*, 117–132.

69. Lou, X.; Detrembleur, C.; Jérôme, R., *Macromol. Rapid Commun.*, **2003**, *24*, 161.

70. Albertsson, A.-C.; Varma, I., *Adv. Polym. Sci.*, **2002**, *157*, 1–40.

71. Wilbon, P. A.; Chu, F.; Tang, C., *Macromol. Rapid Commun.*, **2013**, *34*, 8–37.

72. Hyon, S.-H.; Jamshidi, K.; Ikada, Y., *Biomaterials*, **1997**, *18*, 1503–1508.

73. Kobayashi, S.; Uyama, H.; Kimura, S., *Chem. Rev.*, **2001**, *101*, 3793–3818.

74. Loos, K.; Stadler, R., *Macromolecules*, **1997**, *30*, 7641–7643.

75. Albertsson, A.-C.; Varma, I. K., *Biomacromolecules*, **2003**, *4*, 1466–1486.

76. Xia, H.; Kan, S.; Li, Z.; Chen, J.; Cui, S.; Wu, W.; Ouyang, P.; Guo, K., *J. Polym. Sci., Part A: Polym. Chem.*, **2014**, *52*, 2306.

77. Thillaye du Boullay, O.; Marchal, E.; Martin-Vaca, B.; Cossío, F. P.; Bourissou, D., *J. Am. Chem. Soc.*, **2006**, *128*, 16442.

78. Wang, R.; Zhang, J.; Yin, Q.; Xu, Y.; Cheng, J.; Tong, R., *Angew. Chem., Int. Ed.*, **2016**, *55*, 13010.

79. Buchard, A.; Carbery, D. R.; Davidson, M. G.; Ivanova, P. K.; Jeffery, B. J.; Kociok-Köhn, G. I.; Lowe, J. P., *Angew. Chem., Int. Ed.*, **2014**, *53*, 13858.

80. Pounder, R. J.; Fox, D. J.; Barker, I. A.; Bennison, M. J.; Dove, A. P., *Polym. Chem.*, **2011**, *2*, 2204.

81. Jacobsen, S.; Fritz, H. G.; Degée, P.; Dubois, P.; Jérôme, R., *Polym. Eng. Sci.*, **1999**, *39*, 1311.

82. Deng, X.; Yuan, M.; Li, X.; Xiong, C., *Eur. Polym. J.*, **2000**, *36*, 1151.

83. Dechy-Cabaret, O.; Martin-Vaca, B.; Bourissou, D., *Chem. Rev.*, **2004**, *104*, 6147.

84. Stanford, M. J.; Dove, A. P., *Chem. Soc. Rev.*, **2010**, *39*, 486.

85. Davies, W. H., *J. Chem. Soc.*, **1951**, 1357.

86. Nederberg, F.; Connor, E. F.; Möller, M.; Glauser, T.; Hedrick, J. L., *Angew. Chem.*, **2001**, *113*, 2784–2787; *Angew. Chem., Int. Ed.*, **2001**, *40*, 2712–2715.

87. Bonduelle, C.; Martín-Vaca, B.; Cossío, F. P.; Bourissou, D., *Chem. Eur. J.*, **2008**, *14*, 5304–5312.

88. Qiu, L.; Hong, C. Y.; Pan, C. Y., *Int. J. Nanomed.*, **2015**, *10*, 3623–3640.

89. Wittmar, M.; Unger, F.; Kissel, T., *Macromolecules*, **2006**, *39*, 1417–1424.

90. Chen, C.; Zhou, B.; Zhu, X.; Shen, M.; Shi, X., *RSC Adv.*, **2016**, *6*, 9232–9239.

91. Gregory, A.; Stenzel, M. H., *Prog. Polym. Sci.*, **2012**, *37*, 38–105.

92. Duncan, R., *Nat. Rev. Drug Discov.*, **2003**, *2*, 347–360.

93. Lee, C. C.; MacKay, J. A.; Fréchet, J. M. J.; Szoka, F. C., *Nat. Biotechnol.*, **2005**, *23*, 1517–1526.

94. Medina, S. H.; El-Sayed, M. E. H., *Chem. Rev.*, **2009**, *109*, 3141–3157.

95. Jansen, J. F. G. A.; de Brabander-van den Berg, E. M. M.; Meijer, E. W., *Science*, **1994**, *266*, 1226–1229.

96. Yan, R.; Liu, X.; Xiong, J.; Feng, Q.; Xu, J.; Wang, H.; Xiao, K., *RSC Adv.*, **2020**, *10*, 13889–13899.

97. Lv, S.; Kim, H.; Song, Z.; Feng, L.; Yang, Y.; Baumgartner, R.; Tseng, K.-Y.; Dillon, S. J.; Leal, C.; Yin, L.; Cheng, J., *J. Am. Chem. Soc.*, **2020**, *142*, 8570–8574.

98. Stefanovic, S.; McCormick, K.; Fattah, S.; Brannigan, R.; Cryan, S.-A.; Heise, A., *Polym. Chem.*, **2023**, *14*, 3151–3159.

99. Walsh, D. P.; Murphy, R. D.; Panarella, A.; Raftery, R. M.; Cavanagh, B.; Simpson, J. C.; O'Brien, F. J.; Heise, A.; Cryan, S.-A., *Mol. Pharm.*, **2018**, *15*, 1878–1891.

100. Li, P.; Song, Y.; Dong, C.-M., *Polym. Chem.*, **2018**, *9*, 3974–3986.

101. Rodríguez-Hernández, J.; Chemtob, J.; Borsali, R.; Gnanou, Y., *Biomacromolecules*, **2003**, *4*, 249–258.

102. Smulders, M. M. J.; van Genderen, M. M.; Meijer, E. W., *Chem. Soc. Rev.*, **2010**, *39*, 775–788.

103. Yang, L.; Wang, H., *J. Mater. Chem. B*, **2013**, *1*, 3338–3352.

104. Kaminskas, L. M.; Kelly, A. M.; McLeod, V. N.; Sberna, M.; Owen, C. J.; Boyd, B. J.; Porter, C. J. H., *Mol. Pharm.*, **2012**, *9*, 422–432.

105. Huang, R.-Q.; Qu, S.; Ke, Y.; Gao, Y.; Ye, H.-L.; Chen, Y.-H.; Liang, J.-L.; Liu, C.-T.; Jiang, J.-L., *FASEB J.*, **2007**, *21*, 1117–1125.

106. Mehta, D.; M.; Kaminskas, L. M.; Porter, C. J. H., *Mol. Pharm.*, **2018**, *15*, 436–449.

107. Ryan, G. M.; Kaminskas, L. M.; Porter, C. J. H., *J. Control. Release*, **2013**, *172*, 128–136.

108. Luo, J.; Lam, K. S.; et al., *Bioconjugate Chem.*, **2010**, *21*, 1216–1224.

109. Ejlsøe, S. M.; Hansen, S.-T.; Holm, S.; et al., *Polymers*, **2020**, *12*, 857.

110. Huang, W.; Wang, L.; Bodman, A.; Luo, J., *Mol. Pharm.*, **2015**, *12*, 1045–1058.

111. Khandare, A.; Kolhe, T. M.; Bhattacharya, S.; Singh, R.; Begum, S. M.; Heise, A.; Kannan, R. M., *Biomacromolecules*, **2012**, *13*, 1337–1348.

112. Grayson, S. M.; Fréchet, J. M. J., *Chem. Rev.*, **2001**, *101*, 3819–3867.

113. Patri, A. K.; Kukowska-Latallo, J. F.; Baker, J. R., *Adv. Drug Deliv. Rev.*, **2005**, *57*, 2203–2214.

114. Chiefari, J.; Evans, R. A.; Hill, M. A.; et al., *Polym. Chem.*, **2014**, *5*, 3111–3121.

115. Hawker, C. J.; Wooley, K. L., *Chem. Rev.*, **2005**, *105*, 1105–1149.

116. Lim, C. W.; Kim, D., *Biomater. Sci.*, **2021**, *9*, 1660–1667.

117. Lim, C. W.; Han, S. H.; Kim, D., *J. Mater. Chem. B*, **2015**, *3*, 1434–1443.

118. Zhang, L.; Liu, F.; Huang, J., *Polym. Chem.*, **2020**, *11*, 3852–3870.

119. Kagalwala, H. N.; Weck, M., *Chem. Soc. Rev.*, **2020**, *49*, 8564–8584.

120. Aliferis, A.; Iatrou, A., *Macromol. Rapid Commun.*, **2011**, *32*, 136–146.

121. Deming, T. J., *J. Am. Chem. Soc.*, **2002**, *124*, 11862–11863.

122. Athanasiou, V.; Moschovas, D.; Varlas, P.; Ntetsikas, G.; Hadjichristidis, N., *Polymers*, **2020**, *12*, 2819.

123. Hnedzko, O. B.; Petersson, J. C.; Hawkins, K. M.; Unrau, P. N. B., *Biomater. Sci.*, **2017**, *5*, 1513–1521.

124. Sui, X.; Xu, J.; Xu, X.; Li, Y.; Liu, R.; Zhou, Y.; Tong, L., *Molecules*, **2014**, *19*, 11915–11930.

125. Xu, J.; Zhao, H.; Chen, Q.; Wang, Y., *J. Mater. Chem. B*, **2019**, *7*, 5512–5523.

126. Sun, Y.; Lin, Y.; Cao, X.; Wang, W.; Li, X.; Sun, Q.; Zhang, J., *Acta Biomater.*, **2018**, *74*, 370–380.

127. Duncan, R.; Izzo, L., *Adv. Drug Deliv. Rev.*, **2020**, *157*, 214–236.

128. Jensen, N. F.; et al., *J. Exp. Clin. Cancer Res.*, **2016**, *35*, 26.

129. Ringsdorf, H., *J. Polym. Sci., Polym. Symp.*, **1975**, *51*, 135–153.

130. Kopeček, J., *Adv. Drug Deliv. Rev.*, **2013**, *65*, 49–59.

131. Yu, Q.; England, R. M.; Gunnarsson, A.; Luxenhofer, R.; Treacher, K.; Ashford, M. B., *Macromolecules*, **2022**, *55*, 505–515.

132. Bae, Y.; Fukushima, S.; Harada, A.; Kataoka, K., *Angew. Chem., Int. Ed.*, **2003**, *42*, 4640–4643.

133. Zhu, L.; Perche, F.; Wang, T.; Torchilin, V. P., *J. Control. Release*, **2014**, *182*, 22–36.

134. Oupický, D.; Parker, A. L.; Seymour, L. W., *J. Am. Chem. Soc.*, **2002**, *124*, 8–9.

135. Maeda, H.; Seki, T.; Matsumura, J.; Fang, A., *J. Control. Release*, **2014**, *187*, 77–86.

136. Uchino, T.; Matsumura, Y.; Negishi, H.; Koizumi, M.; Hayashi, T.; Honda, K.; Nishiyama, N.; Kataoka, T.; Naito, Y.; Kakizoe, K., *J. Control. Release*, **2005**, *103*, 511–522.

137. Cao, X.; Zhang, H.; Li, S.; Zhao, L., *Bioconjugate Chem.*, **2017**, *28*, 1891–1900.

138. Ojima, H.; Nishida, R.; Suzuki, T.; Ishihara, M., *Bioorg. Med. Chem. Lett.*, **2015**, *25*, 5760–5764.

Chapter 2: Instrumentation, Materials and Methods

2.1 Nuclear Magnetic Resonance (NMR) Spectroscopy

^{1}H and ^{13}C NMR spectra for macromolecular samples were recorded on a Bruker AV-NEO 500 MHz NMR spectrometer equipped with a 5 mm DCH cryoprobe. Small molecule samples were analysed on a Bruker AV3HD 400 MHz NMR spectrometer equipped with a 5 mm BBO Probe for polymers and small molecules respectively. Chemical shifts (in ppm) were referenced to a trimethylsilane (TMS) standard whose chemical shift is 0 ppm. Norell® XR-55 NMR tubes and WILMAD 528-PP NMR tubes were used for the 400 MHz and 500 MHz spectrometers respectively. NMR spectra were analysed using MestreNova® Research Lab software. The following abbreviations are used in ^{1}H NMR analyses: s = singlet, d = doublet, t = triplet, q = quartet, m = multiplet, dd = doublet of doublets, J = coupling constants (in Hertz).

2.2 Diffusion-Ordered Spectroscopy (DOSY)

DOSY samples were prepared in-house by the author in accordance with practices described in **Section 2.1**. Acquisition of DOSY data and presentation in 2D form were provided by Alex Heyam within facilities at the University of Leeds. Subsequent interpretation of data was perfomed by the author. Diffusion-ordered ^{1}H NMR spectra (DOSY) were acquired on a 600 MHz NMR spectrometer, equipped with a 5 mm broadband probe. Samples were prepared in DMSO-d_6 and equilibrated for at least 10 min in the magnet prior to acquisition. DOSY experiments used a stimulated-echo bipolar gradient pulse sequence with convection compensation, with 16–32 linearly incremented gradient amplitudes, diffusion delay $\Delta \approx 80$–150 ms and gradient pulse duration $\delta \approx 2$–4 ms. Between 16 and 64 scans were collected per increment, with a relaxation delay of 2–4 s. The temperature was regulated at 298 K and calibrated using methanol-d_4. Data were processed using Topspin and diffusion coefficients (D) were obtained by mono-exponential fitting of signal attenuation as a function of gradient strength using the built-in DOSY analysis module.

2.3 Fourier Transform Infrared (FTIR) Spectroscopy

Samples were dried in a vacuum oven (50 °C) for a minimum of 24 hours prior to infrared spectroscopic analysis. Spectra were recorded for solid samples using a Perkin Elmer Spectrum One equipped with Bruker OPUS 7.0 software and a Specac Golden Gate Attenuated Total Reflection (ATR) diamond top plate, accumulating 100 scans. Vibrational frequencies are expressed in cm^{-1}.

2.3.1 FTIR in-situ monitoring

A Bruker MATRIX-F FTIR spectrometer equipped with an IN355 diamond ATR fiber-optic probe (Ø 6.3 mm) was used for in situ monitoring of reaction progress. The probe was immersed directly into the reaction mixture such that the diamond ATR tip was fully submerged and positioned away from vessel walls and stirring components. Spectra were collected continuously at a rate of 256 scans per minute using Bruker OPUS software, with a background spectrum acquired under identical solvent and temperature conditions prior to reagent addition. Time-resolved spectra were processed and analysed in OPUS, and characteristic absorbance bands associated with reactants and products were used to follow conversion throughout the reaction.

2.4 Size-Exclusion Chromatography (SEC)

AstraZeneca Aqueous Method

Multi-detector size exclusion chromatography (MD-SEC). MD-SEC was performed on a Malvern Panalytical OMNISEC instrument equipped with RI, UV, RALS, LALS and viscometer detectors and analysed using OMNISEC software V11.36. Two PSS Novema Max columns (100 Å (10 µm) + 30 Å (5 µm)) were used in series with an aqueous eluent of 50 mM NaCl after pre-equilibrating the columns with 0.1% TFA in water overnight. A range of narrow PEO standards (1-24 kg mol^{-1} , dn/dc = 0.132 for aqueous) was used as the calibrant. Samples were made up at 5 mg ml^{-1}.

AstraZeneca Organic Method

Multi-detector size exclusion chromatography (MD-SEC). MD-SEC was performed on a Malvern Panalytical OMNISEC instrument equipped with RI, UV, RALS, LALS and viscometer detectors and analysed using OMNISEC software V11.36. A PSS Polarsil linear M analytical column (4.6 mm × 300 mm) was used in combination with DMF containing 50 mM LiBr as the mobile phase, operated at 70 °C after full equilibration. A range of narrow molecular weight standards appropriate for DMF was used for calibration. Samples were prepared at 5 mg mL^{-1} and injected at a volume of 100 µL.

2.5 Advanced Polymer Chromatography (APC)

APC analyses (DMF solution phase, 1 g/L LiBr) were carried out using an ACQUITY APC AQ (200Å, 2.5 µm) column packed with bridged poly(ethylene) hybrid particles, on a Waters ACQUITY APC system, equipped with an ACQUITY refractive index (ACQ-RI) detector. The column temperature was maintained at 40 °C and the flow rate was 0.4 mL/minute. System calibration was carried out using PEG standards and data were process using Empower 3 software to provide polymer Đ values.

2.6 Matrix-Assisted Laser Desorption/Ionisation – Time of Flight Mass Spectrometry (MALDI-TOF MS)

Matrix-Assisted Laser Desorption/Ionisation Time-Of-Flight (MALDI-TOF) Spectroscopy Mass Spectrometry was carried out using a MALDI-TOF spectrometer (Shimadzu AXIMA performance) in positive mode. An α-Cyano-4-hydroxycinnamic acid matrix was used with NaI salt as a cationisation reagent and chloroform used as the solvent.

2.7 Liquid Chromatography – Mass Spectrometry (LC-MS)

LC-MS analysis was performed using a Thermo Scientific Ultimate 3000 HPLC system (Thermo Fisher Scientific, Waltham, MA, USA), interfaced with a mass spectrometer equipped with an electrospray-ionization source operated in the positive mode (Bruker amaZon Speed, Bruker Daltonik GmbH, Billerica, MA, United States). Chromatographic separations were performed using a Kinetex C18 (2.1×50 mm i.d., 2.6 µm particle size; Phenomenex, Torrance, CA, USA) at a column temperature of 40 °C.

The mobile phases were (A) 0.1% Formic acid in water and (B) 0.1% Formic acid in acetonitrile. A gradient was used starting at 98% of A and 2% of B over 1.2 minutes, ending with 2% A and 98% B at a flow rate of 1.3 mL/min.

2.8 Centrifugation, Sample-Drying and Lyophilisation

Samples were centrifuged using a HERMLE Z 326 K centrifuge unit, maintained at 0 °C (0 – 4500 rpm). Samples were dried for a minimum of 24 hours in a Fistreem vacuum oven, equipped with a variable temperature control unit (0 °C – 200 °C) and a pressure gauge (0 mbar – 1020 mbar). Samples were lyophilised using a Thermoelectrion Heto Powerdry LLI500 freeze-dryer, equipped with an Edwards two stage vacuum pump. Samples were lyophilised in deionised water in 50 mL polypropylene centrifuge tubes.

2.9 Preparation of Phosphate Buffered Saline (PBS) and Sodium Acetate Buffer Solutions

One PBS tablet was dissolved in deionised water (200 mL) under vigorous stirring to obtain a PBS buffer solution (pH 7.4). A sodium acetate buffer solution (pH 5.0) was prepared by homogenously mixing 0.1M acetic acid glacial solution (357mL) with 0.1M sodium acetate trihydrate solution (643mL).

2.10 Dynamic Light Scattering (DLS)

DLS analyses were conducted using a Malvern Zetasizer Nano ZSP instrument equipped with a 4 mW He-Ne laser, operating at a wavelength of 633 nm, and an avalanche photodiode (APD) 59 detector. The non-invasive back-scatter-optic arrangement was used to collect the light scattered, at an angle of 173 25 °C. Samples were equilibrated for two minutes and then analysed at 37 °C in disposable 12 mm poly(styrene) cuvettes. Data were processed by cumulative analysis of the experimental correlation function. The diameter of particles was computed from the diffusion coefficients, using Stokes-Einstein's equation. Measurements were carried out in triplicate. Analysis of the results was carried out using the Malvern Zetasizer Software.

2.11 Ultra Violet – Visible (UV-Vis) Spectrophotometry

Absorbance readings (200 – 800 nm) were performed on a dual beam Varian Cary 50 UV0902M112 UV-vis spectrophotometer (Agilent Technologies), equipped with a xenon pulse lamp and Varian Cary WinUV 3.0 software. Samples were analysed in UV micro quartz cuvettes (10 mm, 700 µL and 1700 µL, black-walled). 'Simple-reads' at fixed wavelengths were carried out using a Jenway 6305 spectrophotometer (Cole-Parmer Ltd). All of the readings were taken in triplicate.

2.12 Transmission Electron Microscopy (TEM)

TEM micrographs were obtained as follows; TEM was carried out using copper TEM grids that were subjected to glow discharge for 60 s. Following dialysis, the samples were diluted in deionised water to a concentration of 10 mg/mL. A drop of suspension was placed on the freshly prepared grid and the excess liquid was absorbed with filter paper.

The grid was subsequently washed with deionised water and a drop of uranyl formate solution (0.75 % w/v) was placed on the grid with excess liquid absorbed using filter paper. The grids were then left to dry under a lamp. TEM characterisation was performed at room temperature by using a FEI Tecnai TF20 operated at 200 keV. The FEI Tecnai is equipped with a field emission gun FEGTEM/STEM and a Fischione HAADF detector and Gatan Orius SC600A CCD camera.

2.13 Drug Encapsulation Efficiency and Drug Loading Content

The drug encapsulation efficiency (EE%) of nanoparticles and the drug loading content (LC%) in the nanoparticles was determined using the following equations;

$$EE\% = \frac{W_0 - W_n}{W_0} \times 100$$

$$LC\% = \frac{W_0 - W_0}{W_{np}} \times 100$$

Where: Wo = total mass of payload administered during nanoprecipitation, Wn = total mass of drug not encapsulated within the nanoparticles, Wnp = mass of drug-loaded nanoparticles.

Quantification of doxorubicin was performed by UV-Vis spectrophotometry, via measurement of the dialysate collected during drug release analysis.

Absorbance values were compared against a calibration curve, prepared from serial dilutions of a doxorubicin stock solution of known concentration, allowing determination of Wn. All remaining variables were determined gravimetrically.

2.14 Drug Release Analysis and UPLC Evaluation of SN38 Content

Nanoparticle preparation via nanoprecipitation and subsequent drug release analysis of SN38-conjugated mPEG-b-PLys polymers (synthesised in-house) was performed externally at AstraZeneca facilities in Macclesfield, as these capabilities were not available at the University of Leeds. Drug release data generated from this analysis were provided by AstraZeneca.

A stock solution of the test sample was initially prepared by dissolving in dimethyl sulfoxide (DMSO) to achieve a final concentration of 10 mg/mL. From this concentrated solution, a 25 µL aliquot was transferred into a 250 µL high-performance liquid chromatography (HPLC) vial insert. To this aliquot, 25 µL of an aqueous 0.2 M sodium hydroxide (NaOH) solution was added. The resulting mixture was homogenized by repeated pipetting to ensure thorough mixing of the organic and aqueous components. The sample was then incubated at room temperature (RT) for a period of one hour to allow the reaction or to proceed.

Following the incubation step, 50 µL of an acid quenching solution, prepared as a 10% (v/v) solution of acetic acid in acetonitrile, was added directly to the vial. The addition of this acidic mixture was intended both to neutralize the previously added NaOH and to stabilize the analyte prior to chromatographic analysis.

The prepared sample was analyzed using a Waters Acquity ultra-performance liquid chromatography (UPLC) system. Chromatographic separation was carried out on a Waters Acquity UPLC BEH Phenyl column with dimensions of 2.1 × 50 mm and a particle size of 1.7 µm. The mobile phase consisted of water (containing 0.1% trifluoroacetic acid, TFA) as solvent A and acetonitrile (MeCN) as solvent B. A linear gradient elution method was applied, beginning at 5% solvent B and increasing to 90% solvent B over a total run time of 5 minutes.

Detection of the analyte, specifically SN-38, was performed using a photodiode array detector set to a wavelength of 360 nm.

Quantification was achieved by measuring the integrated peak area corresponding to SN-38 and comparing it against a calibration curve. The calibration curve was generated from a series of standard solutions prepared by diluting a concentrated stock solution of SN-38 in DMSO into acetonitrile, with absorbance also monitored at 360 nm.

2.17. Materials Inventory

All of the chemicals listed in **Table 2.1** were used as received from suppliers unless otherwise specified.

Raw feedstock of mPEG-NH_2 (5000 g mol^{-1}) was supplied by Thermofisher for activities performed throughout **Sections 5.2.3-5.2.4**. Suppliers were changed following SEC analysis of the raw material at AstraZeneca, which revealed significant shoulder peaks tailing towards low retention time on the mPEG peak. Iris Biotech GmbH was selected as an alternative supplier, as a specialist manufacturer of PEGylation reagents and drug delivery polymers whose products are specifically characterised and qualified for pharmaceutical applications, in contrast to the broad research-use portfolio of general laboratory chemical suppliers.

Table 2.1: Chemicals used within the research conducted.

Chemical	Supplier	Chemical	Supplier
Acetate buffer	Fluorochem	Magnesium sulfate	Sigma-Aldrich
Acetic acid Glacial (≥ 99.9%)	Sigma-Aldrich	Mandelic Acid	Fluorochem
Activated charcoal	ACROS	N,N-diisopropylethylamine	Alfa-Aesar
Bis(4-nitrophenyl) carbonate	Sigma-Aldrich	n-Hexane	Sigma-Aldrich
Chloroform	Sigma-Aldrich	PBS tablets	Sigma-Aldrich
Chloroform-*d*	Sigma-Aldrich	PEG methyl ether (5000 g mol^{-1})	Fluorochem
Dichloromethane (DCM)	Fluorochem	PEG methyl ether amine (5000 g mol^{-1})	ThermoFisher/ Iris
Diethyl ether (≥99%)	Fluorochem	Propylene oxide	Sigma-Aldrich
Dimethylformamide (dry)	Fluorochem	PYBOP	Sigma-Aldrich
Diphosgene	Fluorochem	7-ethyl-10-hydroxy camptothecin (SN38)	Sigma-Aldrich
DMAP	Sigma-Aldrich	T3P	Fluorochem
DMSO-*d6*	Euristop	tert-Butyl methyl ether (TBME)	Sigma-Aldrich
Doxorubicin hydrochloride (≥ 95%)	Sigma-Aldrich	Tetrahydrofuran (dry)	ACROS
HBr/Acetic Acid (33 wt%)	Sigma-Aldrich	Triethylsilane	Sigma-Aldrich
L-lysine(Boc)	Fluorochem	Triflouroacetic acid	Sigma-Aldrich
L-lysine(Fmoc)	Fluorochem	Triphosgene	Sigma-Aldrich
L-lysine(Z)	Fluorochem	α-pinene	Fluorochem

Chapter 3: Monomer Synthesis

As discussed in **Chapter 1**, cyclisation of amino acids and hydroxyl acids into NCA and OCA molecules is a crucial step in the process of developing biomimetic nanocarriers for therapeutic delivery, as their strained, 5-member heterocyclic structure enables controlled, efficient polymerisation via ROP under mild conditions. Phosgene-dependent methodologies remain the primary synthetic pathway for the production of these monomers, making up the majority of protocols reported within this chapter. However, the health and safety hazards posed by these toxic materials presents a significant limitation for future uptake by the pharmaceutical industry, leading to the investigation of alternative methods, reported for critical evaluation below.

3.1 Experimental Details

3.1.1 NCA Synthesis

3.1.1.1 Phosgene-Mediated NCA Synthesis

Synthesis of Lys(Fmoc)-NCA

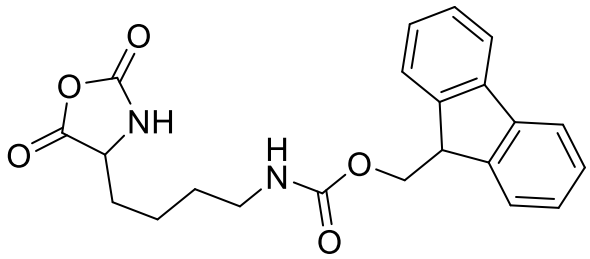

Figure 3.1: Lys(Fmoc)-NCA Structure.

N^6-(fluorenylmethyloxycarbonyl)lysine (5 g, 14 mmol) and α-pinene (3.7 mL, 27 mmol) were added to a dry, three-neck round bottom flask. The flask was fitted with a reflux condenser, a pressure-equalising dropping funnel fitted with a suba-seal, and a stopper in the third neck. These materials were dried under vacuum (1 h) before being dissolved in anhydrous THF (60 mL) and stirred at 60 °C. Concurrently, triphosgene (3.0 g, 11 mmol) was dissolved in additional dry THF (10 mL) before being added dropwise to the stirred reaction mixture. The reaction was left to stir at 60 °C until completion (2 h), which was indicated by the complete dissolution of the NCA product, leaving a clear yellow solution. This solution was filtered *via* hot gravity filtration, before being concentrated to ca. 10 mL on the rotary evaporator.

The resulting crude product solution, a yellow liquor, was subsequently precipitated into ice cold hexane (100 mL) and collected *via* vacuum filtration. This crude solid product was then dissolved into additional THF (ca. 10 mL) and the recrystallisation procedure was repeated twice to ensure a pure product, yielding a fine, off-white powder.

Yield: 3.85 g, 72 %

IR (λ / cm^{-1}): 2992w, 2984w, 2971w, 2950w, 2933w, 2923w (C–H stretch), 1846s (NCA C=O asym. stretch), 1810s (NCA C=O sym. stretch), 1780m (Fmoc carbamate C=O), 1500–1450m (aromatic C–C stretch), 1250–1200m (C–N and C–O stretches).

^{1}H NMR (400 MHz, $CDCl_3$, ppm): 9.15 (s, 1H, N-H), 7.90-7.29 (m, 8H, Ar-H), 4.43 (m, 1H, CH_2-C**H**-Ar), 4.31 (m, 2H, CH_2), 4.29 (m, 1H, (C=O)-CH), 2.98 (m, 2H, NH-CH_2), 1.78-1.40 (m, 6H, CH_2-CH_2-CH_2-NCA).

^{13}C NMR (400 MHz, $CDCl_3$, ppm): 172.14, 152.45 (2C, C=O conj. anhydride), 156.56 (1C, C=O carbamate), 144.41, 141.21, 128.06, 127.52, 125.60, 120.59 (12C, Fmoc-ring carbons), 65.65 (1C, Ar-CH_2), 57.59 (1C, αC), 40.00 (1C, Lys CH_2), 31.12 (1C, NH-C), 29.23 (1C, Lys CH_2), 22.03 (1C, Lys CH_2).

Synthesis of Lys(Z)-NCA

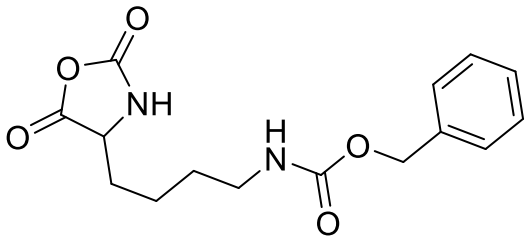

Figure 3.2: Lys(Z)-NCA Structure

N^{6}-(benzyloxycarbonyl)lysine (5 g, 14 mmol) and α-pinene (3.7 mL, 27 mmol) added to a dry, three-neck round bottom flask. The flask was fitted with a reflux condenser, a pressure-equalising dropping funnel fitted with a suba-seal, and a stopper in the third neck. These materials were dried under vacuum (1 h) before being dissolved in anhydrous THF (60 mL) and stirred at 60 °C. Concurrently, triphosgene (3.0 g, 11 mmol) was dissolved in additional dry THF (10 mL) before being added dropwise to the stirred reaction mixture.

The reaction was left to stir at 60 °C until completion (2 h), which was indicated by the complete dissolution of the NCA product, leaving a clear yellow solution. This solution was filtered *via* hot gravity filtration, before being concentrated to ca. 10 mL on the rotary evaporator.

The resulting crude product solution, a yellow liquor, was subsequently precipitated into ice cold hexane (100 mL) and collected *via* vacuum filtration. This crude solid product was then dissolved into additional THF (ca. 10 mL) and the recrystallisation procedure was repeated twice to ensure a pure product, yielding a fine, off-white powder.

Yield: 3.55 g, 65 %

^{1}H NMR (400 MHz, $CDCl_3$): 7.37-7.33 (m, 5H, Ar-H), 5.01 (s, 2H, Ar-CH_2), 4.43 (t, 1H, (C=O)-CH), 3.00 (m, 2H, NH-CH_2), 1.74-1.31 (m, 6H, aliphatic CH_2).

^{13}C NMR (400 MHz, $CDCl_3$, ppm): 172.13, 152.44 (2C, C=O conj. anhydride), 156.57 (1C, C=O carbamate), 137.74, 128.82, 128.19 (6C, Aryl-ring carbons), 65.60 (1C, Ar-CH_2), 57.48 (1C, αC), 39.57, 31.10, 29.25, 22.07 (4C, aliphatic CH_2).

Synthesis of Sarcosine NCA

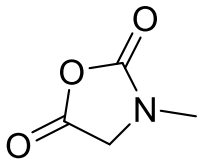

Figure 3.3: Sarcosine NCA Structure

Sarcosine (4.0 g, 45 mmol) and α-pinene (14.0 mL, 88 mmol) added to a dry, three-neck round bottom flask. The flask was fitted with a reflux condenser, a pressure-equalising dropping funnel fitted with a suba-seal, and a stopper in the third neck. These materials were dried under vacuum (1 h) before being dissolved in anhydrous THF (60 mL) and stirred at 60 °C. Concurrently, triphosgene (10 g, 34 mmol) was dissolved in additional dry THF (10 mL) before being added dropwise to the stirred reaction mixture. The reaction was left to stir at 60 °C until completion (4.5 h), which was indicated by the complete dissolution of the NCA product, leaving a clear yellow solution.

This solution was filtered *via* hot gravity filtration, before being concentrated to ca. 10 mL on the rotary evaporator. The resulting crude product solution, a brown liquor, was then stored overnight under vacuum at 60 °C. This resulted in the formation of a brown solid crude product, which was subsequently dissolved into minimal THF (ca. 10 mL) and precipitated into ice cold hexane (100 mL) before collection *via* vacuum filtration.

This dissolution and recrystallisation procedure were repeated twice to ensure a pure final product, collected as a fine, off-white powder.

Yield: 3.44 g, 66 %

IR (λ / cm^{-1}): 2925w (C-H stretch), 1849s (C=O stretch), 1760s (C=O stretch) 1490s (C-H bend) 1403s, 1317s, 1277s, 1221s.

^{1}H NMR (400 MHz, $CDCl_3$, ppm): 4.23 (s, 2H, CH_2), 2.47 (s, 3H, N-CH_3).

^{13}C NMR (400 MHz, $CDCl_3$, ppm): 167.85 (1C, C=O conj. anhydride), 153.08 (1C, C=O conj. anhydride), 51.61 (1C, CH_2) 30.28 (1C, N-CH_3).

PO-Mediated Synthesis of Sarcosine NCA

In an ice-bathed round-bottom flask, Boc-Sarcosine (5.0 g, 26.43 mmol), propylene oxide (18.49 mL, 264.26 mmol) were sequentially dissolved in acetonitrile (100 mL) under magnetic stirring. Triphosgene (3.92 g, 13.21 mmol) was finally added in one portion and the flask was left half-open, to facilitate the *in situ* deprotection of Boc. The reaction was stirred at ca. 4 °C for 1.5 h, Excess triphosgene was quenched by adding 100 ml ca. 4 °C water, with an additional 3 min of stirring. The mixture was extracted with ethyl acetate (2 x 100 mL) at room temperature. The combined organic phases were washed with brine and dried using anhydrous $MgSO_4$, before concentration by rotary evaporation to a crude product, which was purified by repeated crystallisation from THF and ice-cold hexane, without N_2 protection. The pure product was obtained as a white granular crystal.

Yield 3.04 g, 68 %

^{1}H NMR (400 MHz, $CDCl_3$, ppm): 4.07 (s, 2H, CH_2), 2.98 (s, 3H, N-CH_3).

^{13}C NMR (400 MHz, $CDCl_3$, ppm): 165.31 (1C, C=O conj. anhydride), 152.35 (1C, C=O conj. anhydride), 50.94 (1C, CH_2) 30.33 (1C, N-CH_3).

3.1.1.2 Phosgene-Free NCA Synthesis

T3P-Mediated Synthesis of Lys(Boc)-NCA

T3P (10.31 mL, 17.32 mmol) was added dropwise to N^2,N^6-bis(tert-butoxycarbonyl)-L-lysine (5g, 14.43 mmol) in anhydrous ethyl acetate (60 mL) at 50 °C under nitrogen. The resulting solution was stirred at 50 °C for 3 hours, then cooled to RT. Water (60 mL) was added to the solution and transferred to a separating funnel. The organic layer was separated and washed further with brine (2 x 60 mL), dried over $MgSO_4$ and concentrated giving a white solid.

The solid was re-dissolved in anhydrous ethyl acetate (30 mL) at 50 °C under nitrogen. Heptane (ca. 15 mL) was added until the product started to precipitate. The solution was left stirring as it cooled to r.t and then placed in an ice bath for 1h. The solid was collected and washed with further heptane (2 x 15 mL). The solid was dried under nitrogen for 20 minutes on the filter pad and then stored at -20 °C under nitrogen until used.

Yield: 2.99 g, 76 %

^{1}H NMR (400 MHz, $CDCl_3$, ppm): 4.43 (t, 1H, αC-**H**), 2.90 (m, 2H, NH-C**H$_2$**-CH_2) 1.64-1.72 (m, 2H, αCH-C**H$_2$**) 1.26-1.41 (m, 13H, C-(C**H$_3$**)$_3$, αCH-CH_2-C**H$_2$**-C**H$_2$**).

^{13}C NMR (400 MHz, $CDCl_3$, ppm): 172.14 (1C, C=O conj. anhydride), 156.05 (1C, C=O carbamate) 152.44 (1C, C=O conj. Anhydride) 77.86 (1C, CH_2) 57.49 (1C, CH_2) 31.10 (1C, CH_2) 29.34 (1C, CH_2) 28.73 (3C, CH_3)$_3$) 22.07 (1C, CH_2).

T3P-Mediated Synthesis of Lys(Z)-NCA

T3P (9.39 mL, 15.77 mmol) was added dropwise to N^2-(tert-butoxycabonyl),N^6-(benzyloxycarbonyl)-L-lysine (5g, 13.14 mmol) in anhydrous ethyl acetate (60 mL) at 50 °C under nitrogen. The resulting solution was stirred at 50 °C for 3 hours, then cooled to RT. Water (60 mL) was added to the solution and transferred to a separating funnel. The organic layer was separated and washed further with brine (2 x 60 mL), dried over MgSO4 and concentrated giving a white solid. The solid was re-dissolved in anhydrous ethyl acetate (30 mL) at 50 °C under nitrogen. Heptane (ca. 15 mL) was added until the product started to precipitate.

The solution was left stirring as it cooled to r.t and then placed in an ice bath for 1h. The solid was collected and washed with further heptane (2 x 15 mL). The solid was dried under nitrogen for 20 minutes on the filter pad and then stored at -20 °C under nitrogen until used.

Yield: 2.82 g, 70 %

^{1}H NMR (400 MHz, $CDCl_3$, ppm): 7.25-7.37 (m, 5H, Aromatic C-H) 5.00 (s, 2H, Ar-C**H$_2$**) 4.42 (t, 1H, αC-**H**) 2.98 (t, 2H, NH-C**H$_2$**) 1.66-1.73 (m, 2H, αCH-C**H$_2$**) 1.26-1.45 (m, 4H, Lys aliphatic C**H$_2$**).

^{13}C NMR (400 MHz, $CDCl_3$, ppm): 176.88, 157.19 (2C, C=O conj. anhydride), 161.31 (1C, C=O carbamate), 142.49, 133.58, 132.95(6C, Aryl-ring carbons), 70.53 (1C, Ar-CH_2), 62.23 (1C, αC), 44.12, 35.85, 33.99, 26.82 (4C, aliphatic CH_2).

T3P-Mediated Synthesis of Sarcosine NCA

T3P (18.88 mL, 31.68 mmol) and Pyridine (2.13 mL, 26.40 mmol) were added dropwise and sequentially to N-(*tert*-butoxycarbonyl)Sarcosine (5g, 26.40 mmol) in anhydrous ethyl acetate (150 mL) at r.t. under nitrogen. The resulting solution was stirred overnight. Water (100 mL) was added to the solution and transferred to a separating funnel. The organic layer was separated and washed further with brine (2 x 100 mL), dried over MgSO4 and concentrated, giving a crude white solid. The solid was re-dissolved in anhydrous ethyl acetate (30 mL) at 50 °C under nitrogen. Heptane (ca. 15 mL) was added until the product started to precipitate. The solution was left stirring as it cooled to r.t and then placed in an ice bath for 1h.

The solid was collected and washed with further heptane (2 x 15 mL). The solid was dried under nitrogen for 20 minutes on the filter pad and then stored at -20 °C under nitrogen until used.

Yield: 1.90 g, 62 %

IR (λ / cm^{-1}): 2929w (C-H stretch), 1850s (C=O stretch), 1755s (C=O stretch) 1488s (C-H bend) 1404s, 1317s, 1287s, 1230s.

^{1}H NMR (400 MHz, $CDCl_3$, ppm): 4.23 (s, 2H, CH_2), 2.47 (s, 3H, N-CH_3).

^{13}C NMR (400 MHz, $CDCl_3$, ppm): 165.25 (1C, C=O conj. Anhydride), 152.33 (1C, C=O conj. Anhydride) 50.94 (1C, CH_2) 30.34 (1C, CH_3).

3.1.2 OCA Synthesis

3.1.2.1 Phosgene-Mediated OCA Synthesis

Synthesis of Mandelic Acid OCA

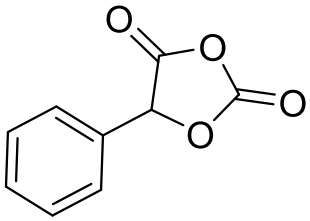

Figure 3.4: Mandelic Acid OCA Structure

To a dry Schlenk tube, mandelic acid (6.0 g, 39 mmol) and activated charcoal (0.58 g) were added, before being dried under vacuum (1 h). The solids were then dissolved in anhydrous THF, and diphosgene (5.5 mL, 46 mmol) was added dropwise to the solution. The reaction mixture was stirred under N_2 flow until reaction completion (18 h). The resulting reaction mixture was then filtered through a plug of Celite® in order to remove the activated charcoal. This yielded a yellow-green solution, which was concentrated on the rotary evaporator to ca. 10 mL before precipitation in ice-cold hexane (ca. 80 mL). The resultant solid was collected via vacuum filtration, washed with additional hexane (2 x 10 mL), and re-dissolved in THF (10 mL). The precipitation and collection stages were then repeated twice to yield a fine, white powder.

Yield: 5.12 g, 74 %

IR (λ / cm^{-1}): 3447w (N-H stretch), 2923w (C-H stretch), 1900m (aromatic C-H bend), 1807 (C=O stretch conj. anhydride), 1786 (C=O stretch conj. anhydride), 1457 (C-H bend), 1296s, 1243s.

^{1}H NMR (400 MHz, $CDCl_3$, ppm): 7.42-7.35 (m, 5H, Ar-H) 5.94 (s, 1H, (C=O)-CH).

^{13}C NMR (400 MHz, $CDCl_3$, ppm): 165.33 (1C, C=O anhydride), 148.02 (1C, C=O anhydride), 130.83 (1C, (C=O)-CH_2C aryl carbon), 129.58 (2C, aryl carbon), 129.27 (1C, aryl carbon), 126.16 (2C, aryl carbon), 80.46 ((C=O)-CH_2)

3.2 Results and Discussion

3.2.1 NCA Products

NCA products, synthesised for the research reported in **Chapters 4**-**6**, are here characterised. This includes three different NCAs of lysine, protected by Fmoc, Boc and Z protecting groups. In addition, phosgene-free syntheses of Lys(Z)-NCA and Lys(Boc)-NCA are also reported, activated by (T3P) in accordance with the methodology outlined by Laconde *et al*.[1] These syntheses are reported in parallel to allow comparison of their respective preparative procedures, inherent safety and percentage yields.

While it was not utilised in subsequent chapters, the synthesis of sarcosine-NCA, *via* phosgene-mediated and phosgene-free routes, has also been reported here. Furthermore, a route wherein propylene oxide provides moisture tolerance throughout the reaction, is also reported. These three routes are similarly critiqued for their respective preparative complexity, robustness to impurities and percentage yields.

3.2.1.1 Lys(Fmoc)-NCA

Whilst the majority of literary examples of lysine NCA syntheses typically involve protection of the pendant chain by a Z-protecting group, there are some examples that have been produced using Fmoc as an alternative.[2,3] Fmoc protection has attracted attention due to literature examples of a procedure for thermally cleaving its connection to the pendant chain at 120 °C,[3,4] leaving a free amine group that can be exploited as a new initiation site to induce polymer chain branching, or as a site for post-polymerisation modification.

This presents an extremely attractive option as a protecting group, both for the economic advantage of deprotection without additional reagents, and for the improvement in health and safety that thermal cleavage provides when compared to the strong-acid cleavage required for Z-protected PLys, which requires use of toxic and corrosive HBr. To better understand the possible enhancements that this trifunctional amino acid can provide, the synthesis of Lys(Fmoc)-NCA has here been reported, with its co-polymerisation from methoxy-poly(ethylene glycol) (M.W. 5000 g mol^{-1}) detailed in **Section 5.3.1**.

Lys(Fmoc)-NCA was synthesised using *via* Fuchs-Farthing carbonylation, using the aforementioned phosgene-mediated preparation. The crude products of this reaction were subjected to repeated recrystallisation steps to remove any side products, impurities or residual starting materials, in order to ensure high purity. As evidenced by the yield of the

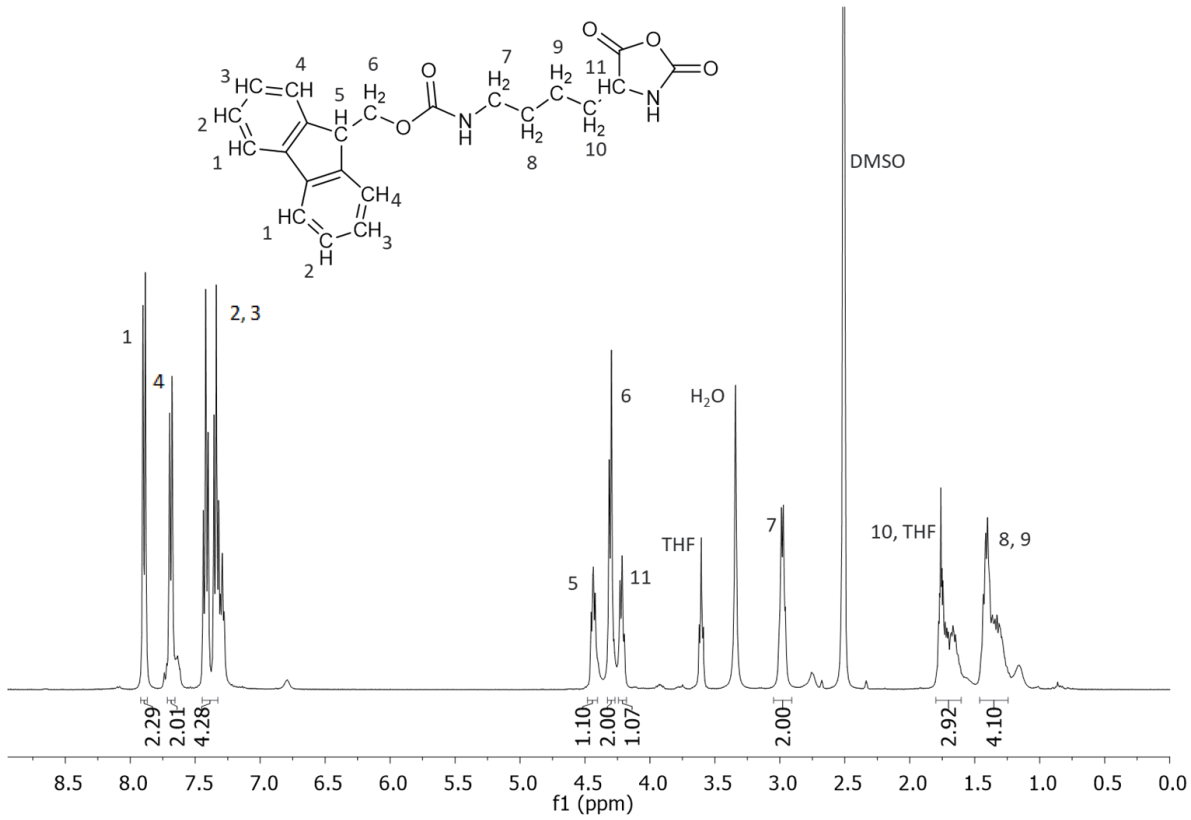

product (72 %) and ^{1}H NMR provided in **Figure 3.5** below, Lys(Fmoc)-NCA was here synthesised successfully and with high purity.

Figure 3.5: ^{1}H NMR (400 MHz, DMSO-d_6) Spectrum of Lys(Fmoc)-NCA.

Figure 3.5 shows clearly that Lys(Fmoc)-NCA was synthesised successfully, and without the presence of impurities. The positions and integrals of the peaks align closely with values reported in the literature.[2] The proton environments of the NCA amide (N-H), α-proton (**11**) and the four ethyl groups along the lysine side-chain (**7-10**) are clearly represented, alongside those bound to the aromatic rings (**1-4**) and aliphatic positions (**5, 6**) upon the Fmoc group. This assessment is supported by the ^{13}C NMR spectrum of the product (**Figure A.3.1.1**) which, alongside the characteristic carbonyl peaks of the product NCA (172.14 ppm, 156.56 ppm) and the additional peak of the Fmoc-carbonyl (152.45 ppm), features a number of peaks in the range of 120 ppm – 145 ppm that represent the carbon environments of the aromatic rings upon the Fmoc protecting group. The FTIR spectrum of Lys(Fmoc)-NCA (**Figure A.3.2.1**) agrees with the available literature,[2] and supports the findings of the spectral analyses described above. Peaks can be observed at the typical 1846 cm^{-1} and 1810 cm^{-1}, evidencing the closure of the NCA ring around its second carbonyl group. In addition, a cluster of peaks at 2992 cm^{-1}, 2984 cm^{-1}, 2971 cm^{-1}, 2950 cm^{-1}, 2933 cm^{-1} and 2923 cm^{-1} can be seen protruding from a broad range of absorbances, representing a number of C-H stretching vibrations across the aliphatic side chain of the lysine NCA and the aromatic rings of its Fmoc protecting group. Furthermore, a third carbonyl C=O stretch, also from the Fmoc group, can be seen at 1780 cm^{-1}. Phosgene-free synthesis of Lys(Fmoc)-NCA is not reported here, as it did not fall within the scope of this research project. This is due to factors reported in **Chapter 5** on the ring-opening polymerisation characteristics of the Fmoc-protected product, and the complexity of Fmoc-group deprotection in comparison to that of the Boc-protecting group.

3.2.1.2 Lys(Z)-NCA

Whilst a number of technical and economic advantages can be gained from the thermal deprotection of lysine repeat units in a block copolymer, it should be noted that this science is still early in its investigation and should not be relied upon for a controlled and selective procedure. Lys(Z)-NCA provides an effective alternative to this experimental pursuit, as it has already been documented in the existing literature, and the orthogonal deprotection of its Z group is well understood.[3,5]

Lys(Z)-NCA has here been synthesised *via* Fuchs-Farthing carbonylation, using the triphosgene method at 60 °C. The crude products of this reaction were subjected to repeated recrystallisation steps to remove any side products, impurities or residual starting materials. As evidenced by the yield of the product (65 %) and ^{1}H NMR provided in **Figure 3.6** below, Lys(Z)-NCA was here synthesised successfully and in high purity.

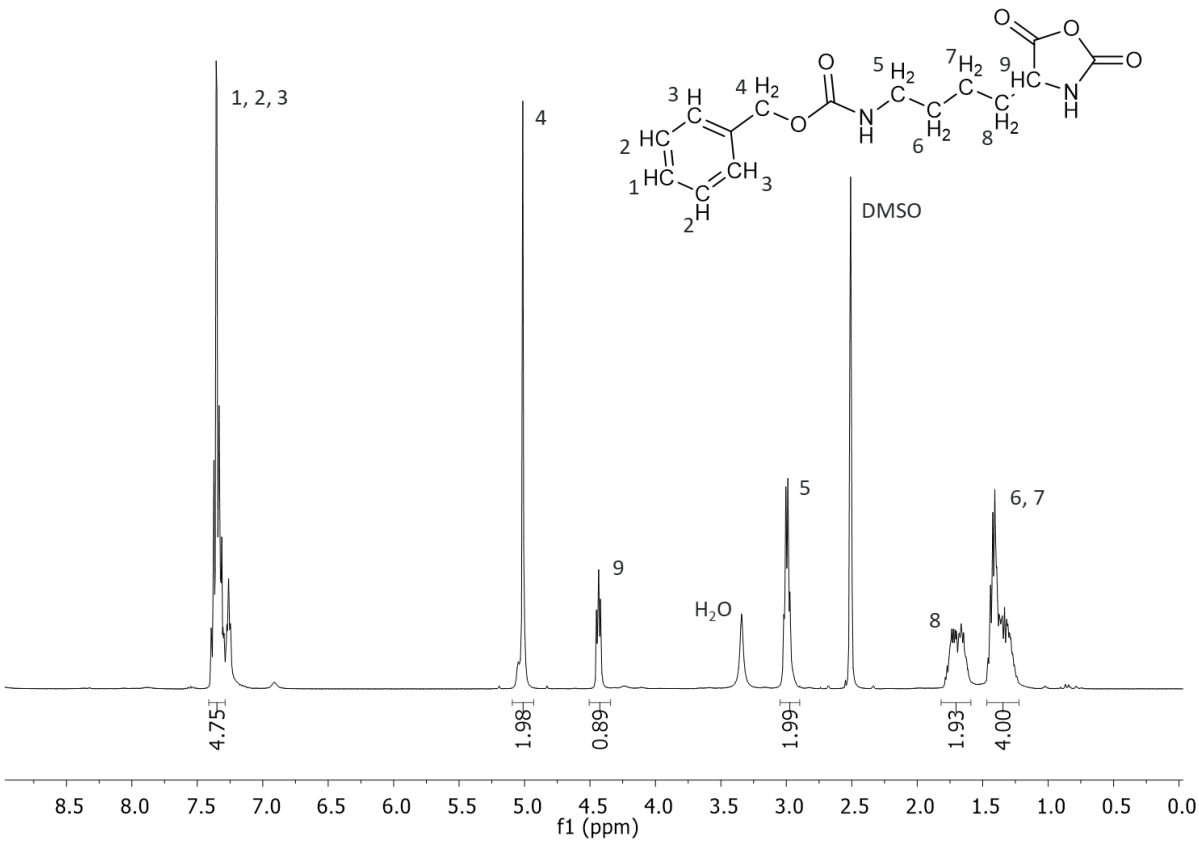

Figure 3.6: ^{1}H NMR (400 MHz, DMSO-d_6) Spectrum of Lys(Z)-NCA.

Figure 3.6 shows clearly that Lys(Z)-NCA was synthesised successfully, and without the presence of impurities. The positions and integral values of the peaks align closely with values reported in the literature,[5] with the α-proton (**9**) and four-ethyl group side chain (**5-8**) of the NCA clearly visible alongside the aromatic (**1-3**) and aliphatic (**4**) proton environments of the benzyloxycarbonyl protecting group. This assessment is supported by the ^{13}C NMR spectrum of the product (**Figure A.3.1.2**) which, alongside the characteristic carbonyl peaks of the product NCA (172.13 ppm, 156.57 ppm) and the additional peak of the Z-carbonyl (152.44 ppm), features peaks in 125 ppm – 140 ppm range that correspond to the carbon environments of the aromatic rings upon the Z protecting group.

Also reported here is the synthesis of Lys(Z)-NCA *via* the phosgene-free, T3P-mediated procedure outlined in **Section 3.1.1.2**. T3P is a nontoxic reagent that requires no specific handling measures and, unlike phosgene-derived compounds, does not generate harmful by-products, such as harmful and corrosive HCl gas. Whereas phosgene-mediated Fuchs-Farthing carbonylation is facilitated by addition-elimination of the highly reactive phosgene acyl chloride, T3P-mediated synthesis exploits the entropic benefit afforded by its ring-opening to activate even poor nucleophiles.[1] The purification procedure following T3P-mediated synthesis differs from the phosgene-route also. Certain by-products are still lost to the gaseous phase during reaction, specifically the isobutene molecule eliminated from the Boc-protecting group during ring closure. However, residual tripropylphosphonium phosphate, as well as any pyridinium cations generated from base-activated synthesis, must be removed *via* repeated solvent extraction from ethyl acetate into an aqueous phase. Subsequent crystallisation by exposure to a minimum quantity of warmed hexane, added slowly to a saturated solution of crude product in ethyl acetate, allows for the slow, controlled formation of high-purity crystalline product, which can then be dried and obtained for analysis. As evidenced by the yield of the product (70 %), and the ^{1}H NMR provided in **Figure 3.7** below, Lys(Z)-NCA was here synthesised successfully and in high purity.

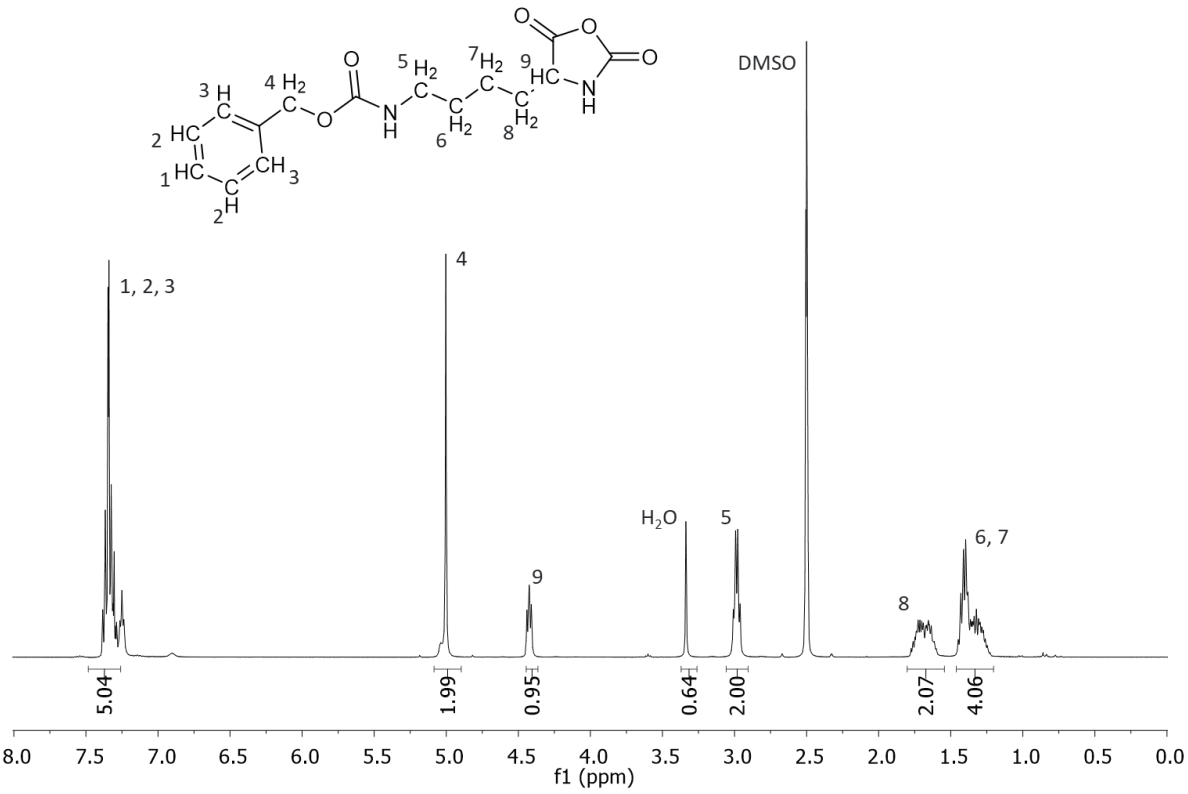

Figure 3.7: ^{1}H NMR Spectrum (400 MHz, DMSO-d_6) of Lys(Z)-NCA, synthesised *via* T3P-mediated methodology.

Figure 3.7 shows clearly that Lys(Z)-NCA was synthesised successfully, and without the presence of impurities. The positions and integral values of the peaks align closely with values reported in the literature,[1,5] with the α-proton (**9**) and four-ethyl group side chain (**5-8**) of the NCA clearly visible alongside the aromatic (**1-3**) and aliphatic (**4**) proton environments of the benzyloxycarbonyl protecting group. This assessment is supported by the ^{13}C NMR spectrum of the product (**Figure A.3.1.5**) which, alongside the characteristic carbonyl peaks of the product NCA (176.88 ppm, 157.19 ppm) and the additional peak of the Z-carbonyl (152.45 ppm), features peaks in 125 ppm – 140 ppm range that correspond to the carbon environments of the aromatic rings upon the Z protecting group. In comparison to the phosgene-mediated Fuchs-farthing carbonylation route outlined in **Section 3.1.1.1**, T3P-mediated synthesis of Lys(Z) has resulted in a similar yield of high purity product, as determined by ^{1}H NMR and ^{13}C NMR.

Importantly, these data agree with the findings by Laconde *et al*., that a suitable phosgene-free replacement for protected NCAs is possible through the use of T3P, representing a far safer preparative methodology for scale-up, should materials derived from these NCA monomers prove viable for pharmaceutical applications.

3.2.1.3 Lys(Boc)-NCA

The tert-butoxycarbonyl-group is the most attractive option for lysine side-chain protection within this research for several factors. Firstly, the purification procedure following Boc-deprotection is significantly less complex than that of the Fmoc- or Z-groups, a point which is visualised in **Scheme 3.1** below.

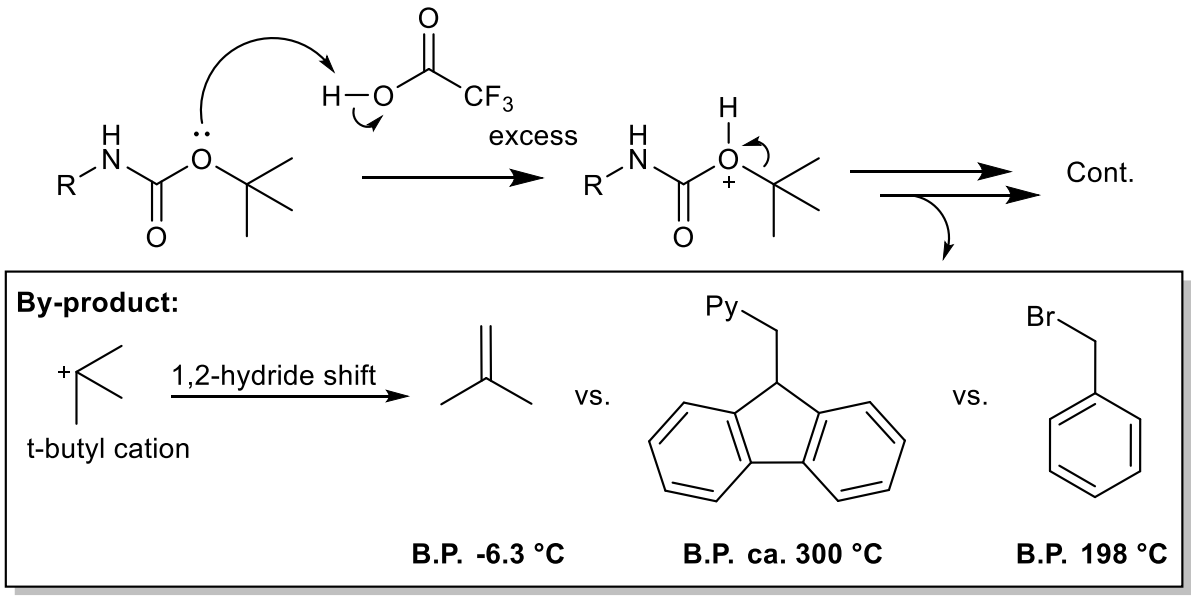

Scheme 3.1: By-products eliminated during the deprotection of Fmoc- Z- and Boc- protecting groups, respectively.

As illustrated in **Scheme 3.1**, base-activated deprotection of the fmoc group yields a molecule of 9-(pyridin-1-yl)-9H-fluorene, whilst hydrogenation of the Z-protecting group by agents such as HBr yield a molecule of benzyl bromide. For the case of polymer deprotection, purification can be subsequently performed by dialysing the product, thereby separating the small-molecule by-products across a membrane. For products detailed within this report, dialysis tubing with a cut-off of 2000 g mol^{-1} was used. In contrast, acid-activated deprotection of Boc-protecting groups generates a molecule of isobutene, the boiling point of which is -6.3 °C.

The generated by-product therefore evaporates from solution and is removed from the system by N_2 flow, as described in the methodology of **Section 5.2.4.1**. As a result, acid-activated and thermal-activated deprotection of Boc-groups can be achieved in high purity without the need for additional purification reducing preparative complexity and expenditure.

Due to the sensitivity of the Boc-group to acidic conditions, it has been reported in the past that the *in-situ* generation of HCl molecules during traditional Fuchs-Farthing carbonylation have been sufficient to trigger unwanted deprotection of the lysine side chains, prior to NCA ROP. Without protection, these active amine units can then contribute to initiation, resulting in both block copolymer products, successfully initiated from the intended macroinitiator, as well as homo-lysine products connected *via* α- and ε-linkages with poorly defined branching architectures. These are entirely unsuitable for therapeutic drug delivery and for this reason, as well as for safety, traditional phosgene-mediated synthesis was avoided in preference of the T3P-mediated route. As evidenced by the yield of the product (76 %) and ^{1}H NMR provided in **Figure 3.8** below, Lys(Boc)-NCA was here synthesised successfully and in high purity.

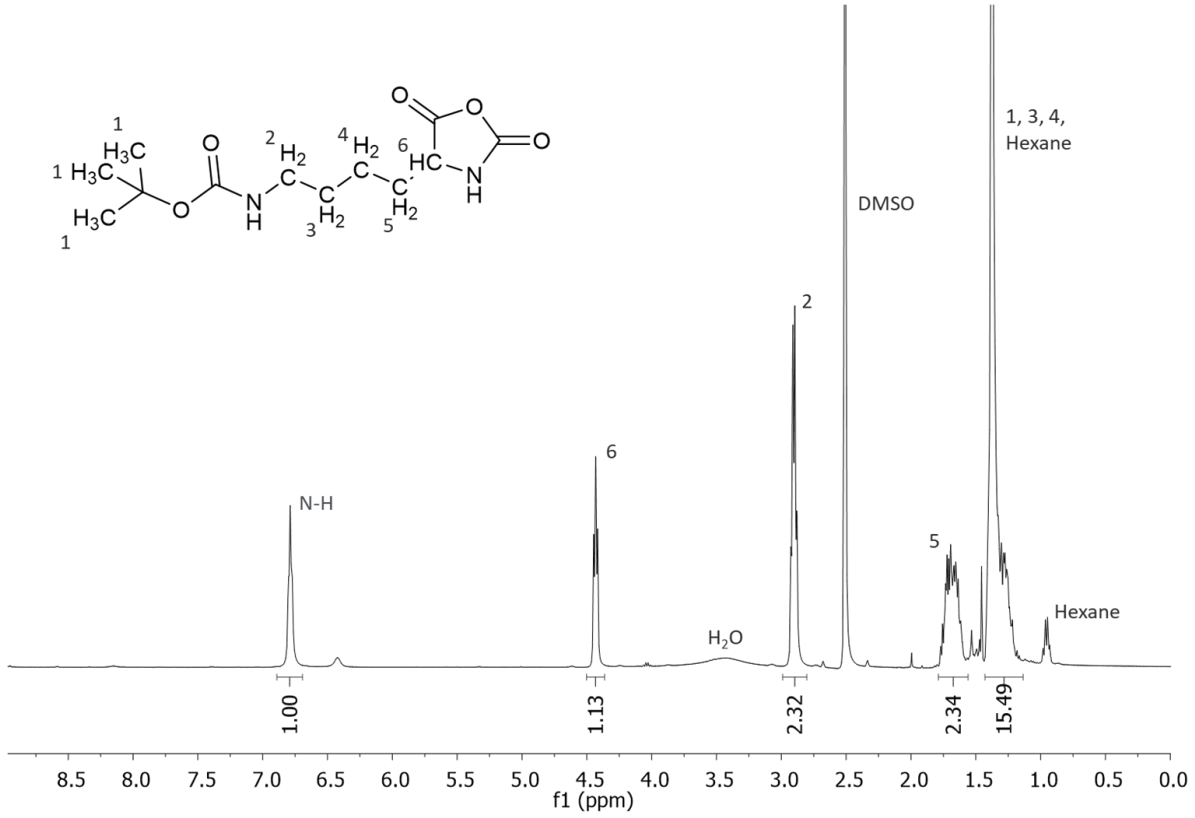

Figure 3.8: ^{1}H NMR Spectrum (400 MHz, DMSO-d_6) of Lys(Boc)-NCA, synthesised *via* T3P-mediated methodology.

Figure 3.8 shows clearly that Lys(Boc)-NCA was synthesised successfully, and without the presence of impurities. The positions and integral values of the peaks align closely with values reported in the literature,[1] with the α-proton (**6**) and four-ethyl group side chain (**2-5**) of the NCA clearly visible alongside the *tert*-butyl proton environment (**1**) of the protecting group. This assessment is supported by the ^{13}C NMR spectrum of the product (**Figure A.3.1.6**) which features the characteristic carbonyl peak of the protecting group (156.05 ppm), as well as those of the NCA (172.14 ppm, 152.44 ppm) alongside aliphatic peaks of both the lysine *α*-carbon and pendant chain (57.59 ppm, 31.10 ppm, 29.34 ppm, 22.07 ppm) and the tert-butyl architecture of the Boc (77.86 ppm, 28.73 ppm).

3.2.1.4 Sarcosine NCA

As discussed in **Section 1.1.1**, whilst PEG is extensively employed as a macroinitiator and hydrophilic component in block copolymer amphiphiles for drug delivery in the literature, it is not without its drawbacks. The human body is incapable of enzymatically degrading the constituent ether bonds of PEG, and as such it cannot break down the polymer following controlled release of the therapeutic payload, nor can it excrete such high molecular weight material as it would small molecules.[6] Consequentially, PEG macromolecules accumulate in organs such as the liver, spleen and kidneys.[7] Whilst this accumulation has previously been considered acceptable, there are growing concerns over recent research which highlights an upward trend of anti-PEG immunoglobulin generation in the human population, especially those with repeated exposed to PEGylated therapeutics. These antibodies can inhibit the activity PEGylated drugs or therapies, thereby reducing their efficacy. In extreme cases, these antibodies can result in allergic and anaphylactic reactions, a low-occurrence side effect noted during administration of the Covid-19 mRNA vaccine, which utilised PEG to stabilise lipid nanoparticles.[8] A study conducted by McSweeney *et al*. in 2021 reported that up to 70 % of people may exhibit detectable traces of these antibodies, and so significant experimental efforts are currently underway to discover physiologically degradable and biocompatible alternatives.[9]

Polysarcosine has been used extensively as a biomimetic alternative to PEG, provided hydrophilic properties and nucleophilic activity as an amine-terminated macroinitiator, without need of additional synthetic complexity, as is required for the conversion of typical methoxy-poly(ethylene glycol) to an active amine following its polymerisation. Whilst polysarcosine was not utilised in the context of this report, it had originally been intended for testing as a mPEG-NH_2 alternative, and so several synthetic routes were trialled for the manufacture of sarcosine NCA, reported here. These include two phosgene-mediated routes, one of which is afforded moisture-tolerance by a highly active HCl scavenger, and one phosgene-free route, again utilising T3P.

Reported first is the synthesis of sarcosine NCA *via* the typical phosgene-mediated route, as described in section **3.1.1.1**. This method requires greater preparative complexity than even other phosgene-mediated routes, due to the difficulty experienced in crystallising the Sar-NCA product. In spite of this, however, the reaction was still performed successfully, as evidenced by the achieved yield (66 %) and in high purity, as can be observed in the ^1H NMR presented in **Figure 3.9** below.

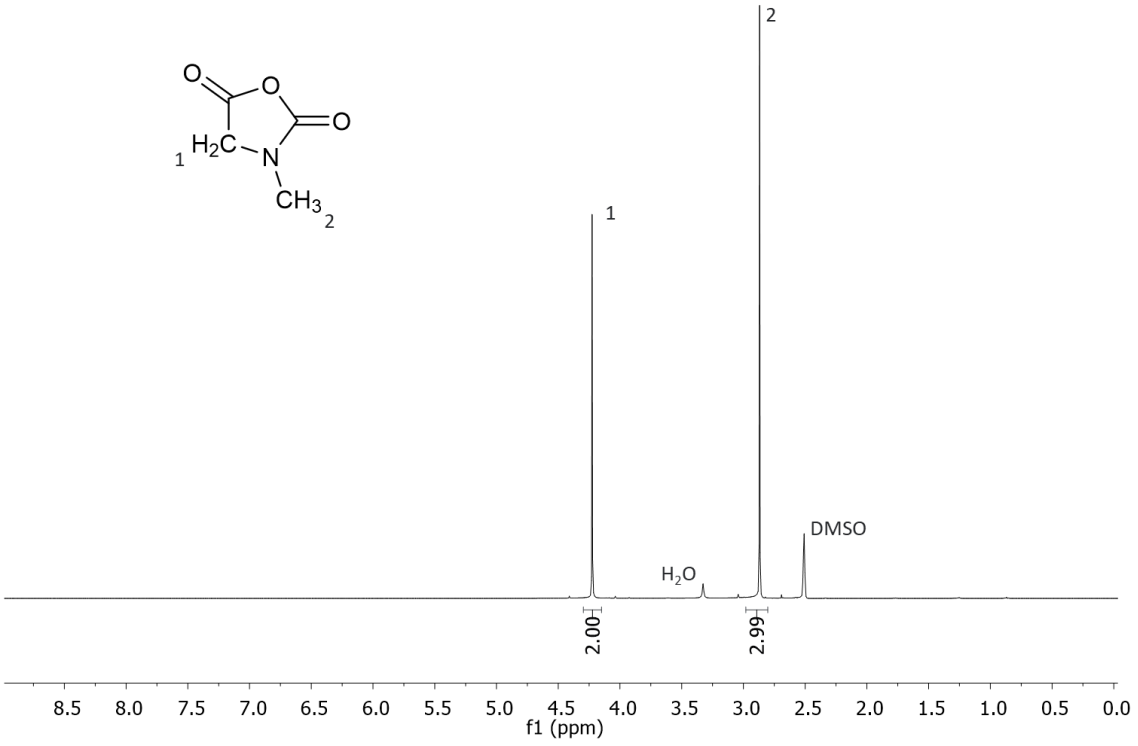

Figure 3.9: ^1H NMR Spectrum (400 MHz, $CDCl_3$) of Sar-NCA, synthesised *via* phosgene-activated methodology.

Figure 3.9 shows clearly that Lys(Boc)-NCA was synthesised successfully, and without the presence of impurities. The positions and integral values of the peaks align closely with values reported in the literature, with the α-proton (**6**) and four-ethyl group side chain (**2-5**) of the NCA clearly visible alongside the *tert*-butyl proton environment (**1**) of the protecting group.[10] This assessment is supported by the ^{13}C NMR spectrum of the product (**Figure A.3.1.3**) which features the characteristic carbonyl peak of the protecting group (156.05 ppm), as well as those of the NCA (172.14 ppm, 152.44 ppm) alongside aliphatic peaks of both the lysine *α*-carbon and pendant chain (57.59 ppm, 31.10 ppm, 29.34 ppm, 22.07 ppm) and the tert-butyl architecture of the Boc (77.86 ppm, 28.73 ppm).

As discussed in the preparative methodology of **Section 3.1.1.1**, phosgene-activated carbonylation of sarcosine has also been reported here in accordance with the preparation described in the literature by Tian *et al*.[11] The authors utilised propylene oxide as a HCl scavenger in their synthesis, which rapidly converts HCl into 1-chloro-2-propanol and 2-chloro-1-propanol, and substantially outpaces traditional α-pinene HCl scavengers. This allows for increased robustness of the reaction procedure against acid-catalysed side reactions, such as NCA hydrolysis, uncontrolled oligo-/polymerisation, or the formation of chloroamide compounds. Furthermore, the authors demonstrated that PO could also be used to achieve moisture-tolerance throughout the reaction, as the additional HCL generated by hydrolysis of *in situ* derived phosgene would likewise be scavenged before it could accumulate meaningfully. As such, this synthesis of Sar-NCA was performed without an inert atmosphere, and utilised Boc-sarcosine as starting material, so as to avoid unwanted aminolysis of PO by the secondary amine. This reaction was performed successfully, as demonstrated by the yield (68 %), and high purity as illustrated in the ^{1}H NMR spectrum, provided in **Figure 3.10** below.

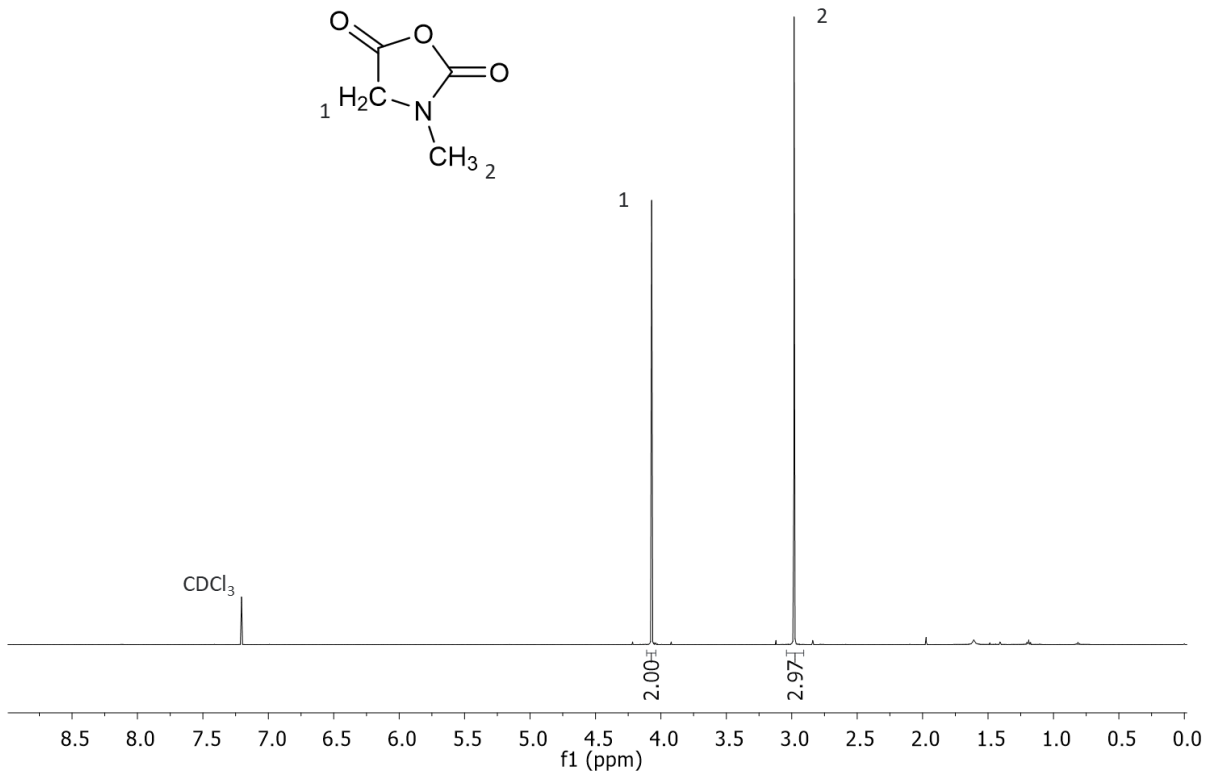

Figure 3.10: ^{1}H NMR Spectrum (400 MHz, $CDCl_3$) of Sar-NCA, synthesised *via* triphosgene-activated, PO-mediated methodology.

Figure 3.10 shows clearly that Sar-NCA was synthesised successfully, and in the presence of only minimal solvent impurities, likely the result of the increased crystallisation cycles required to remove the higher quantity of PO-derived side products. The positions and integral values of the peaks align closely with values reported in the literature, both for the α-protons (**1**) and N-methyl protons (**2**).[11] This assessment is supported by the ^{13}C NMR spectrum of the product (**Figure A.3.1.4**) which features the characteristic carbonyl peaks of the NCA (165.31 ppm, 152.35 ppm) alongside those of the α-carbon and N-methyl carbon (50.94 ppm, 30.33 ppm).

Finally, in the pursuit of a safer route to Sar-NCA, the phosgene-free T3P route is also reported here, in accordance with the methodology prescribed by Laconde *et al*.[1] Similarly, this reaction was performed successfully, as is shown in the yield (62 %). However, several solvent impurities, as well as unreacted sarcosine starting material, were observed in this case and are illustrated in **Figure 3.11**.

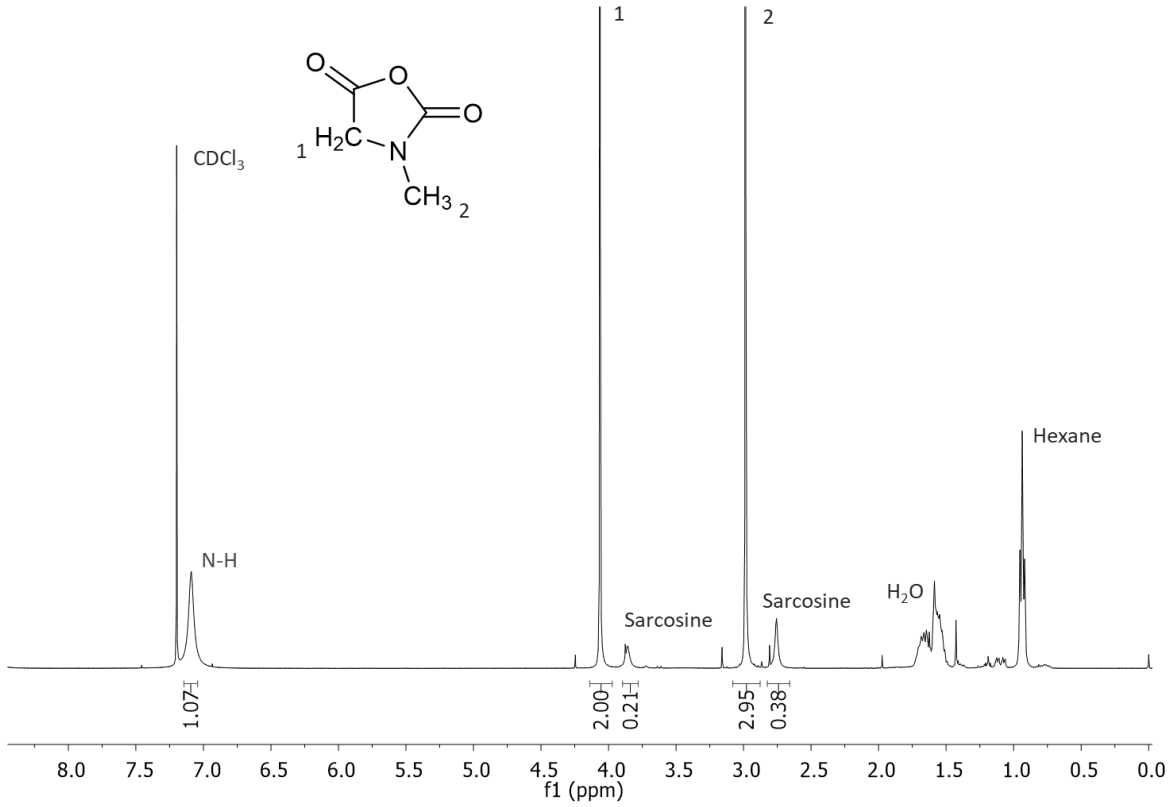

Figure 3.11: ^{1}H NMR Spectrum (400 MHz, $CDCl_3$) of Sar-NCA, synthesised *via* T3P-mediated methodology.

Notably, the data presented in **Figure 3.11** are does suggest that a high quantity of Sar-NCA was achieved, relative to the concentrations of the other materials in solution. This can be evidenced by the relative sizes of the ^{13}C satellite peaks either side of the α-protons (**1**) and N-methyl protons (**2**), in comparison to those presented in **Figure 3.10**, suggestive that significant scale-up of the product peaks was required to visualise the impurities. Nonetheless, it is clear that a number of solvent impurities are present in the product, including water, unsuccessfully separated during $MgSO_4$ drying, and hexane, a remnant of the crystallisation procedure. Furthermore, peaks representing non-cyclised sarcosine residue are present in the system, potentially remnants of unreacted Boc-sarcosine starting material, which might be attributed to the right-hand peak of the integral range attributed to water. Nevertheless, longer reaction times and more rigorous control of the purification procedure would likely nullify these impurities, steps which would have been undertaken had the scope of the research not shifted away from sarcosine polymers.

It is more important in this case to evaluate the overall complexity, safety and efficacy of the three reactions reported here, should the decision be made to revisit polysarcosine.

Whilst propylene oxide may represent an attractive option for NCA synthesis, allowing for management of both generated HCl during reaction and tolerance to moist atmosphere, it should be noted that PO has its own swath of health hazards associated with it. These include acute toxicity *via* inhalation and ingestion, as well being a sensitizer, carcinogenic and mutagenic and toxic to the reproductive system. For these reasons, its safety in a manufacturing environment should be called into question as with phosgene and its derivatives. Furthermore, the preparative complexity is equal amongst procedures, shown by the more intensive purification of the latter two reactions, versus the involved process of low-pressure crystallisation required for the former. As a result, only the phosgene-free methods can be distinguished for its improved safety above other methods.

3.2.2 OCA Products

3.2.2.1 Mandelic Acid OCA

As reported previously by Buchard *et al.* and Zhang *et al.*, the synthesis of mandelic acid OCA (Man-OCA) has been achieved several times in the recorded literature.[12] Of specific importance in the work of Buchard *et al*. is the reduction of reaction temperature for hydroxyl acid carbonylation (room temperature) in comparison to the classical, triphosgene-activated route (ca. 60 °C). This is due to the significantly reduced thermal stability of OCA molecules, which undergo reactions (decarboxylation, back-biting, oligomerisation) at increased temperatures, as corroborated by other prominent authors in the field.[13,14] As such, this reaction utilises diphosgene which, unlike triphosgene, degrades readily to phosgene *in situ* at room temperature. In addition, activated charcoal has here been employed as a heterogeneous HCl scavenger that operates at room temperature, whereas α-pinene would require increased reaction temperatures to work effectively.[15,16] The products of this reaction were filtered using a celite® plug to remove all traces of activated charcoal, as well as being subjected to repeated crystallisation from THF into n-hexane. As evidenced by the yield of the product (74 %) and ^{1}H **Figure 3.12** below, Man-OCA was here synthesised successfully and with high purity.

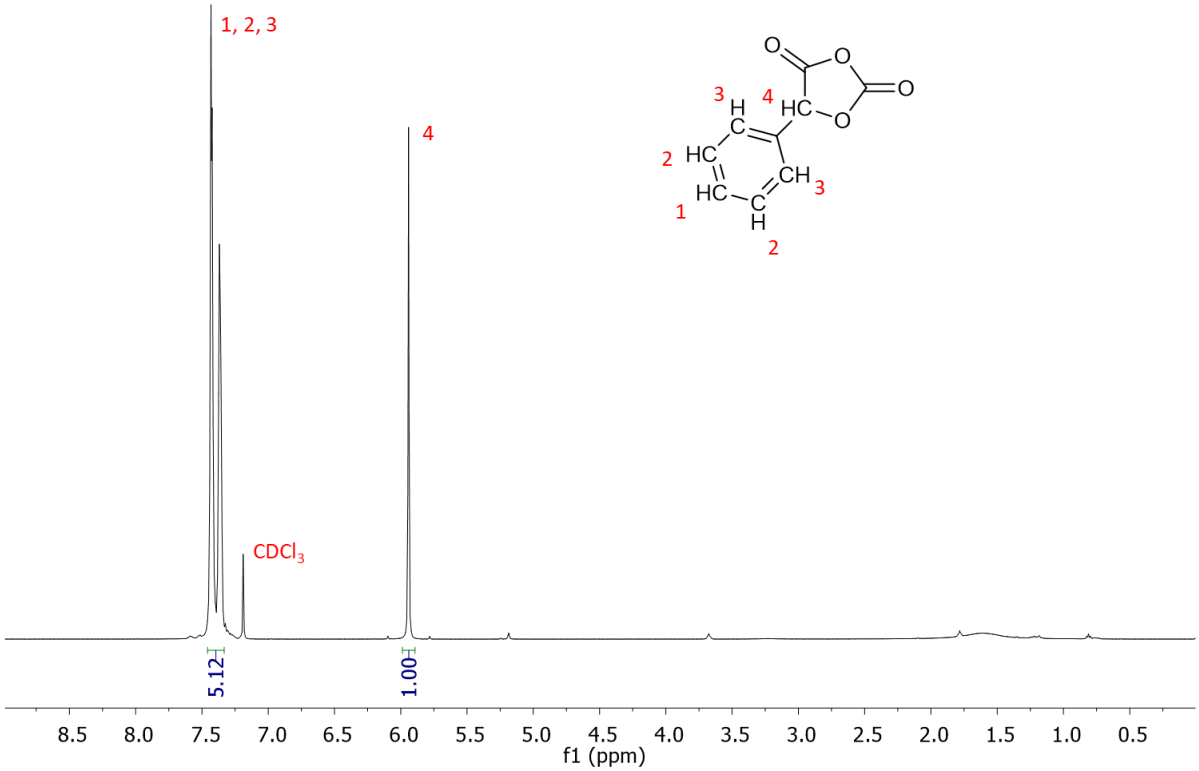

Figure 3.12: ^{1}H NMR Spectrum (400 MHz, $CDCl_3$) of Man-OCA.

Figure 3.12 shows clearly that Man-OCA was here synthesised successfully, with no impurities present. The positions and integral values of the peaks align closely with values reported in the literature, both for the α-proton (**4**), and phenyl ring protons (**1-3**).[12] This assessment is supported by the ^{13}C NMR data obtained (**Figure A.3.1.8**), which features the characteristic carbonyl peaks of the OCA (165.33 ppm, 148.02 ppm) alongside those of the phenyl ring carbon atoms and α-carbon (125 ppm – 135 ppm, 80.46 ppm).

Further agreement with this assessment can be found within the IR spectrum of the product (**Figure A.3.2.3**), which features diagnostic absorbance values at 2923 cm^{-1}, 1900 cm^{-1}, corresponding to the bending and stretching vibrations of the aromatic C-H bonds, as well as at 1807 cm^{-1} and 1786 cm^{-1}, owing to the two distinct conjugated anhydride C=O signals of the OCA molecule. [12]

3.3 References

1. Laconde, G.; Amblard, M.; Martinez, J., *Org. Lett.*, **2021**, *23*, 6412–6416.
2. A V. Athanasiou, P. Thimi, M. Liakopoulou, F. Arfara, D. Stavroulaki, I. Kyroglou, D. Skourtis and H. Iatrou, Polymers, **2020**, *12*, 2819.
3. X. Jin and P. D. Thornton, RSC Adv., **2025**, *15*, 17397–17404.
4. S. Höck, R. Marti, R. Riedl and M. Simeunovic, Chimia, **2010**, *64*, 200–202.
5. Canalp, M. B.; Binder, W. H., *RSC Adv.*, **2020**, *10*, 1287–1295.
6. Padín-González, E.; Oliveira, R. G.; Miguel, S. P.; Serro, A. P.; Fernandes, B. F., *Front. Bioeng. Biotechnol.*, **2022**, 10, 882363.
7. You, J.; Guo, R.; Frey, L. K.; Fréchet, R. A.; Szoka, F. C., *J. Controlled Release*, **2014**, 184, 1–10.
8. Chen, B.-M.; Su, Y.-C.; Chang, Y.-T.; Burnouf, A. W.; Roffler, S.-R., *ACS Nano*, **2021**, 15, 8605–8618.
9. McSweeney, M. D.; Mohan, M.; Commins, S. P.; Nelson, S. M.; Griffith, J. F., *Front. Allergy*, **2021**, 2, 715844.
10. H. Yu, N. Ingram, J. V. Rowley, D. C. Green and P. D. Thornton, *Chem. Eur. J.*, **2020**, *26*, 13352–13358.
11. Tian, Z.-Y.; Zhang, Z.; Wang, S.; Lu, H., *Nat. Commun.*, **2021**, *12*, 1–10.
12. Buchard, A.; Carbery, D. R.; Davidson, M. G.; Ivanova, P. K.; Jeffery, B. J.; Kociok-Köhn, G. I.; Lowe, J. P., *Angew. Chem., Int. Ed.*, **2014**, *53*, 13858.
13. Dove, A. P.; Pounder, R. J.; Fox, D. J., *Polym. Chem.*, **2011**, 2, 2204–2212.
14. Nederberg, F.; Hedrick, J. L. *Angew. Chem. Int. Ed.*, **2001**, 40, 2712–2715.
15. V. Dmitrovic, G. J. M. Habraken, M. M. R. M. Hendrix, W. J. E. M. Habraken, A. Heise, G. de With and N. A. J. M. Sommerdijk, Polymers, **2012**, 4, 1195–1210.
16. J. E. Semple, Synth. Commun., **2017**, 47, 2059–2067.

Appendices

A.3.1 ^{13}C NMR Spectra

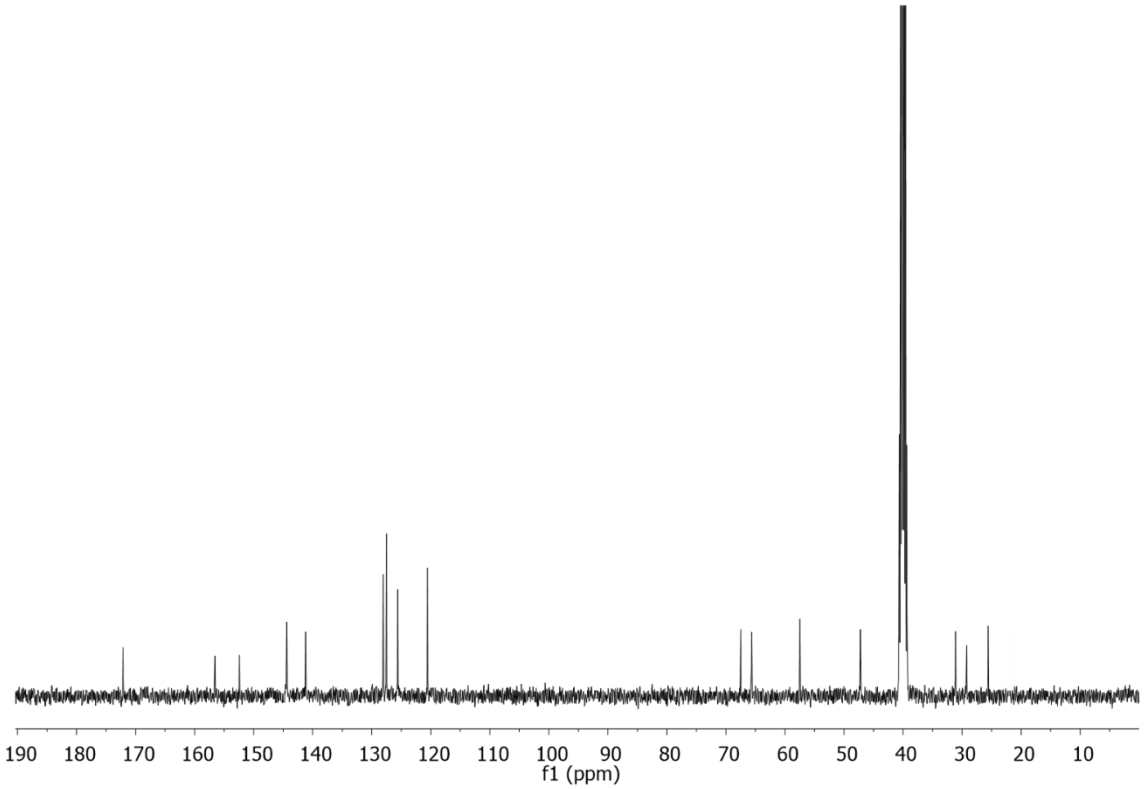

Figure A.3.1.1: ^{13}C NMR (400 MHz, DMSO-d_6) spectrum of Lys(Fmoc)-NCA.

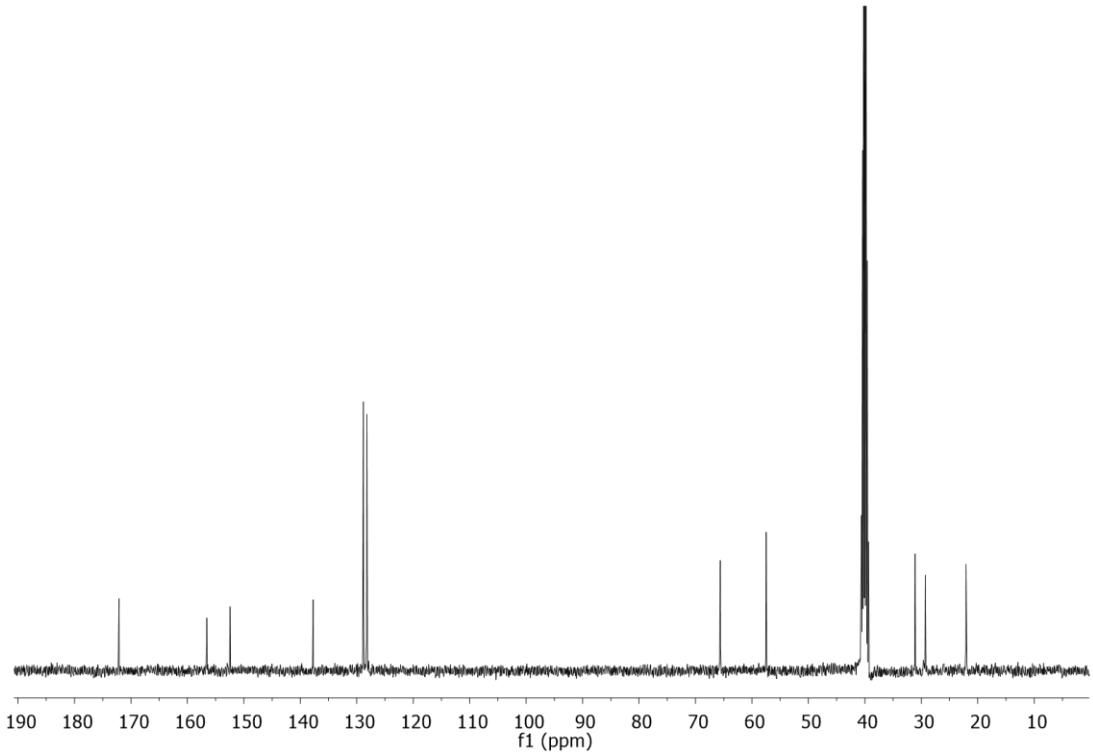

Figure A.3.1.2: ^{13}C NMR (400 MHz, DMSO-d_6) spectrum of Lys(Z)-NCA.

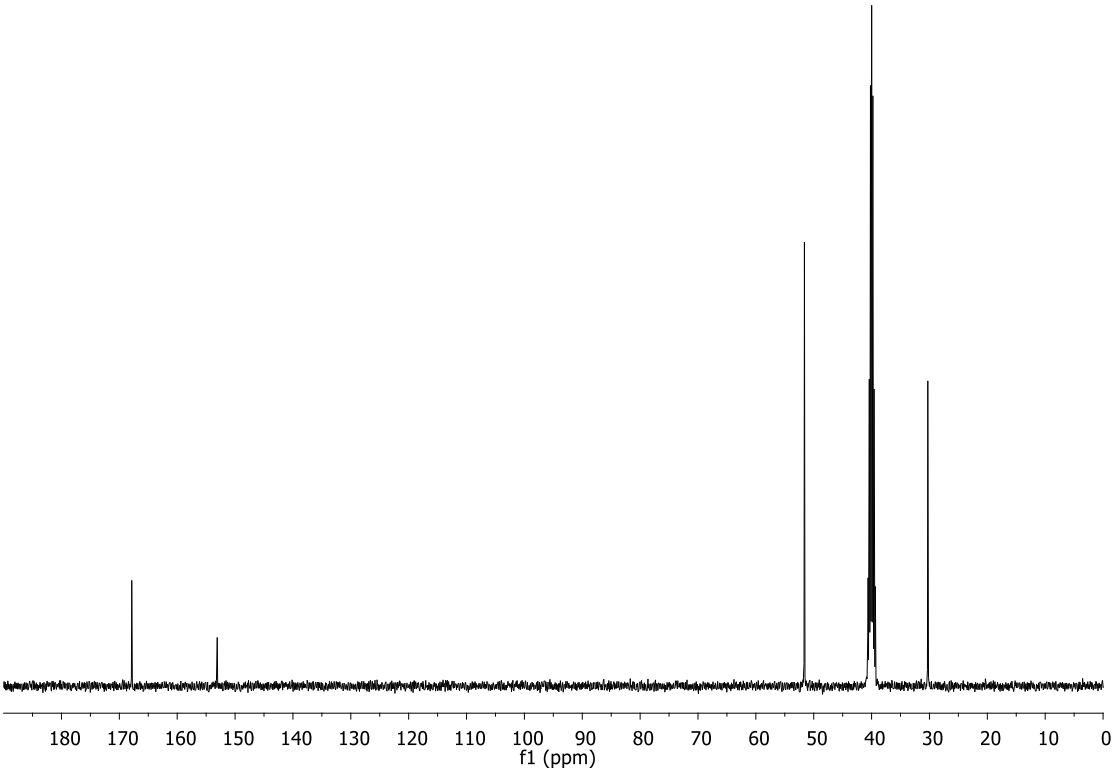

Figure A.3.1.3: ^{13}C NMR (400 MHz, DMSO-d_6) spectrum of Sar-NCA.

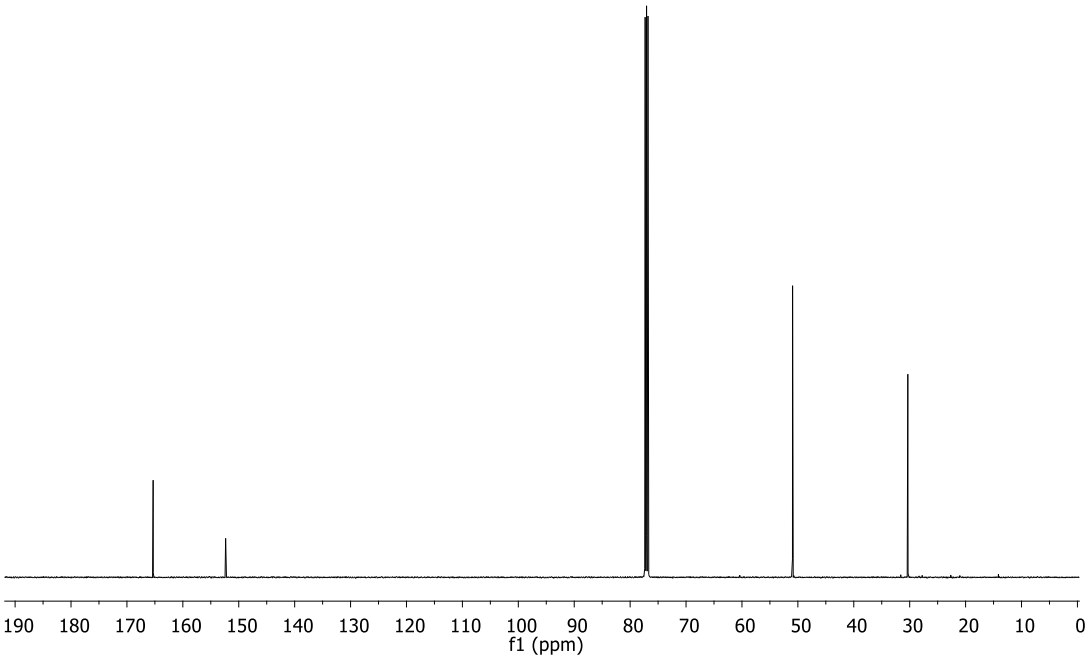

Figure A.3.1.4: ^{13}C NMR (400 MHz, DMSO-d_6) spectrum of Sar-NCA (PO-mediated synthesis).

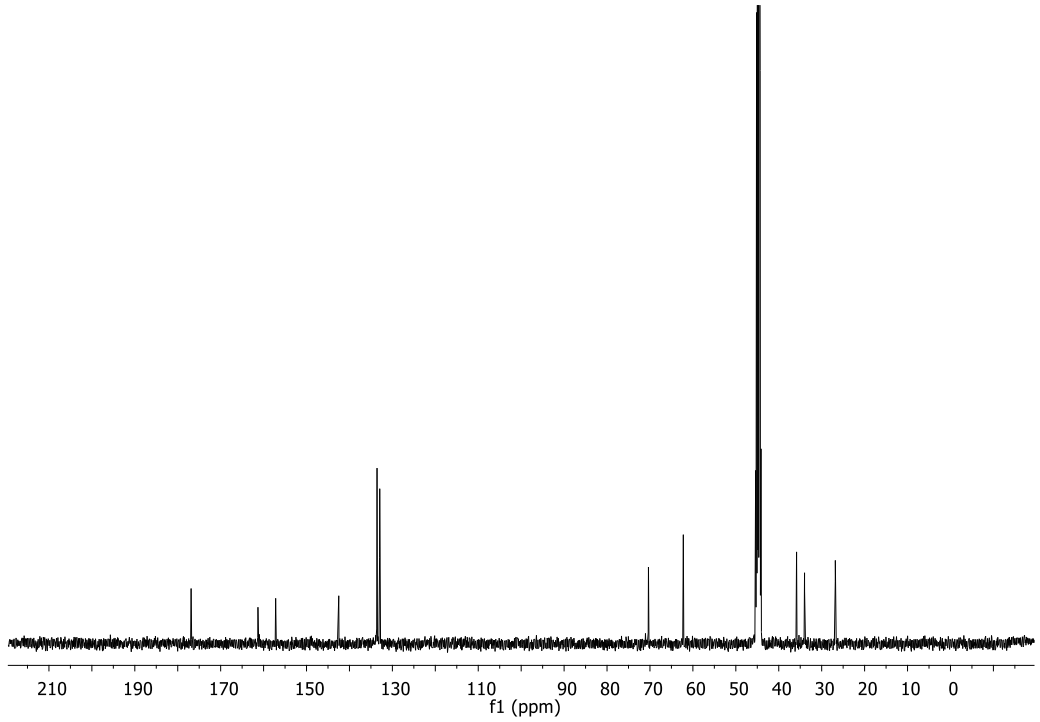

Figure A.3.1.5: ^{13}C NMR (400 MHz, DMSO-d_6) spectrum of Lys(Z)-NCA (T3P synthesis).

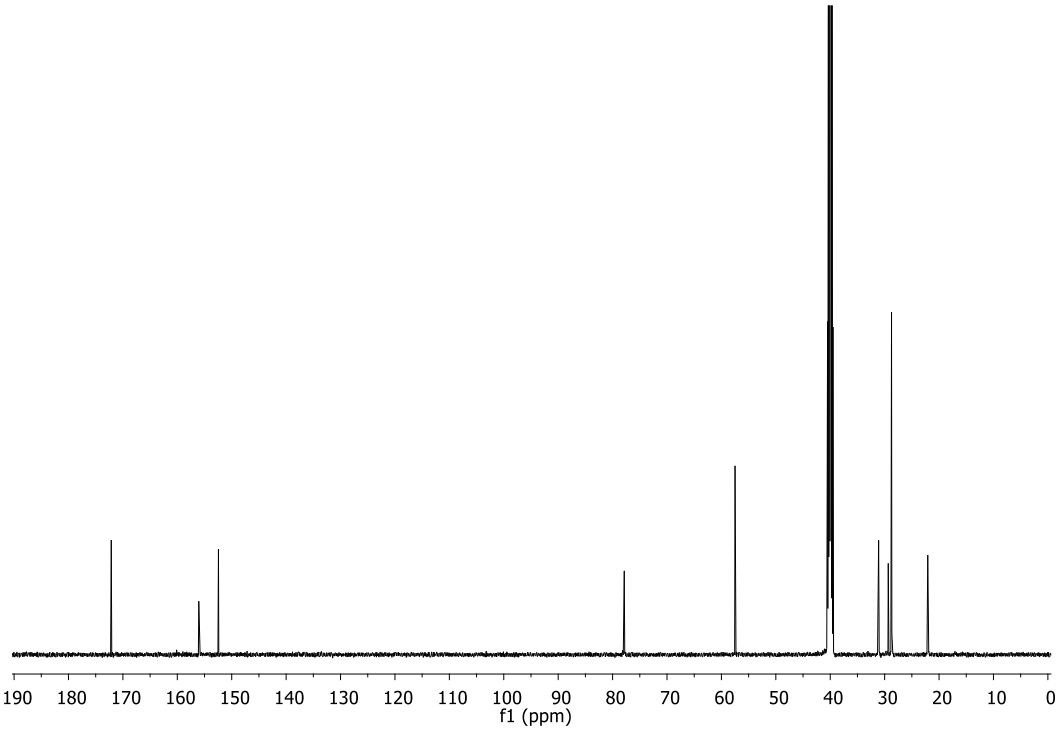

Figure A.3.1.6: ^{13}C NMR (400 MHz, DMSO-d_6) spectrum of Lys(Boc)-NCA (T3P synthesis).

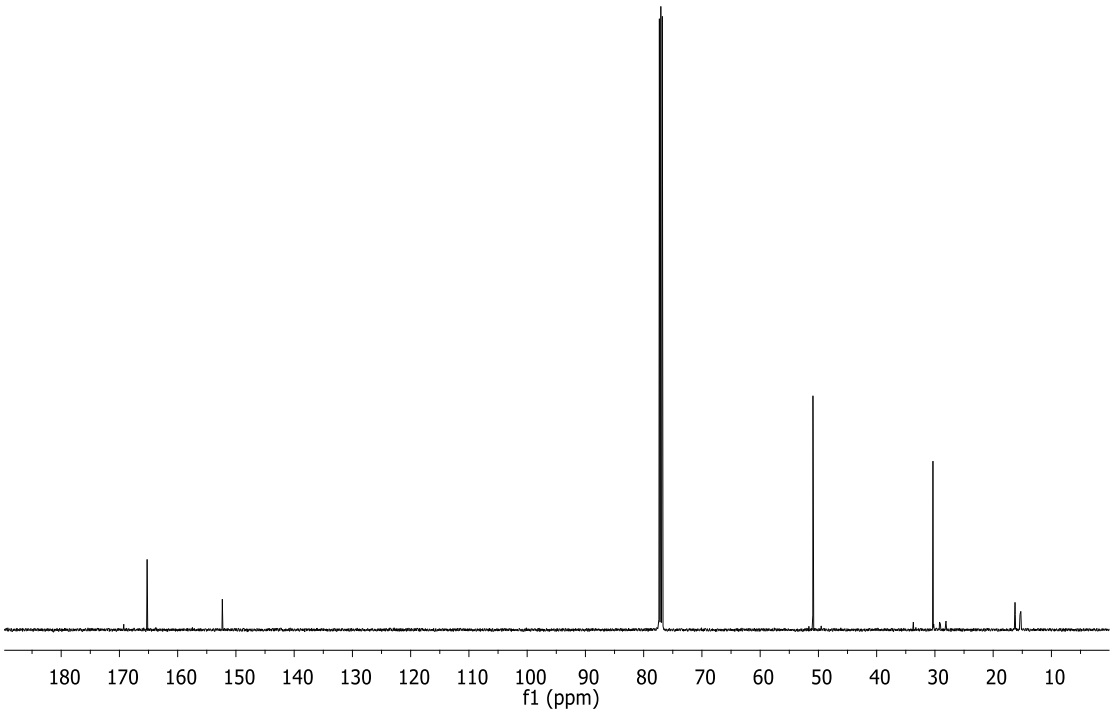

Figure A.3.1.7: ^{13}C NMR (400 MHz, $CDCl_3$) spectrum of Sar-NCA (T3P synthesis).

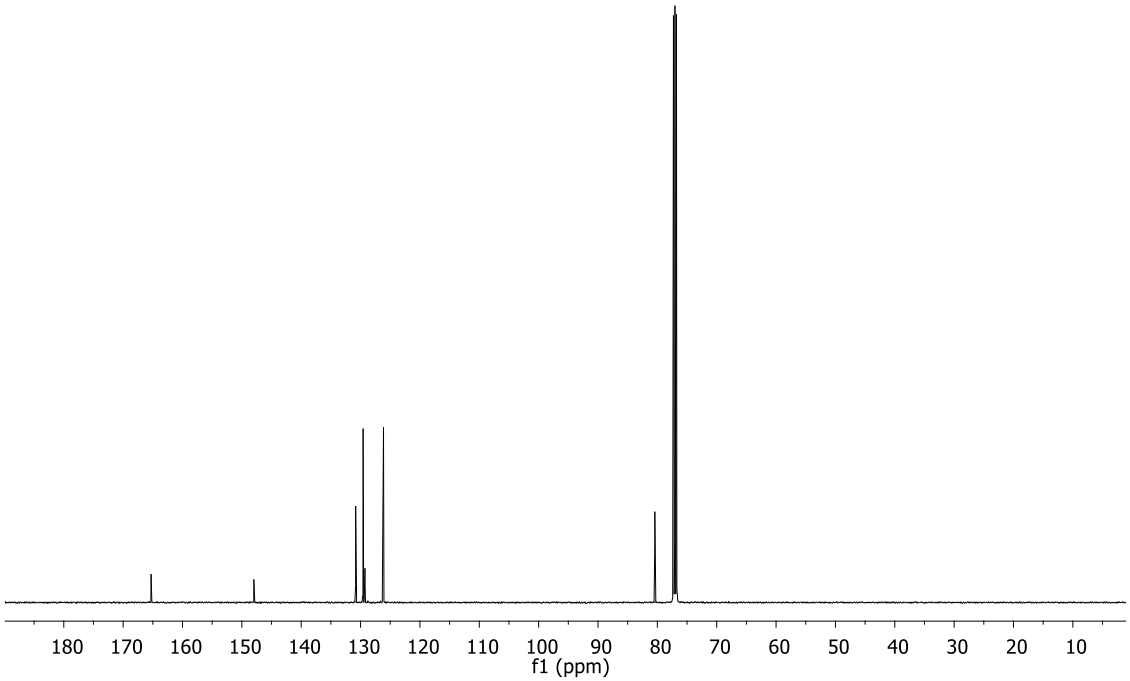

Figure A.3.1.8: ^{13}C NMR (400 MHz, $CDCl_3$) spectrum of Man-OCA.

A.3.2 FTIR Spectra

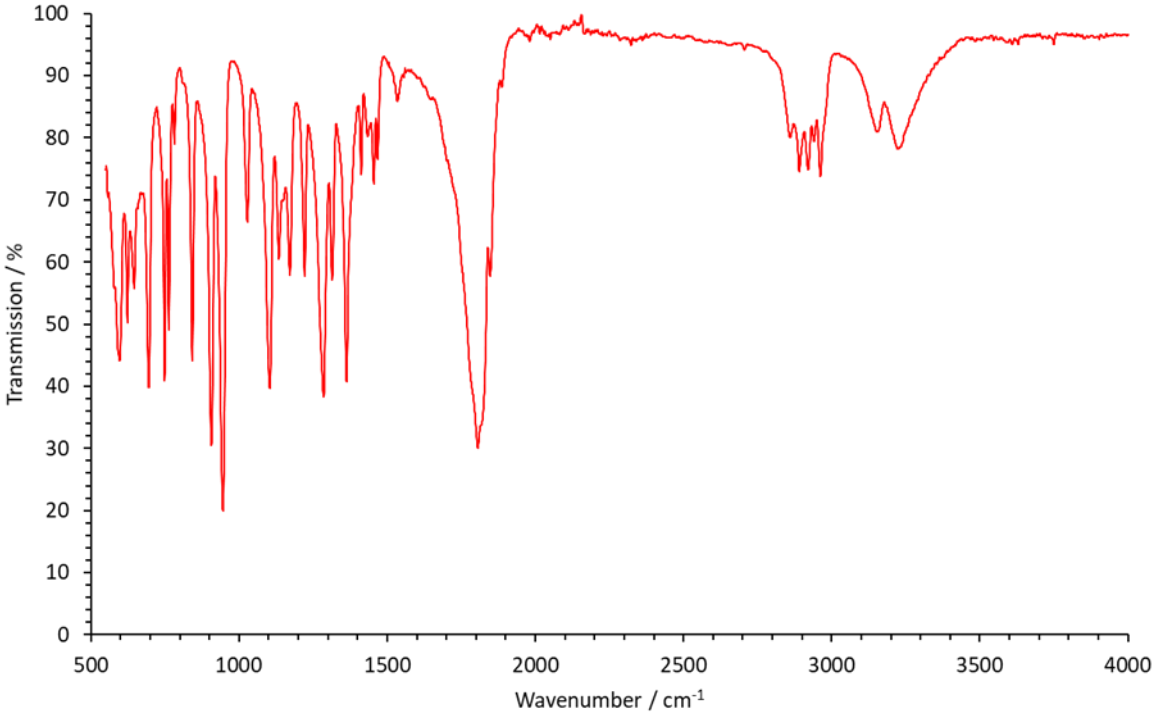

Figure A.3.2.1: FTIR spectrum of Lys(Fmoc)-NCA

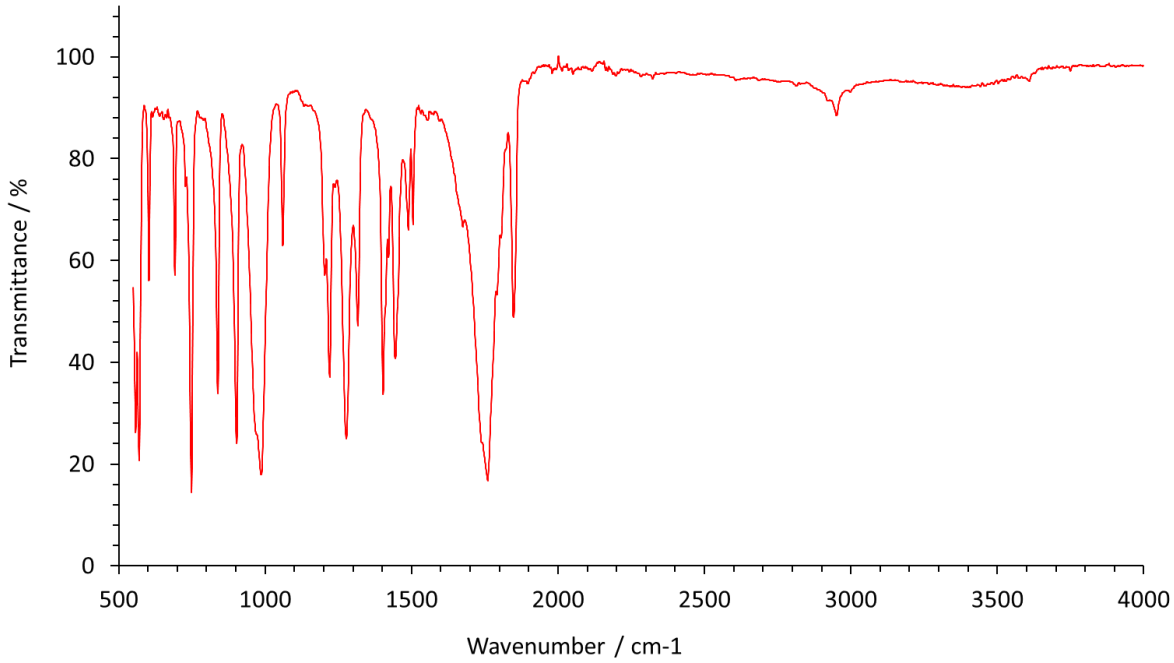

Figure A.3.2.2: FTIR spectrum of Sar-NCA

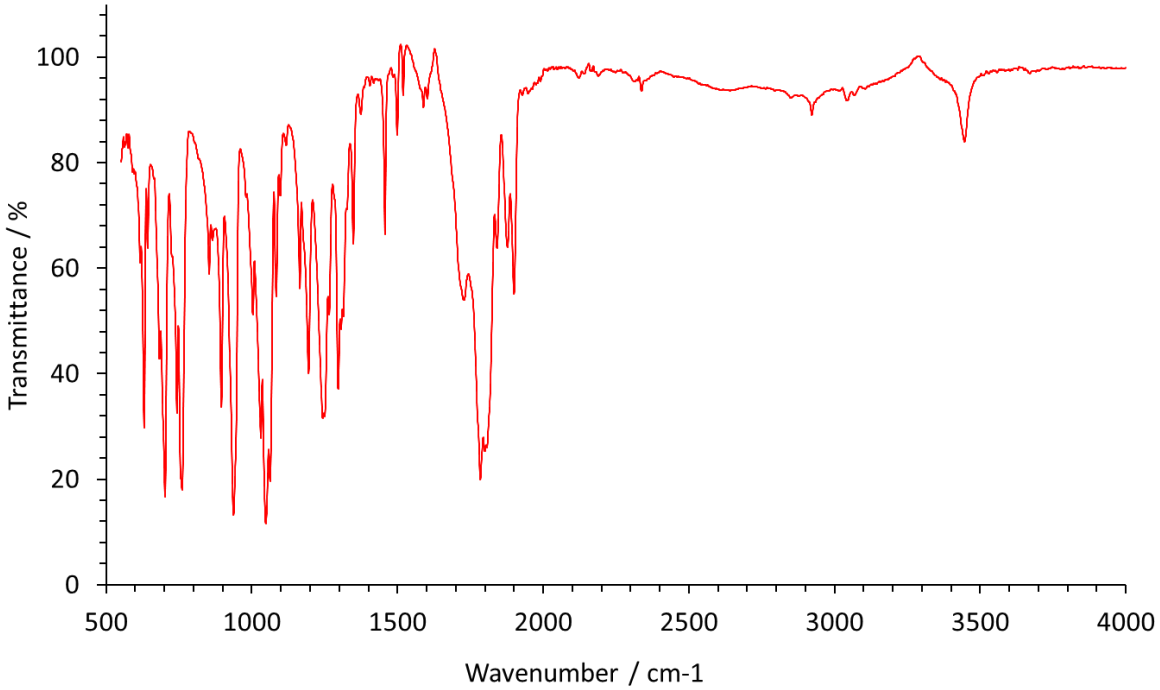

Figure A.3.2.3: FTIR spectrum of Man-OCA

Chapter 4: Synthesis and Application of mPEG-*b*-PMA

Abstract

Mandelic acid was investigated as the hydrophobic component of amphiphilic block copolymers, intended for the controlled therapeutic delivery of doxorubicin (Dox). Fuchs-Farthing carbonylation was utilised to yield mandelic acid O-carboxyanhydride (Man-OCA). This strained, 5-membered heterocycle was then polymerised *via* six OCA-ROP protocols, with varying reaction parameters. The six polymer products were then subjected to analysis *via* ^{1}H and ^{13}C NMR spectroscopies, FTIR spectroscopy and size-exclusion chromatography. It was determined that the polymers synthesised were achieved with narrow molecular weight distributions, in a well-controlled manner. For most polymer products, dispersity (Đ) remained unchanged in comparison to the macroinitiator. As such, the polymers were taken forward for DLS analysis, to determine their capacity for self-assembly and subsequent drug encapsulation.

DLS confirmed that each polymer was self-assembled into well-defined nanoscale structures. Only one polymer exceeded an average size of 200 nm, and PDI values for the nanomaterials fell below 0.2, sufficiently low to be considered well controlled. From these polymer products, one was selected for drug-release study between pH 5.0 and pH 7.4, to evaluate the encapsulation of Dox, as well as their sensitivity to acid-triggered hydrolysis. By parallel incubation of two solutions of dox-loaded nanoparticles at different pH levels, with samples extracted and submitted for UV-Vis spectrographic analysis at pre-defined intervals, it was determined that at lower pH the dox-loaded nanoparticles released ca. 30 % of their payload over the course of 300 hours. In comparison to only a 10 % release at pH 7.4, and with the data exhibiting a slow, controlled release profile with no sign of burst release, it was determined that the mPEG-*b*-PMA nanoparticles synthesised here were viable for the encapsulation, transit and selective release of therapeutic doxorubicin, which also suggests further utilisation with similarly aromatic and bulky drug molecules.

4.1 Introduction

Mandelic acid (MA) is a naturally abundant α-hydroxy acid, derived commercially from benzaldehyde, with major applications in pharmaceuticals. In 2020, commercial MA production exceeded $195m, with pharmaceutical use alone expected to reach $255m by 2027.[1] Within the pharmaceutical industry, MA has been used for a variety of applications including antibiotic UTI treatment and API synthesis.[2,3] Other polyester materials, specifically those derived from lactic and glycolic acid (LA and GA, respectively), have also been used extensively in drug delivery.[4] As is evidenced by the increased Pauling electronegativity of oxygen atoms within poly(hydroxy acid) ester linkages, in comparison to the amide linkages of poly(amino acids), a greater effective nuclear charge is experienced by the valence and bonding electrons of oxygen in comparison to nitrogen.[5] This increased draw on electrons within the ester linkage greatly reduces electron density in the constituent carbonyl carbon, making the linkage more susceptible to nucleophilic attacks, including hydrolysis. For this reason, polyesters present an attractive option for the manufacture of drug delivery technologies with increased acid lability, allowing for greater sensitivity to triggered release in low-pH, including that of the tumour vasculature (pH ca. 6.5) and lysosomes (pH ca. 5.0), compared to polyamides. Discussed in **Section 1.3.3** was the successful polymerisation of LA and GA *via* cyclic dimers (lactide, glycolide), which could not be achieved for the more sterically strained mandelide dimer.[6] As a result, development of poly(mandelic acid) had been restricted until the advent mandelic acid O-carboxyanhydride (Man-OCA) synthesis, and its subsequent ring-opening polymerisation (OCA ROP).[7,8] As discussed in **Section 1.3.3**, during OCA ROP, ring-opening is followed by the elimination of one molecule of CO_2 per repeat unit of mandelic acid. This results in the formation of an oxyanion as the active chain end which, in comparison to the amine active chain end of NCA ROP, is a far weaker nucleophile. As a result, catalyst options such as 4-dimethylamino pyridine (DMAP) are used to activate the chain end or monomer species for nucleophilic attack. The bi-functional action of DMAP is illustrated in **Scheme 1.9**. For this chapter, the effects of varied catalyst concentration, [M]:[I] ratio, temperature, and reaction dilution will be investigated for their imparted effects on the resultant purity, degree of polymerisation and molecular weight distribution of the polymer products.

4.2 Experimental

4.2.1 Monomer Synthesis

Mandelic acid OCA monomers were synthesised in accordance with the methodology prescribed in **Section 3.1.2**. Man-OCA was synthesised in good yield and high purity, as determined by ^{1}H NMR and FTIR spectroscopy. mPEG-OH (5000 g mol^{-1}; Fluorochem) was used as macroinitiator for all mPEG-*b*-PMA syntheses.

4.2.2 Block Copolymer Synthesis

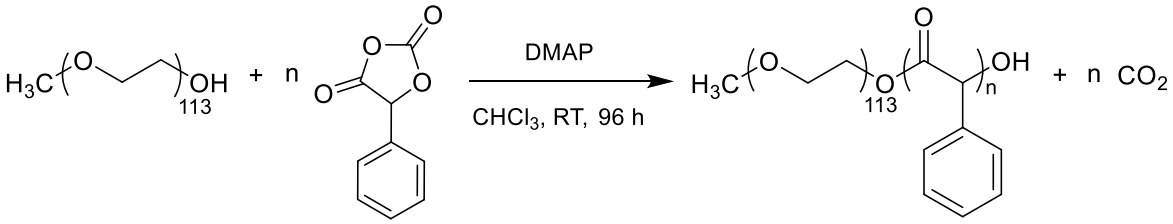

Scheme 4.1: OCA ROP of mandelic acid from mPEG (5000 g mol^{-1}).

A general methodology for the synthesis of PEG-*b*-PMA block copolymers is outlined here and pertains to each of the OCA ROP reactions reported within this section. A more comprehensive breakdown of the quantities of reagents, catalyst, and solvent, as well as the temperature of the reaction, is tabulated in **Section 4.3.1** below. Notable differences between the conditions for each reaction are also discussed in greater detail within **Section 4.3.1**.

Man-OCA (**Table 4.1**) and DMAP (**Table 4.1**) were added to an oven-dried Schlenk tube, fitted with a suba-seal, and dried under vacuum (1 h). The solid mixture was then dissolved in $CHCl_3$ before mPEG (M.W. 5000 g mol^{-1}, **Table 4.1**), dissolved separately into $CHCl_3$, was added in one aliquot and the solution was stirred under a N_2 atmosphere over the course of the reaction (96 h). During the course of the reaction, $N_{2(g)}$ flow was periodically introduced to the system *via* installation of an outlet needle in the suba-seal of the reaction vessel. Once the reaction had reached completion, the crude product was precipitated by ice-cold diethyl ether (150 mL) and collected *via* centrifuge (see Section 2.3). The collected solids were then washed with ice-cold diethyl either (3 x 30 mL) and dried under vacuum overnight. All purified products were collected as fine off-white powders.

Polymer 1 – PEG-*b*-PMA$_{15}$

Yield: 72 wt%

IR (λ / cm^{-1}): 2888s (C-H stretch), 1756s, (C=O ester), 1648s, 1600s, 1562m (C=C stretch, aromatic) 1466s, 1456m, 1360s, 1343m, 1278s, 1242s, 1150s.

^{1}H NMR (400 MHz, $CDCl_3$): 7.40-7.12 (m, 75H, Ar-H), 6.58-5.78 (m, 15H, (C=O)-CH), 3.72-3.42 (m, 452H, 2 x PEG CH_2), 3.31 (s, 3H, PEG-CH_3)

^{13}C NMR (400 MHz, $CDCl_3$): 129.77-123.93 (90C, phenyl carbons), 70.57 (226C, PEG-carbons), 59.05 (1C, PEG CH_3 terminal).

Polymer 2 – PEG-*b*-PMA_{14}

Yield: 74 wt%

IR (λ / cm^{-1}): 2884s (C-H stretch), 1756s, (C=O ester), 1647s, 1640s, (C=C stretch, aromatic) 1468s, 1456m, 1360s, 1342m, 1281s, 1242s, 1149s.

^{1}H NMR (400 MHz, $CDCl_3$): 7.24-7.20 (m, 70H, Ar-H), 6.59-5.16 (m, 14H, (C=O)-CH), 3.57 (m, 452H, 2 x PEG CH_2), 3.31 (s, 3H, PEG-CH_3)

^{13}C NMR (400 MHz, $CDCl_3$): 128.81-124.55 (84C, phenyl carbons), 70.57 (226C, PEG-carbons), 59.05 (1C, PEG CH_3 terminal).

Polymer 3 – PEG-*b*-PMA_{13}

Yield: 55 wt%

IR (λ / cm^{-1}): 2885s (C-H stretch), 1757s, (C=O ester), 1647s, (C=C stretch, aromatic) 1468s, 1359s, 1341m, 1278s, 1241s, 1149s.

^{1}H NMR (400 MHz, $CDCl_3$): 7.24-7.20 (m, 65H, Ar-H), 6.59-5.16 (m, 13H, (C=O)-CH), 3.57 (m, 452H, 2 x PEG CH_2), 3.31 (s, 3H, PEG-CH_3)

^{13}C NMR (400 MHz, $CDCl_3$): 128.81-124.55 (78C, phenyl carbons), 70.57 (226C, PEG-carbons), 59.05 (1C, PEG CH_3 terminal).

Polymer 4 – PEG-*b*-PMA$_{20}$

Yield: 69 wt%

IR (λ / cm^{-1}): 2890s (C-H stretch), 1756s, (C=O ester), 1648s, 1640s, (C=C stretch, aromatic) 1468s, 1456m, 1360s, 1342m, 1281s, 1242s, 1149s.

^{1}H NMR (400 MHz, $CDCl_3$): 7.24-7.20 (m, 100H, Ar-H), 6.59-5.16 (m, 20H, (C=O)-CH), 3.57 (m, 452H, 2 x PEG CH_2), 3.31 (s, 3H, PEG-CH_3)

^{13}C NMR (400 MHz, $CDCl_3$): 128.81-124.55 (120C, phenyl carbons), 70.57 (226C, PEG-carbons), 59.05 (1C, PEG CH_3 terminal).

Polymer 5 – PEG-*b*-PMA$_{48}$

Yield: 75 wt%

IR (λ / cm^{-1}): 2890s (C-H stretch), 1756s, (C=O ester), 1648s, 1640s, (C=C stretch, aromatic) 1468s, 1456m, 1360s, 1342m, 1281s, 1242s, 1149s.

^{1}H NMR (400 MHz, $CDCl_3$): 7.24-7.20 (m, 240H, Ar-H), 6.59-5.16 (m, 48H, (C=O)-CH), 3.57 (m, 452H, 2 x PEG CH_2), 3.31 (s, 3H, PEG-CH_3)

^{13}C NMR (400 MHz, $CDCl_3$): 128.81-124.55 (288C, phenyl carbons), 70.57 (226C, PEG-carbons), 59.05 (1C, PEG CH_3 terminal)

Polymer 6 – PEG-*b*-PMA$_{10}$

Yield: 65 wt%

IR (λ / cm^{-1}): 2890s (C-H stretch), 1756s, (C=O ester), 1648s, 1640s, (C=C stretch, aromatic) 1468s, 1456m, 1360s, 1342m, 1281s, 1242s, 1149s.

^{1}H NMR (400 MHz, $CDCl_3$): 7.24-7.20 (m, 50H, Ar-H), 6.59-5.16 (m, 10H, (C=O)-CH), 3.57 (m, 452H, 2 x PEG CH_2), 3.31 (s, 3H, PEG-CH_3)

^{13}C NMR (400 MHz, $CDCl_3$): 128.81-124.55 (60C, phenyl carbons), 70.57 (226C, PEG-carbons), 59.05 (1C, PEG CH_3 terminal).

4.2.3 Preparation of mPEG-*b*-PMA Nanoparticles

mPEG-*b*-poly(mandelic acid) copolymer nanoparticles were prepared based upon a previously established nanoprecipitation method.[9] Each polymer (10 mg) was dissolved in chloroform (1 mL) and the solution added dropwise to deionised water (10 mL) under vigorous stirring. The dispersions were stirred overnight whilst the chloroform evaporated and then examined to ensure there was no visible organic phase. All nanoparticle dispersions were made at a concentration of 1 mg mL^{-1}.

4.2.4 Preparation of Dox Free Base

Dox hydrochloride (2.00 mg, 3.67 µmol) was added to a solution of triethylamine (20 µL, 55 µmol) in anhydrous chloroform (3 mL). The solution was isolated from light and stirred at room temperature for 4 hours.

4.2.5 pH-mediated release of doxorubicin from Dox-Loaded Nanoparticles

Polymer **1** (10 mg) was dissolved in chloroform (1 mL). The polymer solution and dox-free base solution (2 mg mL^{-1}, 3.67 µmol) were then added simultaneously, in a dropwise fashion, to vigorously stirring PBS buffer solution (pH 7.4, 10 mL). The nanoparticles were dialysed (2000 g mol^{-1} MWCO) for three days to remove non-encapsulated doxorubicin. The dox-loaded nanoparticle dispersion was split into two equal portions by volume and decanted into fresh dialysis tubing (2000 Da M.W.C.O.). One dox-loaded nanoparticle dispersion was then dialysed against 100 mL acetate buffer (pH 5.0) solution, whilst the other was dialysed against 100 mL PBS buffer solution (pH 7.4). The vessels were incubated in the dark, with the dialysate under constant agitation, at 37°C. At predetermined intervals, 1 mL aliquots were removed from the dialysate and analysed by UV-vis spectrophotometry. The concentration of dox in the dialysate at each time point was quantified by UV-vis spectrophotometry using a prepared standard calibration curve. The release from the nanoparticles was studied over the course of 194 hours.

4.3 Results and Discussion

Success by Kricheldorf in the 1980s in synthesising poly(lactic acid) and poly(glycolic acid) from the ring-opening polymerisation of their respective cyclic diesters spurred interest in the application of poly(hydroxy acid) materials.[10] However, even as recently as 2010 the limitations of more functionalised cyclic diesters as monomers remains apparent, as demonstrated by challenges experienced by Dove *et al*. in dimerising L-malic acid, detailed in **Section 1.3.1**.[11] In more recent years, Buchard *et al.* and Zhang *et al.* demonstrated greater success in the synthesis of poly(mandelic acid) homopolymer *via* ROP of mandelic acid OCA.[7,8] These poly(hydroxyl acids) represent a significant opportunity in the field of drug delivery, due to their biodegradability and biocompatibility. In addition, their increased susceptibility to hydrolysis can be exploited for pH-mediated, controlled therapeutic release.

4.3.1 Synthesis of mPEG-*b*-PMA Block Copolymers

Man-OCA was here polymerised under a variety of reaction conditions, and the resultant block copolymers analysed by ^{1}H NMR spectroscopy, FTIR spectroscopy and DLS analysis. Polymerisation was conducted in anhydrous $CHCl_3$ under N_2 atmosphere, over a period of 96 hours. The reaction conditions varied within this study are detailed in **Table 4.1** below.

Table 4.1: Reaction conditions for Mandelic Acid OCA ROP reactions.

No.	Initiator		Monomer		Catalyst		Solvent	T / °C
	Mass / mg	Mol / mmol	Mass / mg	Mol / mmol	Mass / mg	Mol / mmol	Vol / mL	
1	168	0.034	300	1.68	20.6	0.168	10	25
2	168	0.034	300	1.68	41.2	0.336	10	25
3	168	0.034	300	1.68	20.6	0.168	15	25
4	168	0.034	300	1.68	20.6	0.168	10	30
5	168	0.034	600	3.36	41.2	0.336	20	60
6	280	0.056	300	1.68	20.6	0.168	20	60

DMAP catalyst content was here varied (**Polymer 1** to **Polymer 2**), to evaluate the effect upon the degree of polymerisation of the PMA block. As demonstrated by Bourissou *et al*., the action of DMAP as a catalyst is bifunctional, activating both the incident nucleophile and the target carbonyl of the OCA molecule via weak non-classical H-bonding.

Increasing the content of this catalyst in solution would therefore act on both the rate of propagation, as well as the rate of any potential side reactions, making catalyst content a crucial aspect within OCA ROP to optimise. Also evaluated here were the effects of increased reaction temperature and dilution, as well as increasing targeted DP upon the resultant copolymer. Reaction temperature was evaluated for its fundamental effect on the kinetic energy of the molecules in solution (**Polymers 4, 5, 6**), allowing higher probability of surmounting the activation energy barrier for reaction, thereby increasing the rate of propagation. However, as the increase in rate due to increased temperature is nonspecific, this would also increase the rate at which side reactions, such as ring-opening by water or linear mandelic acid monomers/oligomers. An argument could also be made for an increase in temperature also increasing the chain mobility of the mPEG-OH macroinitiator, allowing for more regular contact of the active chain end with active monomer species. Such an effect would first have to be observed in the product analysis, however, supporting the necessity for this research. Whilst increasing the dilution of the reaction materials uniformly cannot be expected to impact side-reactions as a result of impurities (**Polymer 3**), the effect of slowing the rate of propagation and side reaction by decreasing concentration of monomer, initiator and catalyst can here be investigated. Finally, the effect of increased target DP at increased temperature, from 50 at 25 °C to 100 at 60 °C (**Polymer 5**) has here been investigated, to determine first whether it is possible to achieve higher degrees of polymerisation for mPEG-*b*-PMA in this solvent system, and to determine whether an increase in temperature would allow this to happen, given the effects of temperature on increased propagation rate and improved solubility.

Polymers **1**-**4** (**Table 4.1**) were characterised using ^{1}H NMR (**Figures A.4.1.1-4**) and FTIR spectroscopy (**Figures A.4.3.1-4**). The primary observation taken from all obtained FTIR measurements is the replacement of the anhydride C=O stretches (1807 cm^{-1}, 1786 cm^{-1}) observed in the spectrum of Man-OCA (**Figure 3.12**) with a singular ester C=O peak (ca. 1750 cm^{-1}), signifying the successful ring opening of all Man-OCA monomers and the completion of the ROP reaction.

The proton environment of the terminal methyl group of methoxypoly(ethylene glycol) is represented in the ^{1}H NMR spectrum by a singlet peak at ca. 3.3 ppm, while the ethyl protons are represented by a larger, pseudo-triplet peak in the range of 3.45 ppm – 3.75 ppm. With an average molecular weight of 5000 g mol^{-1}, the PEG block of these products comprises an average of 113 repeat units. With 4 protons per repeat, it stands that the ethyl peak integral should equal 452, relative to the methyl peak's 3. The ratio between these peaks is often skewed, particularly in the case of the small methyl peak, which can be impacted by both the presence of impurities, moisture, or as a result of inaccuracy of the ^{1}H NMR equipment. As such, for an estimation of the number of poly(mandelic acid) repeat units in a block copolymer products, comparison is typically made against the ethyl peak. For the PMA block, α-proton integrals are here observed in a range between 5 ppm – 7 ppm, dependent on the position of the respective repeat unit within the polymer chain, and their sum can be compared directly with the PEG ethyl integral to estimate the number of PMA repeat units. PMA phenyl proton peaks are observed in the range of 7.0 ppm – 7.5 ppm, the integral value of which can be divided by 5 to provide a second estimation for the repeat unit, which can then be compared to the value obtained from the α-proton range. Due to the presence of the $CDCl_3$ solvent peak within this aromatic region, selective subtraction was employed to estimate the phenyl proton integral values. As a result, all aromatic integral values here reported are underestimates of their true values. As both estimation methods are therefore subject to suppression, whether from solvent peak overlab or from the instability of the methyl peak, all D.P. values reported below should be interpreted as conservative lower-limit estimations as opposed to absolute values. The overlaid ^{1}H NMR spectra of **Polymers 1**-**6**, as well as the comparison of the calculated D.P. values to those targeted (**Table 4.1**) are presented in **Figure 4.1** and **Table 4.2** below.

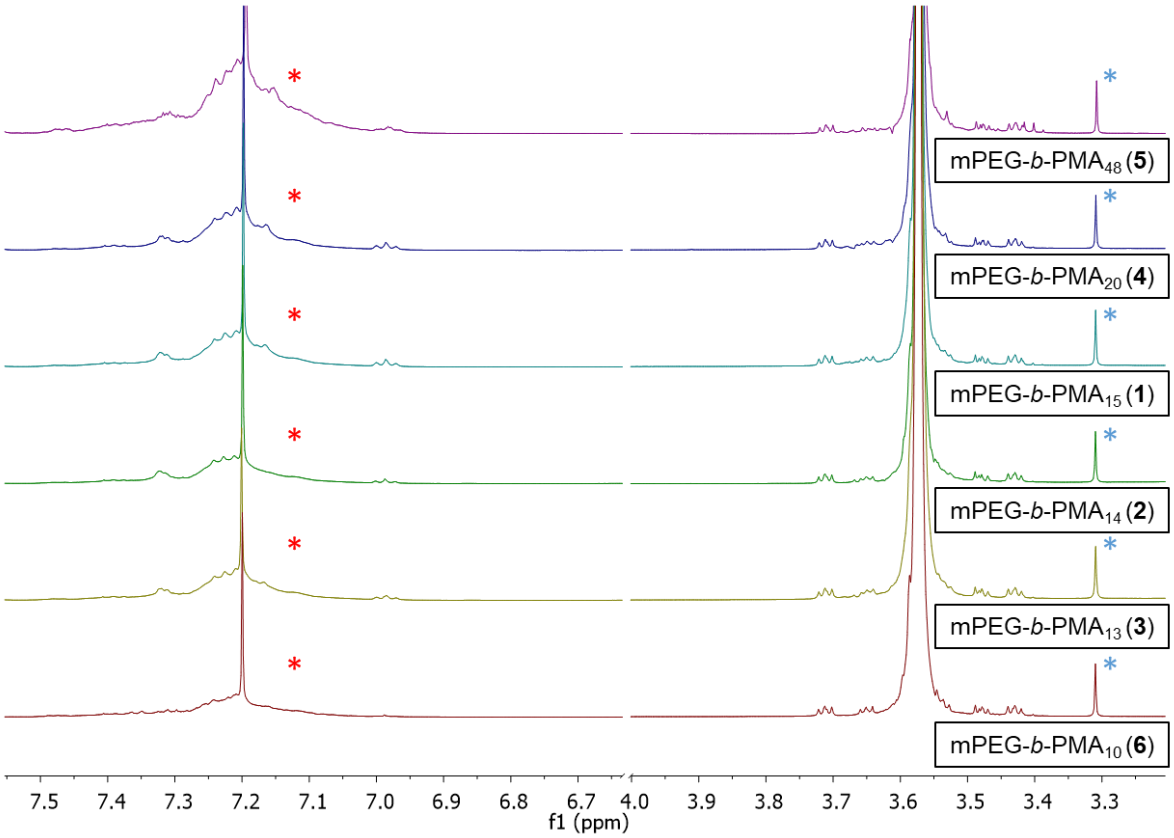

Figure 4.1: Stacked ^{1}H NMR Spectrum (500 MHz, $CDCl_3$) of mPEG-*b*-PMA **1**-**6**, highlighting aromatic (*) and PEG-methoxy (*) proton environments.

Table 4.2: [M]:[I] ratios of **Polymers 1**-**6**, versus calculated D.P. values.

Number	[M]:[I]	Calculated D.P.
1	50	15
2	50	14
3	50	13
4	50	20
5	100	48
6	50	10

Compared to the intended DP for these copolymers, the calculated values are relatively low, suggesting monomer conversion for each polymer of no more than 40 %. Whilst this does not agree with the suggested reaction completion observed in the FTIR data, it is possible that any residual monomer was removed during precipitation of the product in diethyl ether.

This observation may also be explained or intensified by the creation of by-products, most likely low-molecular weight oligomers, initiated by small-molecule impurities during the reaction procedure.

It should be noted here that there appears to be little difference between the achieved molecular weights of **Polymers 1, 2** and **3** (max. 304 g mol^{-1}), with the largest apparent DP increase achieved by increasing reaction temperature for **Polymer 5**. Whilst an increase in catalyst concentration might suggest an increase in rate, at 1:10 [C]:[M] ratio, catalyst content in this reaction outnumbers the initiator by a factor of 5, and by a factor of 10 in the case of ROP **2**. As such, the active chain ends in solution are likely saturated by H-bonded DMAP molecules, limiting the impact that additional catalyst content could make. Furthermore, the decreased DP observed for ROP reaction **3**, though only slight, might be attributed to the increase in reaction volume and concurrent decrease in both initiator and monomer concentration, decreasing the rate of propagation. In reality, this decrease in the frequency of successful active chain end interactions with monomer decreases with respect to potential impurity-monomer interactions, thereby allowing side-reactions to prosper, limiting the available monomer concentration, which may have resulted in the restricted DP observed here for polymer **3**.

As for the apparent effects of changing polymerisation conditions on the relative purity of each polymer sample, it is difficult to identify the presence of non-polymer impurities such as hydrolysed mandelic acid and small-chain oligomeric species. The respective proton environments (α-adjacent and aromatic protons alike) of these molecules experience broadly similar chemical shift to those of the polymeric species, and so cannot be distinguished from within the multiplet regions reported across **Figures A.4.1.1**-**6**. More representative conclusions about these small molecule impurities could be drawn by separating them out of the polymer product. However, this procedure is technically complicated due to the lack of solvent systems in which mandelic acid units are soluble, that are also compatible with separation procedures such as filtration and dialysis. As such it is more effective to observe the different species present in the obtained products using size-exclusion chromatography. Whilst SEC equipment was not available at the time that these ROP reactions were conducted, such spectra have been collected in retrospect and are presented later in this section.

Examination of **Polymers 5** and **6** (**Figure 4.1**, **Figures A.4.1.5**-**6**), again comparing the relative integrals of the PEG methyl and ethyl peaks versus the aromatic and α-protons of the poly(mandelic acid) block, suggests that D.P. values of 48 and 10 were achieved for these respective products. It should be noted here that a larger solvent reservoir was maintained for these higher-temperature reactions, to account for temporary solvent loss during reflux. As demonstrated by the values in **Table 4.1**, this had subsequent effect on the concentrations of materials in solution, highlighted by the reduced concentration of initiator in the case of **5**, and reduced monomer concentration for **6**. The effects of these conditions are pronounced in the case of **Polymer 6**, for which the number of repeat units achieved was calculated as only 10, representing a monomer conversion of 20 %.

This can be attributed to the reduced concentration of monomer species concurrently restricting the number of successful interactions with the active chain end, effectively slowing the rate of propagation and allowing impurity-driven side-reactions to dominate, limiting the achievable degree of polymerisation. For the case of **Polymer 5**, monomer and catalyst content has been increased to reflect the increase in targeted DP, meaning no change in concentration relative to the initiator decrease. The apparent result has been an increase in the number of repeat units to 48, representing also an effective monomer conversion of 48 %, higher than those of the other polymers (conflicting FTIR data notwithstanding). This can likely be attributed the increased reaction temperature acting to increase the rate of propagation and reduce overall reaction time, offering less opportunity for side reactions to impact monomer concentration and resulting in a higher DP poly(mandelic acid) block. While the initiator:catalyst ratio was also higher in this case, the ratio is comparable with that **Polymer 2**, which did not experience any increase in achieved DP as a result of this change.

Whilst the data illustrated in **Figure 4.1** provides key evidence for the achieved DP values for the hydrophobic block of polymer **1**-**6**, the context was not fully established until complimentary size-exclusion chromatography (SEC) data was obtained for the products. SEC apparatus was made available approximately 18 months after completion of mPEG-*b*-PMA drug release, reported in **Section 4.3.5**, and all polymer products excluding **5** (for which stock had been depleted) were analysed. This data was collected to provide a more comprehensive understanding of the conflicting findings ^{1}H NMR and FTIR analyses, conducted here.

SEC allows for separation materials dependent on their relative size, meaning that only polymeric species in the relevant molecular weight range will be observed. Whilst chemical difference between the products and calibrant for this system (polystyrene) prevent statement of absolute molecular weight values for these products, the SEC data presented in **Figure 4.2** does provide a qualitative comparison of the relative molecular weight values achieved for the products in comparison to mPEG-OH (M.W. 5000 g mol^{-1}), as well as relative dispersity values (Đ), which indicate the uniformity of the polymer products.

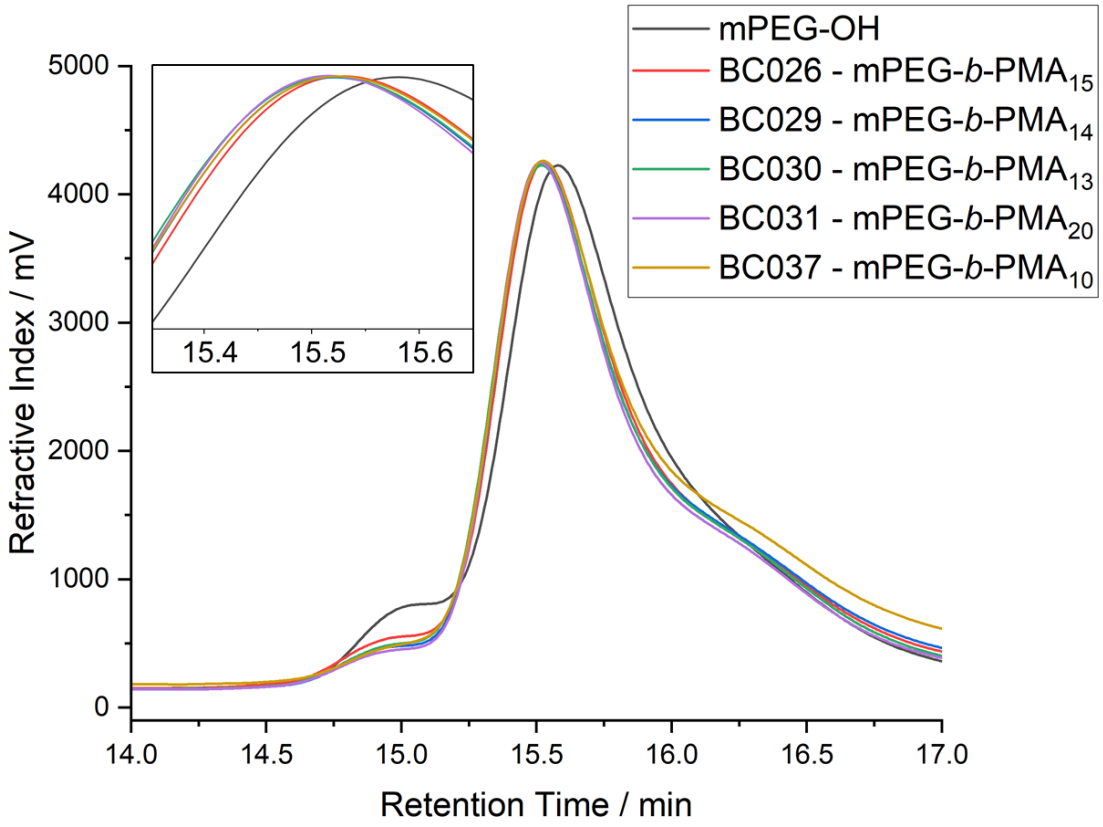

Figure 4.2: SEC data for mPEG-OH macroinitiator and polymer products 1, 2, 3, 4, and 6, taken in THF mobile phase.

As illustrated in **Figure 4.2**, each of the polymer products appears to have an increased molecular weight in comparison to the mPEG-OH macroinitiator, as indicated by the slight shift of their peaks towards a lower elution time. Furthermore, there appears to be little broadening of the peaks, suggestive of a minimal change in their uniformity and corresponding dispersity values in comparison to the macroinitiator.

It should be noted here that a shoulder peak is visible in the SEC traces of not only the products, but also the mPEG-OH macroinitiator. This shoulder appears at a lower elution time than the main chain population, and is therefore indicative of a higher M.W. fraction within the commercial starting material. Such shoulder features are often a consequence of the anioni ring-opening polymerisation of ethylene oxide used to manufacture mPEG and are well characterised in the literature. If residual moister is present during synthesis, water can act as a bifunctional initiator, producing HO-PEG-OH diol chains alongside the intended mPEG-OH product and yielding a heterogeneous distribution of chain lengths detectable by SEC.[12,13] As mPEG-OH acts as the macroinitator for OCA-ROP here, all chain-length populations present within the starting material, including this higher molecular weight fraction, are capable of initiation. The shoulder is therefore maintained across all polymer populations (1-6), with the shoulder shifting to lower elution times in tandem with the main peak, consistent with successful chain extension from the higher-MW fraction. This behaviour is discussed further in **Section 5.3.3**, where analogous shoulders feature in work using mPEG-NH_2.

Both of these observations can be evidenced by the calculated values for number-average molecular weight (M_n), weight-average molecular weight (M_w) and dispersity (Đ) of these polymers, provided in **Table 4.3** below.

Table 4.3: Comparative molecular weight data obtained from ^{1}H NMR estimation and SEC analysis, as well as dispersity values calculated from SEC.

Polymer	M.W. (est.) / g mol^{-1}	M_n / g mol^{-1}	M_w / g mol^{-1}	Đ
mPEG-OH	5000	6563	7816	1.19
1	6996	7646	9053	1.18
2	6863	7093	8782	1.24
3	6730	7581	9028	1.19
4	7661	7472	8986	1.20
6	6331	6604	8472	1.28

It should be noted here that the determined values for M_n and M_w are noticeably different from the expected M.W. values suggested by ^{1}H NMR. This is primarily due to the use of a polystyrene calibrant for the SEC apparatus here utilised.

Whilst styrene and mandelic acid do have a phenyl group in common, they are chemically distinct from one another in their interactions with THF solvent, as well as their mobility across an SEC column, an effect which is only more pronounced when comparing the mPEG copolymer block with styrene. As such, whilst these values have been reported, they are only to be taken for qualitative comparison against one another, and not as a quantitative representative of true molecular weight values. With the context added by **Table 4.3**, it can be more confidently surmised from the data that each the product polymers has experienced some degree of polymerisation from the macroinitiator. In addition, the value for Đ remained relatively consistent between the macroinitiator and the products polymers, with the exception of polymers **2** and **6**. This suggests that the ROP of Man-OCA was achieved with narrow dispersity in a well-controlled manner, consistent with expectations for a controlled polymerisation such as OCA ROP.

For polymer **2**, the increase in dispersity of 0.05, while small, is relevant to note in the context of a controlled ring-opening polymerisation. The increased catalyst content of this reaction should not have influenced this change, as in all cases here catalyst concentration was in minimum 5:1 excess over the concentration of initiator.

One potential explanation could instead be the effect of increased catalyst concentration on the total relative volume (RV) of solid materials in this reaction, as RV for polymerisation **2** was higher than that of any of the other reactions. If this were to have a detrimental effect on the solubility of the reaction materials, namely the solubility of the macro-initiator, then the subsequent decrease in rate of initiation could then affect the final dispersity value. Furthermore, this can be linked to the apparent decrease in the M_n and M_w values for polymer **2** in comparison to polymers **1** and **3**, run at the same temperature. A decreased solubility of the active chain end may also result in retardation of the rate of propagation which, in tandem with the increased rate of side reaction due to higher catalyst content, would act to reduce the achievable degree of polymerisation, correspondingly reducing the number of PMA repeat units in the product. This effect can also be seen for polymerisation **6**, for which the decreased reagent concentration has imparted a similar decrease in propagation rate, as discussed earlier. Slower propagation rate can allow for inconsistent chain growth across the sample, giving larger values for Đ.

Furthermore, the increased reaction temperature may have acted to increase Đ by exacerbating inconsistent chain growth through hotspots of non-uniform heating, as well as increasing the possibility for side reactions of the active chain end with non-constructive impurities, resulting in premature chain termination. However, it should be noted that across the range of polymerisation reactions reported here, Đ values are still largely unchanged and all lie below 1.3, suggesting that narrowly controlled polymerisation has still been achieved.

An expanded view of the SEC peaks has been provided within **Figure 4.2**, to allow greater distinction between them and to support the differences in M_n and M_w values obtained. Importantly, whilst molecular weight values between have been determined for the polymers, upon qualitative comparison against one another disparities can be observed between the values of M.W. obtained *via* estimation repeat unit estimation from ^{1}H NMR, and the values determined by SEC.

Most notably, these differences can be observed for polymer **2**, for which recorded M_n is significantly lower than those of polymers **1** and **3**, contrasting with the estimation obtained *via* ^{1}H NMR, and for polymer **4**, for which M_n values suggest a similar molecular weight to polymers **1** and **3**, despite estimation from ^{1}H NMR indicating a difference of 5-7 repeat units between them. In fact, calculation from the values estimated by ^{1}H NMR provides values for the peak molecular weight (M_p) ranging from 15.49 min to 15.70 min, whereas in the values obtained from SEC exhibited Mp values closely centred around 15.52 min, which can be visualised by the strong overlap of peaks in **Figure 4.2**. From these data, it can be inferred that there is a significant disparity between the estimations made from ^{1}H NMR and the values obtained from SEC. Whilst this can to some extent be attributed to the subjectivity of manual integral range selection in NMR analysis, the more likely contribution comes from the presence of low-molecular weight, hard to remove impurities such as the low-M.W. oligomers and hydrolysed mandelic acid molecules discussed previously. These materials cannot be distinguished from the product polymer integral ranges of ^{1}H NMR, but it is possible to visualise these separated species *via* SEC. It should be noted, however, that materials of such low molecular weight correspond to a retention time that falls outside the calibration range of the polystyrene standards for this SEC analysis, and as such cannot be accurately measured. However, low-M.W. peaks can be observed in the expanded SEC spectra provided within

Figure 4.2. Without any material to conduct SEC of **BC036**, it was not possible to determine to what extent polymerisation had been achieved, nor was it possible to determine the accuracy of the ^{1}H NMR-derived DP estimate of 48.

The results obtained demonstrate that controlled OCA-ROP of mandelic acid OCA from mPEG-OH has here been achieved, representing a viable route to novel mPEG-*b*-PMA block copolymer amphiphiles with narrow dispersity. The potential of these polymers to undergo self-assembly into the nanoparticles, capable of encapsulating and delivering a therapeutic payload was then evaluated. Should encapsulation prove possible, it is then necessary to evaluate the stability of such nanoparticles under physiological conditions, as well as any controlled-release properties that might be expedited in the presence of low-pH environments, thanks to the poly(ester) backbone of PMA.

4.3.2 Preparation of mPEG-PMA Nanoparticles

Each of the PEG-*b*-PMA copolymers (**1**-**6**) reported in **Section 4.3.1** was subjected to analysis by DLS, to better visualise their capacity to self-assemble into physiologically-compatible nanoparticles. The method for the self-assembly of these nanoparticles in water is described in **Section 4.2.3**, whilst that of DLS is provided in **Section 2.10**. Using DLS analysis, it was possible to determine both the average particle size (in nanometres) and polydispersity index (PDI) for each of the products. Note here that PDI differs from Đ, as the latter value is obtained primarily *via* chromatographic methods. While the DLS data for these samples are displayed graphically in **Appendix A.4.5**, the relative sizes and PDI values of the nanoparticles is displayed in **Table 4.4** below.

Table 4.4: Size values and PDI values for polymers **1**-**6**, alongside ^{1}H NMR-estimated PMA repeat units. Values represent the mean of triplicate measurements.

Polymer Number	Calculated PMA Repeat Units	Average Size / nm	PDI / a.u
1	15	188.3	0.128
2	14	188.5	0.147
3	13	145.7	0.163
4	20	211.8	0.133
5	48	173.7	0.164
6	10	179.3	0.187

From **Table 4.4** it can be seen that each polymer has undergone some association into a nanoscale particle, though no statement can be made as to their structure (micellar, polymersomal) nor their morphology (spherical, worm-like). Most of these nanoparticles remained below 200 nm in size, and all were reported with PDI values below 0.2. This is suggestive that the polymers are likely to have coalesced not into well-defined micelles but rather more complex, yet still stabilised, aggregate species. The length of even the largest mPEG-*b*-PMA chain (**5**), if laid linearly, can be calculated as 63.53 nm, which can be extrapolated to a maximum diameter of 127.07 nm for two chains end-to end.[14] The reality for a spherical micelle may be even smaller, with overlap between repeat units in the hydrophobic core as a result of π-π stacking interactions between phenyl groups.

While the length scales observed in this analysis are closer in size to the theoretical diameter of a polymersome organisation of the polymers, this is highly unlikely, and would require techniques such as transmission electron microscopy to properly visualise and evidence. A more realistic explanation of the data therefore lies with more poorly-defined aggregate species. However, these results still reflect positively on the objectives of the research.

For the specific purpose of drug delivery to tumour sites within the body, existing literature praises particles below 200 nm on their ability to act as long-circulating carriers to tumour sites whereupon they can undergo selective release, or are preferentially absorbed due to the enhanced permeation and retention (EPR) phenomenon.[15] Crucially this suggests that, provided there are minimal changes in size upon encapsulation of a chemotherapeutic molecule, may indeed be suitable for anticancer applications. Whilst this will of course require further study, the data presented above supports a positive trajectory. Other alternative routes of drug administration, beyond the delivery of anticancer therapeutics, are also available to drug molecules of this size range.[16] These administration forms, as well as the required particle size ranges for them are provided in **Table 4.5** below, adapted from Danaei *et al*.[16]

Table 4.5: Required particle sizes for distribution within the body *via* several different administration and dosage routes. Adapted from [16].

Route of Administration / Dosage Form	Particle Size Range
Long-circulating carriers (brain, tumours)	50 – 200 nm
Transdermal	10 – 600 nm
Intravenous / intramuscular	200 – 2000 nm
Ocular	100 – 3000 nm
Aerosol	1 – 10 µm
Nasal	8 – 20 µm
Lymphatic (Reticuloendothelial System)	10 – 50 nm

Here it can be seen that a variety of potential administration routes may be possible for therapeutic systems designed using PEG-*b*-PMA self-assembled nanoparticles. It should be noted briefly however, that while these nanoparticles do fall into the size range necessary for long-circulating carriers, they do not meet the size requirement of 100 nm or less, for particles intended to cross the blood-brain barrier (BBB).[14] While this is an unfortunate limit on the potential applications of the materials produced for this report, further optimisation of the PEG-*b*-PMA system may eventually yield suitable particles for this purpose in the future. This will most likely be achieved by optimising a strategy for nanoparticle self-assembly, which would allow the amphiphilic macromolecules to pack more efficiently and ensure that they do so more consistently, thereby reliably reducing the overall size of the particle.

Returning briefly to **Table 4.5**, it should be noted that the PDI values of 0.187 and below for these products is extremely encouraging. Specifically PDI, also known as 'heterogeneity index' describes the level of non-uniformity of a particle's size distribution, calculated from a two-parameter fit to the correlation data (the cumulants analysis).[14] The scale of the PDI is such that extremely monodisperse samples approach a value of 0.05, whilst a value of PDI greater than 0.7 indicates that a sample has such a broad particle size distribution that they are unlikely to be suitable for DLS analysis.

Using this scale, it can be evidenced by the obtained PDI values that the syntheses and self-assembly procedures of the polymers in this report were under sufficient control as to produce nanoparticles of narrow Đ, supporting their potential future use in the encapsulation of drug molecules.

Final observations can be made from the table when comparing the size values for each of the polymer nanoparticles, relative both to their respective PMA repeat unit values (as determined by ^{1}H NMR spectroscopy, and to the qualitative data obtained from SEC analysis. Firstly, the values obtained do not align with the estimated numbers of repeat units, as can be seen by the significant increases in size observed for polymer **4** over polymers **5**, as well as the size increase observed between polymers **3** and **6**. This contrasts with the expectation set by Israelachvili's packing parameter equation (see **Equation 1**, **Section 1.1.2**), which is inversely proportional to the length of the solvophobic block of the copolymer. That being said, it is entirely possible that this model, designed for surfactant molecules, translates poorly to aggregate dispersions such as those observed here.

Corroborating evidence can be gathered when comparing to trends within the SEC data presented in **Table 4.4**, which suggest that polymers **1** and **3** should instead correspond to the largest average size nanoparticle. The contrast in these data are further the previous claim that, upon self-assembly, the block copolymer amphiphiles have adopted more poorly-defined aggregate structures, as opposed to organised micellar or polymersomal motifs. The average size values of these aggregates are independent of their relative M_n values.

4.3.3 pH-mediated release of doxorubicin from DOX-Loaded Nanoparticles

In preparation for encapsulation, DOX hydrochloride was converted to DOX free-base by stirring for 4 hours with trimethylamine. **Polymer 1**, here chosen overall as the most uniform mPEG-*b*-PMA system (PDI 0.128, Đ = 1.19), was dissolved in chloroform and added to PBS buffer simultaneously with DOX free-base solution.

Once the chloroform had evaporated, the nanoparticles were dialysed for three days to remove excess, un-encapsulated DOX, the mass of which was later measured, to determine the drug loading and encapsulation efficiency. The nanoparticles were then collected by lyophilisation.

To investigate the pH-mediated release of doxorubicin from mPEG-*b*-PMA, simultaneous dialyses of DOX-loaded nanoparticles were run for 1 week at 37 °C, with 1 mL aliquots taken at regular intervals to investigate the dialysate by UV-Vis spectroscopy. Increasing absorption of light at ca. 500 nm was used to determine changing concentration *via* a calibration curve, which was then scaled using the total volume of both sample and dialysate to determine the mass of released doxorubicin, expressed as a percentage of the total encapsulated.

This process was conducted in both PBS buffer solution (pH 7.4) and acetate buffer solution (pH 5.0), providing a physiological control against which acid-mediated release kinetics could be compared.

For the dox-loaded nanoparticles of polymer **1**, the recorded mass of dox-free base not encapsulated was determined to be 0.26 mg. Using equations defined in **Section 2.13**, the drug encapsulation efficiency of these nanoparticles was thereby calculated as 87 ± 3 wt%, with an average drug-loading content of 17.4 ± 1 wt%, where errors represent the deviation across triplicate measurements. These values compare well with existing literature for current poly(amino acid)-based nanoparticles.[17,18] The release profiles for dox-loaded nanoparticles of polymer **1**, incubated at 37 °C under physiological control conditions (PBS buffer, pH 7.4) and simulated acidic conditions (acetate buffer, pH 5.0) are presented in **Figure 4.3** below.

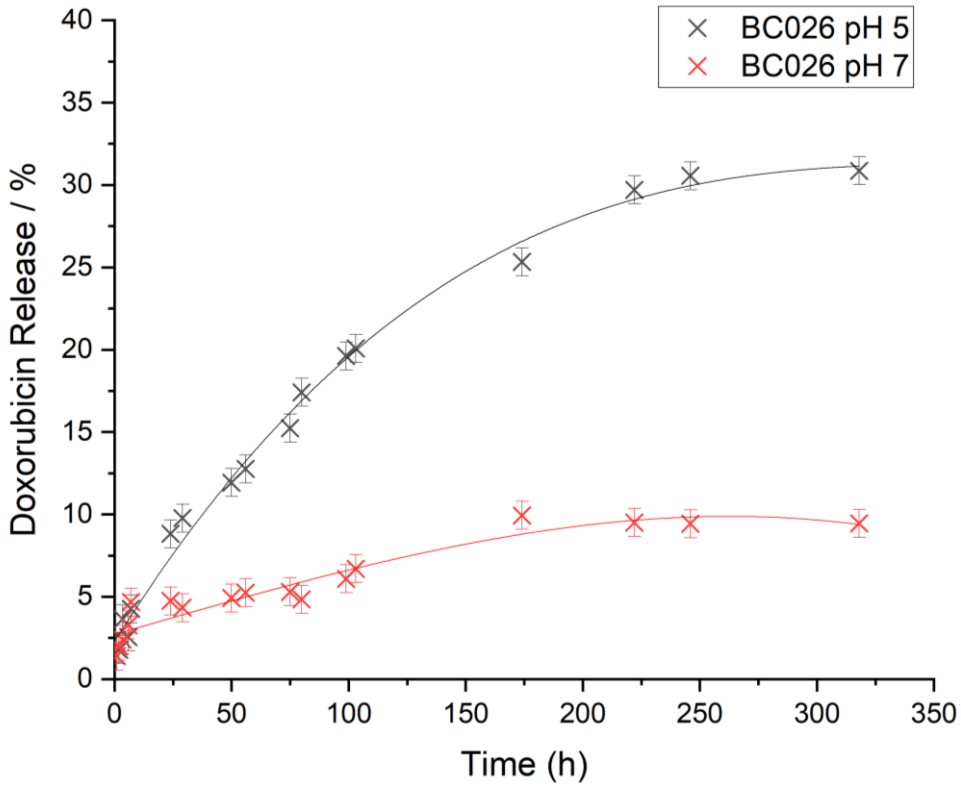

Figure 4.3: Drug release profiles for mPEG-*b*-PMA **Polymer 1**, incubated under pH 7.4 (X) and pH 5.0 (X) conditions. Each data point represents the mean of triplicate measurements, with error bars denoting the standard deviation.

For both sets of release parameters, it can be observed that nanoparticles were able to avoid uncontrolled burst release of DOX, demonstrating the stability of the nanoparticle system within each incubation environment. Such release would be detrimental for the effective treatment of cancers, with rapid DOX leakage resulting in similar non-specific cytotoxicity to non-encapsulated dox, negating the benefits intended with controlled-release. **Figure 4.3** illustrates a profound difference in the release kinetics for dox-loaded nanoparticles of polymer **1** incubated under acidic conditions, in comparison to those incubated at physiological pH. Dox release from nanoparticles incubated at pH 7.4 reached a maximum of only 9 % throughout the timespan of the experiment, demonstrating that the PMA backbone ester linkages remained robust against hydrolysis and that the nanoparticle system experienced minimal leakage as a result of deformation, under both physical agitation and thermal fluctuation.

This result is promising for the application of these materials in drug delivery, as their resistance to degradation and leakage under physiological pH are critical for effective for both storage prior to treatment, and for *in vitro* circulation to target delivery sites.

In stark contrast, the final dox release percentage obtained at pH 5.0 for polymer **1** was 33 %, a 3.7-fold increase over release a physiological pH, highlighting the sensitivity of this nanoparticle system to degradation under acidic conditions. This evidences the significant effectiveness of mPEG-*b*-PMA block copolymer amphiphiles and their corresponding dox-loaded nanoparticle systems as drug delivery vehicles. These nanoparticles can remain stable during encapsulation and circulation to tumour sites, whereupon their selective, pH-triggered release can strategically deliver the payload, minimising non-specific exposure and toxicity.

4.4 Conclusions and Future Work

Mandelic acid OCA was successfully polymerised from mPEG *via* straightforward OCA ROP to yield a series of novel mPEG-*b*-PMA BCP amphiphiles. Once synthesised, the products were characterised using ^{1}H NMR spectroscopy and SEC analysis. Achieved degrees of polymerisation were lower than expected for these polymers, likely owed to insufficient reaction temperatures and poor nucleophilicity of the initiator and/or active chain end, as evidenced by the increased D.P. for **Polymer 5**, for which ROP was conducted at increased temperature.

The lowest achieved D.P. values were those of **Polymer 2**, for which increased catalyst content may be linked increased side-reaction and depletion of monomer species, and for **Polymer 6**, for which low combined monomer concentration and high temperature likely contributed to the retardation of chain propagation and proliferation of side reactions, again limiting DP.

Nevertheless, these polymer products were obtained in good yield, and with consistently uniform Đ compared to the mPEG initiator, which compares favourably to related OCA syntheses in the literature and evidences the applicability of this synthetic route in creating future drug delivery vehicles.[19,20] Each of the polymers synthesised was capable of self-assembly into nanoparticle structures which, as determined by DLS analysis, likely presented as aggregate species as opposed to well-defined micelles or polymersomes.

Nevertheless, these nanoparticles were predominantly identified with average size below 200 nm and narrow PDI indices, suitable for the majority of applications in drug encapsulation, transport and delivery. For **Polymer 1**, DOX encapsulation efficiency was determined to be excellent in comparison to literature, and the stability and controlled-release profiles at pH 7.4 and 5.0 were further examined *via* dialysis under incubation and sequential UV-Vis spectrophotometry.[21,22] These analyses determined that under both environments, nanoparticles were resistant to burst release and leakage, and that acid-labile degradation and accelerated release were achievable under low-pH incubation.

With further optimisation of the preparative methodology for these materials, including more tuneable control of PMA D.P. and a more exacting procedure for nanoparticle self-assembly, this research represents an effective and reproducible template for the synthesis of mPEG-*b*-PMA drug delivery vehicles, capable of pH-triggered controlled release that may be applied to other bulky, aromatic payloads. These nanoparticles are applicable in a wide-range of drug delivery applications, and represent an exciting new technology for the pharmaceutical industry.

4.5 References

1. Mandelic Acid Market, www.gminsights.com/industry-analysis/mandelic-acid-market, (accessed 28/11/24).
2. Cochrane, G.; et al., *Cochrane Database Syst. Rev.*, **2020**, 4, CD003265.
3. Tufvesson, P.; et al., *ChemCatChem*, **2017**, 9, 1324–1330.
4. Makadia, H. K.; Siegel, S. J., *Polymers*, **2011**, 3, 1377–1397.
5. Zhang, L.; et al., *J. Control. Release*, **2017**, 257, 108–117.
6. Lide, D. R., ed., *CRC Handbook of Chemistry and Physics*, 84th edn, CRC Press, Boca Raton, **2003**, Section 9, *Electronegativity of the Elements*.
7. Buchard, A.; et al., *Angew. Chem., Int. Ed.*, **2014**, 53, 13858–13861.
8. Wang, R.; et al., *Angew. Chem., Int. Ed.*, **2016**, 55, 13010.
9. Patrick Wall, PhD Thesis, University of Leeds, **2023**.
10. Kricheldorf, H. R., Springer-Verlag, Berlin, **1987**.
11. Dove, A. P., *Polym. Chem.*, **2011**, 2, 1737–1751.
12. M. Brunzel, T. C. Majdanski, J. Vitz, I. Nischang and U. S. Schubert, Polymers, 2018, 10, 1395.
13. C. Bento, M. Katz, M. M. M. Santos and C. A. M. Afonso, Org. Process Res. Dev., 2024, 28, 860–890.
14. Duncan, T. M., *J. Mol. Struct.*, **1985**, 129, 51–59.
15. Maeda, H., *Adv. Drug Deliv. Rev.*, **2015**, 91, 3–6.
16. Maeda, H.; Fang, J.; Inutsuka, T.; Kitamoto, Y., *Int. J. Mol. Sci.*, **2018**, 19, 1469.
17. Price, D. J.; Khuphe, M.; Davies, R. P. W.; McLaughlan, J. R.; Ingram, N.; Thornton, P. D., *Chem. Commun.*, **2017**, 53, 8687–8690.
18. Kataoka, K.; Matsumoto, T.; Yokoyama, M.; Okano, T.; Sakurai, Y.; Fukushima, S.; Okamoto, K.; Kwon, G. S., *J. Control. Release*, **2000**, 64, 143–153.
19. He, H.; Li, D.; Zhang, Y.; Dai, Y.; Tang, H., *Molecules*, **2013**, 18, 12768–12782.
20. Vaca, S. H.; Bailey, T. S.; Martin, D. K.; Hillmyer, M. A., *ACS Macro Lett.*, **2015**, 4, 792–795.
21. Khuphe, C.; Thornton, P., *Macromol. Chem. Phys.*, **2018**, 219, 1800191.
22. Abioye, O. O.; Issahaku, D.; Aminu, G. A.; Attama, H. O., *J. Drug Deliv. Sci. Technol.*, **2019**, 52, 780–789.

Appendices

A.4.1 ^{1}H NMR Spectra

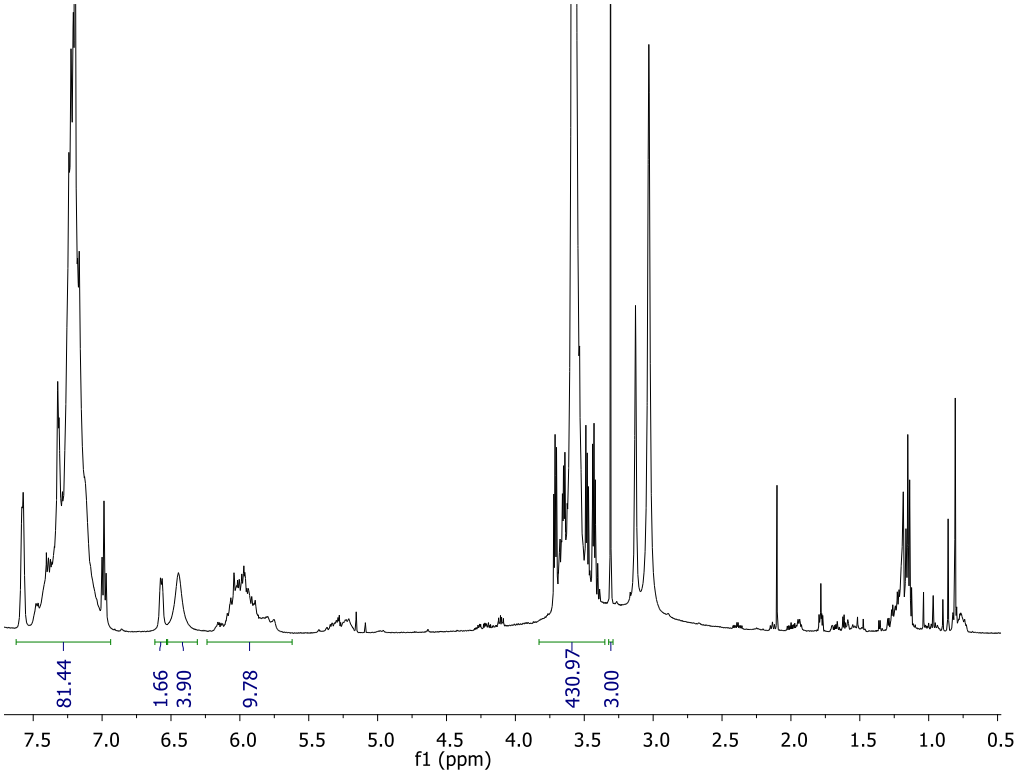

Figure A.4.1.1: ^{1}H NMR spectrum (500 MHz, $CDCl_3$) of **Polymer 1**, mPEG-*b*-PMA_{15}

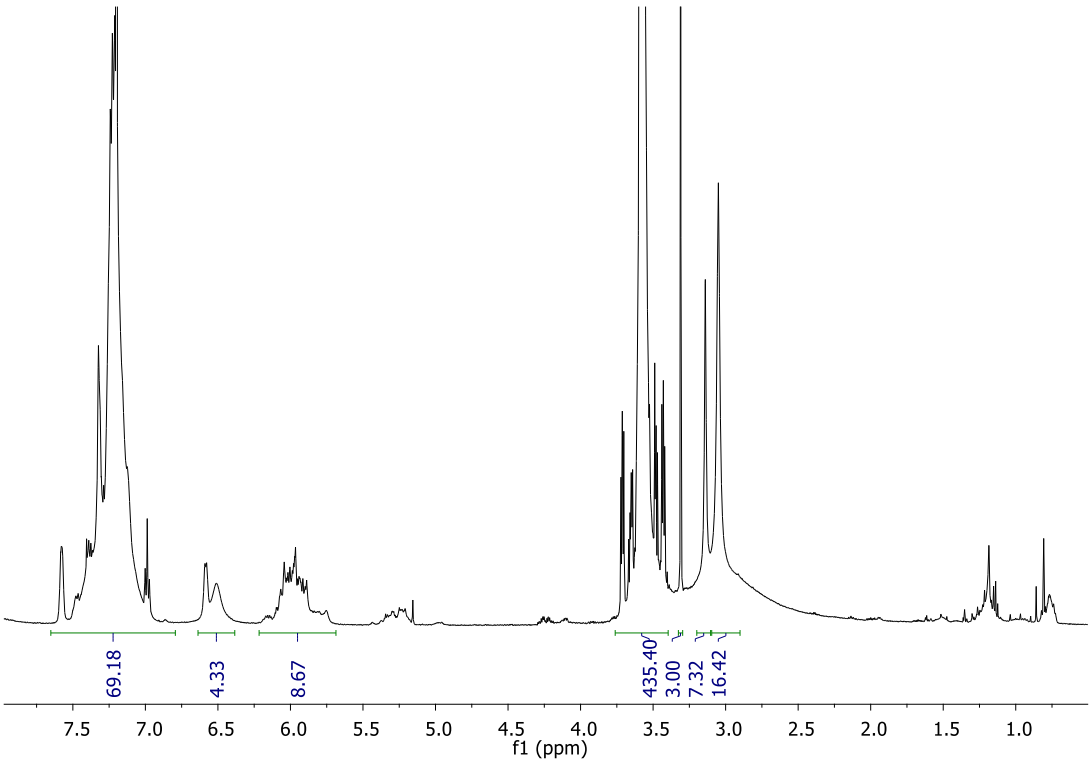

Figure A.4.1.2: ^{1}H NMR spectrum (500 MHz, $CDCl_3$) of **Polymer 2**, mPEG-*b*-PMA_{14}

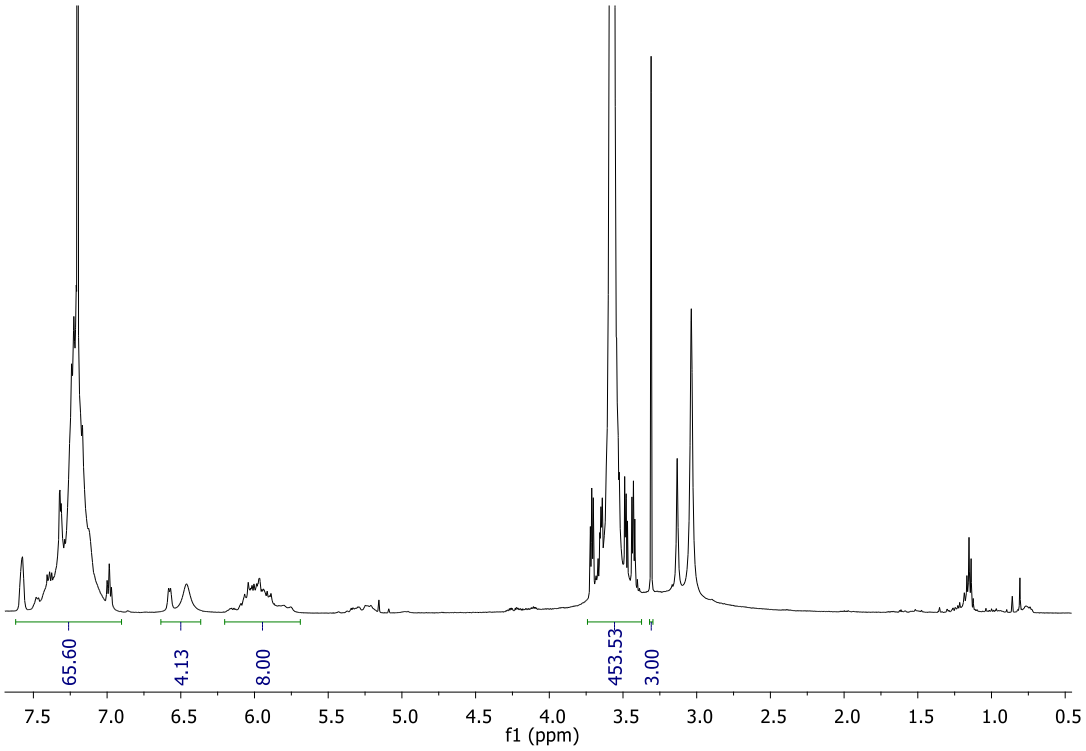

Figure A.4.1.3: ^{1}H NMR spectrum (500 MHz, $CDCl_3$) of **Polymer 3**, mPEG-*b*-PMA_{13}

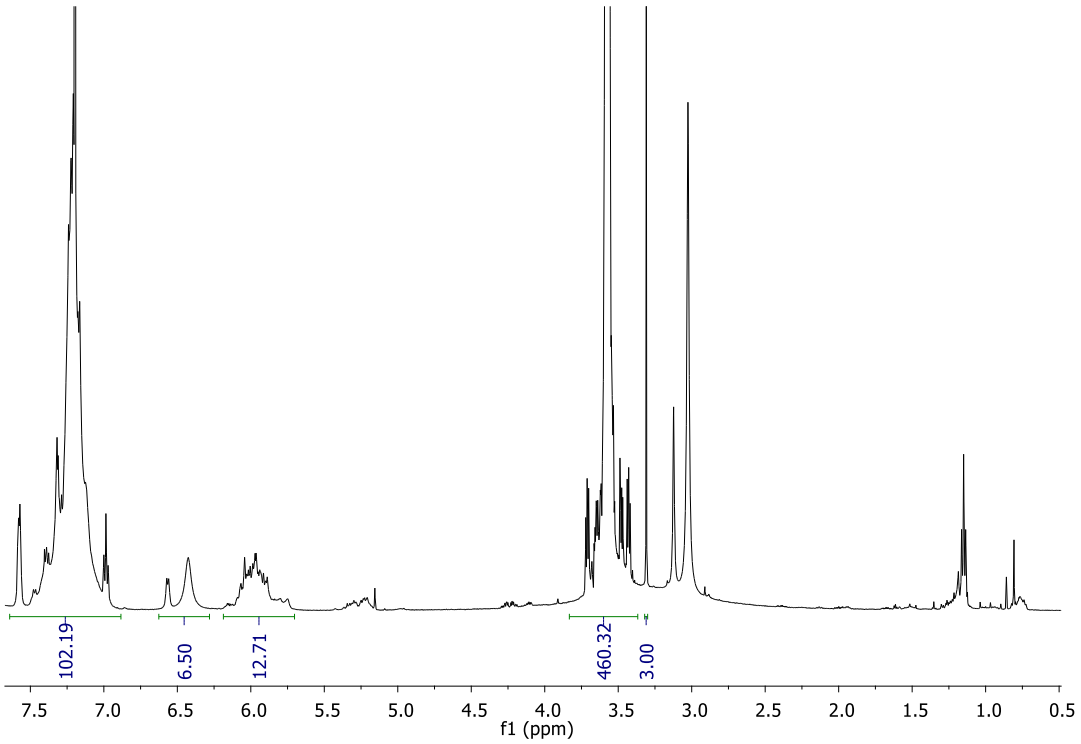

Figure A.4.1.4: ^{1}H NMR spectrum (500 MHz, $CDCl_3$) of **Polymer 4**, mPEG-*b*-PMA_{20}

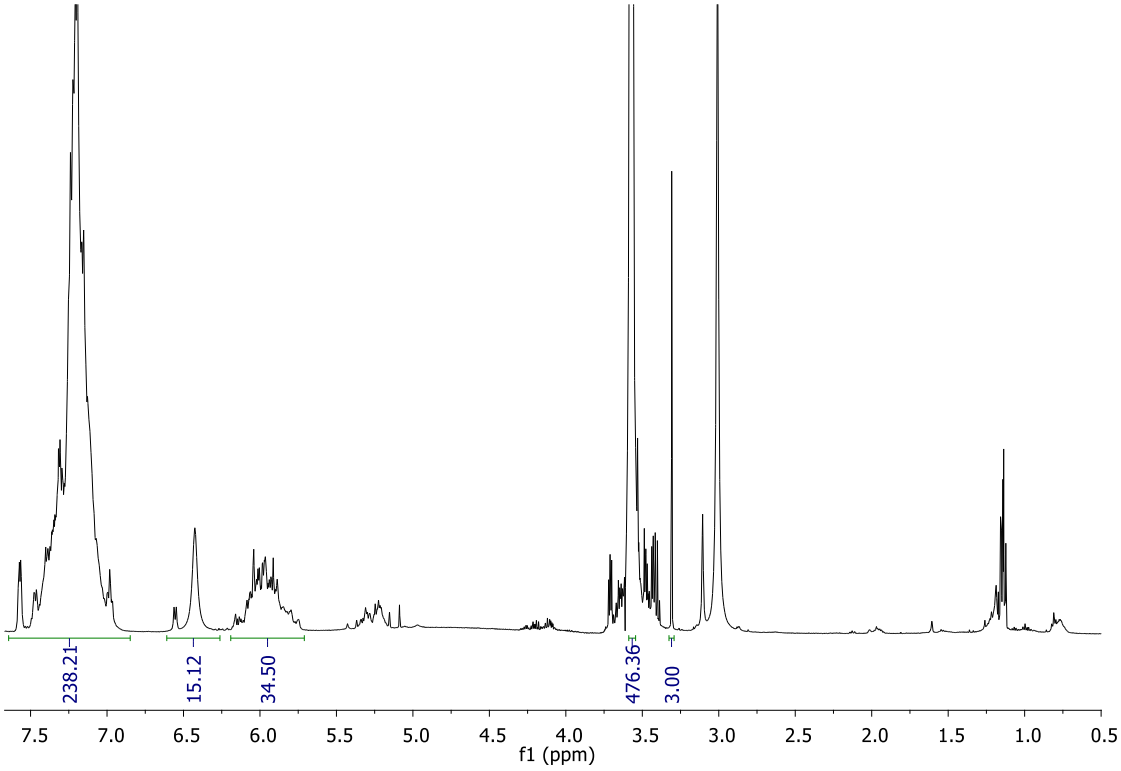

Figure A.4.1.5: ^{1}H NMR spectrum (500 MHz, $CDCl_3$) of **Polymer 5**, mPEG-*b*-PMA_{48}

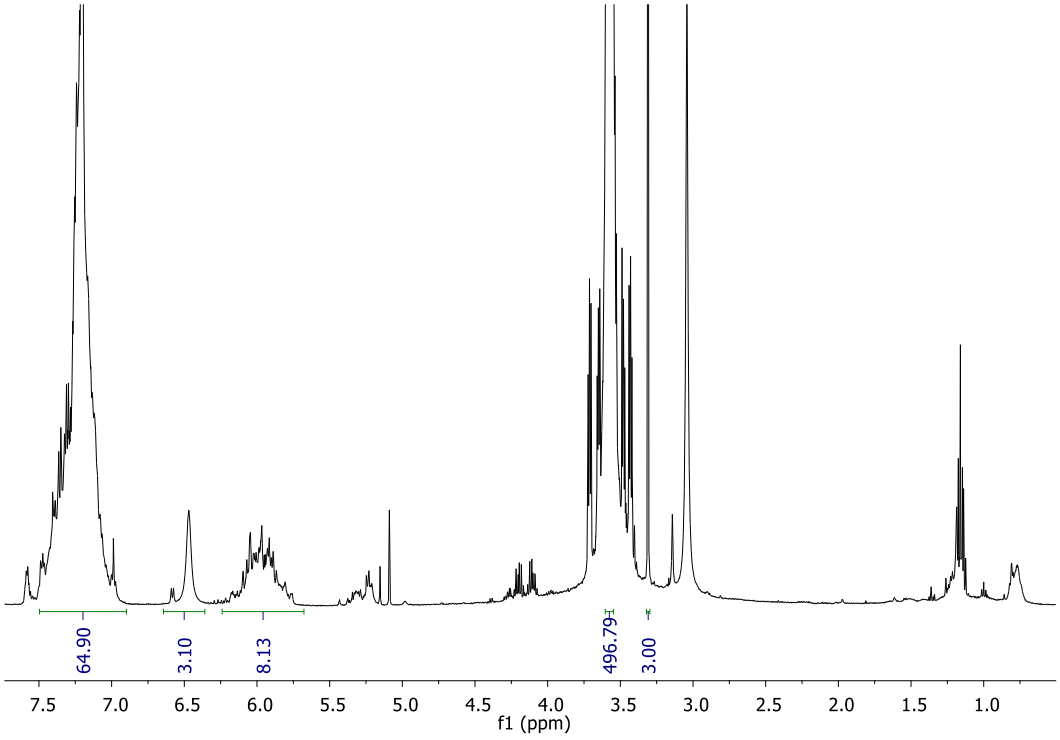

Figure A.4.1.6: ^{1}H NMR spectrum (500 MHz, $CDCl_3$) of **Polymer 6**, mPEG-*b*-PMA_{10}

A.4.2 ^{13}C NMR Spectra

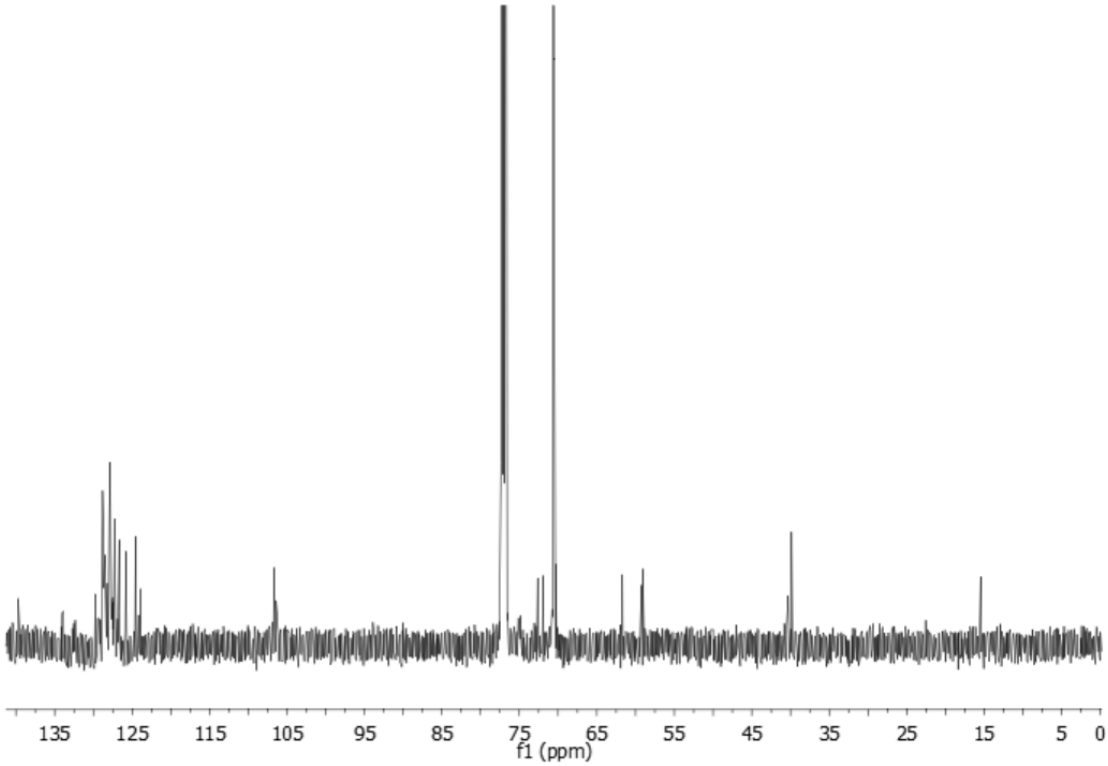

Figure A.4.2.1: ^{13}C NMR spectrum (500 MHz, $CDCl_3$) of **Polymer 1**, mPEG-*b*-PMA_{15}

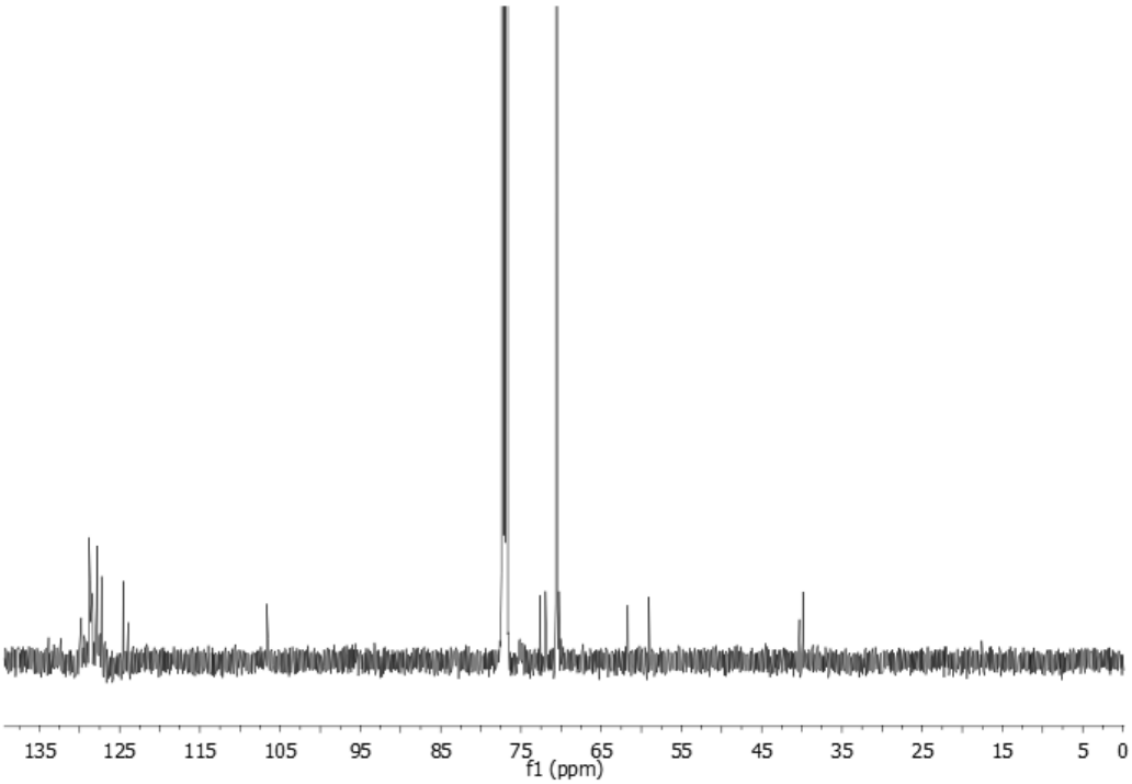

Figure A.4.2.2: ^{13}C NMR spectrum (500 MHz, $CDCl_3$) of **Polymer 2**, mPEG-*b*-PMA_{14}

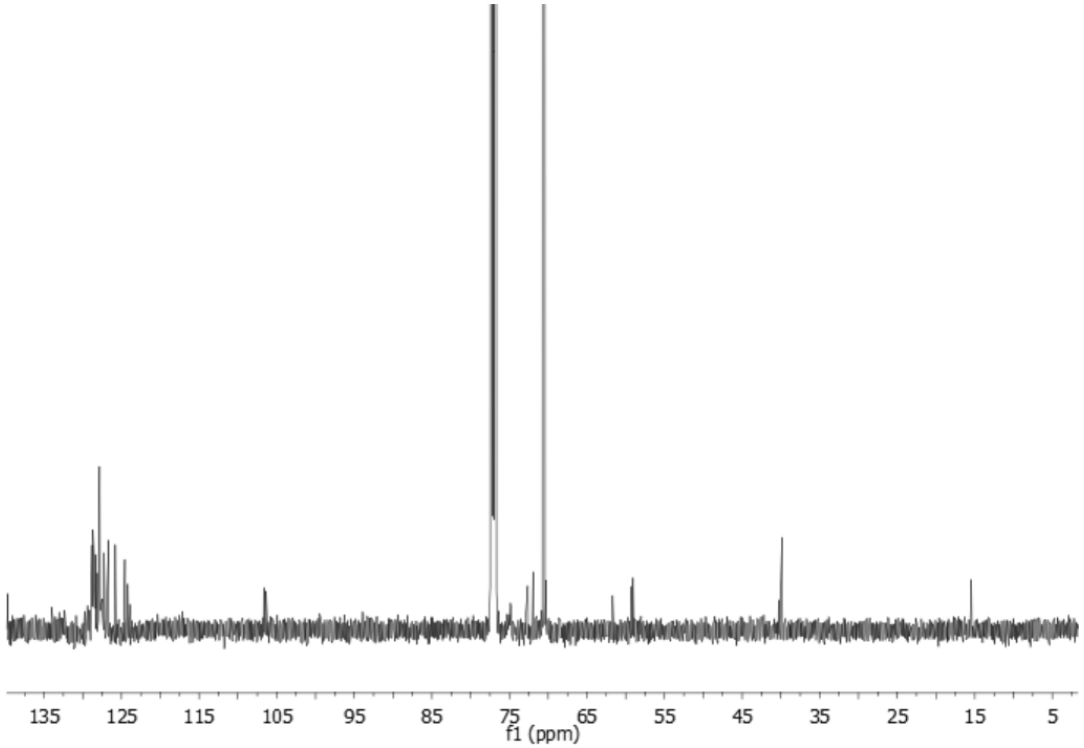

Figure A.4.2.3: ^{13}C NMR spectrum (500 MHz, $CDCl_3$) of **Polymer 3**, mPEG-*b*-PMA_{13}

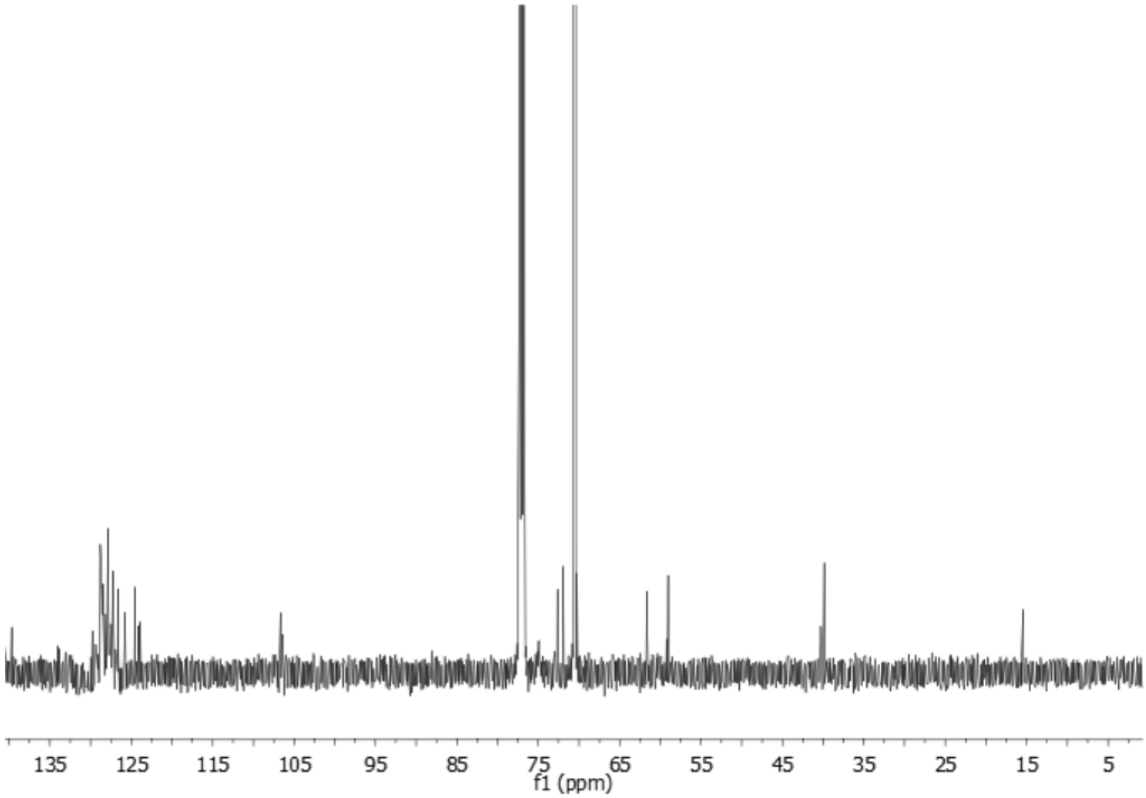

Figure A.4.2.4: ^{13}C NMR spectrum (500 MHz, $CDCl_3$) of **Polymer 4**, mPEG-*b*-PMA_{20}

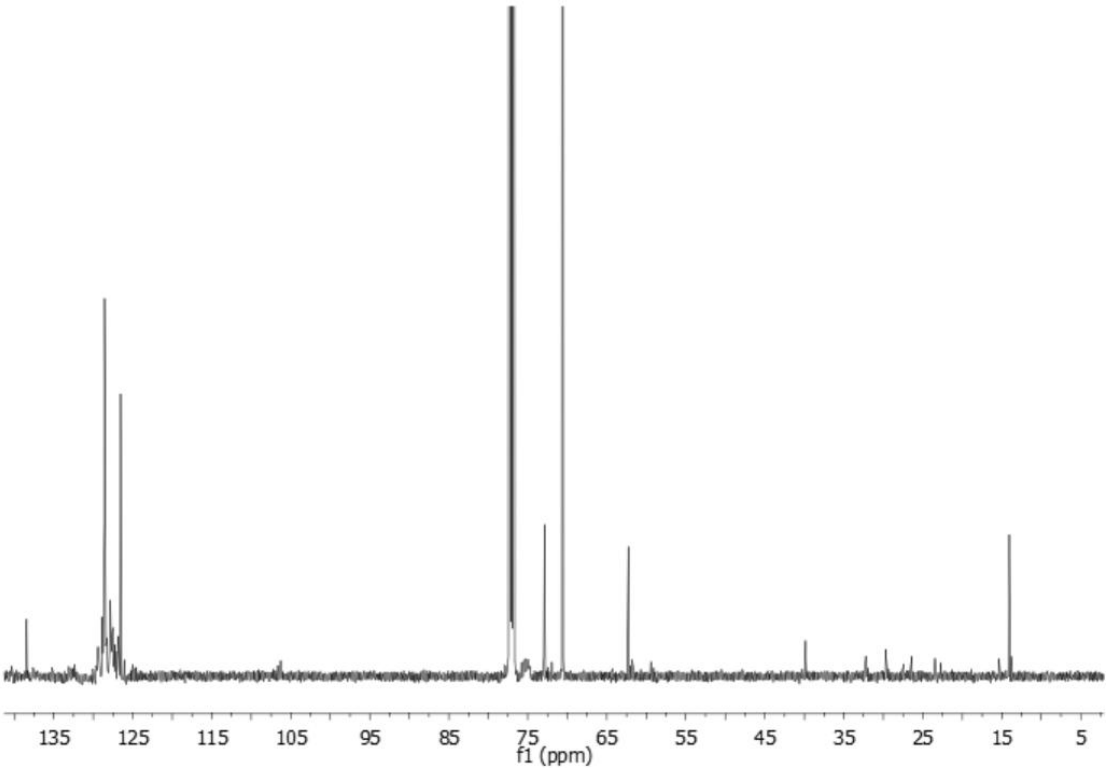

Figure A.4.2.5: ^{13}C NMR spectrum (500 MHz, $CDCl_3$) of **Polymer 5**, mPEG-*b*-PMA_{48}

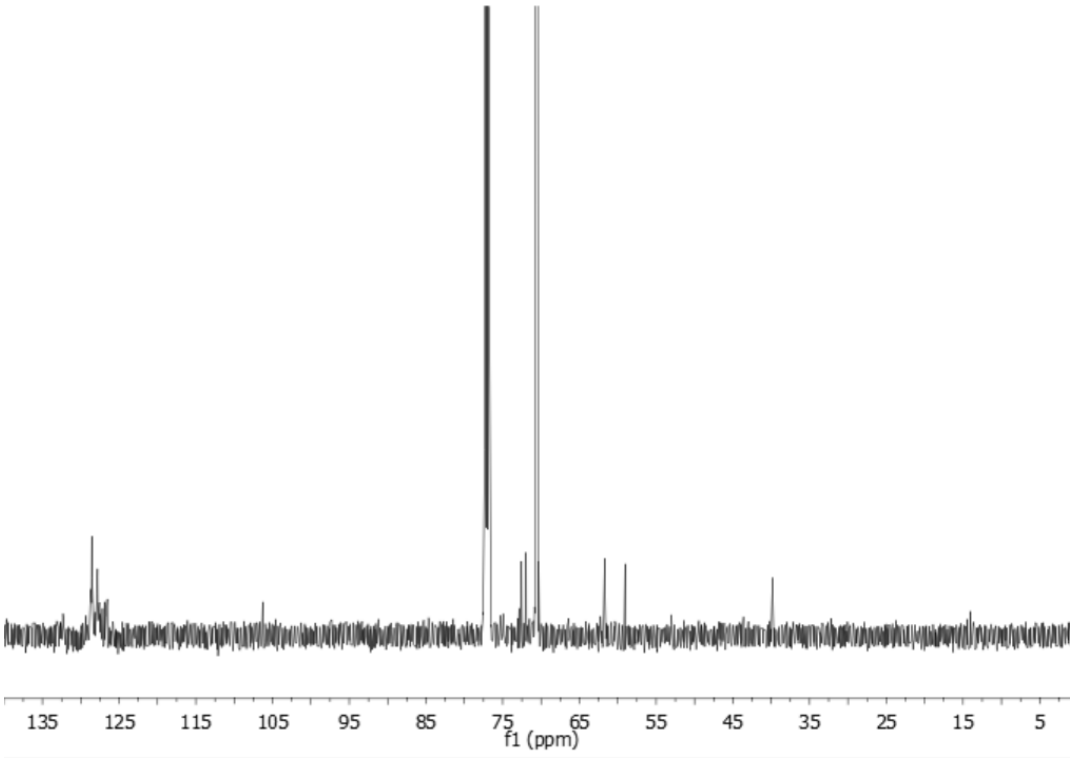

Figure A.4.2.6: ^{13}C NMR spectrum (500 MHz, $CDCl_3$) of **Polymer 6**, mPEG-*b*-PMA_{10}

A.4.3 FTIR Spectra

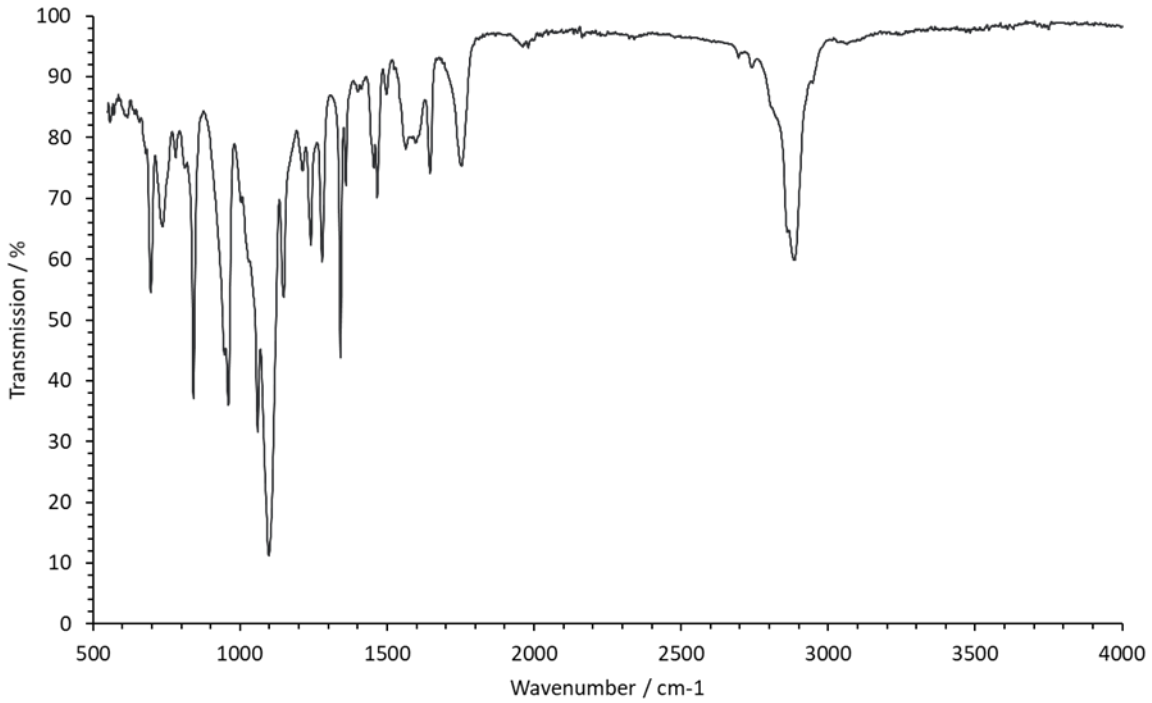

Figure A.4.3.1: FTIR spectrum of **Polymer 1**, mPEG-*b*-PMA_{15}

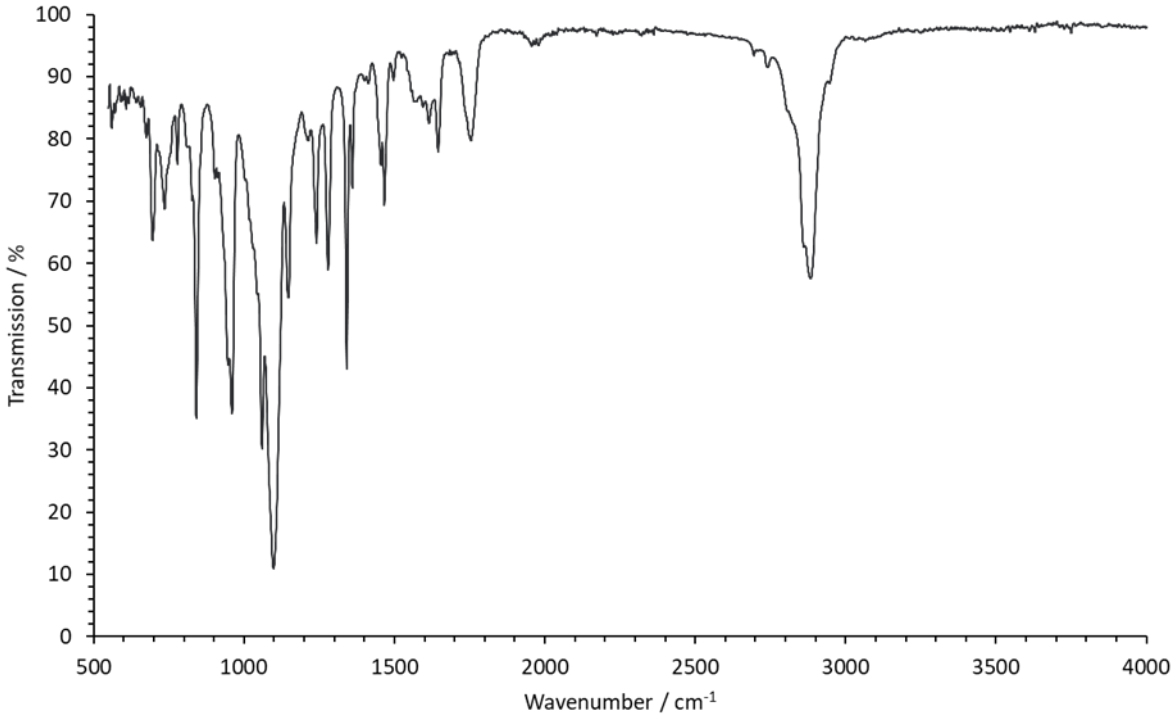

Figure A.4.3.2: FTIR spectrum of **Polymer 2**, mPEG-*b*-PMA_{14}

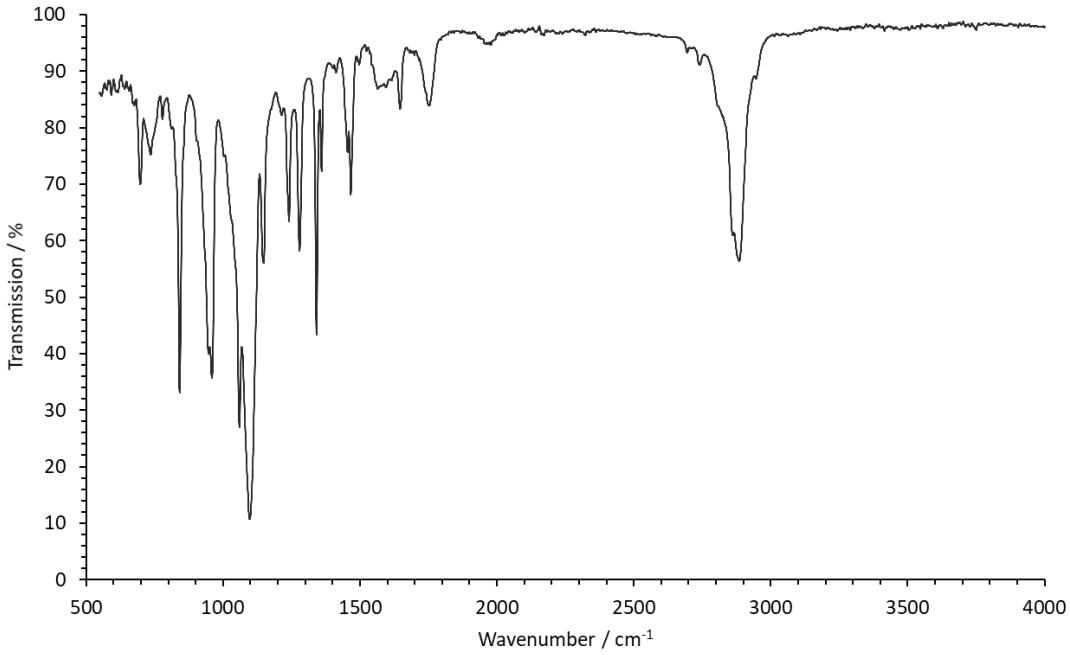

Figure A.4.3.3: FTIR spectrum of **Polymer 3**, mPEG-*b*-PMA_{13}

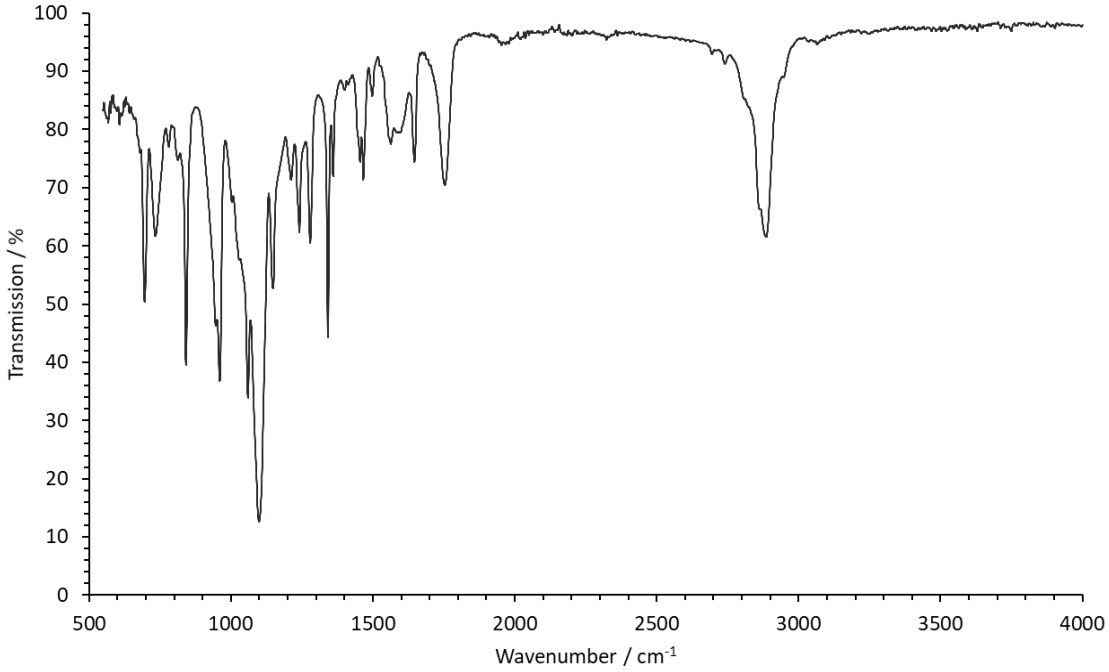

Figure A.4.3.4: FTIR spectrum of **Polymer 4**, mPEG-*b*-PMA_{20}

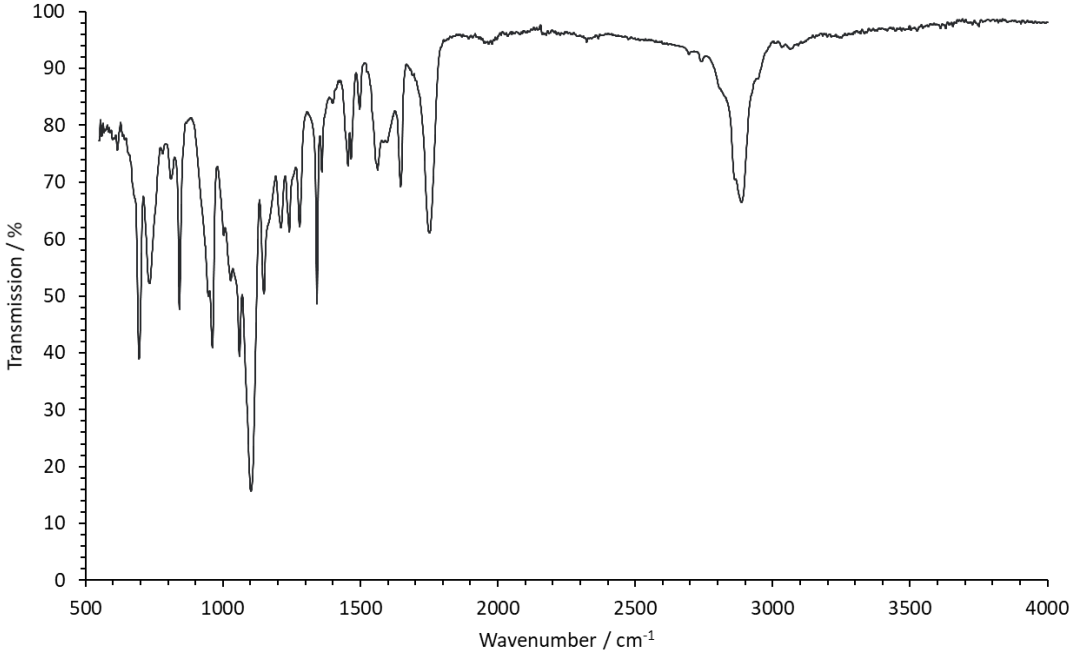

Figure A.4.3.5: FTIR spectrum of **Polymer 5**, mPEG-*b*-PMA_{48}

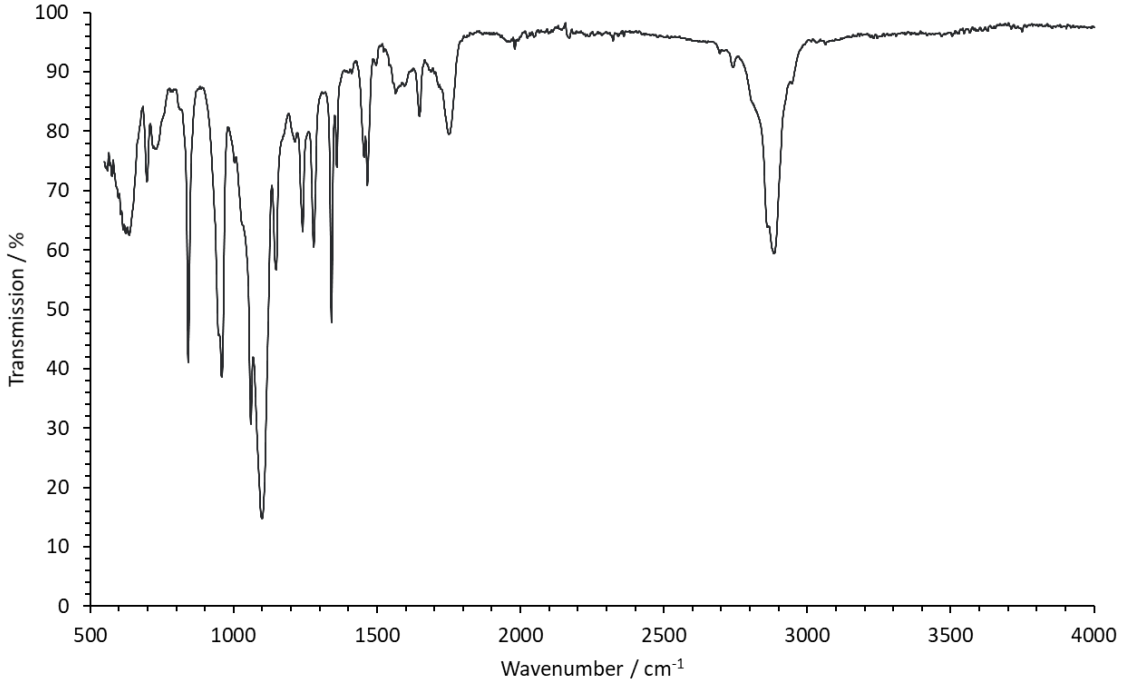

Figure A.4.3.6: FTIR spectrum of **Polymer 6**, mPEG-*b*-PMA_{10}

A.4.4 Size Exclusion Chromatography

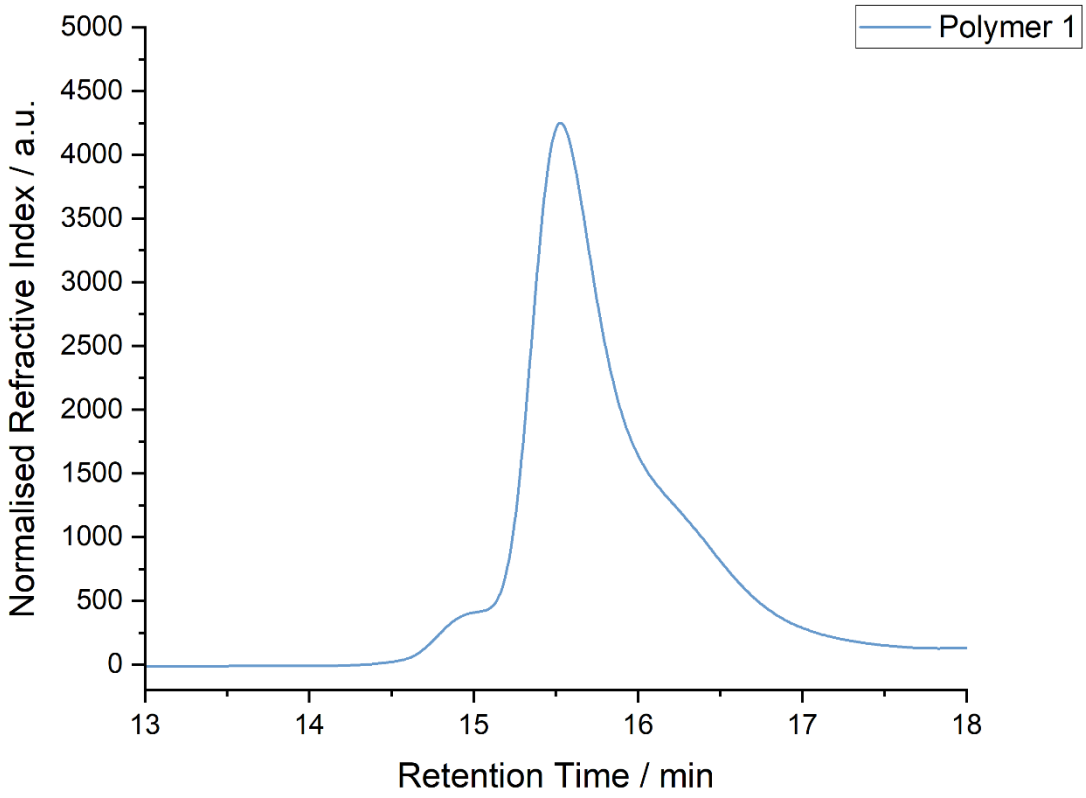

Figure A.4.4.1: SEC chromatogram of **Polymer 1**, mPEG-*b*-PMA_{15}

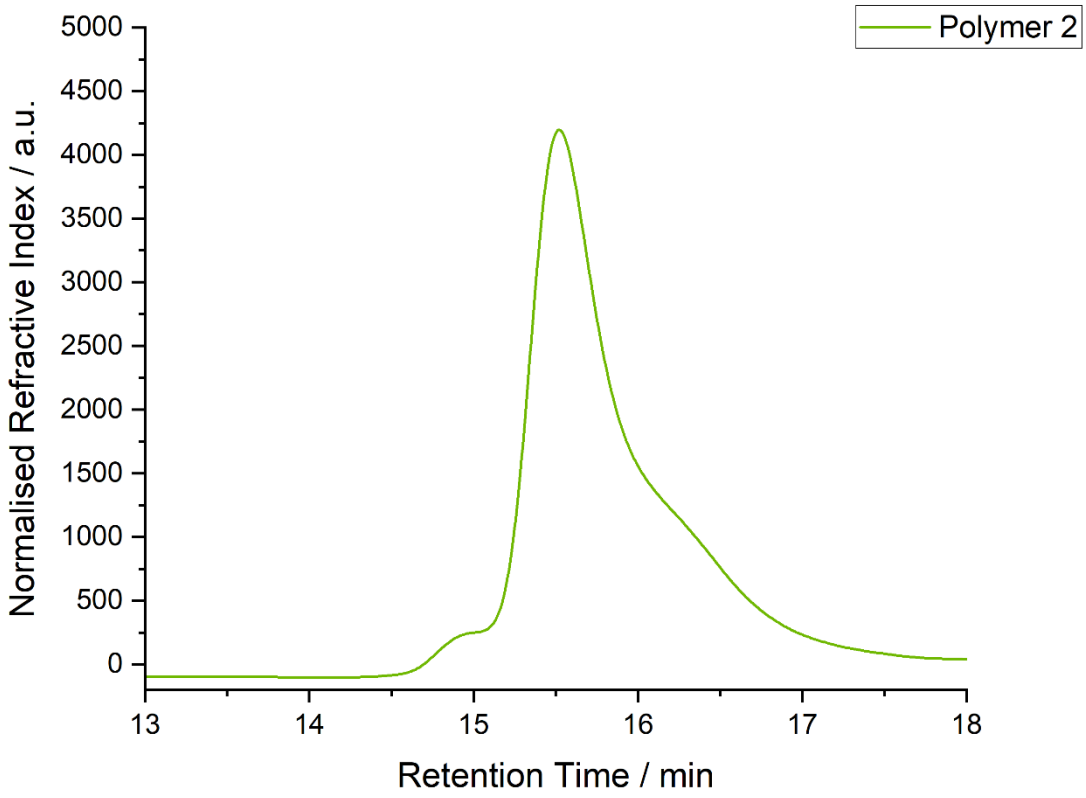

Figure A.4.4.2: SEC chromatogram of **Polymer 2**, mPEG-*b*-PMA_{14}

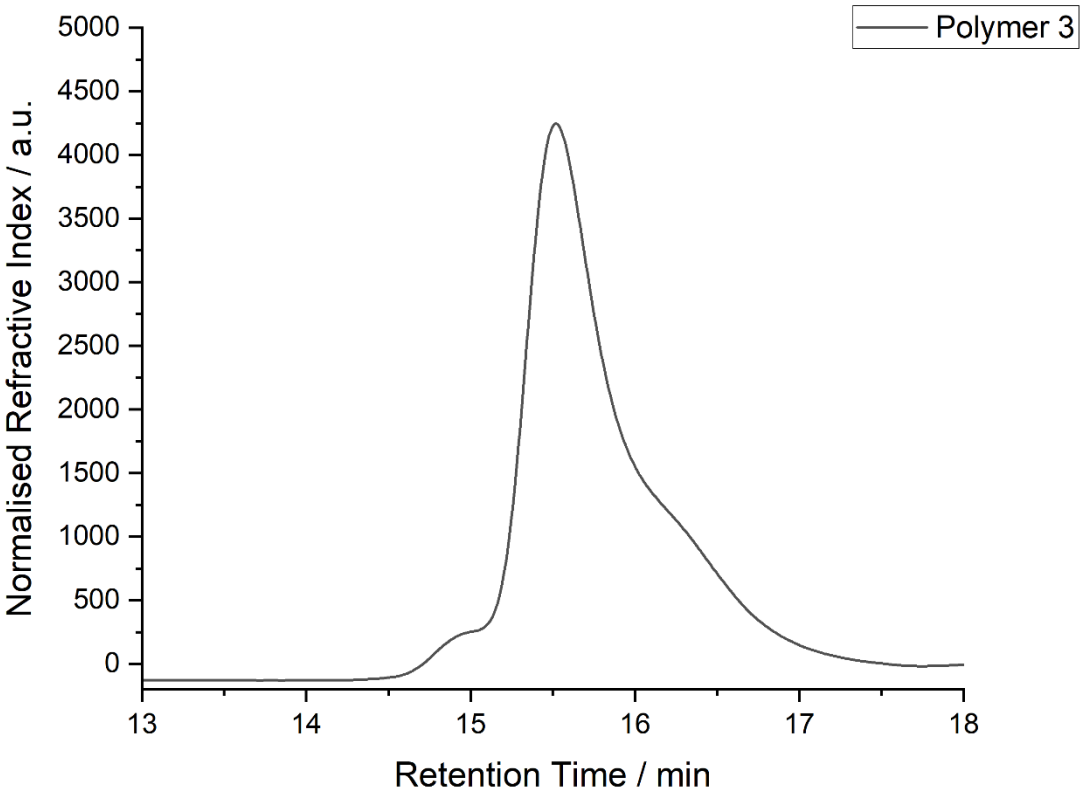

Figure A.4.4.3: SEC chromatogram of **Polymer 3**, mPEG-*b*-PMA_{13}

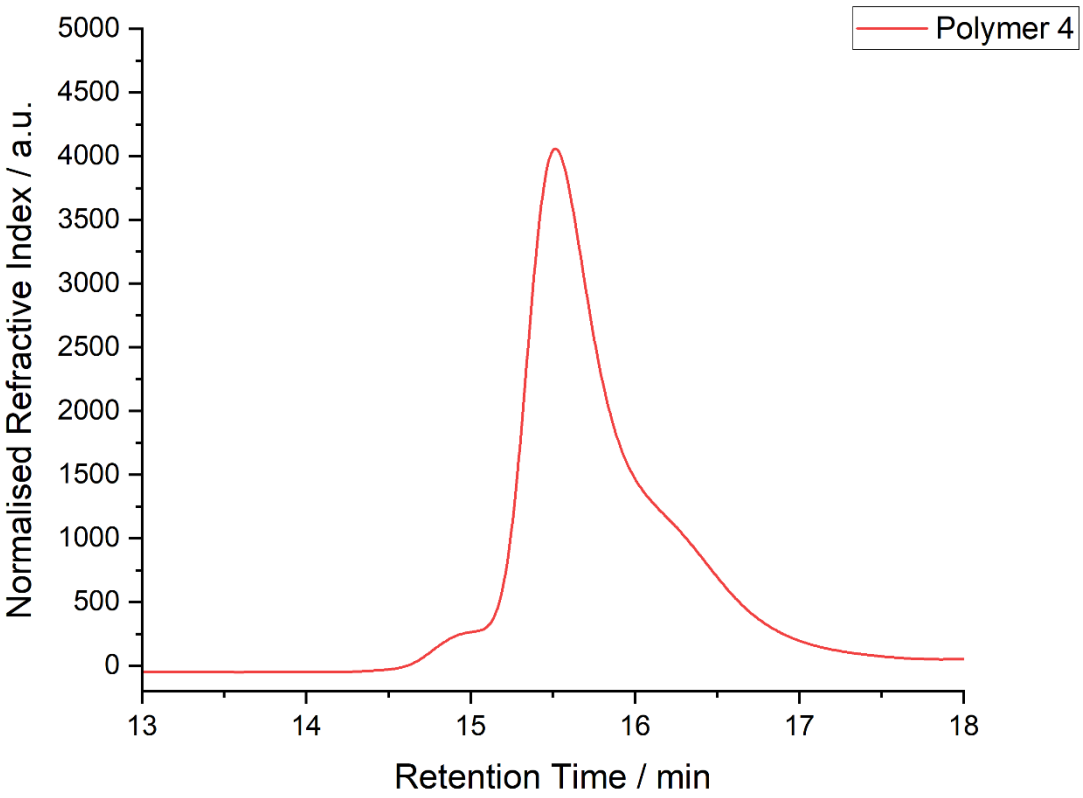

Figure A.4.4.4: SEC chromatogram of **Polymer 4**, mPEG-*b*-PMA_{20}

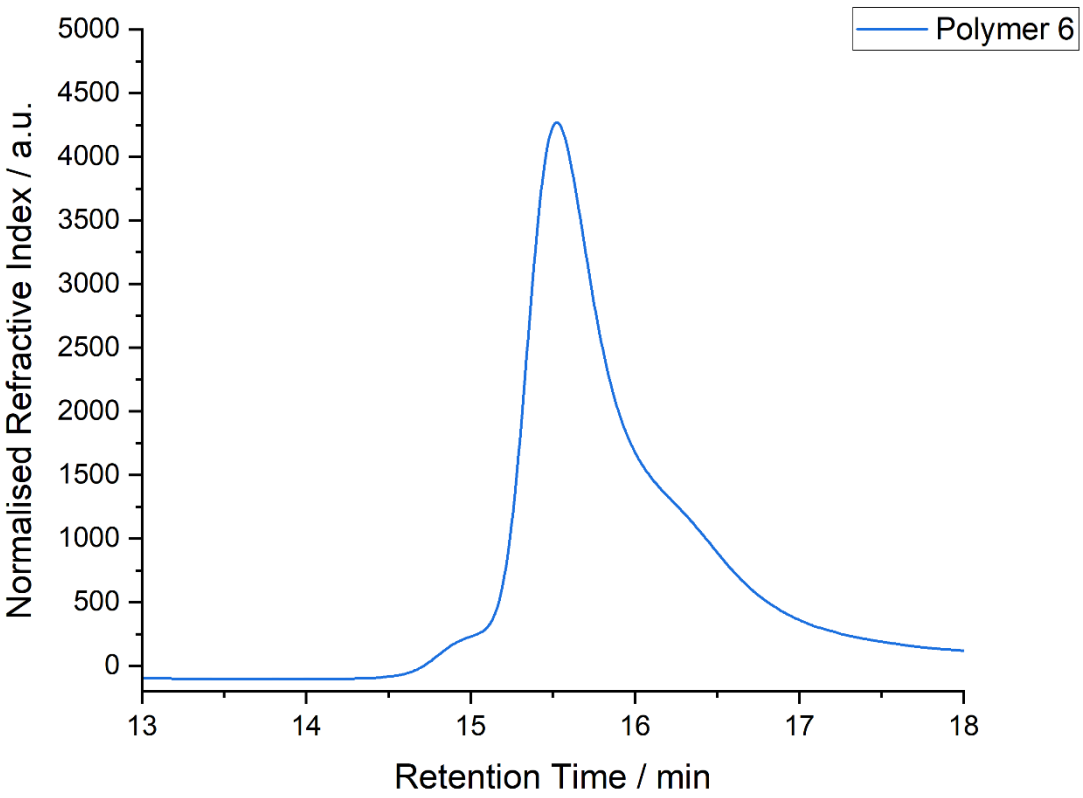

Figure A.4.4.5: SEC chromatogram of **Polymer 6**, mPEG-*b*-PMA_{10}

A.4.5 Dynamic Light Scattering

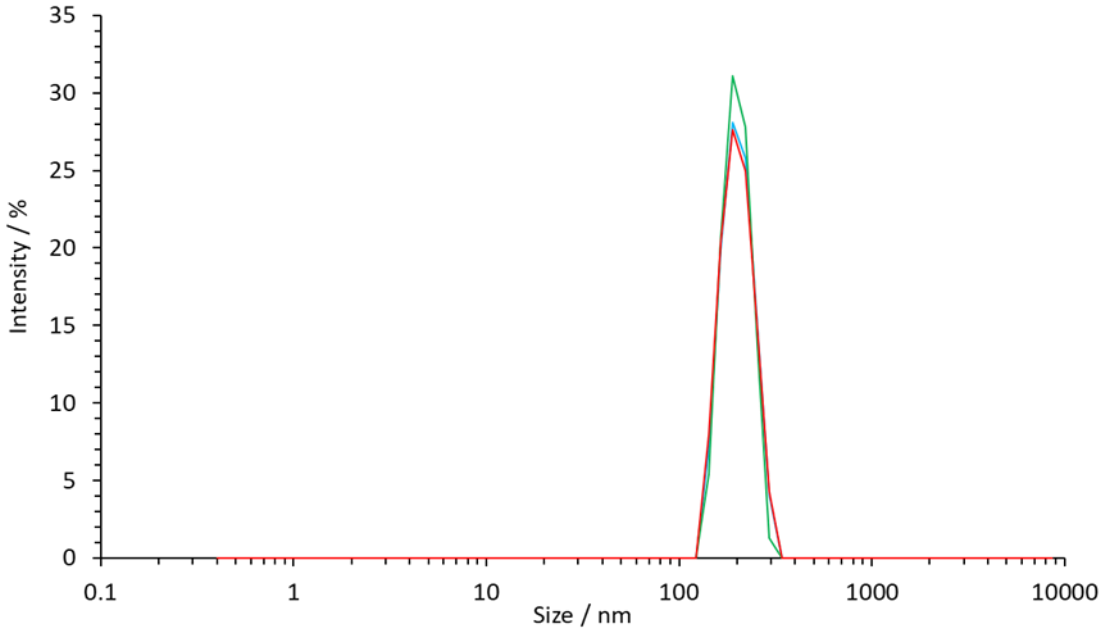

Figure A.4.4.1: DLS size distribution of **Polymer 1**, mPEG-*b*-PMA_{15}

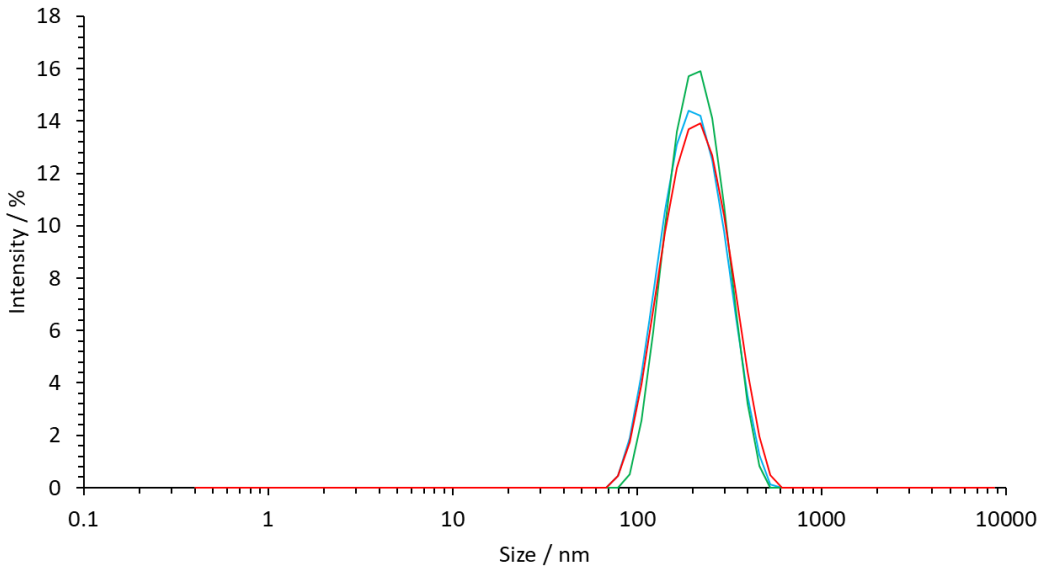

Figure A.4.4.2: DLS size distribution of **Polymer 2**, mPEG-*b*-PMA_{14}

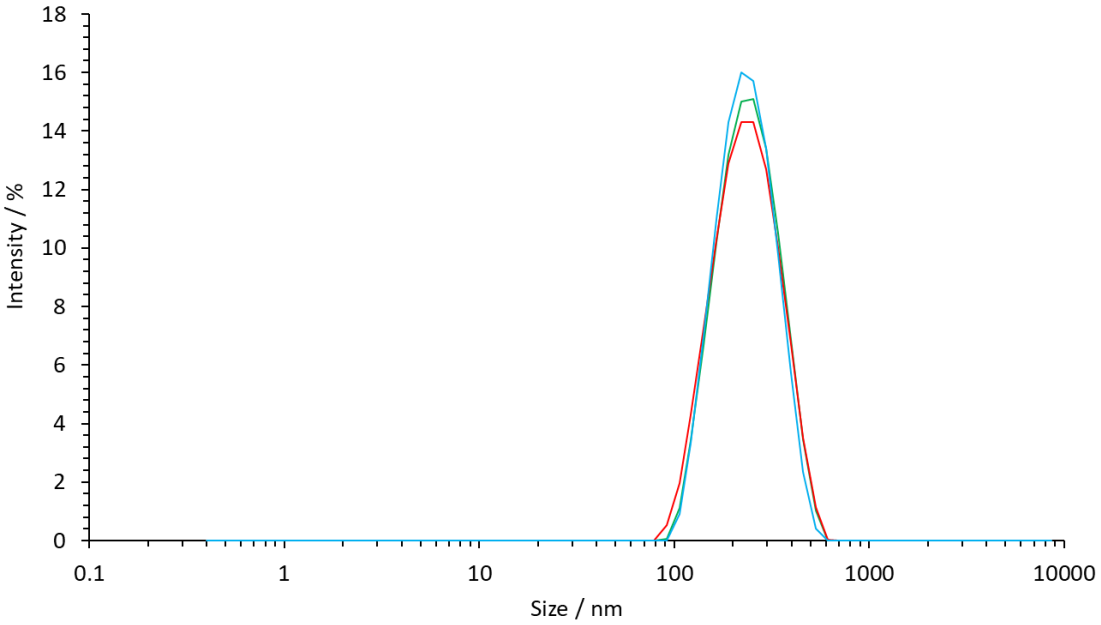

Figure A.4.4.3: DLS size distribution of **Polymer 3**, mPEG-*b*-PMA_{13}

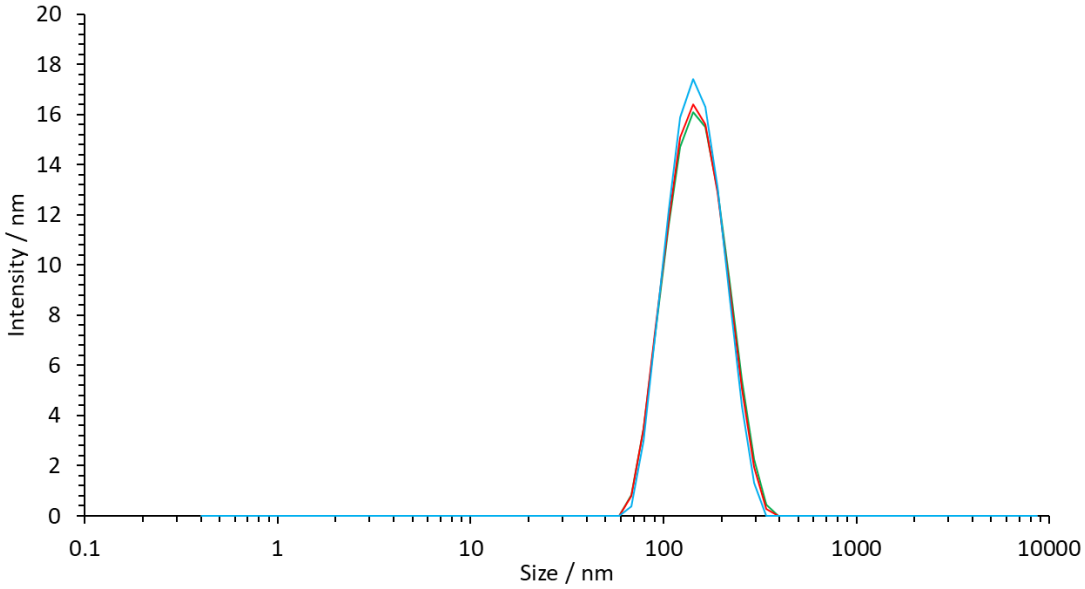

Figure A.4.4.4: DLS size distribution of **Polymer 4**, mPEG-*b*-PMA_{20}

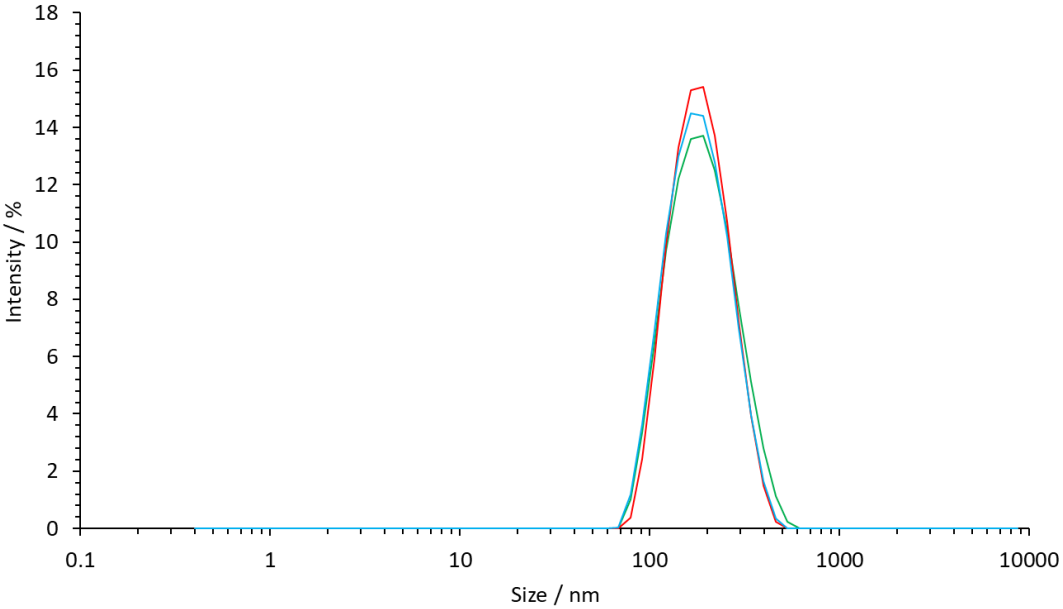

Figure A.4.4.5: DLS size distribution of **Polymer 5**, mPEG-*b*-PMA_{48}

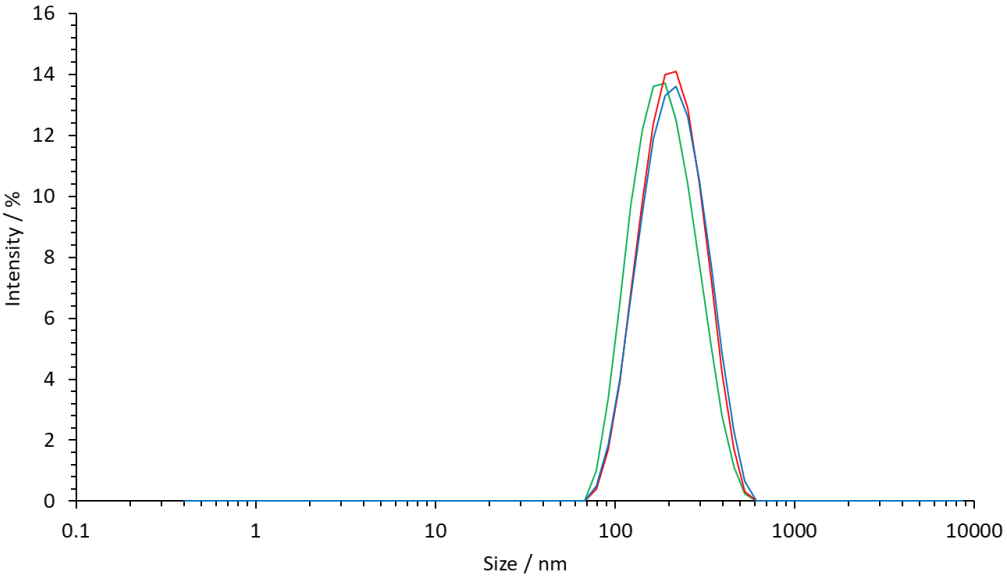

Figure A.4.4.6: DLS size distribution of **Polymer 6**, mPEG-*b*-PMA_{10}

Chapter 5: Optimisation of the Synthesis, Deprotection and Purification of mPEG-*b*-PLys Block Copolymers.

Abstract

The optimisation of the NCA-ROP procedure for Lys-NCA is reported in this chapter. Specifically, the procedures and associated complications involved in ROP of Lys-NCA monomers under the protection of Fmoc, Z and Boc groups are evaluated. These groups each present potential benefits for the resultant BCP system, such as the capability of Fmoc groups to undergo green thermal deprotection, the robustness of Z groups to acidic and basic environments during ROP, and the technical simplicity of Boc-group deprotection, which requires minimal purification strategies in comparison to the former two groups.

Long reaction timescales and the combination of poorly-reactive mPEG-OH initiator with DMAP catalyst lead to the *in-situ* deprotection of Fmoc units, as determined by ^{1}H NMR kinetic analysis. These features also lead to the side-reaction of Lys(Z)-NCA monomers, and the formation of homopolymeric side products, as determined by DOSY NMR analysis. Lys(Boc)-NCA proved to be the most effective monomer of the three. NCA ROP was achieved successfully, as was evidenced by in-line FTIR spectroscopic monitoring, which determined full monomer conversion. Furthermore, deprotection procedures for the resulting products were made substantially easier, due to the formation of by-products as volatile organics, removed during the procedure, leaving minimal purification. There was complication with the ROP procedure for BCPs of 10 repeat units and above, in the formation of high-M.W. impurities. Whilst several potential causes for these species were identified, and experimentation was performed to minimise their impact (reduced-temperature reactions, use of non-interactive solvents) this problem persisted in a number of the final products. As such, this problem has been scrutinised throughout this chapter, and remains the primary candidate for future work related to these products.

5.1 Introduction

Similar to PAAs discussed prior in **Chapter 1**, PLys has been reported extensively throughout the literature in the synthesis of polymeric drug delivery vehicles, as both a homopolymer and as part of an amphiphilic block copolymer system.[1-3] What sets P(Lys) apart from other PAAs is the functionality of its pendant primary amine group, which allows for both cationic complexation with, and nucleophilic conjugation to, a broad spectrum of additive species, from active therapeutics such as oligonucleotides and drug molecules to further PAA chains.[3-5] The latter of these contains within itself a multitude of customisation for multi-functional PAAs, opening the door to polymer branching and more complex architectures, themselves an avenue to greater functionality and therapeutic impact.

One of the earliest documented cases of lysine-based therapeutic delivery agents was performed by Kataoka *et al*. in 1996, wherein chains of cationic P(Lys) underwent electrostatically-induced polyion complexation with the antisense oligonucleotide c-Ha-*ras*.[3] This system was relevant to the development of a novel *in vivo* vector system for oligonucleotides in general, and demonstrated significant potential thanks to the inclusion of a PEG block in the polymer backbone, which compatibilised the otherwise insoluble polyion complex by forming a soluble corona, as confirmed by DLS analysis. This worked paved the way for further PEG-*b*-PLys block copolymer systems, as discussed below.

Whilst lysine is intrinsically pH-responsive, as was demonstrated here, what has been further explored is the conjugation of PEG-*b*-PLys systems to other functional species, imparting smart stimuli-responsive activity to triggers such as pH, temperature, hypoxia, redox, and enzyme activity.[6-9] Recently, this has been demonstrated by authors such as Iatrou *et al*. who, in exploring pH-responsiveness, grafted short histidine chains to a P(Lys) backbone.[10] This was done using orthogonal deprotection, which has been discussed in greater detail in **Section 1.4.1.1**. In grafting histidine to this lysine backbone, the authors imparted substantial pH-responsive effects into the resultant nanoparticle, including transitions in secondary structure from random coil to β-sheet, and changes in size of over 100 nm as pH was tuned. These effects represent tremendous versatility in the products of P(Lys) conjugation, a facet of the technology that has been a core motivator of the work conducted throughout this Chapter.

Similar inspiration for this research was derived from examples of conjugative drug encapsulation within the literature, whereby lysine ε-amine functional groups are covalently linked to drug molecules. These linked drug molecules often stimulate self-assembly *via* hydrophobic and π-stacking interactions, thus avoiding the processes of amphiphilic BCP synthesis and encapsulation. In doing so, these conjugative nanoparticle systems sidestep the commonly-associated challenges with typical delivery systems. Whilst drug loading capacity is often limited to less than 20 wt% for most platforms, including polymeric micelles, drug conjugation sets a minimum loading at the number of drug molecules linked within, providing consistent dosing for therapeutic use.[11] Furthermore, whilst the polymer-drug linkages of these systems are capable of tuning for controlled release, they remain robust under physiological conditions, ensuring triggered release under the desired circumstances and avoiding premature (or "burst") release, often observed with simpler encapsulation. A notable example of these conjugative delivery systems was performed by Wang *et al*. in 2018.[2] Doxorubicin was conjugated alongside 4-carboxybenzaldehyde to lysine side chains of PLys-*b*-PMPC BCPs *via* pH-sensitive imine linkages. Once self-assembled, BCPs were then capable of both charge-conversion for enhanced deep-tissue penetration, as well as pH-mediated release of doxorubicin under acidic conditions. Another example of polymer-drug conjugation for improved delivery, and a direct precursor to work conducted in this report, is that of England *et al*.[12] For this work, the authors utilised a linear PSar macroinitiator as opposed to traditional PEG, from which they built mutli-generational, hyperbranched dendritic PLys blocks to conjugate fulvestrant. This was done *via* Steglich esterification of its 3-position phenol group with t-butyl succinate and subsequent deprotection to yield a succinic acid functional group, before conjugation *via* amide coupling to the amino termini of the lysine dendron using DMTMM as the coupling reagent. Furthermore, the high compatibility of the fulvestrant-composed hydrophobic core provided an excellent environment for further fulvestrant encapsulation, with the authors achieving up to 77 wt% total drug content within the micelles (conjugated + encapsulated), and an encapsulation efficiency of over 98 %. This conjugation also lowered the micelles' CMC, increasing the stability of the platform in dilute conditions such as physiological administration. This work represents the gold standard for the potential of drug-conjugated polymer systems, a standard that this work aims to emulate.

5.2 Experimental

5.2.1 Monomer Synthesis

Lys-NCA with different protecting groupsspecies were synthesised for this investigation according to the preparative methodologies described in **Section 3.1.1**, *via* both phosgene-mediated and phosgene-free synthetic routes. Each NCA monomer was synthesised in good yield and high purity, as was determined by ^{1}H NMR and FTIR spectroscopies. The attached protecting groups were maintained throughout the process.

5.2.2 NCA ROP of Lys(Fmoc)-NCA

Non-monitored Synthesis of PEG-b-PLys(Fmoc)

Lys(Fmoc)-OH NCA (400 mg, 1.05 mmol) and mPEG (M.W. 5000 g mol^{-1}, 52.6 mg, 0.01 mmol) were added to an oven-dried Schlenk tube, fitted with a suba-seal, and dried under vacuum (1 h). Anhydrous DMF (6 mL) was added to dissolve the mixture, and stirred under an atmosphere of $N_{2(g)}$ over the course of the reaction (168 h). Once the reaction had reached completion, the reaction mixture was precipitated by ice-cold diethyl ether (150 mL) and collected *via* centrifugation (see **Section 2.8**). The collected solid was then washed with ice-cold diethyl either (2 x 30 mL) and toluene (1 x 30 mL) and dried under vacuum overnight. The purified product was then collected as a dense off-white powder.

Yield: 60 wt%

IR (λ / cm^{-1}): 3278 (N-H stretch), 2889 (C-H stretch), 1643 (C=O amide stretch), 1625 (C=O Fmoc stretch), 1544 (C=C aromatic stretch) 1467s, 1388s, 1342m, 1281s, 1240s, 1150m.

^{1}H NMR (500 MHz, DMSO-*d6*, ppm): 8.25-7.76 (m, 386H, Fmoc Ar-H), 4.51-3.79 (m, 90H, Fmoc) 3.52 (s, 452H, PEG-CH_2), 3.24 (s, 3H, PEG-CH_3), 1.72-1.37 (m, 528H, 85 x 3 x Lys aliphatic CH_2).

5.2.2.1 Kinetic Investigation of Lys(Fmoc)-NCA ROP

NCA ROP was performed *via* the methodology described in **Section 5.2.2** above. Reaction sampling was performed at several intervals across the duration of the reaction. Samples of the reaction mixture were taken at 0 hours, 3 and 6 hours, 24 hours and then at additional 24-hour intervals up until 96 hours. From this point, the reaction proceeded for an additional 72 hours before the final product was obtained. The removal of samples from the reaction mixture throughout this process limited the accuracy of yield calculations for the final product. Hence, yield data is not presented here.

IR (λ / cm^{-1}): IR (λ / cm^{-1}): 3278 (N-H stretch), 2889 (C-H stretch), 1643 (C=O amide stretch), 1625 (C=O Fmoc stretch), 1544 (C=C aromatic stretch) 1467s, 1388s, 1342m, 1281s, 1240s, 1150m.

^{1}H NMR (500 MHz, DMSO-*d6,* ppm): 7.88-7.29 (m, 380H, Fmoc aromatic protons), 4.51-3.79 (m, 147H, Ar-CH-CH_2 Fmoc aliphatic protons) 3.52 (s, 348H, PEG CH_2), 3.24 (s, 3H, PEG-CH_3), 1.72-1.37 (m, 261H, 60 x 3 x Lys CH_2 protons).

5.2.3 NCA ROP of Lys(Z)-NCA

DMAP-Catalysed Synthesis of mPEG-*b*-Plys(Z)

Lys(Z)-NCA (400 mg, 1.31 mmol) poly(ethylene glycol) methyl ether (M.W. 5000 g mol^{-1}, 65.29 mg, 0.013 mmol) and DMAP (15.95 mg, 0.13 mmol) were added to an oven-dried Schlenk tube, fitted with a suba-seal, and dried under vacuum (1 h). The solid mixture was then dissolved in anhydrous DMF (6 mL) and stirred under an atmosphere of $N_{2(g)}$ over the course of the reaction (168 h). Once the reaction had reached completion, indicated by the formation of a white and opalescent gel, the reaction mixture was precipitated by ice-cold diethyl ether (150 mL) and collected *via* centrifugation (see **Section 2.4**). The collected solid was then washed with ice-cold diethyl either (2 x 30 mL) and toluene (1 x 30 mL) and dried under vacuum overnight. The purified product was then collected as a dense off-white powder. Yield calculation was not performed here, as the product was not well-defined.

^{1}H NMR (500 MHz, DMSO-*d6*, ppm): 6.99-7.32 (m, 134H, Ar-H), 4.75-5.00 (m, 45H, Ar-CH-CH_2) 3.45 (s, 488H, PEG CH_2, αC-H), 3.15 (s, 3H, PEG-CH_3), 2.85 (s, 42H, Lys CH_2) 0.9-2.19 (m, 133H, 3x Lys CH_2 protons).

Amine-Initiated Synthesis of mPEG-*b*-PLys(Z) (BC115-118)

The following is a generalised methodology for the ROP of Lys(Z)-NCA from mPEG-NH_2 (1000g mol^{-1} and 5000 g mol^{-1}) . Mass and mole quantities, molar equivalents, and temperature conditions are described for all reactions (BC115-118) in **Table 5.1** below. All reactions were run over the course of 168 h and within 8 mL of anhydrous DMF solvent.

Lys(Z)-NCA (**Table 5.1**) and poly(ethylene glycol) methyl ether (**Table 5.1**) were added to an oven-dried Schlenk tube, fitted with a suba-seal, and dried under vacuum (1 h). The solid mixture was then dissolved in anhydrous DMF (8 mL) and stirred under an atmosphere of $N_{2(g)}$ over the course of the reaction (168 h). Following reaction completion, the reaction mixture was precipitated by ice-cold diethyl ether (3 x 15 mL) and collected *via* centrifugation (see **Section 2.4**). The collected solid was then washed with ice-cold diethyl either (2 x 15 mL) and toluene (2 x 15 mL) and dried under vacuum overnight. The purified product was then collected as an off-white powder. Yield calculations have been performed for these reactions following assessment *via* APC analysis, and are presented in **Section 5.3.2.**

Table 5.1: Reaction conditions for the syntheses of products BC115-118.

Reaction	Temp / °C	Reagent	Equiv.	Mass / mg	Moles / mmol
BC115	25	Lys(Z)-NCA	30	600.0	1.950
		mPEG-NH2 (1000 g mol^{-1})	1	65.3	0.066
BC116	60	Lys(Z)-NCA	30	600.0	1.950
		mPEG-NH2 (1000 g mol^{-1})	1	65.3	0.066
BC118	60	Lys(Z)-NCA	100	600	1.950
		mPEG-NH2 (5000 g mol^{-1})	1	19.6.0	0.020

5.2.3.1 Deprotection of mPEG-*b*-PLys(Z)

Deprotection was performed for BC115 and BC116 *via* the following generalised method. Quantities and preparative procedures were kept consistent between reactions. mPEG-*b*-PLys(Z) (250 mg) was dissolved in TFA (10 mL) under N_2 flow, prior to addition of HBr (33 wt% in AcOH, 2.2 mL, 30 mmol). The solution was stirred for 24 hours before concentration *in vacuo* and precipitation in diethyl ether. The products were subjected to multiple ether washes until the red colouration of the HBr reagent had been removed. The crude product was then dissolved in a minimal quantity of deionised water and submitted for dialysis under agitation for three days, with water changes every 24 hours. The purified product was then collected *via* lyophilisation. Yield calculations have been performed using APC-derived M_n values for polymers BC115 and BC116, in comparison to the maximum theoretical yield. ^1H NMR data was not collected for these products due to oversaturation of the spectrum by the water peak at 3.3 ppm.

BC115

Yield: 112.1 mg, 72 %

BC116

Yield: 121.8 mg, 75 %

5.2.4 Initial NCA ROP of Lys(Boc)-NCA

A generalised preparative methodology is here presented for initial ROP reactions of Lys(Boc)-NCA from mPEG-NH_2 (5000 g mol^{-1}). Reaction quantities, conditions and product yields (as calculated from expected M.W. values – further discussed in **Section 5.3.3**) are presented in **Table 5.2** below.

Lys(Boc)-NCA (**Table 5.2**) was added to an oven-dried Schlenk tube, fitted with a suba-seal, and dried under vacuum (1 h) before dissolution in a 5:1 mixture of anhydrous DCM/DMF (**Table 5.2**). Separately, mPEG-NH_2 (**Table 5.2**) was then dissolved in anhydrous DCM/DMF (**Table 5.2**), and added in one aliquot to the NCA in solution.

The reaction mixture was stirred under N_2 atmosphere at room temperature for 24h before the reaction mixture was precipitated by ice-cold diethyl ether (15 mL) and collected *via* centrifugation (see **Section 2.4**). The collected solid was then washed with ice-cold diethyl either (2 x 30 mL) and dried under vacuum overnight. The purified product was then collected as a dense off-white powder.

Table 5.2: Reagent quantities, reaction conditions and estimated percentage yield values for the syntheses of 5 mPEG-*b*-PLys(Boc) copolymers.

Experiment Title	mPEG-NH_2 (5000 g mol^{-1})		Lys(Boc)-NCA		Solvent	Product	
	Mass / g	Moles / mmol	Mass / g	Moles / mmol	Vol / mL	Mass / g	Yield* / %
BC183 - mPEG-b-PLys(Boc)$_{10}$	1.82	0.37	0.99	3.68	22	1.88	69
BC191 - mPEG-b-PLys(Boc)$_{10}$	0.91	0.18	0.50	1.82	17	0.91	68
BC180 - mPEG-b-PLys(Boc)$_{20}$	0.75	0.15	0.80	2.94	17	1.05	71
BC184 - mPEG-b-PLys(Boc)$_{50}$	0.29	0.059	0.80	2.94	17	0.82	81
BC181 - mPEG-b-PLys(Boc)$_{100}$	0.15	0.030	0.82	3.00	17	0.66	75

BC183/191 - mPEG-*b*-PLys(Boc)$_{10}$

^{1}H NMR (500 MHz, DMSO-*d6*, ppm): 3.7 – 4.5 (m, 8H, αC-H), 3.47 – 3.57 (m, 452H, PEG CH_2-CH_2) 3.24 (s, 3H, PEG-CH_3), 2.80 – 2.95 (m, 37H, Lys CH_2) 1.14 – 1.99 (m, 152H, Boc $C(CH_3)_3$ + Lys CH_2-CH_2-CH_2).

BC180 - mPEG-*b*-PLys(Boc)$_{20}$

^{1}H NMR (500 MHz, DMSO-*d6*, ppm): 3.7 – 4.5 (m, 19H, αC-H), 3.47 – 3.57 (m, 447H, PEG CH_2-CH_2) 3.24 (s, 3H, PEG-CH_3), 2.80 – 2.95 (m, 41H, Lys CH_2) 1.14 – 1.99 (m, 292H, Boc $C(CH_3)_3$ + Lys CH_2-CH_2-CH_2).

BC184 - mPEG-*b*-PLys(Boc)$_{50}$

^{1}H NMR (500 MHz, DMSO-*d6*, ppm): 3.7 – 4.5 (m, 51H, αC-H), 3.47 – 3.57 (m, 452H, PEG CH_2-CH_2) 3.24 (s, 3H, PEG-CH_3), 2.80 – 2.95 (m, 37H, Lys CH_2) 1.14 – 1.99 (m, 740H, Boc $C(CH_3)_3$ + Lys CH_2-CH_2-CH_2).

BC181 - mPEG-*b*-PLys(Boc)$_{100}$

^{1}H NMR (500 MHz, DMSO-*d6*, ppm): 3.7 – 4.5 (m, 80H, αC-H), 3.47 – 3.57 (m, 452H, PEG CH_2-CH_2) 3.24 (s, 3H, PEG-CH_3), 2.80 – 2.95 (m, 184H, Lys CH_2) 1.14 – 1.99 (m, 1393H, Boc $C(CH_3)_3$ + Lys CH_2-CH_2-CH_2).

5.2.4.1 Deprotection of Initial mPEG-*b*-PLys(Boc) Copolymers

Products of Lys(Boc)-NCA ROP were synthesised, collected and purified as per the preparative procedures specified above. For each of these products, the following generalised method describes how Boc-deprotection was performed, and how the subsequent mPEG-*b*-PLys[NH_2.TFA] salts were obtained and purified.

mPEG-*b*-PLys(Boc) (**Section 5.2.4**) was added to a round-bottom flask, and dissolved in a 1:1 mixture of DCM/TFA (5 mL). The reaction mixture was stirred for 1 h at room temperature in air, to allow for the escape of eliminated gaseous by-products. The products was then precipitated in ice-cold diethyl ether (15 mL) and collected by centrifugation (**Section 2.4**).
The product was then dried *in vacuo* overnight to remove excess ether, whereupon it was dissolved in deinonised water and dialysed (2000 g mol^{-1} M.W.C.O) for three days, before re-collection *via* freezing and lyophilisation. Raw ^{1}H NMR data for both the Boc-protected and unprotected products can be found in **Section A.5.1**.

BC190 - mPEG-b-PLys[NH_2.TFA]$_{10}$

Yield: 1.22 g, 65 %

^{1}H NMR (500 MHz, DMSO-*d6*, ppm): 3.8 – 4.3 (m, 9H, αC-H), 3.60 – 3.65 (m, 488H, PEG CH_2-CH_2) 3.24 (s, 3H, PEG-CH_3), 2.80 – 2.95 (m, 19H, Lys CH_2) 1.14 – 1.99 (m, 58H, Boc $C(CH_3)_3$ + Lys CH_2-CH_2-CH_2).

BC187 - mPEG-b-PLys[NH_2.TFA]$_{20}$

Yield: 0.63 g, 60 %

^{1}H NMR (500 MHz, DMSO-*d6*, ppm): 3.8 – 4.3 (m, 18H, αC-H), 3.60 – 3.65 (m, 452H, PEG CH_2-CH_2) 3.24 (s, 3H, PEG-CH_3), 2.80 – 2.95 (m, 40H, Lys CH_2) 1.14 – 1.99 (m, 117H, Boc $C(CH_3)_3$ + Lys CH_2-CH_2-CH_2).

BC193 - mPEG-b-PLys[NH_2.TFA]$_{50}$

Yield: 0.63 g, 59 %

^{1}H NMR (500 MHz, DMSO-*d6*, ppm): 3.8 – 4.3 (m, 46H, αC-H), 3.60 – 3.65 (m, 452H, PEG CH_2-CH_2) 3.24 (s, 3H, PEG-CH_3), 2.80 – 2.95 (m, 96H, Lys CH_2) 1.14 – 1.99 (m, 283H, Boc C(CH_3)$_3$ + Lys CH_2-CH_2-CH_2).

BC188 - mPEG-b-PLys[NH_2.TFA]$_{100}$

Yield: 0.40 g, 61 %

^{1}H NMR (500 MHz, DMSO-*d6*, ppm): 3.8 – 4.3 (m, 91H, αC-H), 3.60 – 3.65 (m, 488H, PEG CH_2-CH_2) 3.24 (s, 3H, PEG-CH_3), 2.80 – 2.95 (m, 182H, Lys CH_2) 1.14 – 1.99 (m, 570H, Boc C(CH_3)$_3$ + Lys CH_2-CH_2-CH_2).

5.2.5 *in-situ* FTIR monitored Syntheses of mPEG-*b*-Lys(Boc)

A generalised preparative methodology is here presented for ROP reactions of Lys(Boc)-NCA from mPEG-NH_2 (5000 g mol^{-1} and 10,000 g mol^{-1}), monitored *in-situ* using a Bruker IN350T diamond ATR FTIR probe, as detailed in **Section 2.3.1**. Reagent quantities, reaction conditions and product mass and estimated percentage yields are presented in **Table 5.3** below.

In a 2-neck RB flask, fitted with a N_2 inlet arm and FTIR probe, Lys(Boc)-NCA (**Table 5.3**) was dissolved in anhydrous DMF (**Table 5.3**). As the probe was equilibrated to the absorbance peak at 1746 cm^{-1}, in order to set a baseline for T_0, mPEG-NH_2 (5000 g mol^{-1}) was dissolved in anhydrous DMF (**Table 5.3**), before addition to the stirring NCA solution as one aliquot. Once the FTIR probe had accounted for the increased dilution of the NCA, decreasing peak area at 1746 cm^{-1} was monitored until no change was observed, at which time reaction completion was achieved (16 - 36 hours). At this point, excess DMF was removed *in vacuo*, and the product was precipitated and triturated in *tert*-butyl methyl ether (TBME). The product was then collected *via* filtration and allowed to dry on the filter pad under a flow of N_2 (ca. 15 min). SEC-TDA analysis for these products is provided and discussed in **Section 5.3.4.** ^{1}H NMR spectra for these products are not here reported, due to the lack of purification in their workup procedures. Raw ^{1}H NMR data is presented in **Section A.5.1**.

Table 5.3: Reagent quantities, reaction conditions and estimated percentage yield values for the syntheses of mPEG-*b*-PLys(Boc) copolymers BC195-BC199.

Experiment Title	mPEG-NH_2			Lys(Boc)-NCA			Solvent	Product	
	Mass / mg	Moles / mmol	Conc. / mol dm^{-3}	Mass / mg	Moles / mmol	Conc. / mol dm^{-3}	Vol / mL	Mass / mg	Yield* / %
BC195 – $mPEG_{113}$-b-$PLys(Boc)_5$	450	0.090	0.008	123	0.45	0.0375	12	490	88
BC196 - $mPEG_{113}$-b-$PLys(Boc)_{10}$	420	0.084	0.012	229	0.84	0.120	7	477	83
BC197 - $mPEG_{113}$-b-$PLys(Boc)_{20}$	315	0.063	0.009	343	1.26	0.180	7	496	90
BC198 - $mPEG_{113}$-b-$PLys(Boc)_{50}$	200	0.040	0.005	545	2.00	0.250	8	481	84
BC199 – $mPEG_{226}$-b-$PLys(Boc)_5$	480	0.048	0.008	65	0.24	0.040	6	461	88
BC200 - $mPEG_{226}$-b-$PLys(Boc)_{10}$	480	0.048	0.008	131	0.48	0.080	6	504	88
BC201 - $mPEG_{226}$-b-$PLys(Boc)_{20}$	420	0.042	0.007	229	0.84	0.140	6	476	82
BC202 - $mPEG_{226}$-b-$PLys(Boc)_{50}$	360	0.036	0.006	490	1.80	0.30	6	444	86

5.2.5.1 Deprotection of *in-situ* FTIR-monitored mPEG-*b*-Lys(Boc) Products

mPEG-*b*-PLys(Boc) (**Section 5.2.5**) was added to a round-bottom flask, and dissolved in a 1:1 mixture of DCM/TFA (5 mL). The reaction mixture was stirred for 1 h at room temperature in air, to allow for the escape of eliminated gaseous by-products. The products was then precipitated in ice-cold diethyl ether (15 mL) and collected by centrifugation (**Section 2.8**). The product was then dried *in vacuo* overnight to remove excess ether, whereupon it was dissolved in deinonised water and dialysed (2000 g mol^{-1} M.W.C.O) for three days, before re-collection *via* freezing and lyophilisation.

BC195D - mPEG-b-PLys[NH_2.TFA]$_5$

^{1}H NMR (500 MHz, DMSO-*d6*, ppm): 4.0 – 4.4 (m, 5H, αC-H), 3.47 – 3.57 (m, 452H, PEG CH_2-CH_2) 3.24 (s, 3H, PEG-CH_3), 2.80 – 2.95 (m, 10H, Lys CH_2) 1.14 – 1.99 (m, 30H, Boc $C(CH_3)_3$ + Lys CH_2-CH_2-CH_2).

BC196D - mPEG-b-PLys[NH_2.TFA]$_{10}$

^{1}H NMR (500 MHz, DMSO-*d6*, ppm): 4.0 – 4.4 (m, 9H, αC-H), 3.47 – 3.57 (m, 452H, PEG CH_2-CH_2) 3.24 (s, 3H, PEG-CH_3), 2.80 – 2.95 (m, 20H, Lys CH_2) 1.14 – 1.99 (m, 57H, Boc $C(CH_3)_3$ + Lys CH_2-CH_2-CH_2).

BC197D - mPEG-b-PLys[NH_2.TFA]$_{20}$

^{1}H NMR (500 MHz, DMSO-*d6*, ppm): 4.0 – 4.4 (m, 21H, αC-H), 3.47 – 3.57 (m, 452H, PEG CH_2-CH_2) 3.24 (s, 3H, PEG-CH_3), 2.80 – 2.95 (m, 43H, Lys CH_2) 1.14 – 1.99 (m, 128H, Boc $C(CH_3)_3$ + Lys CH_2-CH_2-CH_2).

BC198D - mPEG-b-PLys[NH_2.TFA]$_{50}$

^{1}H NMR (500 MHz, DMSO-*d6*, ppm): 4.0 – 4.4 (m, 49H, αC-H), 3.47 – 3.57 (m, 452H, PEG CH_2-CH_2) 3.24 (s, 3H, PEG-CH_3), 2.80 – 2.95 (m, 101H, Lys CH_2) 1.14 – 1.99 (m, 310H, Boc $C(CH_3)_3$ + Lys CH_2-CH_2-CH_2).

5.2.6 Lys(Boc)-NCA ROP Reaction Optimisation

5.2.6.1 Investigating THF-Solvated Lys(Boc)-NCA ROP

The preparative methodology for the THF-solvated ROP of Lys(Boc)-NCA from mPEG-NH_2 (5000 g mol^{-1}) is reported here. Reaction quantities, conditions and product mass and estimated percentage yields are presented in **Table 5.4** below.

To an oven-dried reaction tube, fitted with a screw-top N_2 inlet system and placed in a modular temperature reactor at 25 °C. Lys(Boc)-NCA (**Table 5.4**), dissolved in anhydrous THF (0.4 mL) was added in one aliquot. The system was allowed to equilibrate, and any changes to solubility or viscosity were recorded. Once equilibrated, mPEG-NH_2 (**Table 5.4**), also dissolved in anhydrous THF (0.4 mL), was added in one aliquot. Solubility and viscosity were once again checked before the solution was left to stir for 24 hr. Following reaction, the crude solution was obtained and excess THF was removed, and the remaining film layer was triturated with ice-cold TBME before vacuum filtration. The product was left to dry under N_2 flow on the filter pad (ca. 15 min) before collection. All samples were collected as white, flakey solids.

Table 5.4: Reagent quantities, reaction conditions and estimated percentage yield values for the syntheses of mPEG-*b*-PLys(Boc) copolymers BC212 and BC213.

Experiment Title	mPEG-NH_2		Lys(Boc)-NCA		Solvent
	Mass / mg	Moles / mmol	Mass / mg	Moles / mmol	Vol / mL
BC212 – mPEG$_{113}$-b-PLys(Boc)$_5$	60	0.012	32.7	0.12	0.8
BC213 - mPEG$_{113}$-b-PLys(Boc)$_{10}$	60	0.012	16.3	0.06	0.8

To allow aqueous-phase SEC-TDA analysis to take place, samples underwent Boc-deprotection before analysis. The method for this process is recorded in **Section 5.2.4.1**. Procedural details for aqueous SEC-TDA analysis are provided in **Section 2.6**.

BC212 – mPEG-b-PLys(Boc)$_5$ (THF)

Yield: 69 mg, 93 %

BC212D – mPEG-b-PLys[NH_2.TFA]$_5$

Yield: 66 mg, 89 %

BC213 – mPEG-b-PLys(Boc)$_{10}$ (THF)

Yield: 83 mg, 93 %

BC213D – mPEG-b-PLys[NH_2.TFA]$_{10}$

Yield: 81 mg, 91 %

5.2.6.2 Investigating Reduced-Temperature Lys(Boc)-NCA ROP

Reactions at Small Scale (ca. 100 mg) for Analysis

The preparative methodology for the reduced-temperature ROP of Lys(Boc)-NCA from mPEG-NH_2 (5000 g mol^{-1}) is reported here. For each reaction, reagent quantities and solvent volume remain the same. Only temperature is varied, as is specified in the ^{1}H NMR characterisation below.

To an oven-dried reaction tube, fitted with a screw-top N_2 inlet system and placed in a modular temperature reactor at a pre-defined temperature. Lys(Boc)-NCA (32.7 mg, 0.12 mmol), dissolved in anhydrous DMF (0.8 mL) was added in one aliquot. The system was allowed to equilibrate, and any changes to solubility or viscosity were recorded. Once equilibrated, mPEG-NH_2 (60 mg, 0.012 mmol), also dissolved in anhydrous DMF (0.8 mL), was added in one aliquot. Once the combined reaction mixture had equilibrated to the target temperature, solubility and viscosity were once again checked before the solution was left to stir for 24 hr. Following reaction, the crude solution was obtained and excess DMF was removed, and the remaining film layer was triturated with ice-cold TBME before vacuum filtration. The product was left to dry under N_2 flow on the filter pad (ca. 15 min) before collection. All samples were collected as white, flakey solids.

To allow aqueous-phase SEC-TDA analysis to take place, samples underwent Boc-deprotection before analysis. The method for this process is recorded in **Section 5.2.4.1**. Procedural details for aqueous SEC-TDA analysis are provided in **Section 2.6**.

BC210 – mPEG-b-PLys(Boc)$_{10}$ (10 °C)

Yield: 66.8 mg, 75 %

^{1}H NMR (500 MHz, DMSO-*d6*, ppm): 3.7 – 4.5 (m, 10H, αC-H), 3.47 – 3.57 (m, 452H, PEG CH_2-CH_2) 3.24 (s, 3H, PEG-CH_3), 2.80 – 2.95 (m, 21H, Lys CH_2) 1.14 – 1.99 (m, 150H, Boc $C(CH_3)_3$ + Lys CH_2-CH_2-CH_2).

BC210D – mPEG-b-PLys[NH_2.TFA]$_{10}$

Yield: 60.0 mg, 90 %

^{1}H NMR (500 MHz, DMSO-*d6*, ppm): 3.7 – 4.5 (m, 5H, αC-H), 3.47 – 3.57 (m, 452H, PEG CH_2-CH_2) 3.24 (s, 3H, PEG-CH_3), 2.80 – 2.95 (m, 10H, Lys CH_2) 1.14 – 1.99 (m, 75H, Boc C(CH_3)$_3$ + Lys CH_2-CH_2-CH_2).

BC211 – mPEG-b-PLys(Boc)$_{10}$ (20 °C)

Yield: 72.1 mg, 81 %

^{1}H NMR (500 MHz, DMSO-*d6*, ppm): 3.7 – 4.5 (m, 12H, αC-H), 3.47 – 3.57 (m, 452H, PEG CH_2-CH_2) 3.24 (s, 3H, PEG-CH_3), 2.80 – 2.95 (m, 24H, Lys CH_2) 1.14 – 1.99 (m, 172H, Boc C(CH_3)$_3$ + Lys CH_2-CH_2-CH_2).

BC211D – mPEG-b-PLys[NH_2.TFA]$_{10}$

Yield: 60.6 mg, 91 %

^{1}H NMR (500 MHz, DMSO-*d6*, ppm): 3.7 – 4.5 (m, 8H, αC-H), 3.47 – 3.57 (m, 452H, PEG CH_2-CH_2) 3.24 (s, 3H, PEG-CH_3), 2.80 – 2.95 (m, 15H, Lys CH_2) 1.14 – 1.99 (m, 43H, Boc C(CH_3)$_3$ + Lys CH_2-CH_2-CH_2).

BC196D – mPEG-b-PLys[NH_2.TFA]$_{10}$

Yield: 370 mg, 93 %

^{1}H NMR (500 MHz, DMSO-*d6*, ppm): 3.7 – 4.5 (m, 9H, αC-H), 3.47 – 3.57 (m, 452H, PEG CH_2-CH_2) 3.24 (s, 3H, PEG-CH_3), 2.80 – 2.95 (m, 18H, Lys CH_2) 1.14 – 1.99 (m, 55H, Boc C(CH_3)$_3$ + Lys CH_2-CH_2-CH_2).

Reactions at Increased Scale (ca. 700 mg) for Multistep Synthesis

Two block copolymers have here been targeted, mPEG-*b*-PLys(Boc)$_{10}$ (**BC219**) and mPEG-*b*-PLys(Boc)$_{20}$ (**BC220**). The preparative procedures for each reaction is provided below, with a combined workup procedure outlined below.

BC219

To an oven-dried reaction tube, fitted with a screw-top N_2 inlet system and placed in a modular temperature reactor at a pre-defined temperature. Lys(Boc)-NCA (218 mg, 0.80 mmol), dissolved in anhydrous DMF (3.5 mL) was added in one aliquot. The system was allowed to equilibrate, and any changes to solubility or viscosity were recorded. Once equilibrated, mPEG-NH_2 (400 mg, 0.080 mmol), also dissolved in anhydrous DMF (3.5 mL), was added in one aliquot.

BC220

To an oven-dried reaction tube, fitted with a screw-top N_2 inlet system and placed in a modular temperature reactor at a pre-defined temperature. Lys(Boc)-NCA (229 mg, 1.2 mmol), dissolved in anhydrous DMF (3.5 mL) was added in one aliquot. The system was allowed to equilibrate, and any changes to solubility or viscosity were recorded. Once equilibrated, mPEG-NH_2 (300 mg, 0.060 mmol), also dissolved in anhydrous DMF (3.5 mL), was added in one aliquot.

Once the combined reaction mixture had equilibrated to the target temperature, solubility and viscosity were once again checked before the solution was left to stir for 24 hr. Following reaction, the crude solution was obtained and excess DMF was removed, and the remaining film layer was triturated with ice-cold TBME before vacuum filtration. The product was left to dry under N_2 flow on the filter pad (ca. 15 min) before collection. All samples were collected as white, flakey solids. To allow aqueous-phase SEC-TDA analysis to take place, samples underwent Boc-deprotection before analysis. The method for this process is recorded in **Section 5.2.4.1**. Procedural details for aqueous SEC-TDA analysis are provided in **Section 2.6**. Raw ^{1}H NMR data for each of the Boc-protected and unprotected products can be found in **Section A.5.1**.

5.3 Results and Discussion

5.3.1 NCA ROP of Lys(Fmoc)-NCA

In order to investigate the effects of polymer branching on the encapsulation of drug molecules, initial syntheses of protected polylysine-containing block copolymers were conducted. The PEG-*b*-PLys(Fmoc) produced here is a novel combination copolymer block constituents and, as such, care was taken during reaction to make note of any differences between this synthesis and those of previous copolymers produced for this report. PEG-*b*-PLys(Fmoc)$_{60}$ was synthesised via ROP, initiated by mPEG (M_w 5000 g mol^{-1}) and catalysed by DMAP under ambient conditions for 7 days. For this reaction, a [M]:[I] ratio of 100:1 was used, with the intention of producing a hydrophobic block with a similar number of repeat units to that of the initiator, which averaged 113 PEG repeat units. After reaction for 96 hours, however, it was observed that the reaction mixture had visually changed from a clear, slightly yellow solution to an off-white opalescent suspension, with gel-like consistency. ^{1}H NMR was used to elucidate the cause of this change and is shown in **Figure 5.1** below. It should be noted that, at this point, analytical equipment capable of size-exclusion chromatography was not available.

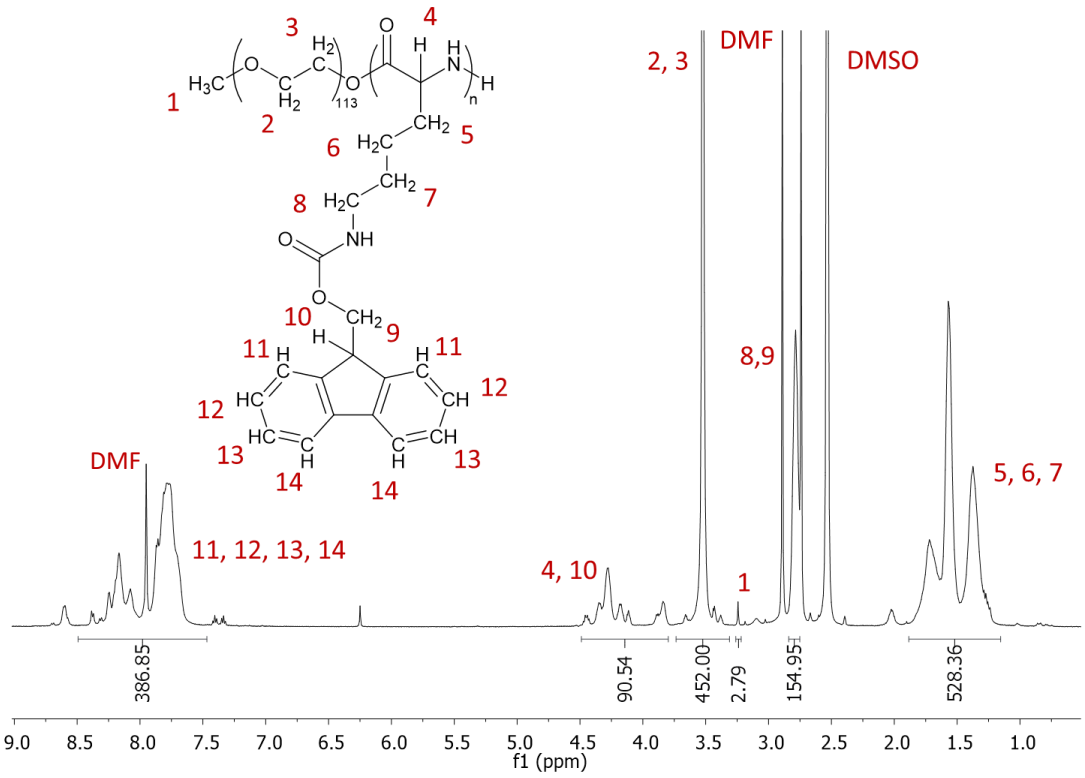

Figure 5.1: ^{1}H NMR (500 MHz, DMSO-d_6) spectrum of mPEG-*b*-PLys(Fmoc).

From **Figure 5.1**, peaks can be identified that represent the terminal methyl protons of the PEG chain (**1**) as well as the PEG ethyl proton environments (**2, 3**). On the PLys(Fmoc) block, environments of the α-proton position (**4**), the aliphatic protons of the lysine side chain (**5-7**), the ethyl protons of the Fmoc protecting group (**9, 10**) and the aromatic Fmoc ring protons (**11-14**) are also present. Importantly, it was noticed that there was an incongruence between the relative integrals of the latter three proton environments, which was investigated further by normalising the integral values to that of the methyl end-cap of the PEG chain. The normalised integral values are displayed in **Table 5.5** below.

Table 5.5: Comparison of the calculated numbers of repeat units from integrals of characteristic peak ranges found in **Figure 7**, highlighting the disparity in degree of polymerisation suggested by each.

Proton Environment	Peak Range / ppm	Integral Value	Scaling Factor	Estimated Repeat Units
Fmoc Aromatic C-H	7.76 – 8.25	386.9	$x/8$	48
Fmoc Aliphatic C-H	3.24 – 4.46	90.5	$x/2$	45
Lysine Aliphatic C-H	1.37 – 1.72	528.4	$x/6$	88

This data, in conjunction with the observed gelation of the product at 96 h, suggests that there may have been some unexpected deprotection of the Fmoc group from the PLys(Fmoc) chain, leading to a reduction in the corresponding Fmoc C-H integral values, and subsequent underestimation of the number of repeat units from these integration ranges. Further investigation was needed to understand this disparity, as well as to identify the cause of gelation. This prompted a kinetic study to be undertaken.

5.3.1.1 Kinetic Investigation of Lys(Fmoc)-NCA ROP

During kinetic analysis, samples were purified in accordance with the procedure outlined in **Section 5.2.2**, with thorough washing by both diethyl ether and toluene to obtain a dense white powder. The ^{1}H NMR spectra of these samples were evaluated for the relative integrals of characteristic lysine and Fmoc group proton environments, after which the normalised values of these integrals were used to estimate the degree of polymerisation at each time interval. The stacked spectra of five of these samples is provided in **Figure 5.2** below.

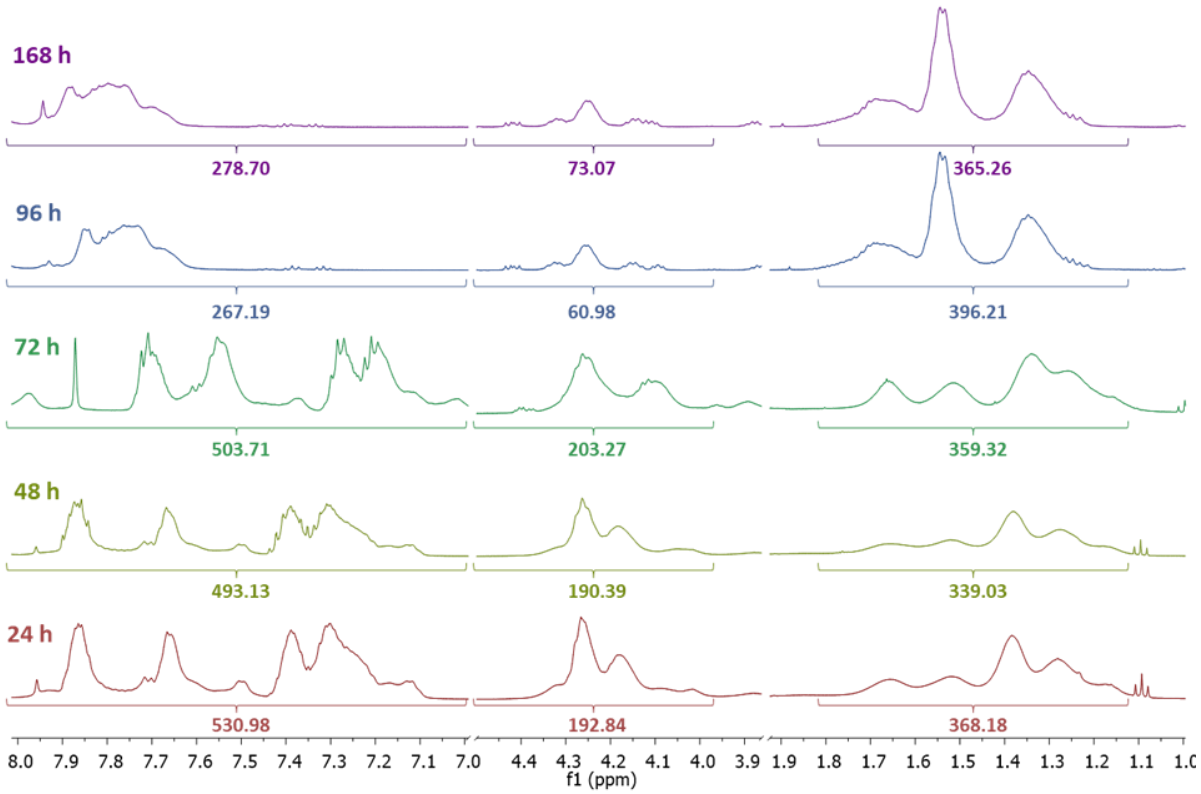

Figure 5.2: Stacked ^{1}H NMR spectra (500 MHz, DMSO-d_6) of mPEG-*b*-PLys(Fmoc) samples during kinetic evaluation of NCA ROP. Characteristic peak ranges have been highlighted and integrals (normalised to methoxy terminus of mPEG) have been provided for scale.

Immediately from **Figure 5.2**, two major observations can be drawn. Initially, it can clearly be seen that large integral values for the characteristic proton environments of the polymer are apparent as early as 24 hours into reaction. This changes the perspective on the ROP of lysine significantly, as it may suggests that polymerisation can be attempted over a matter of hours, rather than days.

Furthermore, a significant decrease in the integrals representing characteristic proton environments of the Fmoc group can be seen to be decreasing at the 96-hour mark. This data has been more clearly illustrated in **Figure 5.3**.

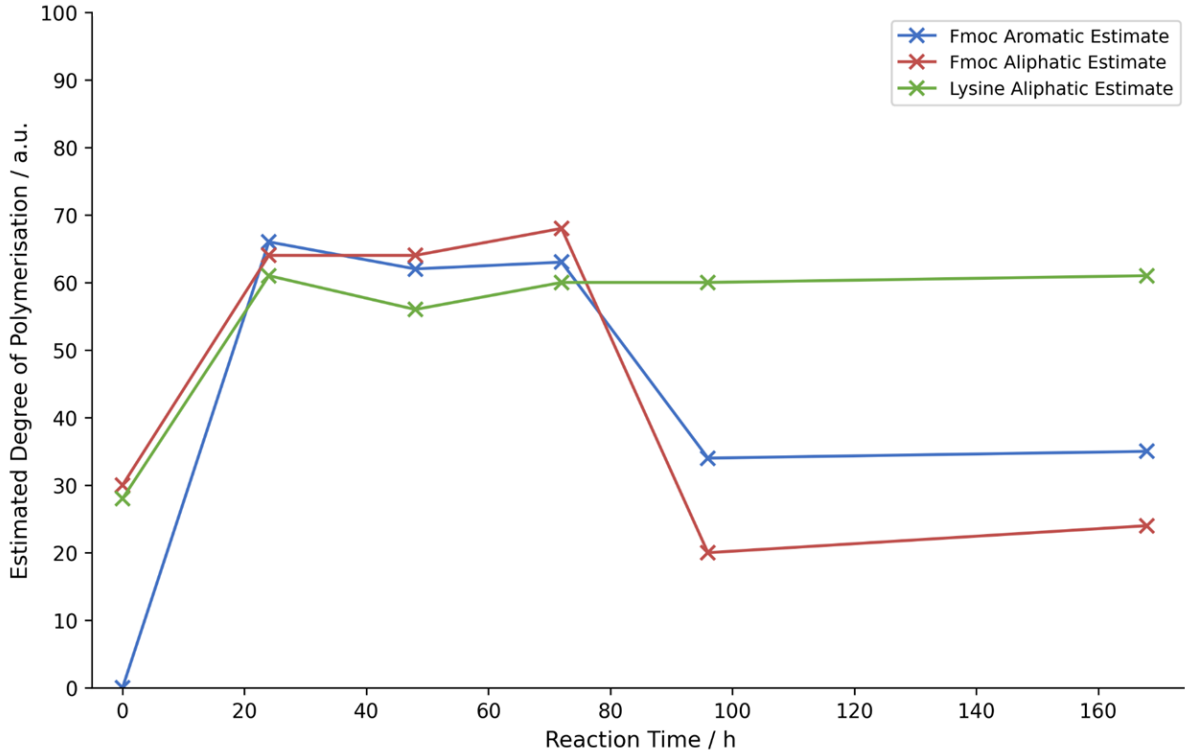

Figure 5.3: Comparative kinetic plots of integrals shown in Figure 8, highlighting discrepancies between values corresponding to Fmoc protons vs. lysine protons, suggestive of *in situ* deprotection.

These data strongly align with the hypothesis made previously, that errant side reaction of the polymer side chains during this reaction may have led to the deprotection of some of the Fmoc groups upon the PLys(Fmoc) chain. The β-proton of the upon the Fmoc protecting groups is highly acidic, owing to the significant resonance stabilisation it is afforded by the aromatic dual-ring system.[13] As such, even a mildly basic interaction can abstract the proton, leaving the resulting carbanion to undergo an internal beta-elimination reaction, resulting in the loss of a CO_2 molecule. The resulting dibenzofulvene (DBF) molecule that remains is then free to undergo further reaction with base present in the system to form a DBF-base adduct.

It should be noted here that, due to the presence of basic DMAP, the required conditions for this reaction are already met within the conditions of the ROP reaction, including the presence of active free-amine chain ends that will likely be sufficiently basic to undergo proton abstraction from the Fmoc protecting groups, as well as the presence of sufficient nitrogen flow, to remove the eliminated CO_2 from the reaction mixture. As a result, it may be possible that Fmoc deprotection is occurring frequently during the later stages of reaction as the concentration of free NCA in solution decreases, thus allowing the active chain end to more frequently encounter the Fmoc groups of other polymer chains. Using isopropyl amine (pK_a 10.63) as an analogue to the active chain end, it is reasonable to expect that it would be capable of abstracting a proton from an Fmoc protecting group, as other Fmoc deprotecting species typically have a pK_a of 9 to 11.[14,15] Partially as a result of this investigation, and in interest of finding other routes to unprotected PLys blocks within future polymer products, the ROP of Lys(Fmoc)-NCA was halted at this time.

5.3.2 NCA ROP of Lys(Z)-NCA

The complications presented during Lys(Fmoc)-NCA ROP under basic conditions prompted the research to explore Lys(Z)-NCA as an alternative monomer choice. The benzyloxy carbonyl group (Z) is resistant to nucleophilic addition/elimination reactions such as hydrolysis, under both acidic and basic conditions. Instead, the (Z) group is sensitive to hydrogenation or strong acid deprotection with HBr/AcOH, requiring harsh reaction conditions for deprotection to take place. This robustness to changing conditions during ROP prompted further investigation, which is reported here. Before exploring the successful attempts at Lys(Z)-NCA polymerisation within this section, it is first pertinent to discuss issues that arose in the optimisation of the ROP methodology.Initial ROP reactions of Lys(Z)-NCA were initiated by mPEG (M_w 5000 g mol^{-1}), meaning that, similar to the case for Man-OCA ROP, the reaction required a DMAP catalyst to compensate for the low rate of initiation. DOSY NMR analysis was performed for one of the Lys(Z)-NCA ROP attempts, to evaluate the effect of DMAP catalysis on the composition of the product chains. This data is presented alongside the ^{1}H NMR spectrum of the polymer product, in **Figures 5.4a** and **5.4b** below.

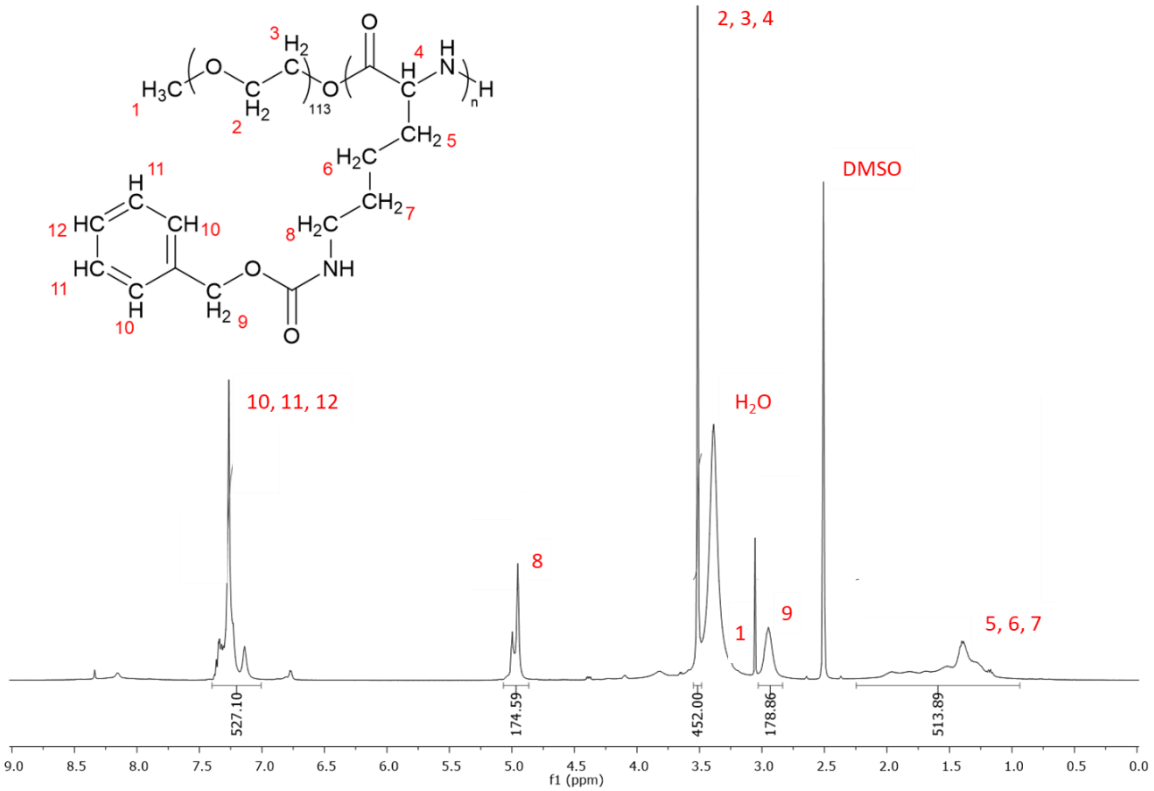

Figure 5.4a: ^{1}H NMR spectrum (500 MHz, DMSO-d_6) of mPEG-*b*-Lys(Z) product.

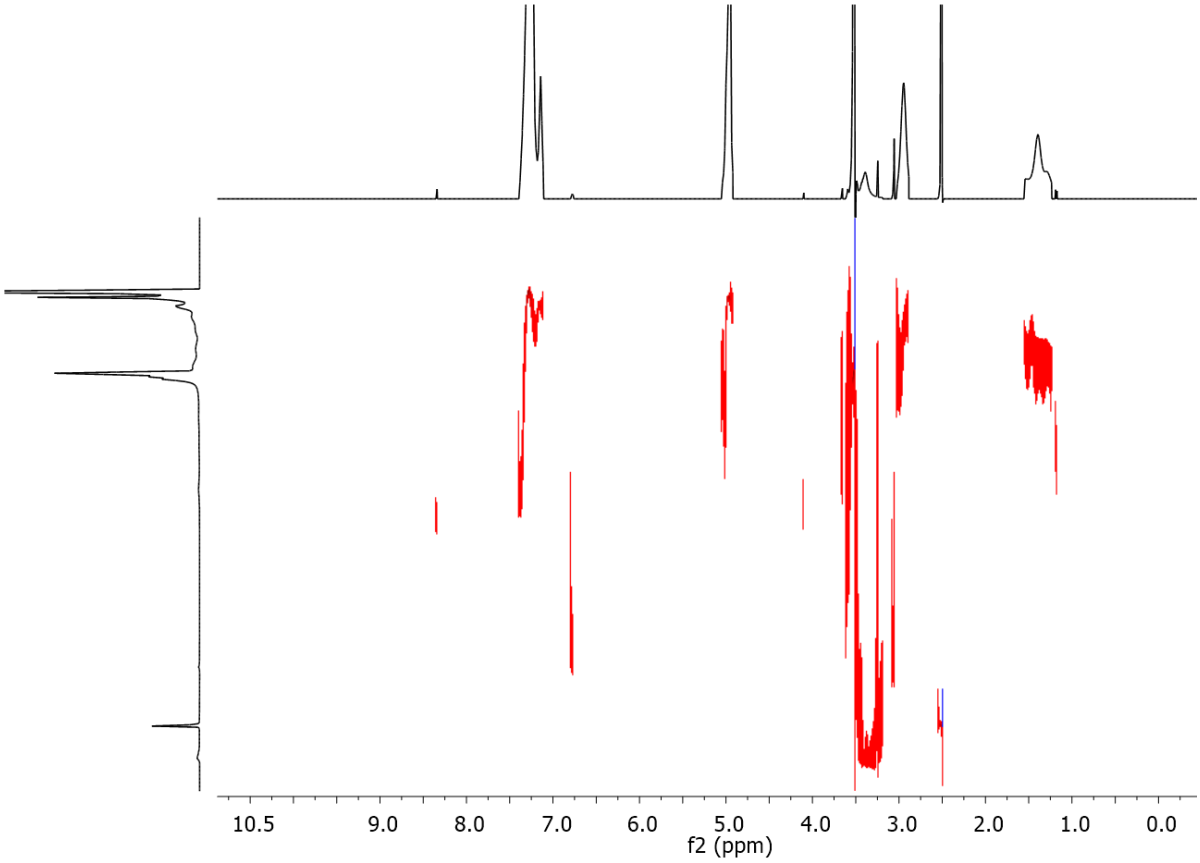

Figure 5.4b: DOSY spectrum (500 MHz, DMSO-d_6) of mPEG-*b*-Lys(Z) product.

The ^{1}H NMR spectrum shown in **Figure 10a** suggests that a successful reaction has taken place, with agreement between characteristic integral regions suggesting a degree of polymerisation of ca. 90. However, the spread of the environments across the differing rates of diffusion in **Figure 5.4b** suggest that not all these proton environments belong to one well-defined polymer, but rather a spread of products, as well as a considerable quantity of unreacted mPEG (5000 g mol^{-1}) as is evidenced by the significant diffusion drift for signals around 3.5 ppm. For this reason, further analysis was performed using MALDI-TOF spectrometry, to better identify the masses of the materials present. This spectrum can be seen in **Figure 5.5** below.

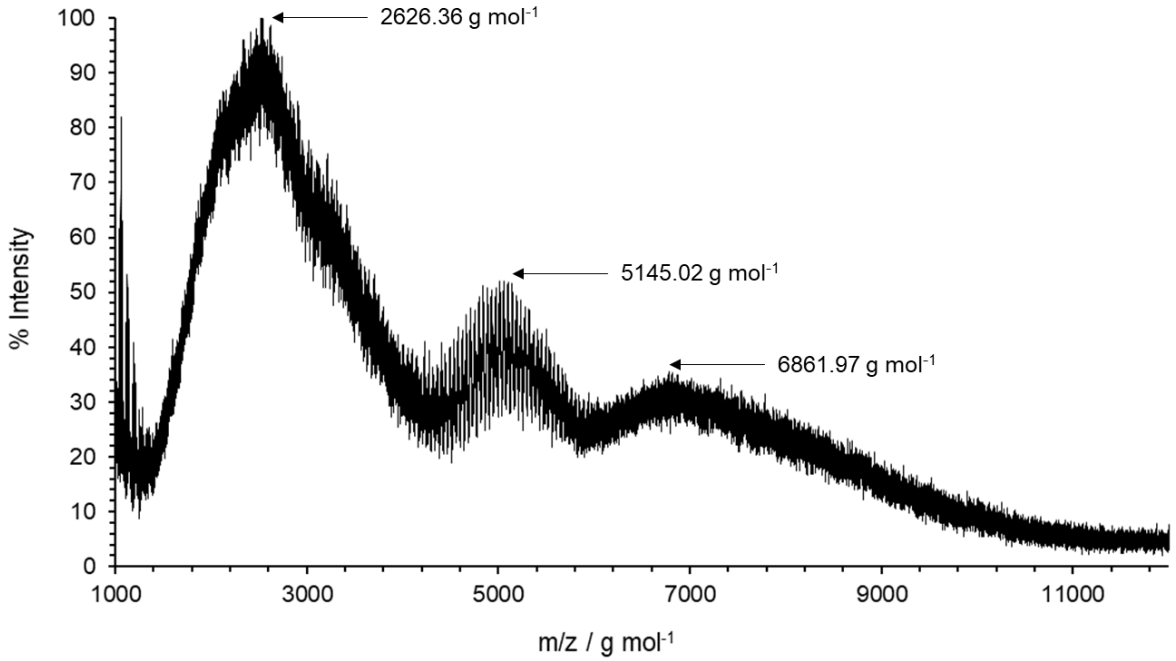

Figure 5.5: MALDI-TOF spectrum of mPEG-*b*-PLys(Z) product.

Using the peaks in **Figure 5.5**, it is possible to elucidate details about the reaction process that led to this mix of products, which will further inform necessary changes to the reaction setup to ensure a more controlled polymerisation. The first observation that can be made is that, despite the addition of the DMAP catalyst to the system, a significant quantity of the mPEG was unable to initiate reaction with its weakly nucleophilic hydroxyl terminus. This is evidenced by the large distribution around 5000 g mol^{-1}, attributable to the macroinitiator by the clearly defined peaks within.

As this polymer was sourced from an external supplier it has a high purity, with each of the peaks separated by ca. 40 g mol^{-1} (PEG repeat unit M_w = 44.05 g mol^{-1}). A further observation to be made is that there are two macromolecules separate from the initiator. While the peak at ca. 6800 g mol^{-1} is suggestive of a successful block copolymerisation, the larger distribution at 2626 g mol^{-1} could not belong to the intended copolymer. It instead implies that unintended homopolymerisation of Lys(Z)-NCA has here occurred, initiated by some other source. It is possible that DMAP could have perhaps initiated this process *via* the activated monomer method, as described in **Section 1.2.3.1**. Alternatively, it is possible that some other nucleophilic small molecule, such as ring-opened Z-Lysine, may have initiated the ROP process *via* the primary amine route. Whilst further research could elucidate the origin of this issue, it was more pertinent to develop a method for Lys(Z)-NCA ROP with greater control.

Following these discoveries, it was decided that the macroinitiator system would be changed to a mPEG-NH_2 derivative, either of molecular weight 1000 g mol^{-1} or 5000 g mol^{-1}. As such, several new polymerisations of Lys(Z)-NCA were attempted with updated sets of conditions, reported in **Table 5.1** of **Section 5.2.3**. The collected products from these reactions were analysed by size exclusion chromatography, using a Waters ACQUITY Advanced Polymer Chromatograph. The data obtained is reported in **Table 5.6** below, while the stacked chromatographs for each polymer are illustrated in **Figure 5.6.**

Table 5.6: APC-derived molecular weight data. Values marked (*) have been determined using partial peak data from bimodal distribution.

Reaction Title	Target M.W. / g mol^{-1}	M_n	Đ
BC115	9370	4804	1.31
BC116	9370	3827	1.29
BC118 (Peak 1)	32,900	12,241*	1.11*
BC118 (Peak 2)		4753*	1.14*

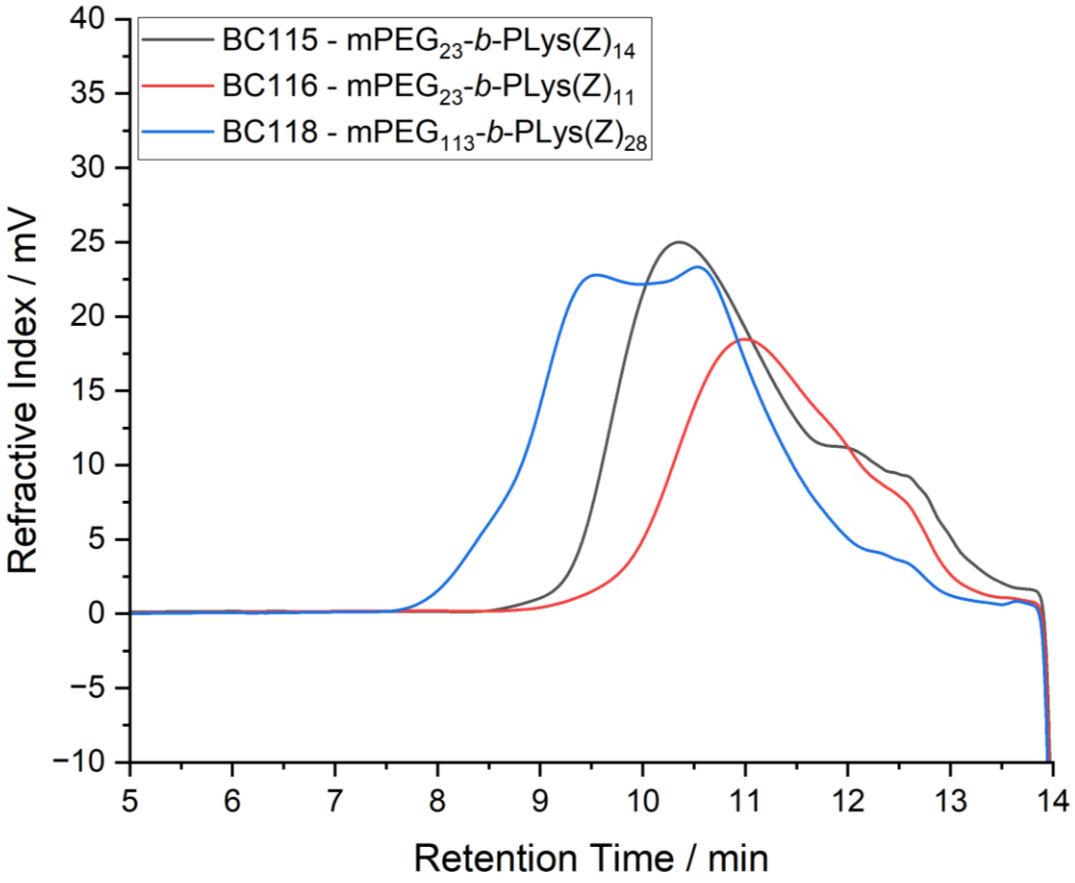

Figure 5.6: Stacked chromatographs of the products for each reaction described in **Table 5.6.** Colour coded values for number-average molecular weight and Đ are provided.

From **Table** and **Figures 5.6**, it is clear ROP of Lys(Z)-NCA has been accomplished in each case. However, there are notable areas of optimisation for each of the polymers that are highlighted within the data. Comparing **BC115** and **BC116** specifically, each reaction has a higher value for Đ than would be ideal for a controlled polymerisation. This is of course due to the shoulders on the right-hand side of each peak, representing lower molecular weight materials, such as oligomers. The presence of these materials in the product may be inflated due to the high sensitivity of the ACQUITY APC system. Regardless, these higher values for Đ can be reduced by further purification of the polymer *via* dialysis.

The most significant observation for products **BC115** and **BC116** are the molecular weight values achieved after 7 days of reaction. The [M]:[I] ratios for these reactions were 30:1, which would suggest a degree of polymerisation in the product of 30. Less than half this D.P. value has been achieved in each case. Factors that may have af fected this value include the length of time for which reactions took place, as well as the solvent choice.

If all NCA in solution had been consumed before the 168-hour mark, and polymers had been left idle in solution, there is a possibility that intramolecular truncation reactions could have taken place at the active chain end. Active amine chain ends could react with the poly(amino acid) amide linkages, causing the formation of cyclic oligomeric products and the shortening of chain ends. Another possibility is the presence of another amine impurity, acting as an unwanted initiator and depleting the effective concentration of NCA in solution. This is possible in the case of DMF, which can undergo decarbonylation in the presence of moisture to dimethylamine. As a result, any water in the storage vessel or reaction vessel may have resulted in the presence of dimethylamine which, with greater mobility in solution than the macroinitiator chain end, would have outcompeted mPEG-NH_2 to consume NCA reagents. This would also explain the difference in degree of polymerisation achieved between the two reactions as, at higher temperature, **BC116** may have experienced an increased rate of dimethylamine generation from the solvent, or perhaps an increased rate of polymerisation from the lower molecular weight impurities. For future reactions, it may be necessary to pursue different solvent options for this reason.

The chromatograph of **BC118** also raises some important questions about the conditions in which these reactions have taken place. The first is that, though poorly resolved from one another, there exist two peaks in a bimodal distribution, with one peak corresponding to the mass of the synthesised block copolymer, and the other to the mPEG-NH_2 macroinitiator. This observation was surprising at first as, compared to the mPEG-OH initiator used previously, the mPEG-NH_2 (M_w 5000 g mol^{-1}) initiator system should have been far more nucleophilic, and low macromolecular mobility should in theory have been compensated for by the increased temperature and longer timescale. One possibility for this unreactive mPEG could be the contamination of the macroinitiator reagent with mPEG-OH, from which mPEG-NH_2 is synthesised during manufacture *via* and azide reduction reaction. As demonstrated in previous sections, the low nucleophilicity of mPEG-OH was likely the origin of the bimodal distribution in this case. Further examination of this mPEG-NH_2 macroinitiator has been conducted in **Section 5.3.4**.

The M_n value of the left-hand peak within the **BC118** chromatogram, while less accurate without separation from the bimodal distribution, is significantly lower than would be expected for the targeted block size of 100 repeat units (>30,000 g mol^{-1}). However, as this reaction was conducted under the same conditions as **BC115/6**, the same opportunities for DMF by-products or nucleophilic impurities to initiate reaction exist, contributing to the formation of oligomeric by-products and depleting the effective monomer concentration and achievable DP. This effect would then have been exacerbated by the contamination of the mPEG-NH_2 macroinitiator as, with an effectively reduced concentration of active chain ends, the reaction rate would have been significantly retarded, affording more time for monomer-consuming side reactions to occur and to reduce the achievable DP. Importantly, however, ring-opening polymerisation of Lys(Z)-NCA has here been achieved. Subsequently, **BC115** and **BC116** have been deprotected, with the intention of producing a range of branched products and investigating the effects of branching on payload encapsulation and release.

5.3.2.1 Deprotection of mPEG-*b*-PLys(Z)

Following the successful ROP reactions of Lys(Z)-NCA, benzyloxy carbonyl group deprotection reactions were attempted on products **BC115** and **BC116**. The process is comprised of a 24-reaction between the product and HBr in a solution of TFA and acetic acid. A generalised mechanism for this reaction is presented in **Scheme 5.1** below.

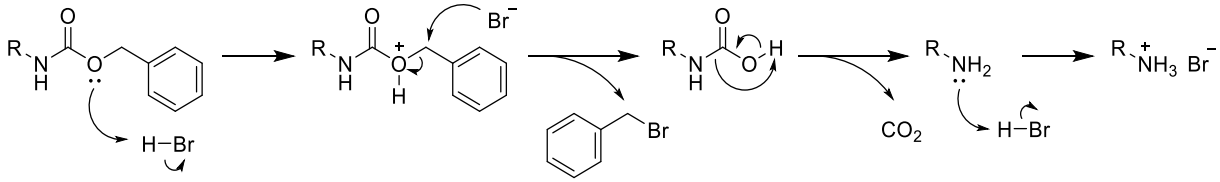

Scheme 5.1: Generalised mechanism for the deprotection of the benzyloxycarbonyl protecting group, which yields a free amine.

Following deprotection, the products were collected *via* precipitation in diethyl ether, before further solvation and re-precipitation from methanol to wash impurities from the product. The collected white solid was dissolved in water and dialysed (MWCO 2000 g mol^{-1}) against water for three days, before collection *via* lyophilisation. The collected products were submitted for APC analysis, and the collected chromatographs are presented beside the deprotected precursor polymers in **Figures 5.7a** and **5.7b** below.

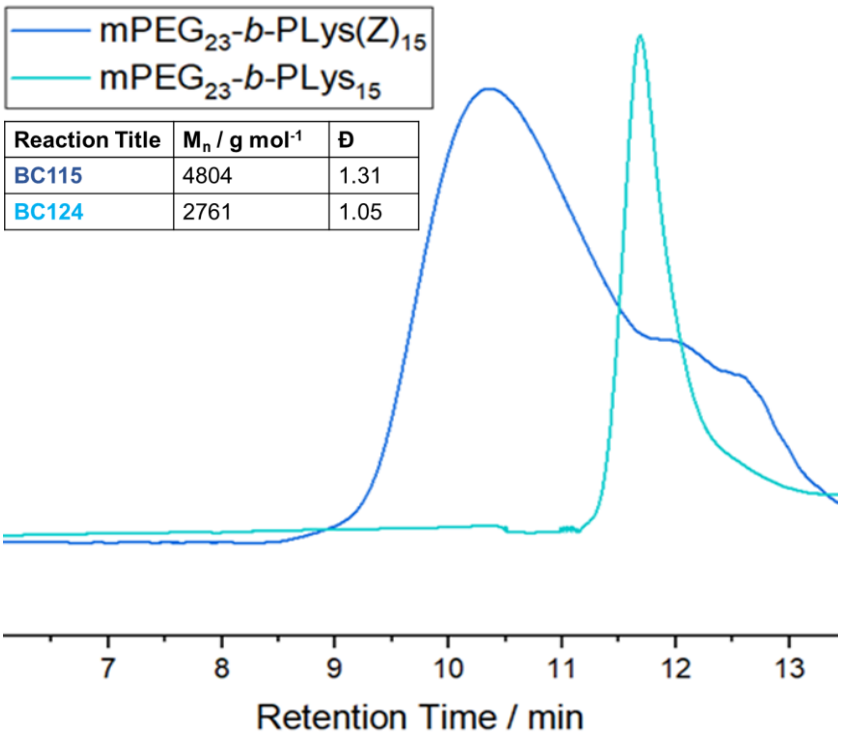

Figure 5.7a: Stacked advanced polymer chromatographs for **BC115**, mPEG-*b*-PLys(Z) and it's deprotected counterpart, **BC124**. Inset: Product M.W. data.

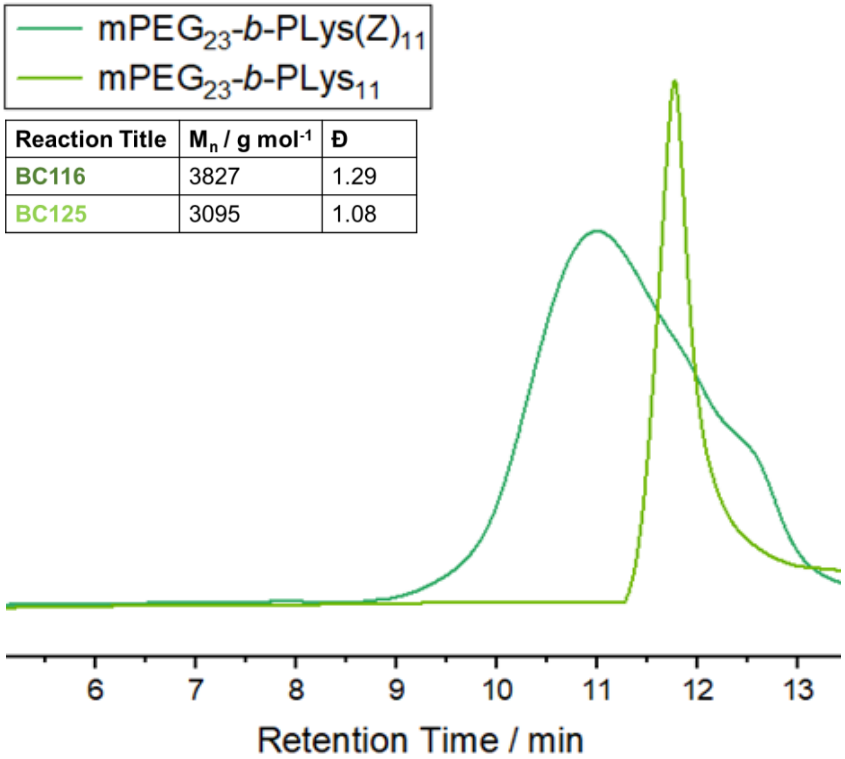

Figure 5.7b: Stacked advanced polymer chromatographs for **BC116**, mPEG-*b*-PLys(Z) and it's deprotected counterpart, **BC125**. Inset: Product M.W. data.

There has been a clear reduction in the molecular weight of each polymer, which is suggestive that the deprotection reactions have been successful. For the case of **Figure 5.7a** this is especially clear, as the reduction of 2043 g mol^{-1} following deprotection is consistent with the loss of 15 equivalents of Z-groups per polymer. For **Figure 5.7b** however, this is not quite the case, as a reduction of only 732 g mol^{-1} per polymer suggests a loss of ca. 5 to 6 equivalents of Z-groups. This could be a result of incomplete deprotection of the polymers, or perhaps a result of inaccuracy within the APC equipment, due to issues involving changes to flow rate between the measurements taken. From the chromatographs of the deprotected polymers, it can also be observed that the Đ values are significantly reduced, with size distributions far more controlled in comparison to those of the precursor protected polymers. This is likely a result of the purification steps taken during deprotection, specifically the dialysis of the product following the precipitation washing stages. The dialysis tubing used for this stage typically allows diffusion of species of molecular weight below 2000 g mol^{-1}, meaning that hydrolysed NCAs, oligomeric materials and by-products of the deprotection stage will have been removed as the dialysate was changed. Thus, a well-defined deprotected product has been obtained.

The Z-group has been demonstrated here as a viable protection system for the controlled synthesis of well-defined mPEG-*b*-PLys block copolymers, with low Đ, under mild conditions. Furthermore, deprotection has been achieved with good yield (72 % and 75 %), generating a high-purity product capable of subsequent post-polymerisation modification, and potential application in the delivery of therapeutic payloads. However, further study was not conducted using Lys(Z) from this point, and instead efforts were made to investigate the ROP of Lys(Boc)-NCA instead. The tert-butoxycarbonyl protecting group, similar to (Z), is insensitive to basic conditions, such as those found during NCA ROP. An added benefit of Boc is the simplicity of its deprotection procedure in comparison to (Z), which requires only reaction with TFA, as opposed to the harsh HBr/AcOH hydrogenation reagent and subsequent purification procedures involved with deprotecting Lys(Z).

As such, and because Boc deprotection generates only CO_2 and gaseous isobutene as a side-product, the need for workup and dialysis procedures following reaction is eliminated and instead, once excess TFA is removed, the pure, deprotected product can be lyophilised as a TFA salt, ready for subsequent modification reaction. For this reason, investigation of Lys(Z) polymers was concluded at this juncture.

5.3.3 Initial NCA ROP of Lys(Boc)-NCA

Prior investigation of the polymerisation, deprotection and covalent drug conjugation of Lys(Boc) systems has been done by England *et al*.[4] During this research, the successful conjugation of fulvestrant to poly(sarcosine)-*b*-PLys yielded block copolymers capable of self-assembly into micellar structures, improved encapsulation efficiency of additional fulvestrant molecules, and controlled release *via* hydrolytic degradation of ester linkages. As such, the synthesis of mPEG-*b*-Lys(Boc)$_n$ block copolymers reported here follows a similar protocol.

Initial ROP of Lys(NCA) was performed using a co-solvent mixture of anhydrous DMF and DCM, which minimised the required quantity of DMF solvent for reaction. Primarily, this was done to simplify the purification of crude product following reaction as, during these initial stage reactions, reduced-pressure equipment capable of removing DMF under ambient conditions was not available. Minimising DMF solvent allowed for efficient precipitation into diethyl ether, and maximal product retrieval. Furthermore, it is widely documented in the literature that DMF is capable of hydrogen bonding interactions with the amine group of the active chain end during reaction, thereby slowing the rate of propagation.[16,17] As such, a substitution of DMF content for DCM should allow for an increased rate of propagation, thought this property has not been studied here.

mPEG-*b*-PLys(Boc)$_n$ copolymers of varied Lys(Boc) block lengths (10, 20, 50, 100) were synthesised according to the preparative methodology prescribed in **Section 5.2.4**, reacting for 24 hours at room temperature. The ^{1}H NMR spectrum of **BC183**, the target formula for which is mPEG-*b*-PLys(Boc)$_{10}$, has been characterised in **Figure 5.8** below.

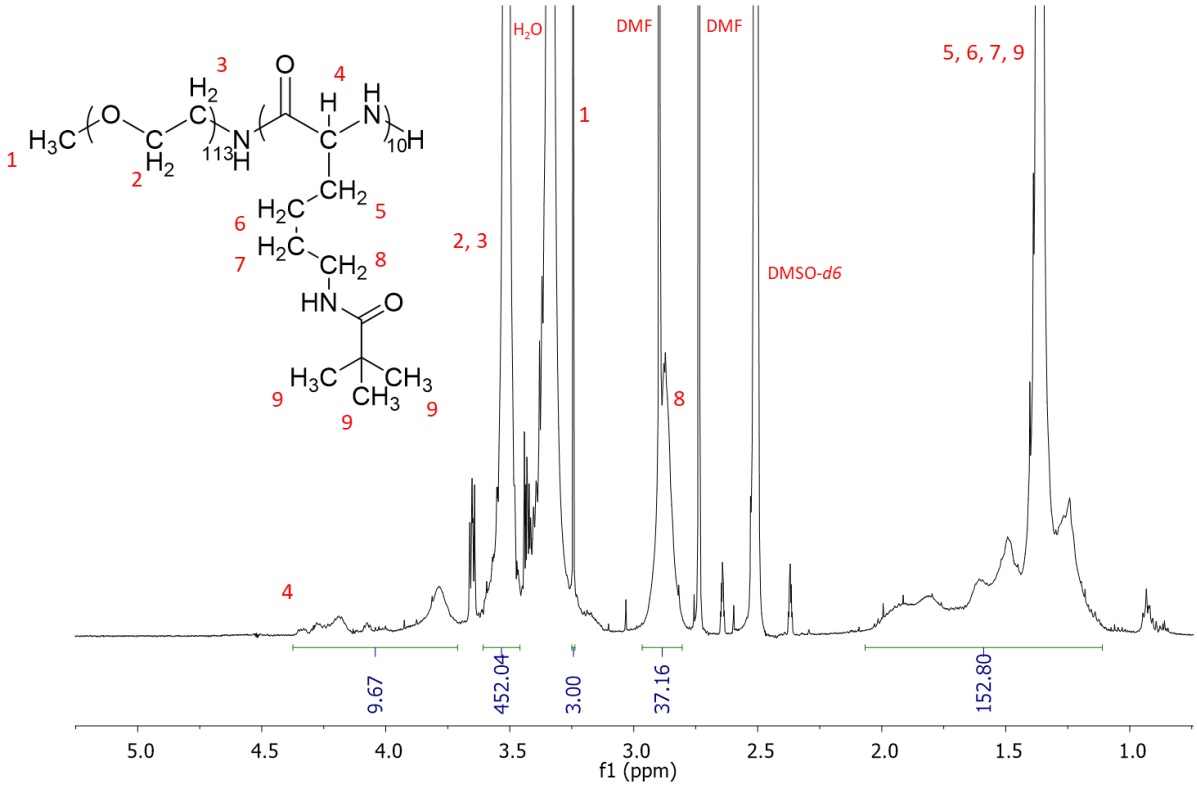

Figure 5.8: Characterised ^{1}H NMR (500 MHz, DMSO-d_6) spectrum of **BC183**, hydrogen-expanded structure has been provided for reference.

The first observation that can be made from **Figure 5.8** is the significant solvent contamination present in the sample. The peak for the deuterated solvent can be observed, as well as a moisture peak, likely the result of the highly hygroscopic DMSO having absorbed atmospheric moisture during previous use. However, there is also significant contamination of DMF, as evidenced by the sharp peaks at 2.73 ppm and 2.89 ppm. Despite efforts to precipitate the sample and wash using diethyl ether, it is clear that some DMF remains within the solid sample. Without stronger reduced-pressure equipment to remove this solvent, and without using high-temperature rotary evaporation which may risk chain degradation, it was decided that this incorporated DMF was acceptable for this stage of reaction, as it would be removed during dialysis following the subsequent deprotection step.

Importantly, it can also be observed from **Figure 5.8** that ROP of Lys(Boc)-NCA appears to have taken place successfully, which can be evidenced by comparing the integral values within the mPEG and pLys(Boc) blocks. The mPEG-ethyl C-H peak at ca. 3.5 has been normalised to 452, representing the 4 ethyl protons of the 113 PEG repeat units within the hydrophilic block.

Furthermore, the αC-H proton environment (3.7 ppm – 4.4 ppm) provides an integral value of ca. 10 which correlated to the 10 repeat units added. This is further supported by the integral value of ca. 150 for the aliphatic C-H region (1.0 ppm – 2.0 ppm), which represents a combined total of 60 lysine ethyl protons and 90 Boc *tert*-butyl protons. This suggests that polymerisation has been carried out successfully, however this cannot be corroborated without corresponding mass data, as has been evidenced in previous chapters. Another important observation is the broad range (0.7 ppm) within which the αC-H protons resonate. This is to be expected in polymeric species, due to the change in resonance experienced by protons relative to their position in the chain. Proton environments towards the ends of the chain often experience stronger electron withdrawal due to reductions in shielding and the withdrawing effects of solvent interactions at the chain end, resulting in higher chemical shift values. However, it should be noted that this region presents as smaller defined peaks as opposed to one larger distribution which, when compared to the DOSY NMR spectrum presented in **Section 5.3.2**, could feasibly represent the proton environments of small-chain, oligomeric by-products as opposed to domains within one well-defined product chain. Without mass data to confirm, however, no such conclusions can be reached.

In order to gather mass data, the polymers were deprotected before submission for MALDI-TOF mass spectrometry. This was done as Boc-protected species were prohibitively difficult to analyse using this technology, potentially due to incompatibilities between the polymer and the matrix, or poor flight of the ionised macromolecules. The deprotection procedure has been outlined in **Section 5.2.4.1**, and the product of **BC183** deprotection, **BC190** (mPEG-*b*-PLys[NH_2.TFA]$_{10}$) is characterised and presented in **Figure 5.9** below.

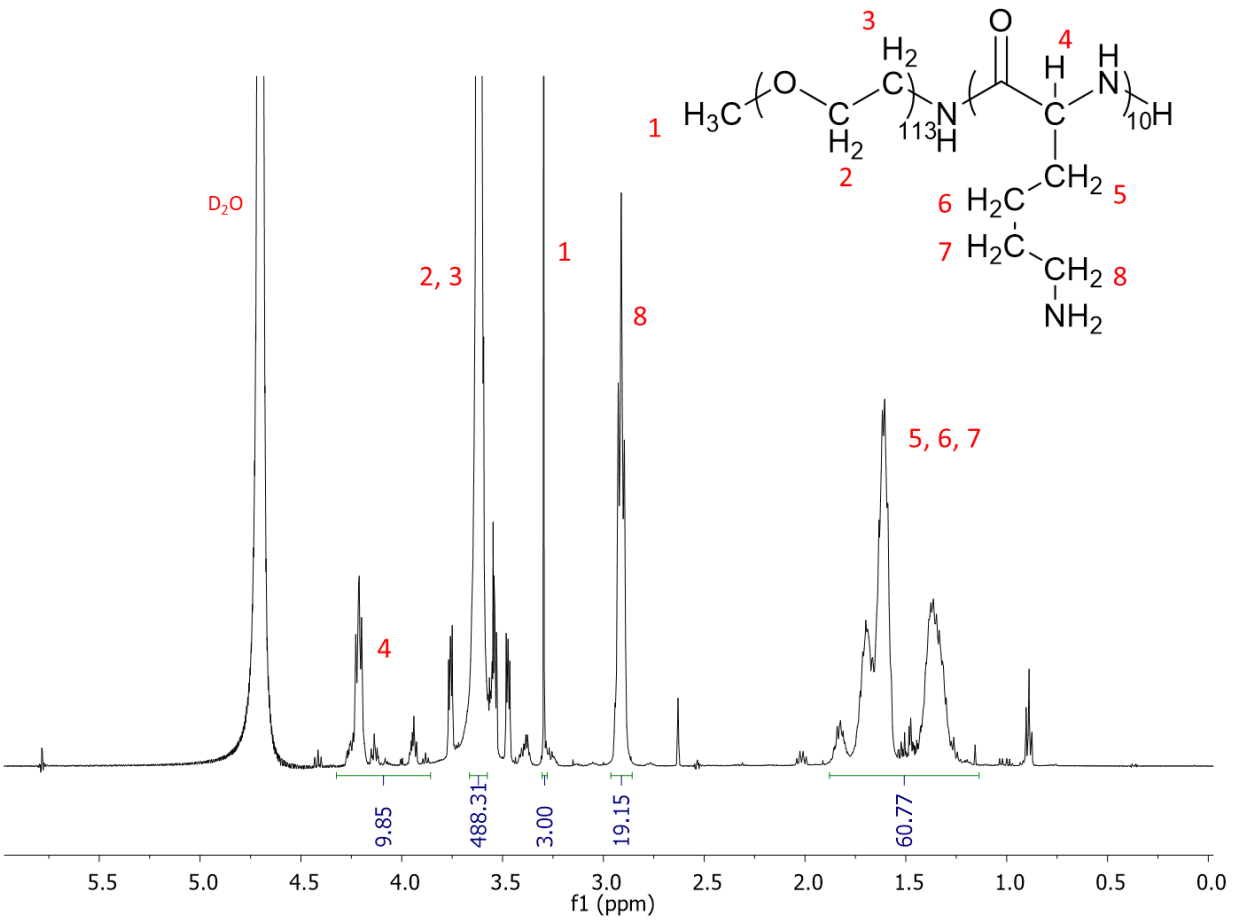

Figure 5.9: Characterised ^{1}H NMR spectrum (500 MHz, D_2O) of **BC190**, hydrogen-expanded structure has been provided for reference.

Initial observations of **Figure 5.9** show no contamination from solvent impurities, other than the D_2O solvent. This is due to the stringent purification procedure outlined in **Section 5.2.4.1**, and the utilisation of a PD10 Sephadex resin column to remove small-molecule impurities. Furthermore, there is clear agreement between the integral values for the lysine αC-H protons, and both lysine ethyl C-H domains (**5** - **7** and **8**) in comparison to the PEG ethyl C-H domain at 3.6 ppm, which each suggest a D.P. value between 9 and 10 for **BC183** and **190**. The SEC chromatographs of **BC190** and **BC192** are presented in **Figures 5.10** and **5.11** below, overlaid against the spectrum of the mPEG-NH_2 macroinitiator.

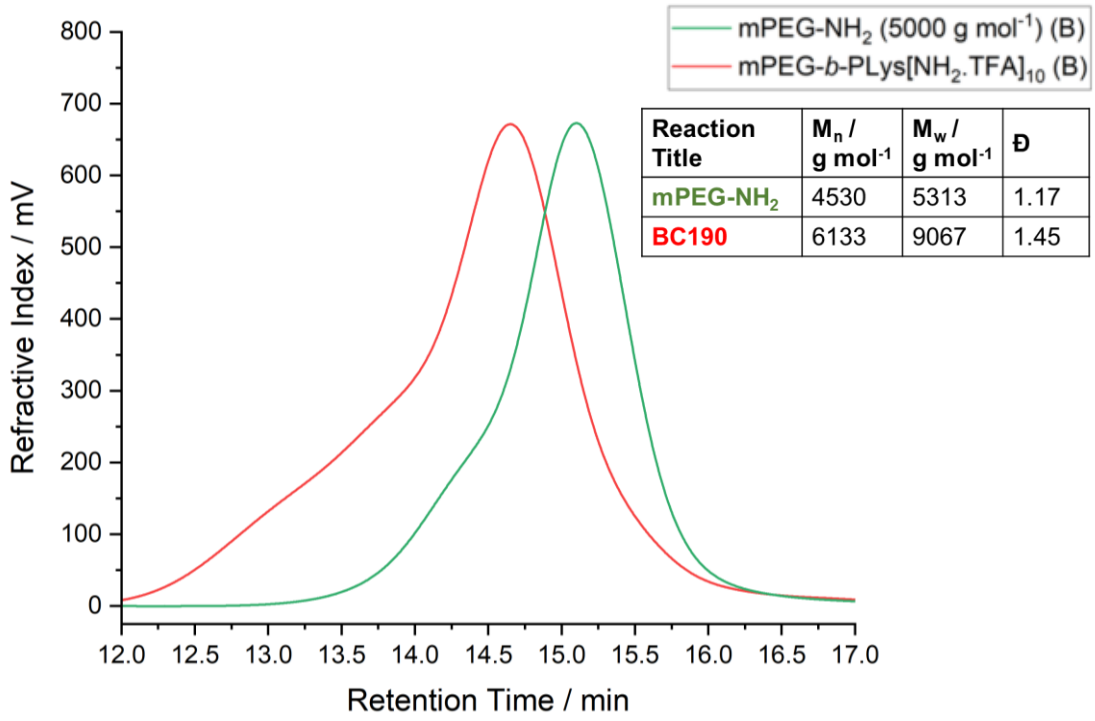

Reaction Title	M_n / g mol^{-1}	M_w / g mol^{-1}	Đ
mPEG-NH_2	4530	5313	1.17
BC190	6133	9067	1.45

Figure 5.10: The SEC-TDA chromatogram of BC190, overlaid with that of mPEG-NH_2 (5000 g mol^{-1}) (Thermofisher Batch B)

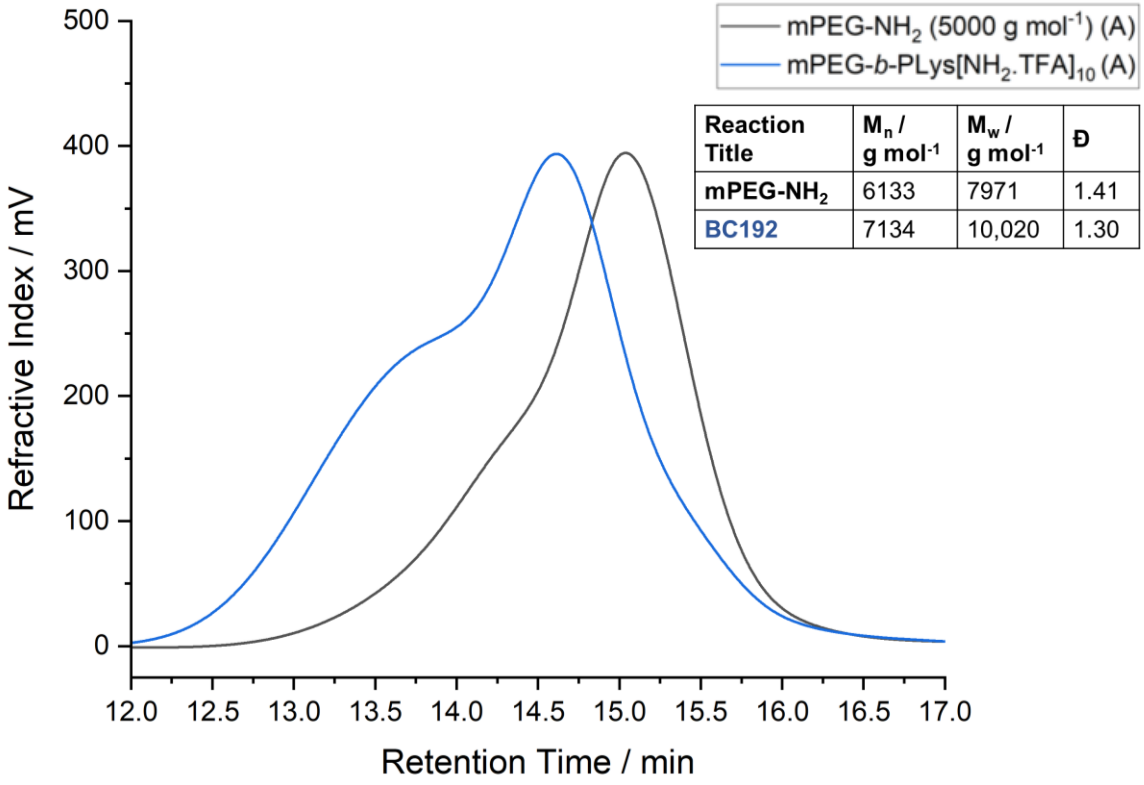

Reaction Title	M_n / g mol^{-1}	M_w / g mol^{-1}	Đ
mPEG-NH_2	6133	7971	1.41
BC192	7134	10,020	1.30

Figure 5.11: The SEC-TDA chromatogram of BC192, overlaid with that of mPEG-NH_2 (5000 g mol^{-1}) (Thermofisher Batch A)

In each mPEG-NH_2 chromatogram within **Figures 5.10** and **5.11**, a significant shoulder can be observed at lower retention times, representing higher-molecular weight impurity. The origin of this high-molecular weight material is unclear without further analysis, but it can be noted that, for each of the derived block copolymer products, the shoulder has been exaggerated, and has shifted with the rest of the peak. This suggests that the higher-MW material is capable of initiation, and has contributed to the overall distribution of peak lengths in the final products, thereby artificially inflating their corresponding Đ values. This is especially pronounced in the Đ increase of 0.23 between mPEG-NH_2 batch B and **BC192**. In terms of molecular weight changes between the macroiniator materials and products, the peaks of each chromatogram experienced very similar shifts in retention time (ca. 36 seconds).

However, this consistent increase is not reflected in the change in M_n value experienced by each block copolymer product. **BC190** demonstrated a 1700 g mol^{-1} increase of M_n over mPEG-NH_2 batch B, whilst **BC192** increased by only 1000 g mol^{-1}, suggestive of an approximate 3-repeat unit difference between the samples. With the synthetic methodologies of these ROP and deprotection procedures being identical, and the clear swelling of the shoulder present in **BC192**, this disparity in M_n can be confidently attributed to the low purity of the starting material. As a result, subsequent syntheses were conducted using mPEG-NH_2 macroinitiator sourced from a different supplier, and analysed prior to ROP initiation using SEC-TDA, as is illustrated in subsequent sections.

The syntheses described in this section laid the groundwork for further investigation of the mPEG-*b*-PLys(Boc) system, as well as its subsequent deprotection protocol. These materials were then re-synthesised as part of a secondment to AstraZeneca, in order to evaluate the effect on increasing hydrophobic block length and post-polymerisation modification on the assembly of amphiphilic block copolymers for controlled therapeutic delivery.

5.3.4 *in-situ* FTIR monitoring of Lys(Boc)-NCA ROP

In accordance with the preparative methodology laid out in **Section 5.2.5** (reagent quantities, reaction conditions), $mPEG_n$-*b*-$PLys(Boc)_m$ block copolymers of varying block lengths (m = 5, 10, 20 and 50) underwent NCA ROP from $mPEG\text{-}NH_2$ (5000 g mol^{-1} and 10,000 g mol^{-1}, both sourced from Iris Biotech GmbH). Whilst the effect of increasing macroinitiator and corresponding hydrophilic unit size had not previously been investigated as part of this project, it was determined that such an increase would likely be necessary to account for the intended increase in hydrophobic block length. *In-situ* FTIR monitoring was achieved using equipment described in **Section 2.3.1**, which acquired 256 FTIR traces per minute. Monomer conversion was calculated by analysing the area reduction of a single C=O stretching peak at ca. 1700 cm^{-1}, corresponding to the carbonyl unit that is eliminated as CO_2 during ring-opening. These monomer conversion plots are displayed overlaid in **Figure 5.12** below.

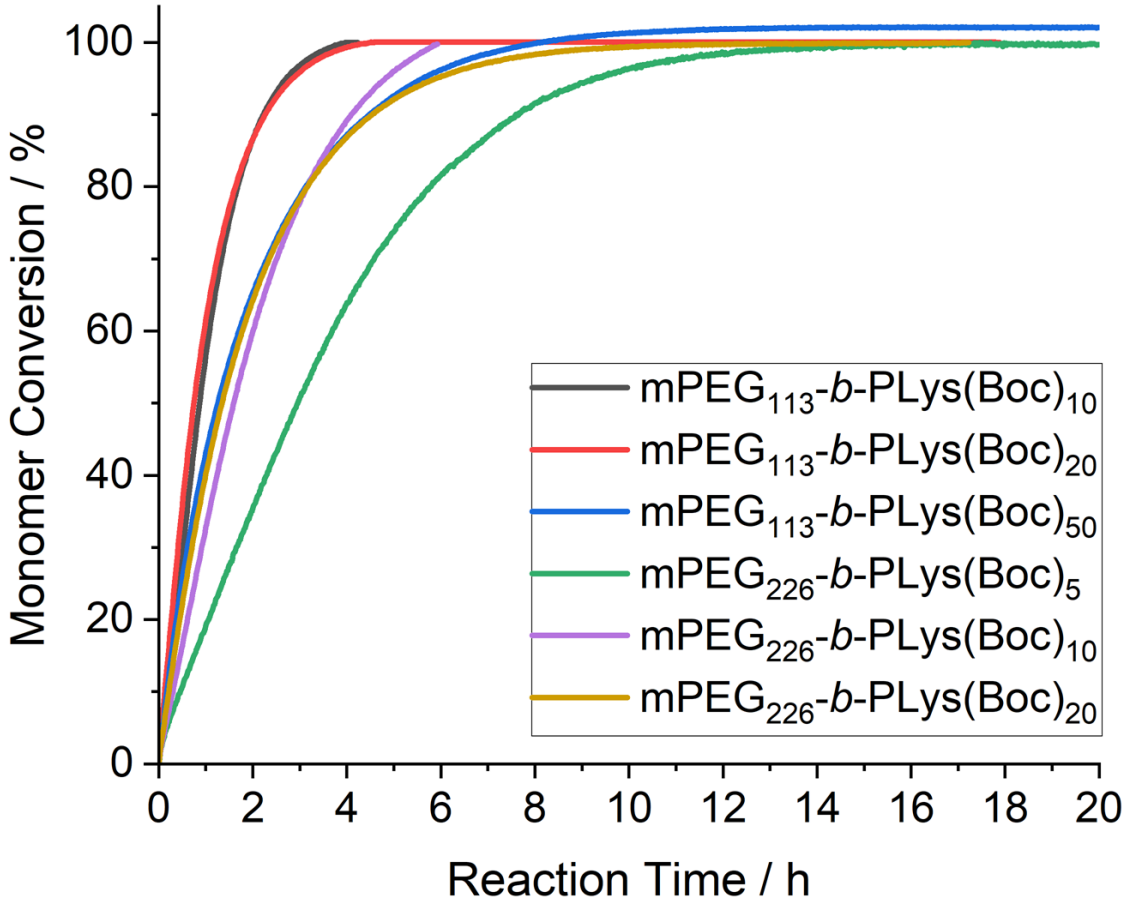

Figure 5.12: Conversion profiles of BC196 – BC202, generated *via in-situ* FTIR analysis of peak deterioration for the eliminated NCA-carbonyl moiety with resonance at ca. 1700 cm^{-1}.

Notably, the conversion profile for **BC195** is excluded from these data. This reaction was run using a higher relative volume for the solvated materials, with a corresponding NCA concentration an order of magnitude lower than other reactions, which prevented FTIR monitoring due to a decreased signal-to-noise ratio. Upon reflection, this high dilution within DMF was considered unnecessary, and was not repeated for subsequent reactions. In addition, FTIR analysis was complicated by the low peak intensity for the NCA in comparison to the larger DMF contribution and, as such, the high level of noise in the signal made analysis of the monomer conversion unreliable. This was addressed for later reactions, as can be seen by the decreasing solvent volume from **BC196** onwards, but the effects of low concentration on the data clarity can be observed for the trace of **BC199**, which has the lowest NCA concentration in comparison to the other polymers (**Table 5.3**). Furthermore, it should be noted here that macroinitiator and monomer masses were inconsistent between the reactions monitored here, as keeping one concentration consistent would require using unnecessary and wasteful quantities of the other. Nevertheless, it can be observed in **Figure 5.12** that each of the monitored reactions was allowed to proceed to completion, with a minimal 95 % conversion achieved in all cases. These reactions were completed within good time, ranging from ca. 5 hours for the shorter-chain products to ca. 15 hours for **BC199**. This can likely be attributed to the reduced concentration of NCA monomer for this reaction, as well as the reduced mobility of the reactive chain end in the case of $mPEG_{226}$-NH_2 initiated ROP.

The polymer products **BC195-198** were evaluated *via* ^{1}H NMR spectroscopy and SEC analysis for their purity and molecular weight distributions, respectively. The stacked ^{1}H NMR spectra for these polymers is presented in **Figure 5.13** below, wherein relative increase in the peak area of the $[Lys\text{-}Boc]_n$ aliphatic protons has been highlighted in comparison to the consistent integral value corresponding to the mPEG-NH_2 methyl peak.

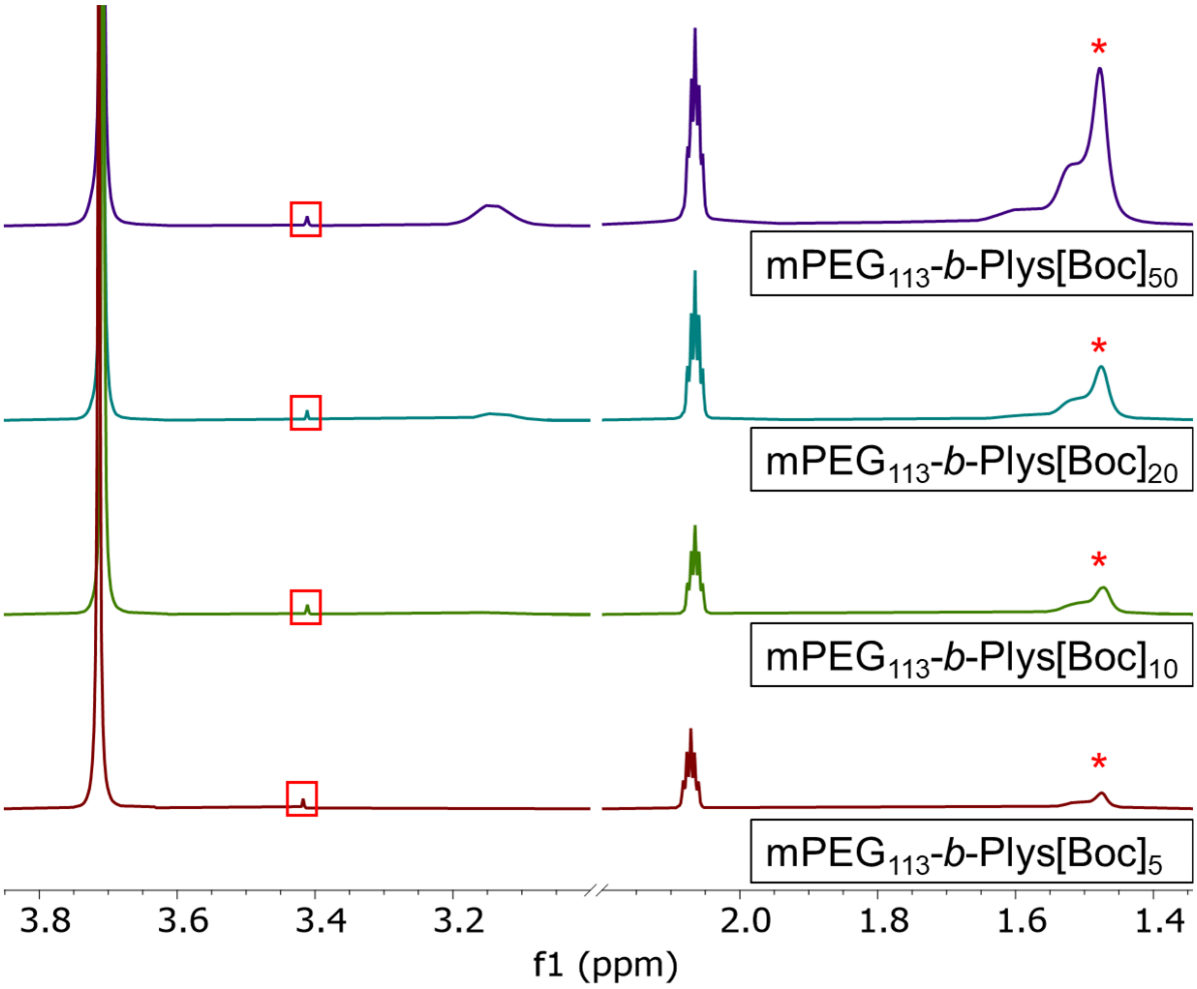

Figure 5.13: ^{1}H NMR spectra (500 MHz, DMSO-d_6) of block copolymers BC195-8, with DP evidenced by increasing aliphatic [Lys-Boc]$_n$ peak area (*) vs. mPEG terminal methylene protons (▢). Spectrum baseline between 3.2 – 2.2 cut to provide space for characteristic peaks.

As can be observed within **Figure 5.13**, consistent increases can be seen between the aliphatic proton regions of each product, indicative of the increased degree of polymerisation achieved. Furthermore, by comparison of the full ^{1}H NMR spectra of the products available in **Section A.5.1**, it can be observed that prior impurities that had caused complications in characterisation (residual DMF solvent and small-molecule impurities) were not present here, suggesting that the purification procedures were successful and satisfactory. For a more comprehensive comparison to be made, attention was then turned to the molecular weight distributions of the polymers, for which SEC-TDA was employed. Overlaid chromatographs are presented in **Figure 5.14** below.

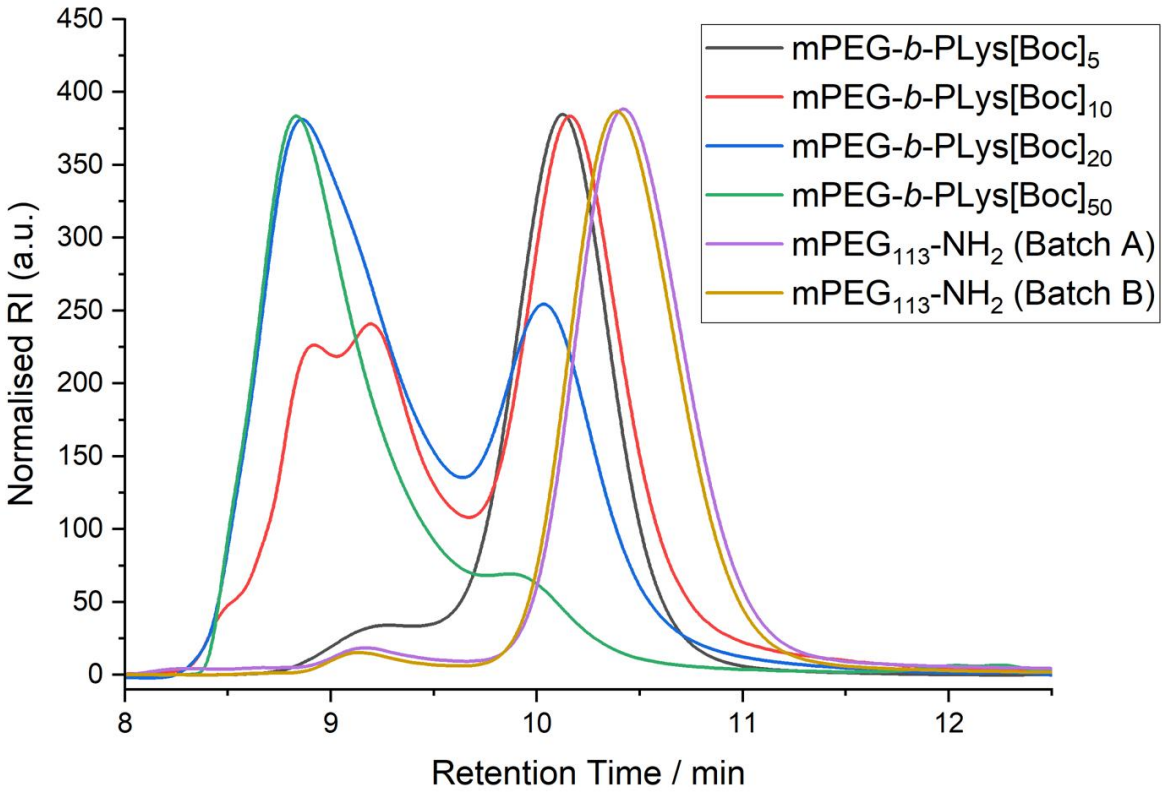

Figure 5.14: SEC-TDA of mPEG-*b*-Plys[Boc]$_n$ block copolymers.

It should be noted that, for SEC analysis run here in DMF, molecular weight data was not collected for the samples by the team at AZ. Hence, it is not provided here and instead qualitative comparisons of samples have been made. Quantitative assessment of molecular weight values and distributions are performed for the deprotected forms of these polymers, run under aqueous conditions in **Table 5.7** further below. It can first be observed that the chromatograms of both mPEG$_{113}$-NH$_2$ Batch A and B (Iris Biopolymers) are better defined and more uniform than those sourced from Thermo Fisher Scientific. There can still be observed a small signal left of the main peak, though the contribution of this is significantly less impactful. Furthermore, when comparing the chromatogram of **BC195** to these macroinitiator peaks, it should be noted that the position of this smaller signal does not shift in comparison to the main peak, which suggests that this high-molecular weight material is not capable of initiation. It has been speculated that this could be some dimer of the mPEG$_{113}$-NH$_2$ polymer, caused by nucleophilic interaction between an mPEG$_{113}$-NH$_2$ unit and an mPEG$_{113}$-N$_3$ azide unit during azide reduction, resulting in the formation of an amine-substituted derivative.

The identity of this signal has not been investigated further, but it is important to note its presence and lack of contribution to the final polymer system.

The most noticeable observation that can be made from **Figure 5.14** is the appearance of bi- and multi-modal peak distributions for three of the synthesised polymer products, **BC196**, **197**, and **198**, for which the targeted degrees of polymerisation for the hydrophobic PLys(Boc) block were 10, 20 and 50, respectively. Initial hypothesis for the origin of this poor peak uniformity lay with the SEC-TDA methodology itself. Factors such as non-size related interactions, viscosity and flow irregularities, and poor solvent compatibility have all previously been attributed to the broadening and 'dragging' of peaks, resulting in pseudo-multimodal distributions.[18-20] Whilst flow rates were monitored closely throughout sample acquisistion and LiBr salt was added to screen non-specific interactions, these may not have been sufficient. There is an existing precedent in the literature for SEC analysis of protected poly(amino acids) in DMF solution of complications with solubility due to aggregation. As such, attention has been paid to polymers analysed using this system in future synthetic steps.

Another observation that can be made for these multimodal distributions is the relative positions of their constituent peaks. While it is not possible to more accurately characterise the M_n and M_w values for the contributing components, remarks can be made on qualitative differences in their appearance. Firstly, it can be seen that minimal shift in retention time has occurred between the right-hand peak of the **BC196** chromatogram and the main peak of **BC195**, despite the intended 5 repeat unit difference between them. It is not expected that there would be a separation between these peaks as large as that between **BC195** and mPEG-NH_2, due to the logarithmic relationship between retention time and molecular weight, however should peak separation be possible for **BC196** it would be necessary to re-evaluate the molecular weight of this peak in particular, to determine the cause. It may be possible, given the significantly larger molecular weight of the left-hand peak distributions for **BC196** (r.t. 8.5-9.5 minutes) that monomer species have been preferentially consumed by whatever has contributed to these higher-M.W. species, resulting in a D.P. for the right-hand species more closely approximating 5, as is the case for **BC195**.

The positions of the right-hand peaks for **BC197/8** appear to experience further r.t. shift in comparison to **BC196**, though without additional separation and characterisation, it is not possible to determine the M.W. increase indicated by such shifts.

A similar observation can be made for the left-most peaks of the three multimodal chromatograms, though without a clear identity for the contributing species, further speculation has not been conducted on the root cause. Another notable observation is the shift in relative peak area with increasing target hydrophobic block length. This is notable between **BC197/8**, wherein an apparent shift of peak area from right to left can be observed, suggesting that a greater proportion of the **BC197** sample is made up of higher molecular weight species, and is most stark for **BC198**, wherein a significant majority of the sample exists as a higher molecular weight species. One hypothesis for this has been based on the presence of an unexpected bi-functional species within initiator species. Leading to the polymerisation of two –[Lys(Boc)]– chains from a single initiator site, resulting in the inflated product molecular weights. This would also account for the increased uptake of monomer species, exacerbated with the increased monomer concentrations present for **BC197/8**, as twice the number of active chain ends would allow this species to dominate the available pool of reactive monomer species. One potential explanation for the presence of a bifunctional initiator, specifically present in the macro-initiator species, is that the synthesis of methoxy-poly(ethylene glycol), prior to azide reduction, was not achieved fully from the PEG starting material. Without ensuring 50% end-capping for each PEG chain, PEG species of similar molecular weight but with two hydroxyl terminals would have then undergone azide reduction, resulting in NH_2-PEG-NH_2 as an impurity in the initiator, un-detectable by the precursory SEC analysis performed on the materials obtained from Iris Biotech. Another possibility is the presence of cross-linking in the product, resulting in a high-M.W., networked polymer system. However, no conclusive insight can be gained without further separative analysis of the products.

In order to verify whether SEC methodology had an impact on the apparent multimodal distributions observed in **Figure 5.14**, the resultant products were subjected to Boc-deprotection, *via* the process outlined in **Section 5.2.4.1**. Samples were stirred for 3-5 minutes in pure TFA until completely dissolved, leaving a pale yellow solution.

Subsequently, excess TFA was removed *in vacuo* and the crude product, now a film layer, was dissolved in deionised water lyophilised until a white, fluffy solid was obtained. The result of this deprotection on **BC195**, as characterised by ^{1}H NMR, is illustrated in **Figure 5.15** below.

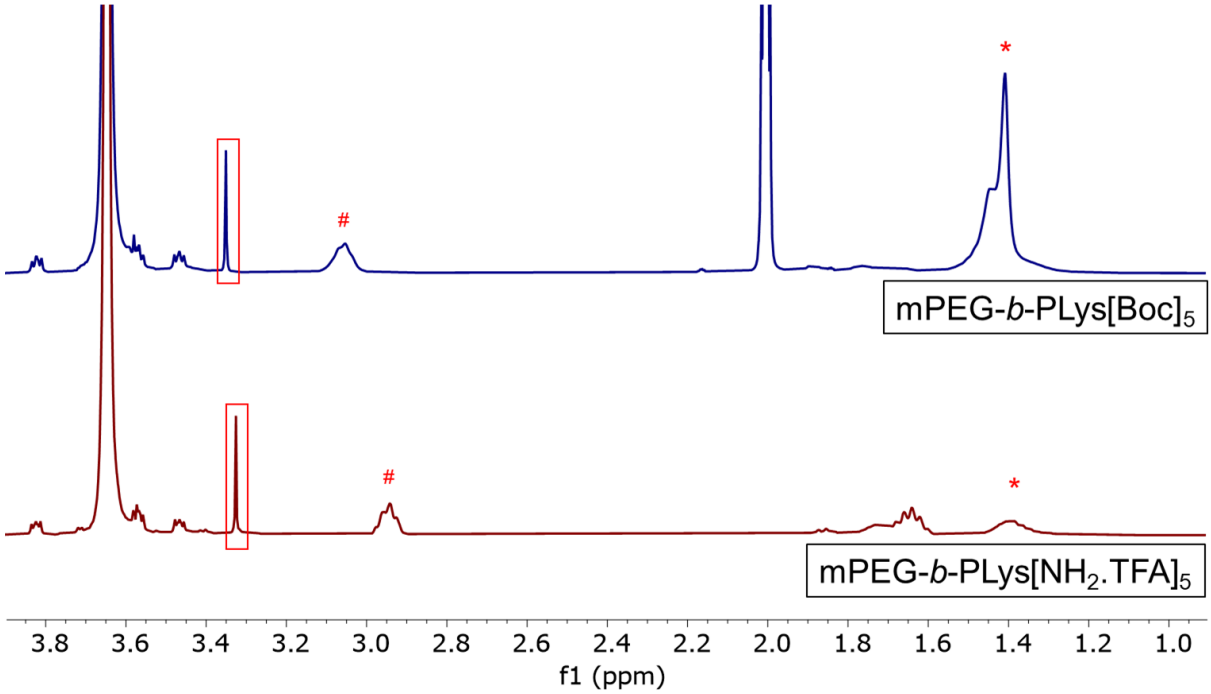

Figure 5.15: Determination of successful Boc- deprotection, as determined by the decreasing Boc methyl proton peak area in the 1.8-1.2 ppm range (*) and consistent lysine ethyl proton area (#) vs. mPEG terminal methylene protons (▢).

As is demonstrated in **Figure 5.15**, deprotection has been achieved with significant reduction in the Boc-methyl corresponding peak area (*) relative to the peak areas representing aliphatic lysine ethyl environments (residual *, #) and the PEG-methoxy environment (▢). The reaction and workup have been performed without introduction of impurities, and the product was obtained in good yield (65 %). The same can be seen for **BC196D**, **197D** and **198D**, in **Section A.5.1**. Notably, the by-products of Boc-deprotection, CO_2 and isobutene, are gaseous at room temperature and therefore do not require further purification.

Deprotected samples were then submitted for SEC analysis using an aqueous eluent (100 mM NaCl + 0.1 v/v% TFA) and corresponding column, as described in **Section 2.6**, to examine the appearance of the peaks under a different preparative methodology. The overlaid chromatographs are presented in **Figure 5.16.**

Importantly for these data, it was possible to elucidate approximate molecular weight values, utilising a PMMA calibrant system. While this cannot provide absolute data for the polymers, it does allow clearer elucidation of the D.P. values achieved and the relative molecular weight distributions of the deprotected polymers. These data are presented in **Table 5.7** below.

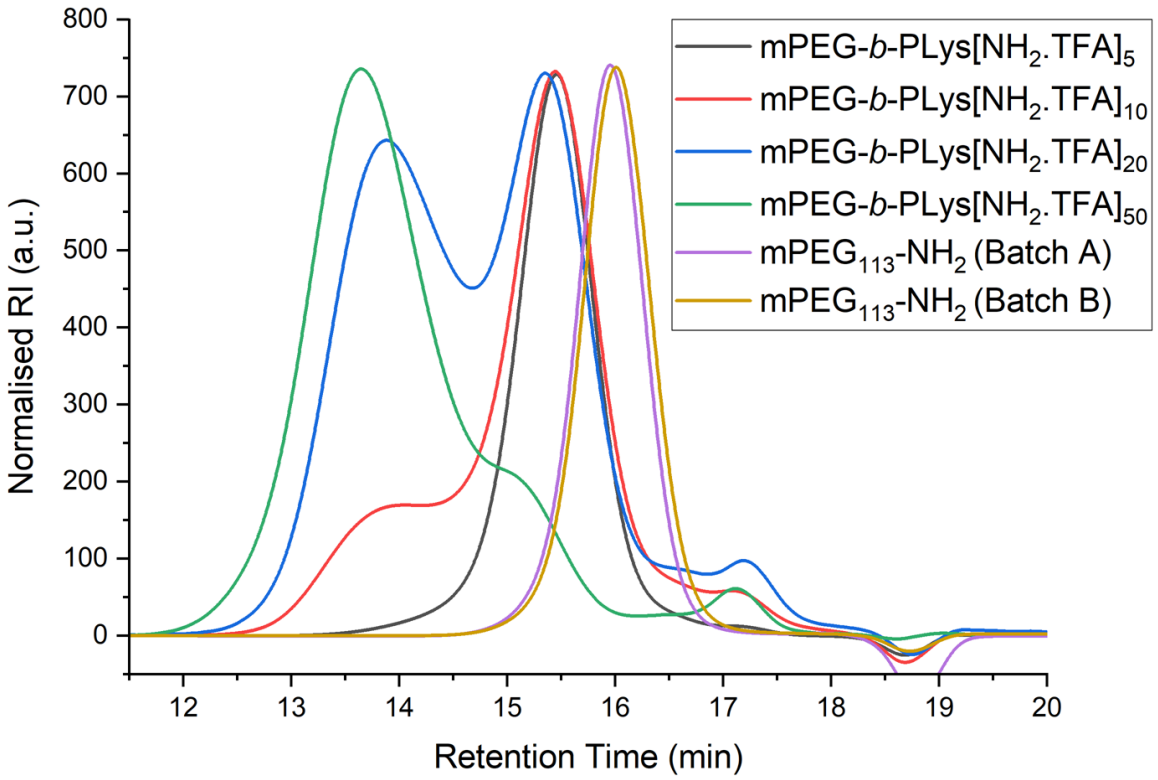

Figure 5.16: Normalised SEC-TDA of **BC195D-198D**, run in TFA-Aqueous eluent.

Table 5.7: SEC data for **BC195D-198D**, with expected M.W. values and calculated D.P.

Experiment Title	Est. M.W. / g mol^{-1}	M_n / g mol^{-1}	M_w / g mol^{-1}	Đ	D.P. (calc.)
mPEG-NH_2 (Iris Biotech Batch A)	5000	4900	4900	1.00	-
mPEG-NH_2 (Iris Biotech Batch B)	5000	4400	4500	1.02	-
BC195D – mPEG$_{113}$-b-PLys[NH_2.TFA]$_5$	6300	8400	8800	1.05	13
BC196D - mPEG$_{113}$-b-PLys[NH_2.TFA]$_{10}$	7600	9000	11,500	1.29	15
BC197D - mPEG$_{113}$-b-PLys[NH_2.TFA]$_{20}$	10,200	11,200	15,700	1.40	24
BC198D - mPEG$_{113}$-b-PLys[NH_2.TFA]$_{50}$	18,000	18,000	23,000	1.27	50

For **BC195D** within **Table 5.7**, M_n appears significantly higher than expected given the reaction conditions outlined in **Section 5.2.5**.

In addition, this data contrasts with the estimated molecular weight values that can be taken from ^{1}H NMR of both **BC195** and **BC195D**, which each agree on a D.P. of 5. It should therefore be reiterated that these values do not represent absolute molecular weight values, but do provide quantitative comparisons between the macroinitiators and BCPs. In addition, there is a significant difference between the M_n values of mPEG-NH_2 between batches A and B that is not clearly explained by differences in their respective ^{1}H NMR spectra (**Section A.5.1**). Whilst this may represent a simple difference in M.W. distribution, it is worth noting in the case that additional findings arise.

For **BC196D**/**197D**/**198D**, a small peak appears at ca. 17 minutes that is not observed in the chromatogram of **BC195D**. This may correspond to short-chain oligomer by-products, a result of increased side-reactions enabled by the increased monomer concentration [M] between **BC196**/**197**/**198.** The ratios of [M] between these reactions and that of **BC195** were 1.9, 2.8 and 4.4, respectively, highlighting a significant increase that may have contributed to the stark contrast between the initial dilute reaction and its concentrated counterparts. It is important also to recognise the persistence of multimodal peak distributions here. The presence of these distributions here means that, if methodological sources of peak broadening and dragging are the cause, they are persistent between differing mobile and stationary phases, which is less likely. For **BC197D**, there appears to be a near-equal division in molecular weight distributions. One of these lies close in M.W. to **BC195D** and **BC196D**, whilst the other lies towards a M.W. comparable to **BC198D**. Whilst the identities of these peaks cannot be clearly elucidated without further separative workup, unavailable at the time of reporting, it raises important questions about the origins of unintended, high M.W. species during reaction. In addition, it places an importance upon the polymerisation methodology to limit by-production of any such impurities, motivating further research into NCA ROP optimisation.

A review of the relevant literature elucidated two primary contributors to side-reactions and the formation of high-M.W. by-products. These are temperature, which has been discussed at length as a likely source of increased side-reaction during mPEG-*b*-mPMA synthesis within **Section 4.3.1**, and DMF solvent. Whilst the decomposition of DMF to dimethylamine and its corresponding contribution to errant initiation reaction has already been discussed in **Section 5.3.2**, Vayaboury *et al*. suggested that DMF could act as an electrophilic target for unwanted

nucleophilic attack by the active chain end.[21] The mechanism for the formation of an N-formyl intermediary by product, and its subsequent chain extension reaction with a further active chain end, are presented in **Scheme 5.2** below.

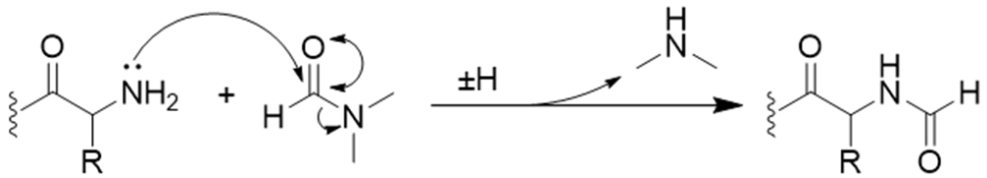

Scheme 5.2: Mechanism for the formation of an N-formyl by-product *via* reaction of the active chain end with DMF. Subsequent attack by a further chain end introduce chain extension.

An additional potential side-reaction was highlighted by Vayaboury *et al*., in which reaction of the active chain end with the carbamate carbon of an NCA monomer generates a ureido-acid functional end group, which can again undergo nucleophilic attack by a growing polymer *via* several reactive routes, to generate a host of chain-extended by-products. The mechanism for the formation of this intermediary product and its subsequent chain extension pathways are provided in **Scheme 5.3**.

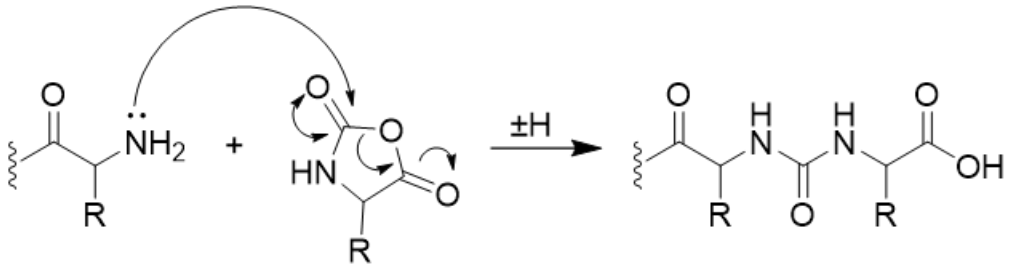

Scheme 5.3: Mechanism for the formation of a ureido-acid by-product *via* reaction of the active chain end with DMF. Subsequent attack by a further chain end reveals routes to chain extension.

These pathways highlight potential side-reactions that could cause chain extension, and routes to the high-M.W. products observed for **BC197** and **BC198**. Vayaboury *et al*. discuss the impact of DMF as a solvent in the generation of active intermediary by-products. For this reason, reactions were planned to investigate the ROP of Lys(Boc)-NCA from $mPEG_{113}$-NH_2 using anhydrous THF as a reaction solvent, as well as reduced temperature reactions, to investigate whether these factors could reduce the presence of unwanted by-products and

reduce the multimodality of the resultant peaks. As discussed in **Section 1.1.3**, the importance to tightly-controlled uniformity in these polymer products is the conveyed effects that this has on resultant size, shape and stability of derived nanoparticles and drug delivery vehicles. For this reason, optimisation of product uniformity is of paramount importance to this project.

5.3.5 Lys(Boc)-NCA ROP Reaction Optimisation

5.3.5.1 Investigating Solvent Variation

THF has here been evaluated as an alternative solvent system to DMF. This is due both to its sufficient capability to dissolve both Lys(Boc)-NCA and $mPEG_{113}$-*b*-$PLys(Boc)_n$ copolymer systems, as well as its significantly lower potential for interaction with the polar active chain end during NCA ROP. Not only is THF unable to hydrogen bond, unlike DMF, but it also possesses a significantly reduced polarity, as evidenced by its decreased dielectric constant (ca. 36.7 vs. 7.6) and dipole moment (1.75 D vs. 3.82 D) in comparison to DMF. When dissolved in THF, the likelihood for electrostatic and hydrogen bonding interactions between the active chain end and solvent system are greatly reduced, which consequently decreases screening of the active nucleophile and allows for more efficient nucleophilic attack. This acts to increase the rate of propagation preferentially, and thereby reduces opportunities for side-reactions during the decreased residence time in solution. Furthermore, the use of THF eliminates all possibilities for reaction with the solvent, avoiding the generation of unwanted N-formyl groups and subsequent chain extension reactions.

The effectiveness of THF as a solvent system was evaluated across two NCA ROP reactions of Lys(Boc)-NCA from $mPEG_{113}$-NH_2, targeting 5 and 10 repeat units, respectively. This was done to allow comparison of the system to the successful **BC195** case, and to evaluate the level to which bimodality could be decreased in relation to **BC196**. Preparative methodology for these reactions is presented in **Section 5.2.6.1**, and highlights the use of a small-batch reactor as opposed to the round-bottom flask layout used for **BC195-198**. However, this reaction was still performed under anhydrous conditions and a dry N_2 atmosphere, over the course of 24 hours and under a maintained temperature of 25 °C. As such, any differences in experimental procedure can be considered of negligible impact. Due to constraints on the available SEC technology, only aqueous eluent was available for these materials, and so deprotection was carried out prior to data acquisition.

Deprotection was performed in an identical manner to the previous polymer products, and characterisation and yield calculations are provided in **Section 5.2.6.1**. ^{1}H NMR spectroscopy data for these products can be found in **Section A.5.1**. The SEC chromatograms for **BC212D** and **BC213D** are presented in **Figure 5.17** below.

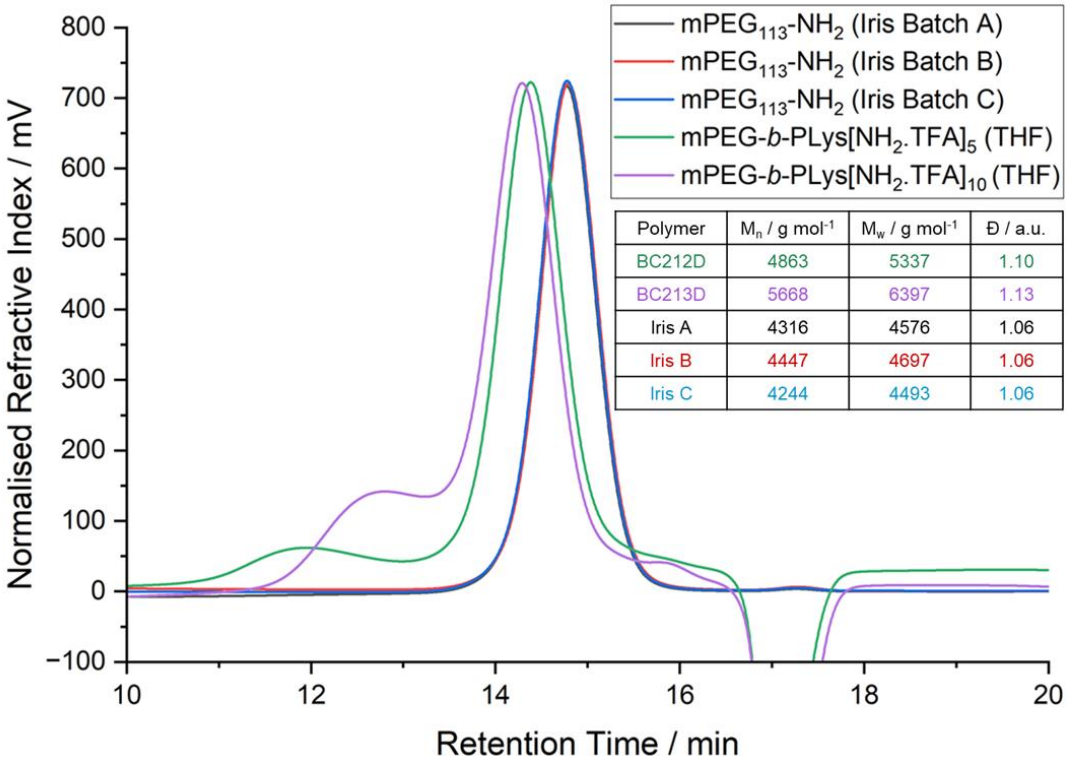

Polymer	M_n / g mol^{-1}	M_w / g mol^{-1}	Đ / a.u.
BC212D	4863	5337	1.10
BC213D	5668	6397	1.13
Iris A	4316	4576	1.06
Iris B	4447	4697	1.06
Iris C	4244	4493	1.06

Figure 5.17: Normalised SEC-TDA of deprotected block copolymers, synthesised *via* NCA-ROP in THF. Run in TFA-Aqueous eluent.

As can be seen in **Figure 5.17**, whilst NCA ROP has been carried out successfully, with an upward shift in molecular weight visible for both materials, there still exists significant shoulder peaks on the left-hand side of traces for both **BC212D** and **BC213D**, in addition to some small tailing on the right hand side also. These effects are reflected in the Đ values for each polymer, which have been inflated from those of the $mPEG_{113}$-NH_2 batches by 0.04 and 0.07, respectively. Whilst the identity of the high-M.W. impurities can only be speculated upon, important observations can be drawn from the M_n data available for the products. For each polymer reduced growth compared to that expected by the targeted D.P. was achieved, with **BC212D** increasing in M_n by only 547 g mol^{-1}, corresponding to an increase of ca. 2-3 repeat units.

BC213D experienced a larger increase of 1221 g mol^{-1}, corresponding to ca. 5 repeat units, but still fell short of the 10 repeat unit increase intended. This can be compared similarly to the DMF case, in which higher-M.W. materials were responsible for significant monomer consumption, restricting the attainable D.P. for the main chain.

This could again be attributed to a bifunctional starting material or potential crosslinking interactions, as was discussed in **Section 5.3.4**, but without additional analysis to separate and identify the left-side impurities present, no conclusive characterisation can be achieved. Whilst further examination is required to determine the exact identity of these high-M.W. materials, it was still concluded here that THF as a solvent system did not provide the desired correction to uniformity in comparison to DMF products. As such, attention was turned to reduced temperature reactions as a method of reducing errant side-reaction.

5.3.5.2 Investigating Temperature Variation

As was outlined by Deming *et al*., the reduction of reaction temperature during NCA ROP has marked effects on the resultant purity of the polymer product, due to preferential monomer consumption by the active chain end favouring chain propagation and improving uniformity.[22] This was due to the lower activation energy barrier of propagation, and corresponding suppression of errant side reactions such as chain extension.

However, decreasing solvent temperature also increases viscosity which, as discussed by Deming *et al*., can lead to poor monomer diffusion and detrimentally impact the uniformity of chain growth.[22] As such, observations of changes to viscosity with decreasing temperature were noted during the reaction. Fortunately, no significant effects upon viscosity were observed at the temperatures investigated. Another issue with reduced temperature reaction is the negative effects that low temperatures can impart upon product solubility, especially as the length of the hydrophobic chain grows and unfavourable solvent-chain interactions are compounded. Poor solubility, especially of the growing chain end, can restrict the ability of the active chain to continue propagation, effectively limiting the final degree of polymerisation to the maximum attainable value in solution.

Therefore, once samples of NCA were equilibrated to the intended reaction temperature, they were re-examined for solubility issues, and samples with poor solubility were excluded from the investigation. For this reason, NCA ROP below 10 °C was not conducted.

SEC data for **BC210D** and **BC211D**, conducted at 10 °C and 20 °C respectively, are presented in **Figure 5.18** alongside the traces for **BC196D** and $mPEG_{113}$-NH_2. Each of these reactions targeted 10 PLys(Boc) repeat units.

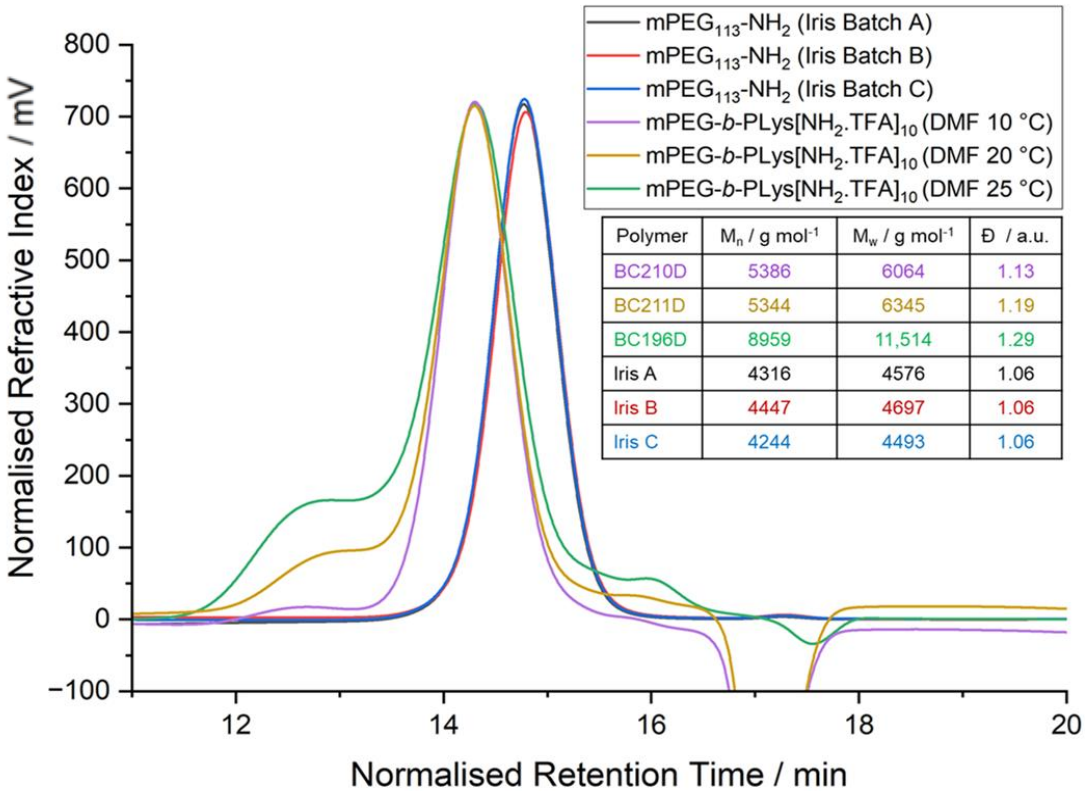

Polymer	M_n / g mol^{-1}	M_w / g mol^{-1}	Đ / a.u.
BC210D	5386	6064	1.13
BC211D	5344	6345	1.19
BC196D	8959	11,514	1.29
Iris A	4316	4576	1.06
Iris B	4447	4697	1.06
Iris C	4244	4493	1.06

Figure 5.18: SEC-TDA of deprotected block copolymers BC210D and BC211D, synthesised at reduced temperature in DMF, alongside traces for mPEG-NH_2 and BC196D.

A number of promising observations can be made from **Figure 5.18**. Initially, it can be observed that polymerisation has successfully occurred in each reduced-temperature case, within the allotted 24-hour reaction time and, for both **BC210D** and **BC211D**, each polymer has achieved the same value for M_p as the room-temperature example, suggestive that the main peaks have grown sufficiently. This is further corroborated by the increased values for M_n reported in **Figure 5.18**, with increases of 1070 g mol^{-1} and 1028 g mol^{-1}, respectively, corresponding to approximate increases of 4-5 repeats units.

Whilst this increase does not reflect the targeted D.P. for the polymerisation, the values are in close agreement with estimations derived from ^{1}H NMR (**Section A.5.1**).

It is possible that, due to the reduced temperature of reactions, propagation rate was suppressed such that Lys(Boc)-NCA molecules were left unreacted. Nevertheless, it is excellent that a trend can be observed with decreasing temperature within **Figure 5.18**. Visually, it is clear that the lower temperature reactions experience a reduction in the presence of high-M.W. and low-M.W. impurities, as evidenced by the decrease in area of the left-hand shoulder and right-hand tail between **BC196D**, **211D** and **210D**. This is further corroborated by the sharp decrease in M_n observed within **Figure 5.18**, between **BC196D** and the products of reduced-temperature reactions (3573 g mol^{-1} and 3615 g mol^{-1}, respectively). This can be attributed to the significant decrease in area of the right-hand shoulder peak, which has inflated the M_n and M_w value of **BC196D**. As a consequence of this reduced inflation, a trend can also be observed between decreasing reaction temperature and a decrease in Đ for the products. Within **Figure 5.18** it can be seen that Đ values for **BC210D/211D** decrease by 0.16 and 0.10, respectively, from the Đ value presented for **BC196D**. This suggests a significant increase in uniformity for the product can be achieved with *via* reaction at decreased temperature, a phenomenon which can be exploited to produce a product capable of more stable nanoparticle formation and, theoretically, greater resistance to burst release and leakage during transit of therapeutic payloads.

To generate polymer products of mPEG$_{133}$-*b*-PLys[NH$_2$.TFA]$_n$ (where n=10, 20), of sufficient batch size for subsequent post-polymerisation modification, reduced-temperature (10 °C) reactions were performed, *via* the preparative methodology described in **Section 5.2.6.2**. Conditions were kept as closely aligned with the successful **BC210** reaction as possible, and deprotection was subsequently performed using the identical techniques to all cases previous. The chromatograms of these reactions and of mPEG$_{113}$-NH$_2$, as well as their corresponding molecular weight data, are presented in **Figure 5.19** below.

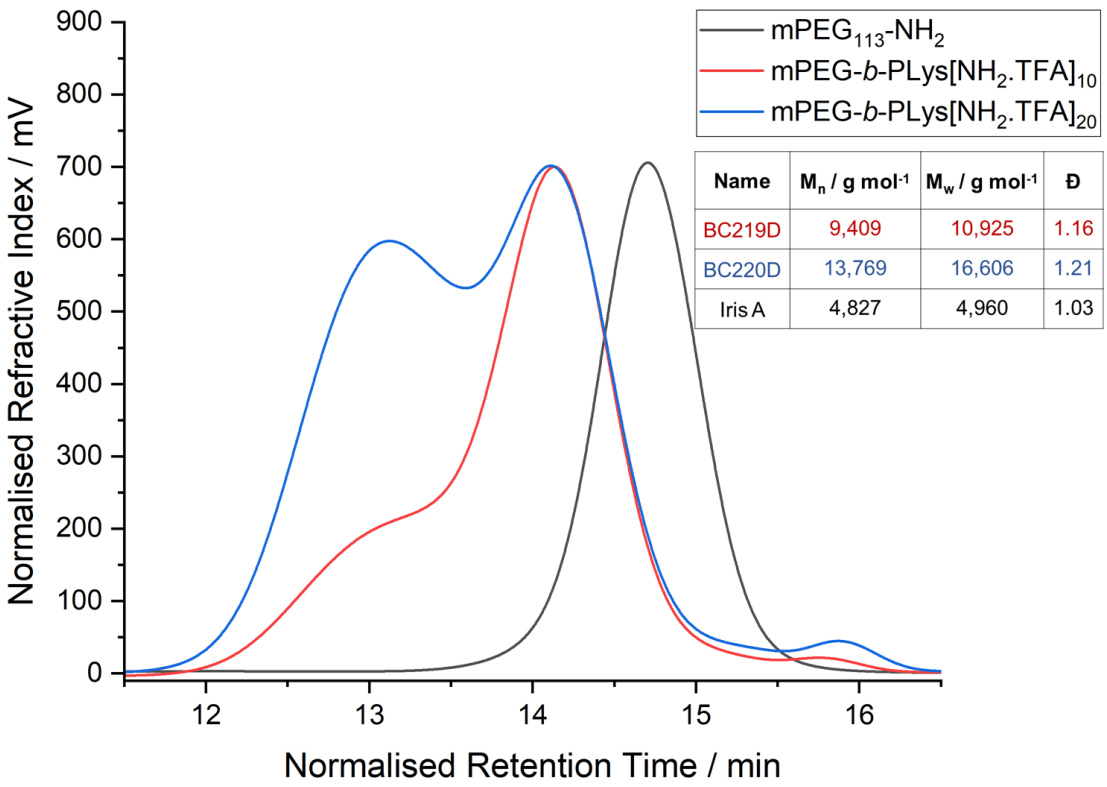

Name	M_n / g mol^{-1}	M_w / g mol^{-1}	Đ
BC219D	9,409	10,925	1.16
BC220D	13,769	16,606	1.21
Iris A	4,827	4,960	1.03

Figure 5.19: Normalised SEC-TDA of deprotected block copolymers **BC219D** and **BC220D**, synthesised *via* NCA-ROP under reduced temperature. Run in TFA-Aqueous eluent.

As can be seen within **Figure 5.19**, for these larger product batches, significant bimodality still remains within the product chromatograms. This is presented as a prominent shoulder in the case of **BC219D** and as a broadly overlapping secondary peak in the case of **BC220D**. In addition, it can be observed that there is significant increase in the value of Đ for each polymer over mPEG-NH_2 (0.13 and 0.18, respectively), as a direct consequence of this. Furthermore, the M_n values for these polymers are significantly inflated from the intended target, with the increase of ca. 4500 g mol^{-1} for **BC219D** corresponding to a Lys[NH_2.TFA]$_n$ D.P. of ca. 19, near double the expected value given the molar equivalents inputted into the reaction. This is only more pronounced for **BC220D**, for which the increased M_n corresponds to an D.P. of 37, again far more than should be possible given the initial [M]:[I] ratio. This unexpected resurgence of multimodality suggests that, with increased batch size, reduction in temperature is insufficient to reduce opportunities for side reaction.

The monomer concentrations for these reactions remained comparable to that of **BC210** ($[M]_{210}$:$[M]_n$ ratio 1:0.66 and 1:1, respectively) and as such, low dilution and the corresponding effects of high viscosity and poor monomer diffusion can be ruled out here as contributors to errant side-reactions. Whilst these products exhibit poorer uniformity than was desired for the final product, they have been taken forward for post-polymerisation modification and subsequent drug release analysis throughout **Section 6**. This was due to significant time constraints on the project, and the necessity to maintain forward momentum towards a completed product.

5.4 Conclusions and Future Work

In conclusion, extensive investigation of the ROP for each NCA system (Lys(Fmoc)-NCA, Lys(Z)-NCA and Lys(Boc)-NCA) has been performed, with specific optimisation of Lys(Boc)-NCA ROP *via in situ* FTIR monitoring and SEC analysis. ^{1}H NMR monitoring during Lys(Fmoc)-NCA ROP revealed that long reaction times were detrimental to propagation of the polymer chain, due to *in situ* Fmoc-deprotection facilitated by the DMAP catalyst system. Following this, NCA ROP of Lys(Z)-NCA from the mPEG-NH_2 was carried out successfully, as well as deprotection of the mPEG-*b*-PLys(Z)$_n$ products to yield block copolymers with free lysine side chains.

Lys(Boc)-NCA was monitored *via in situ* FTIR analysis. Products were obtained in good yield and characterised by ^{1}H NMR and SEC analyses. For mPEG-*b*-PLys(Boc)$_n$ products with n > 5, multi-modality was observed within the products. To ensure that this issue did not stem from methodological effects, the products underwent deprotection and were re-analysed *via* SEC under aqueous conditions. The observed multimodal distribution was maintained and further investigation was undertaken into exploring alternative NCA ROP conditions to limit generation of unwanted by-products that may have contributed. In line with suggestions by Deming *et al*., NCA-ROP of Lys(Boc)-NCA was successfully carried out in THF solvent and at reduced reaction temperature (10 °C, 20 °C). Excitingly, it was observed at 10 °C that a proportional reduction in high-M.W. impurities had occurred evidenced by a stark decrease in both M_n and Đ values compared to the 25 °C product (**BC196D**). These data indicated a preferable route to mPEG-*b*-PLys(Boc)$_n$ polymers for n > 5. Subsequently, synthesis of mPEG-*b*-PLys(Boc)$_{10}$ and mPEG-*b*-PLys(Boc)$_{20}$ at larger scale were conducted successfully at 10 °C.

In summation, a controlled and reproducible route for the synthesis of mPEG-*b*-PLys[NH_2.TFA]$_n$ (n = 5, 10 and 20) was here demonstrated. Boc-deprotection was performed with high yield and purity, affording products capable of post-polymerisation modification (PPM).

For future development, it is pertinent to explore other alternative NCA ROP solvent systems, as well as providing a deeper exploration of THF solvation and control. Examples include DMAc, which should be considered for its improved polymer solvation and reduced toxicity, as well as cyrene, for reduced environmental impact. Additionally, future exploration of alternative SEC solvents (HFIP, TFA) and detection methods (MALS, MALDI-TOF MS) would allow decoupling of non-specific interactions or aggregation from true molecular weight values for the polymers, allowing more accurate assessment of synthetic progress.

These products represent a conclusion to the iterative experimental pathway outlined for optimised synthesis mPEG-*b*-PLys[NH_2.TFA] BCPs and a step forward in the broader synthesis of SN38-conjugated mPEG-*b*-PLys. This research builds upon the work of Chen *et al*. and Agwa *et al*. in the fast and controlled synthesis of PLys-based amphiphilic BCPs for drug delivery, and discusses measures to eliminate unwanted by-production of high-M.W. impurities using methods first elucidated by Deming *et al.* in 1997.[23-25] The successful reduction of peak area at low retention times for **BC210D** *via* ROP at low temperature opens for discussion a wide range of synthetic strategies that could be explored to improve control of final product M.W. and uniformity. This is vital for the application of mPEG-*b*-PLys drug delivery systems across the pharmaceutical industry.

5.5 References

1. Lim, C. W.; Han, S. H.; Kim, D., *J. Mater. Chem. B*, **2015**, 3, 1434–1443.
2. Golla, K.; Reddy, P. S.; Bhaskar, C.; Kondapi, A. K., *Drug Deliv.*, **2013**, 20, 156–167.
3. T. Oishi, Y. Nagasaki, N. Itaka, N. Nishiyama and K. Kataoka**,** *Biomacromolecules*, **2005**, *6*, 2449–2454.
4. Lee, C. C.; MacKay, J. A.; Fréchet, J. M. J.; Szoka, F. C., *Nat. Biotechnol.*, **2005**, 23, 1517–1526.
5. Medina, S. H.; El-Sayed, M. E. H., *Chem. Rev.*, **2009**, 109, 3141–3157.
6. Y. Wang, Y. Zhang, X. Zhang, X. Yang, *Eur. J. Pharm. Biopharm.*, **2020**, *152*, 16–24.
7. S. K. Mishra, R. S. Kesharwani, A. K. Jain, *Int. J. Nanomedicine*, **2019**, *14*, 6131–6145.
8. Y. Liu, Y. Zhang, Y. Liu, X. Wang, *J. Mater. Chem. B*, **2019**, *7*, 2761–2770.
9. Y. Wang, Y. Liu, Y. Liu, Y. Zhang, *RSC Adv.*, **2023**, *13*, 12345–12354.
10. D. Mavrogiorgis, P. Bilalis, A. Karatzas, D. Skoulas, G. Fotinogiannopoulou, and H. Iatrou, *Polym. Chem.*, **2014**, *5*, 6256–6278.
11. Aliabadi, H. M.; Lavasanifar, A. *Expert Opin. Drug Delivery* **2006**, 3, 139−162.
12. Q. Yu, R. M. England, A. Gunnarsson, R. Luxenhofer, K. Treacher and M. B. Ashford**,** *Macromolecules*, **2022**, *55*, 171–183.
13. Fields, G. B.; Noble, R. L. *Int. J. Pept. Protein Res.* **1990**, *35*, 161–214.
14. Hall, H. K., Jr. *J. Am. Chem. Soc.* **1957**, *79*, 5441–5444.
15. Luna, O. F.; Gomez, J.; Cárdenas, C.; Albericio, F.; Marshall, S. H.; Guzmán, F. *Molecules* **2016**, *21*, 1–12.
16. J. E. S. Schier and R. A. Hutchinson, *Polym. Chem.*, **2016**, *7*, 4567–4574.
17. Kodaira, T., Yang, J.-Z., & Aida, H., *Polym. J.* **1988**, *20*, 1021–1029
18. A. Berthod, *J. Chromatogr. A*, **1997**, *780*, 1–12.
19. A. De Wit, Y. Bertho, M. Martin, *Phys. Rev. Lett.*, **2005**, *95*, 044501.
20. Gritti, F.; Chen, E. Y.; Datta, S. S. *Proc. Natl. Acad. Sci. U.S.A.* **2024**, *121*, e2320962121.
21. Vayaboury, W.; Giani, O.; Kricheldorf, H. R. *Macromol. Chem. Phys.* **2004**, *205*, 1392–1399.
22. Cheng, J.; Deming, T. J. *Polymerization of N-Carboxyanhydrides*; Deming, T. J., Ed.; Springer: Berlin, **2011**; pp 1–26.

23. Deming, T. J., *Adv. Mater.*, **1997**, *9*, 299–311.

24. Chen, K.; Wu, Y.; Liu, R., *ACS Cent. Sci.*, **2024**, *10*, 1234–1243.

25. Agwa, M. M.; Thakkar, S.; Erothu, H.; Korupolu, R.; Khan, N.; Dandamudi, R. B., *RSC Adv.*, **2024**, *14*, 23520–23542.

A.5.1 ^{1}H NMR Spectra

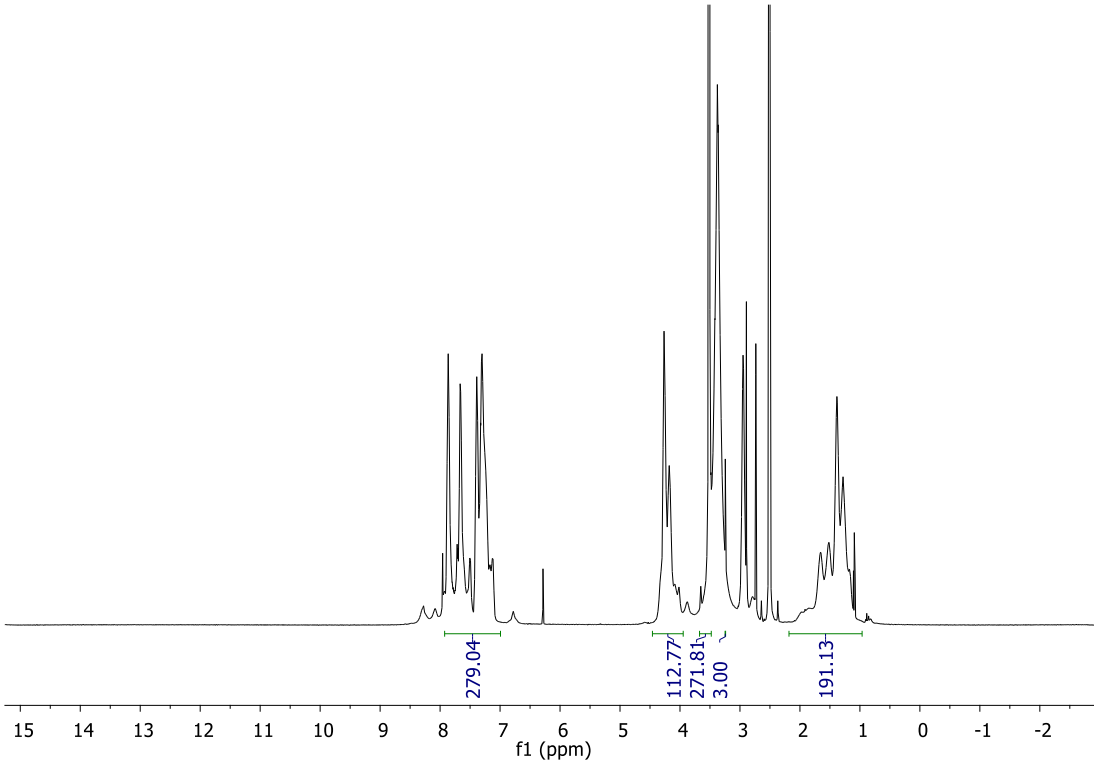

Figure A.5.1.1: ^{1}H NMR spectrum (500 MHz, DMSO-d_6) of **BC56** (24 h).

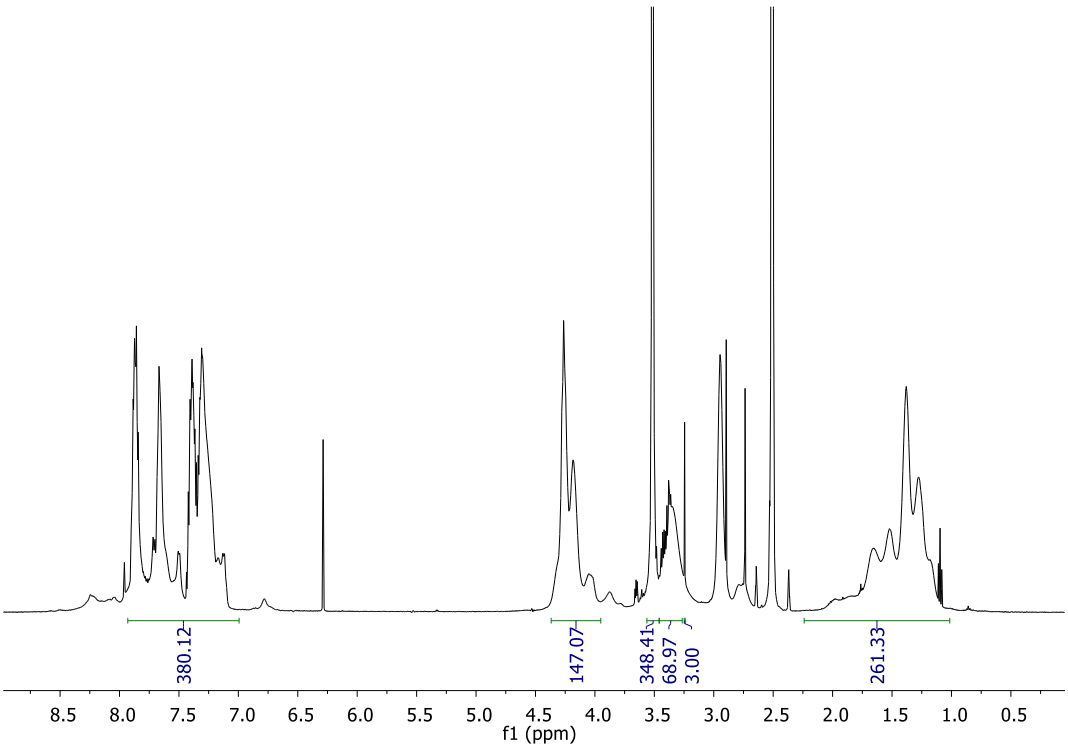

Figure A.5.1.2: ^{1}H NMR spectrum (500 MHz, DMSO-d_6) of **BC56** (48 h).

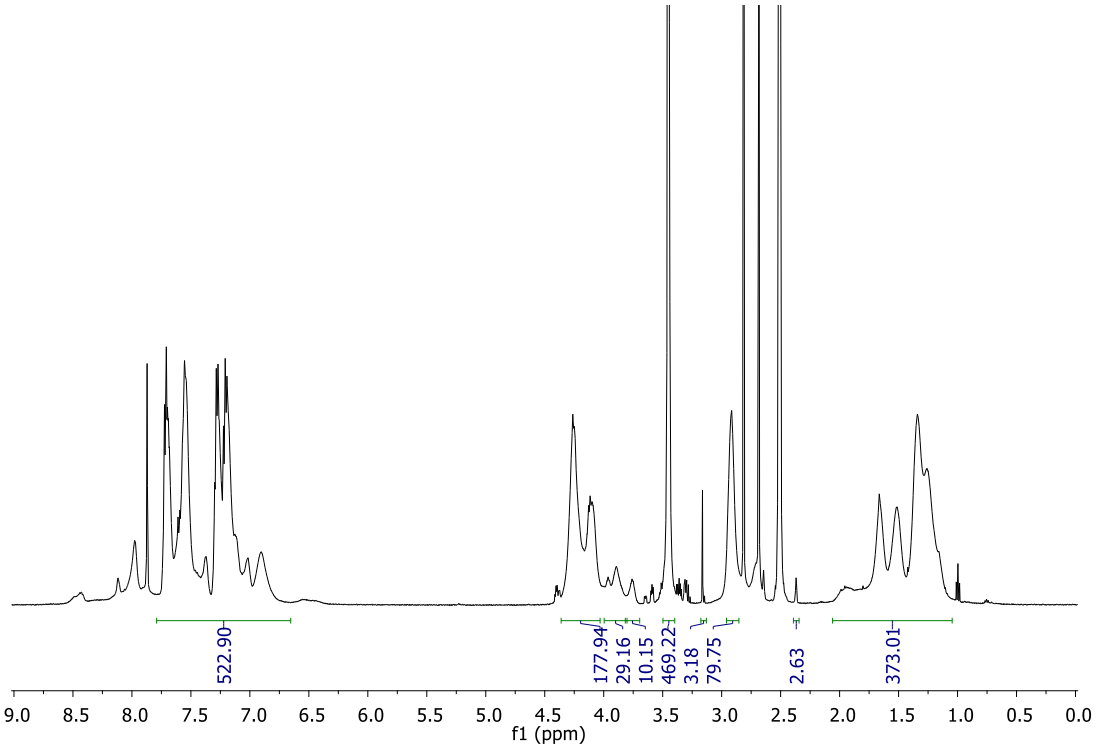

Figure A.5.1.3: ^{1}H NMR spectrum (500 MHz, DMSO-d_6) of **BC56** (72 h).

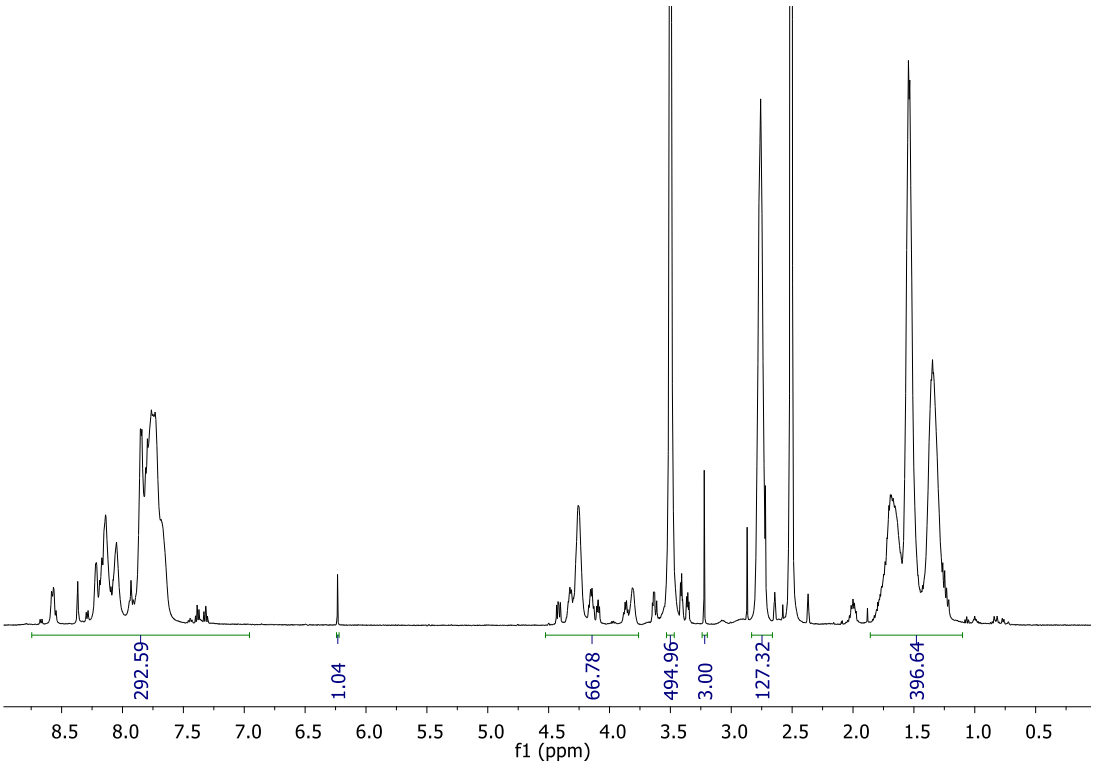

Figure A.5.1.4: ^{1}H NMR spectrum (500 MHz, DMSO-d_6) of **BC56** (96 h).

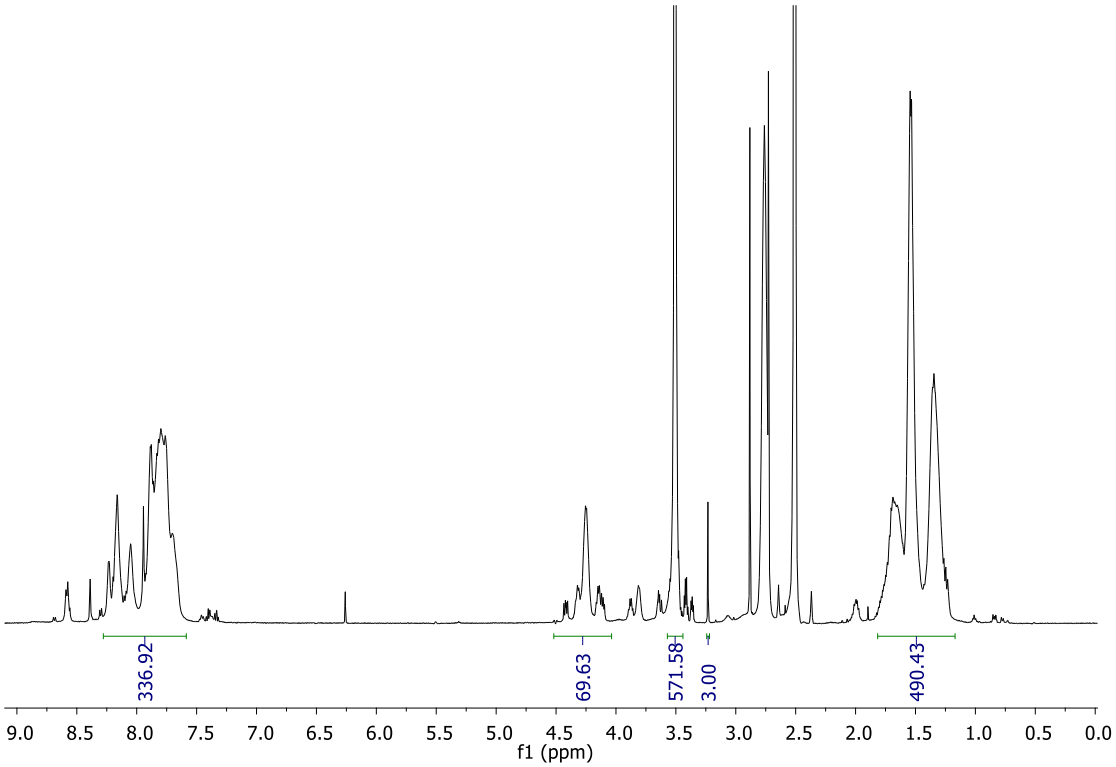

Figure A.5.1.5: ^{1}H NMR spectrum (500 MHz, DMSO-d_6) of **BC56** (164 h).

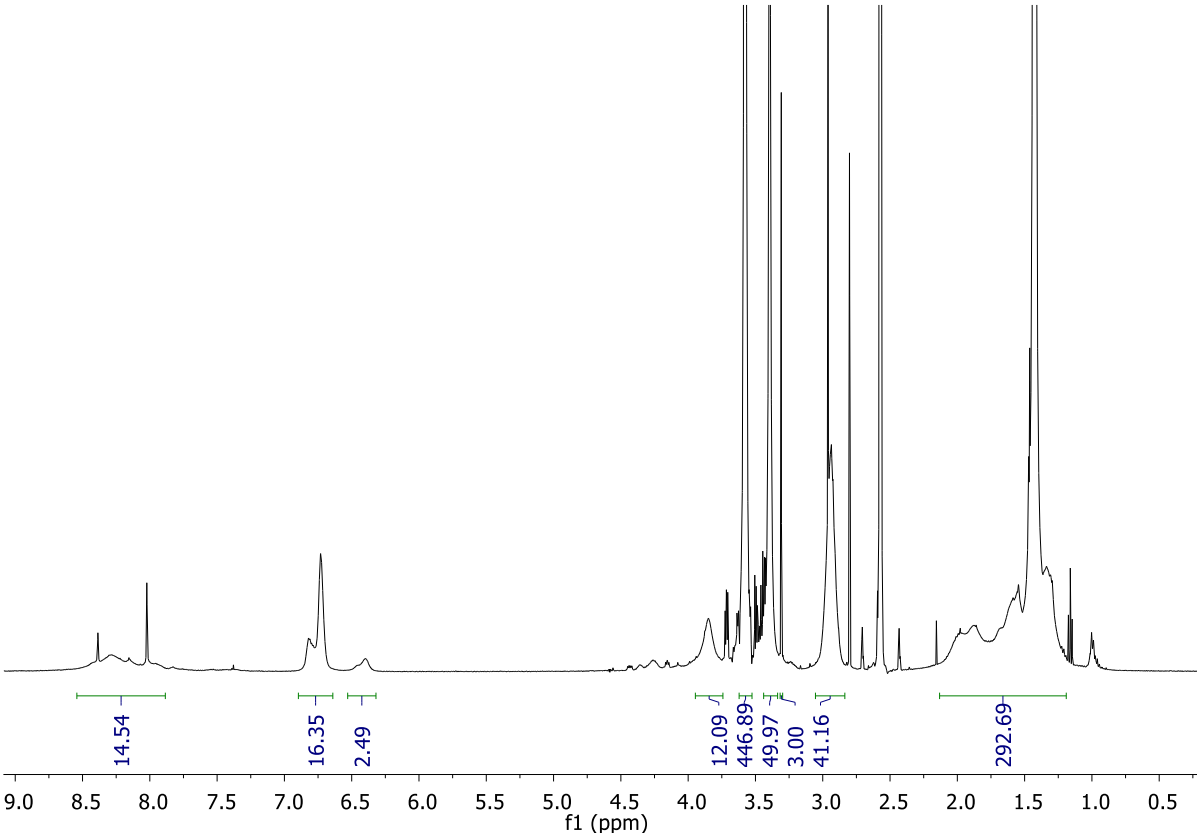

Figure A.5.1.6: ^{1}H NMR spectrum (500 MHz, DMSO-d_6) of **BC180**, mPEG-*b*-PLys(Boc).

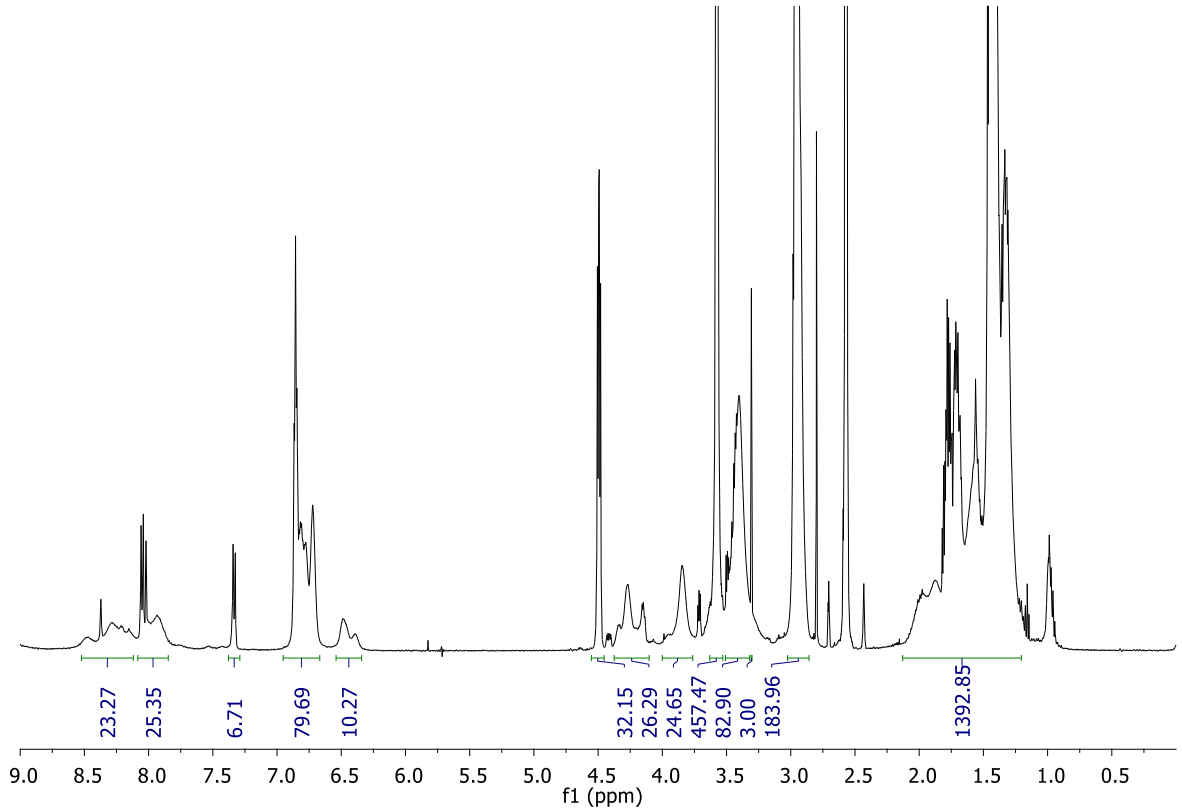

Figure A.5.1.7: ^{1}H NMR spectrum (500 MHz, DMSO-d_6) of **BC181**, mPEG-*b*-PLys(Boc).

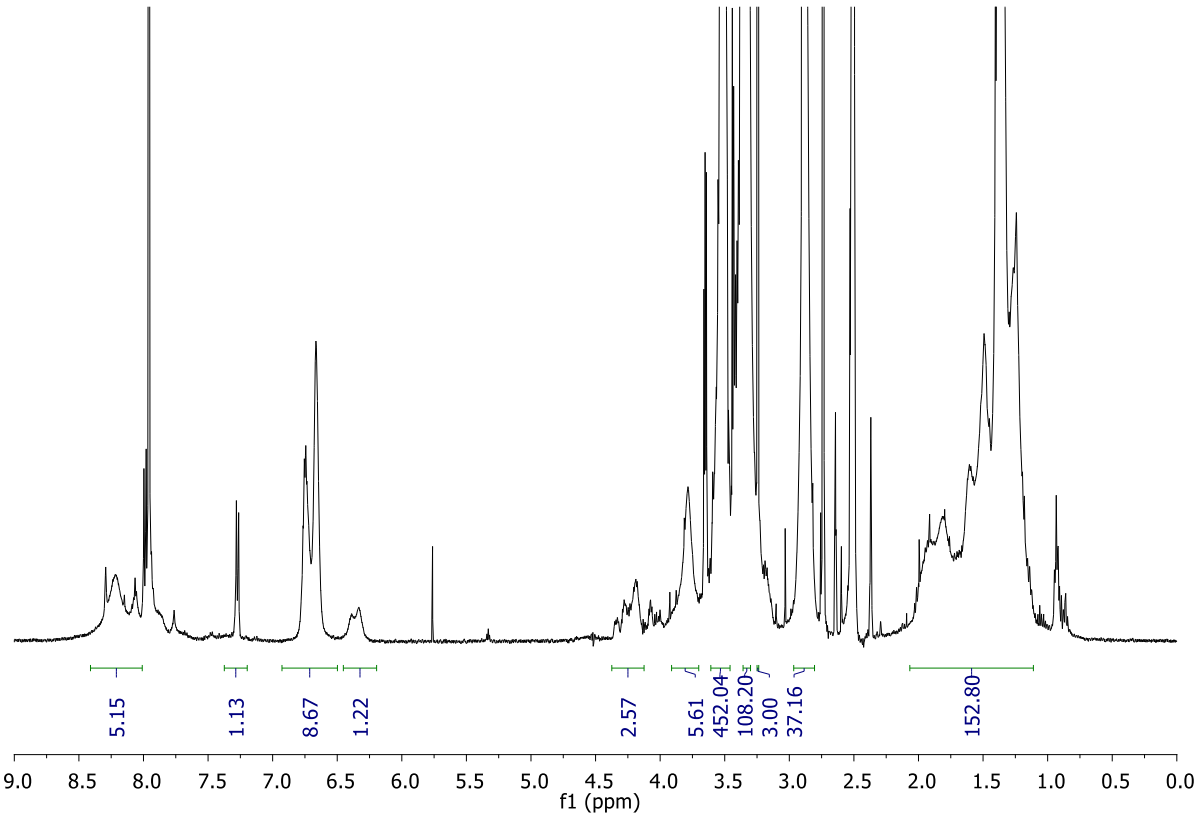

Figure A.5.1.8: ^{1}H NMR spectrum (500 MHz, DMSO-d_6) of **BC183,** mPEG-*b*-PLys(Boc).

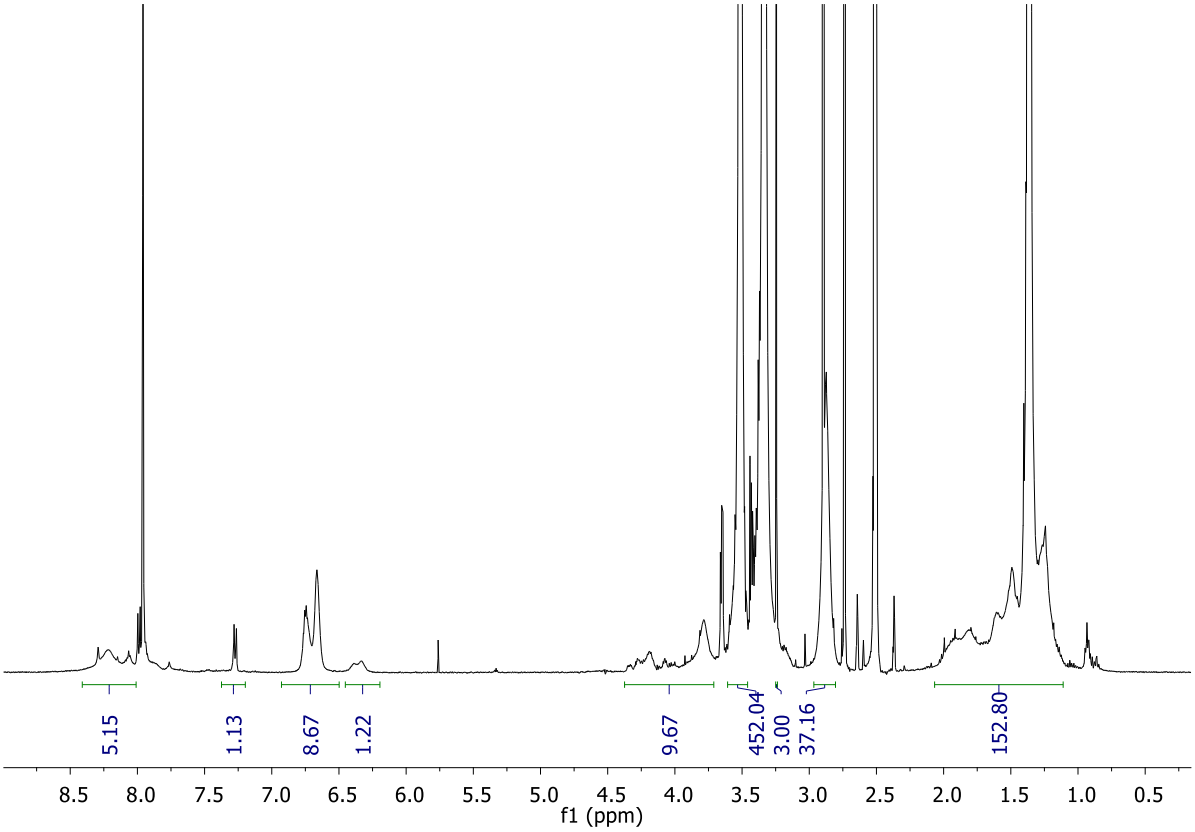

Figure A.5.1.9: ^{1}H NMR spectrum (500 MHz, DMSO-d_6) of **BC184**, mPEG-*b*-PLys(Boc).

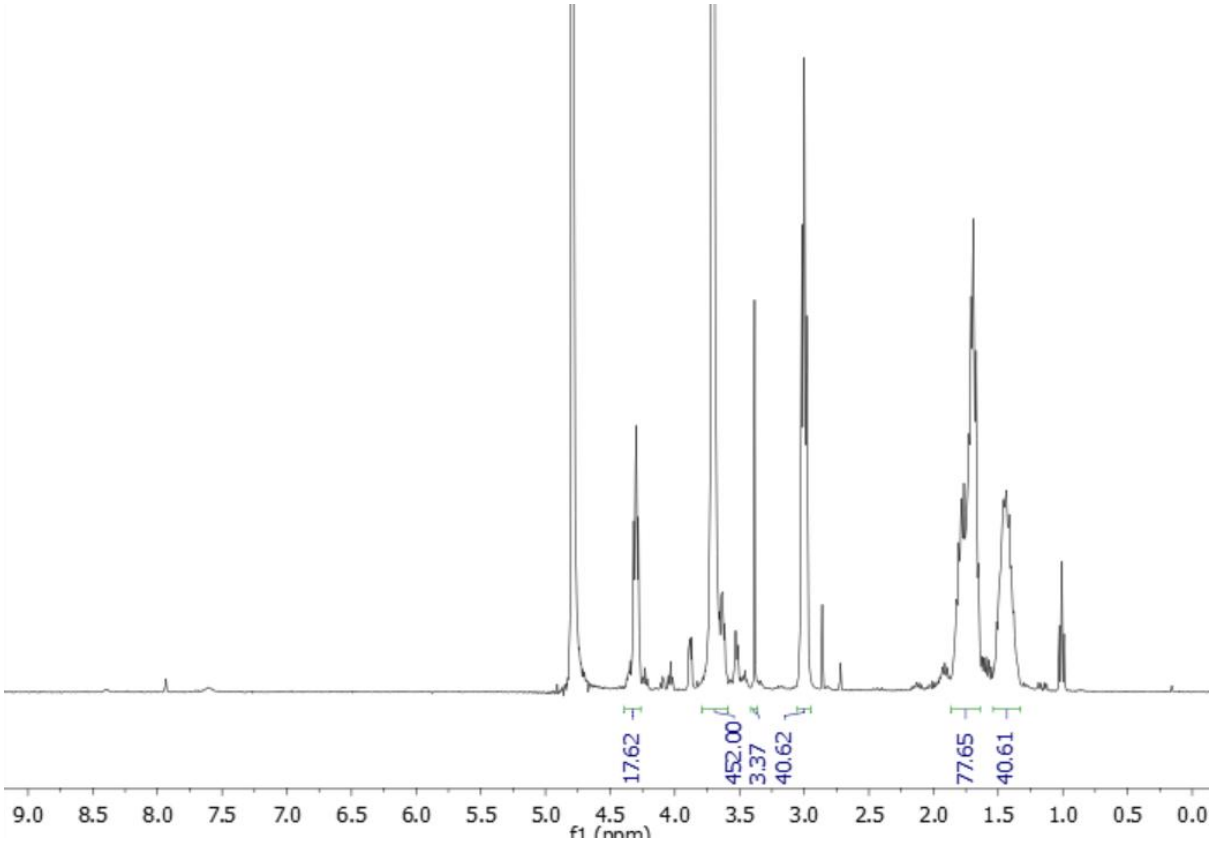

Figure A.5.1.10: ^{1}H NMR spectrum (500 MHz, DMSO-d_6) of **BC187**, mPEG-*b*-PLys[NH_2.TFA].

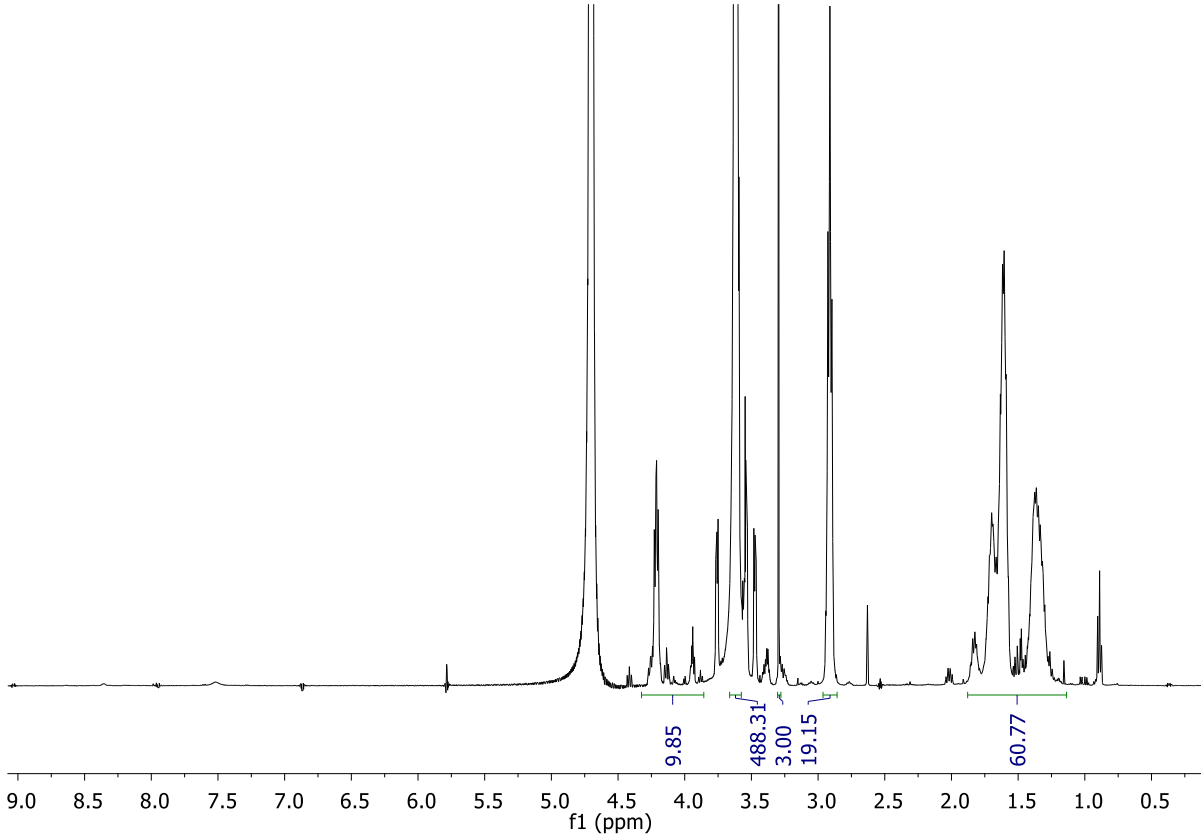

Figure A.5.1.11: ^{1}H NMR spectrum (500 MHz, DMSO-d_6) of **BC190**, mPEG-*b*-PLys[NH_2.TFA].

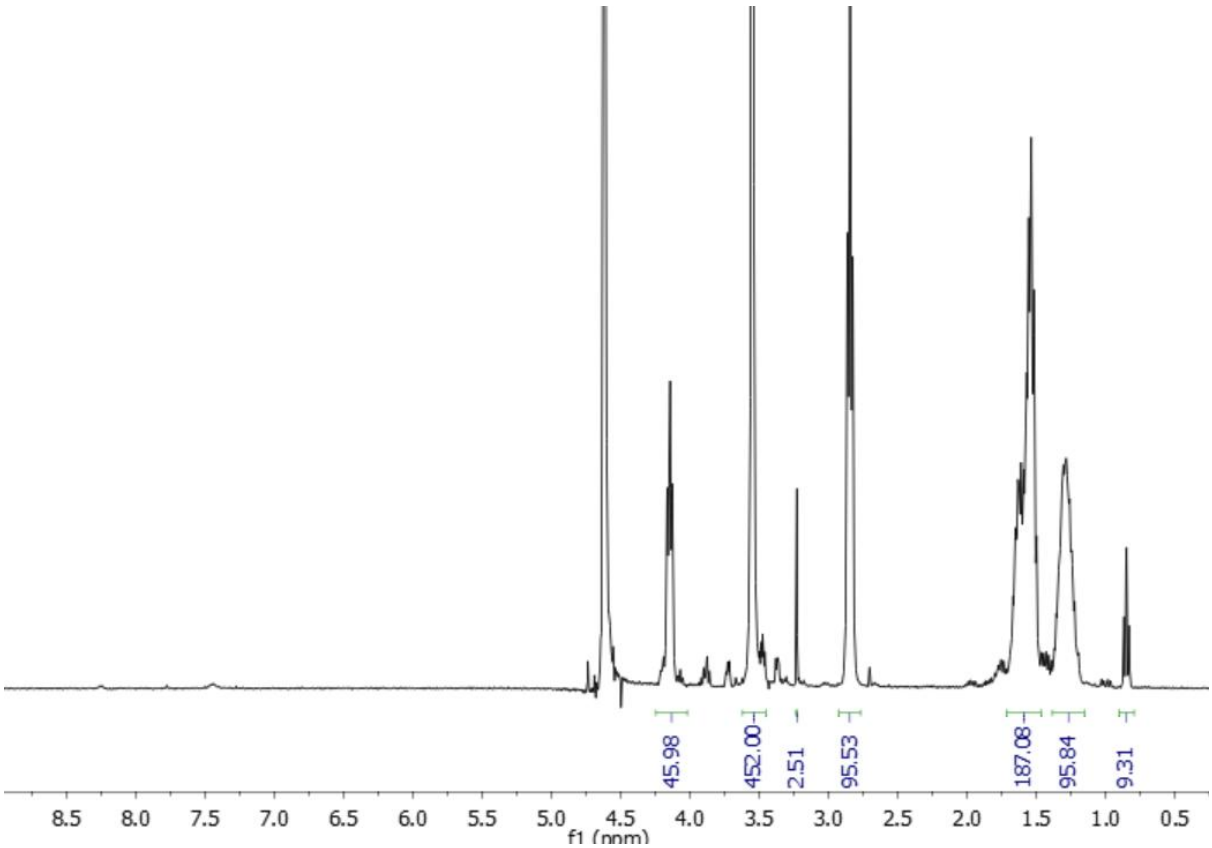

Figure A.5.1.12: ^{1}H NMR spectrum (500 MHz, DMSO-d_6) of **BC193**, mPEG-*b*-PLys[NH_2.TFA].

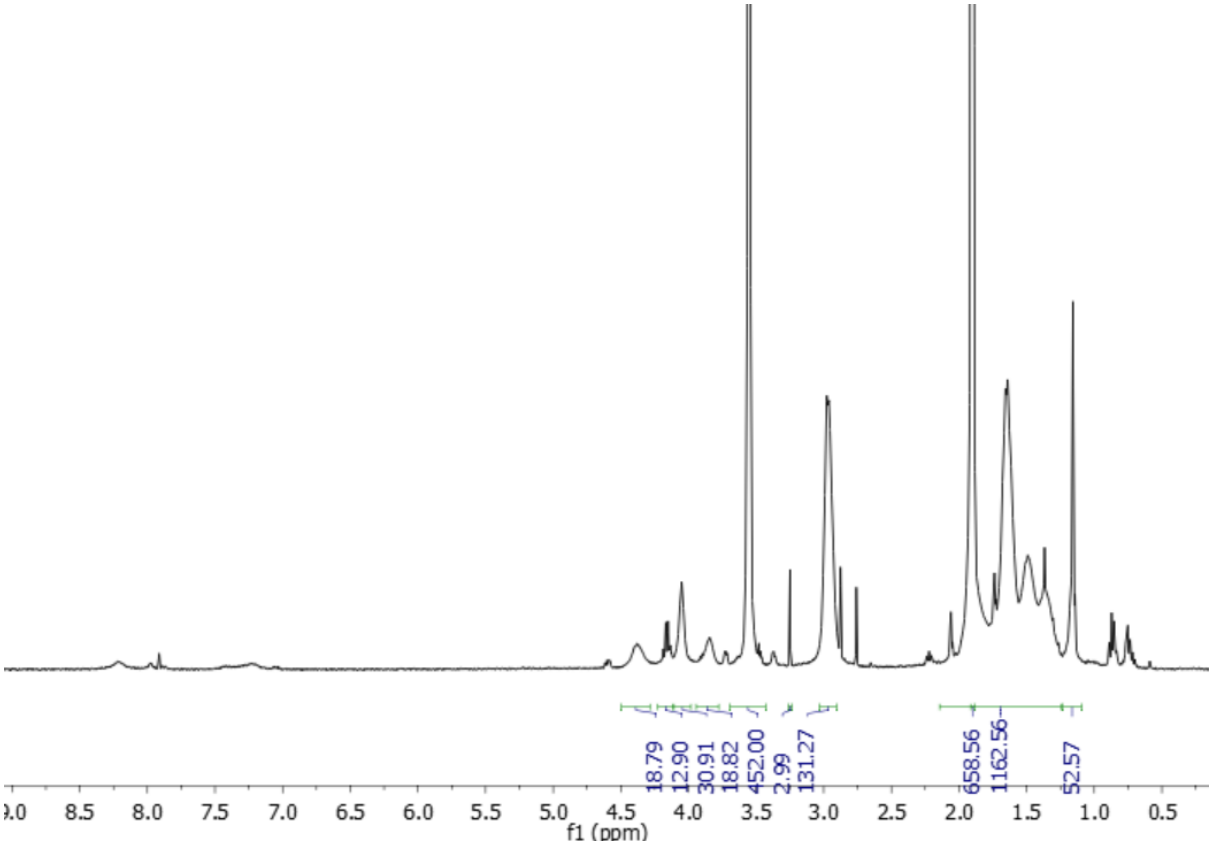

Figure A.5.1.13: ^{1}H NMR spectrum (500 MHz, DMSO-d_6) of **BC188**, mPEG-*b*-PLys[NH_2.TFA].

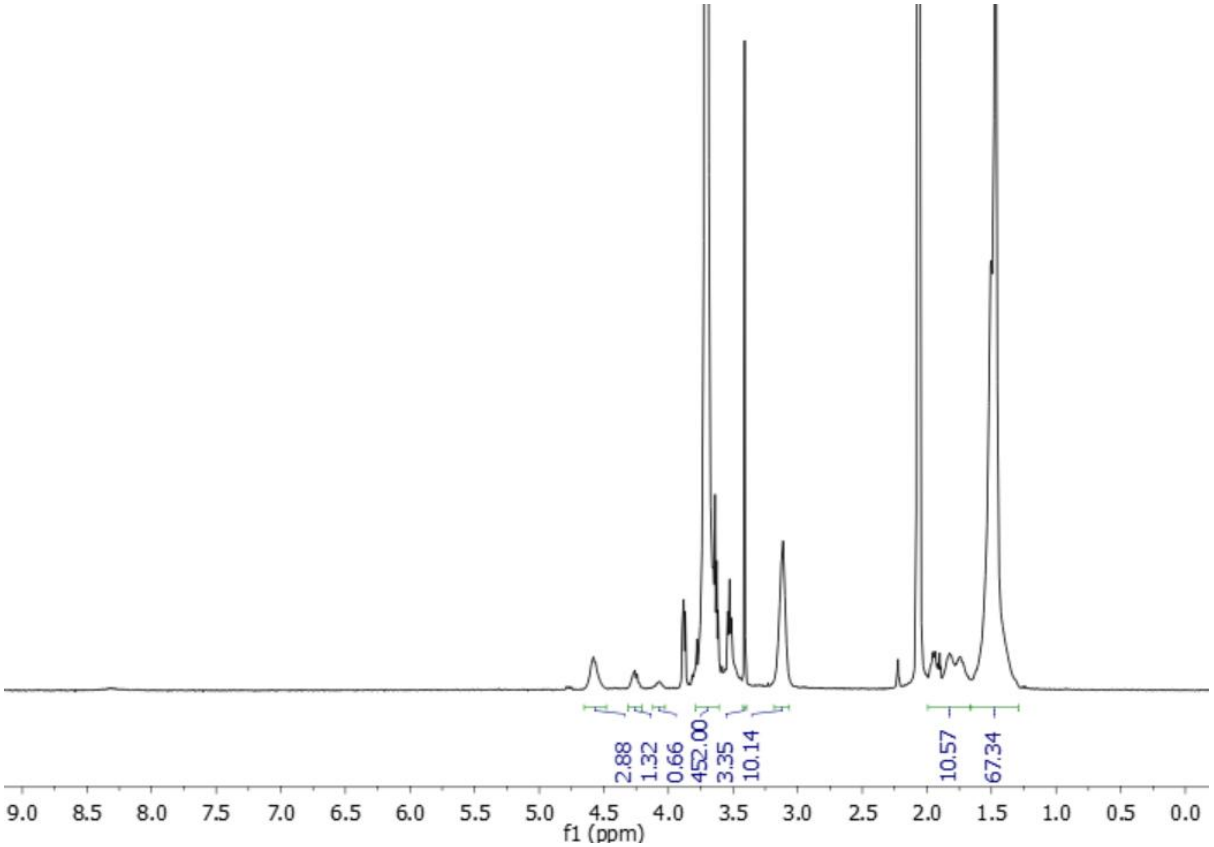

Figure A.5.1.14: ^{1}H NMR spectrum (500 MHz, DMSO-d_6) of **BC195** mPEG-*b*-PLys(Boc).

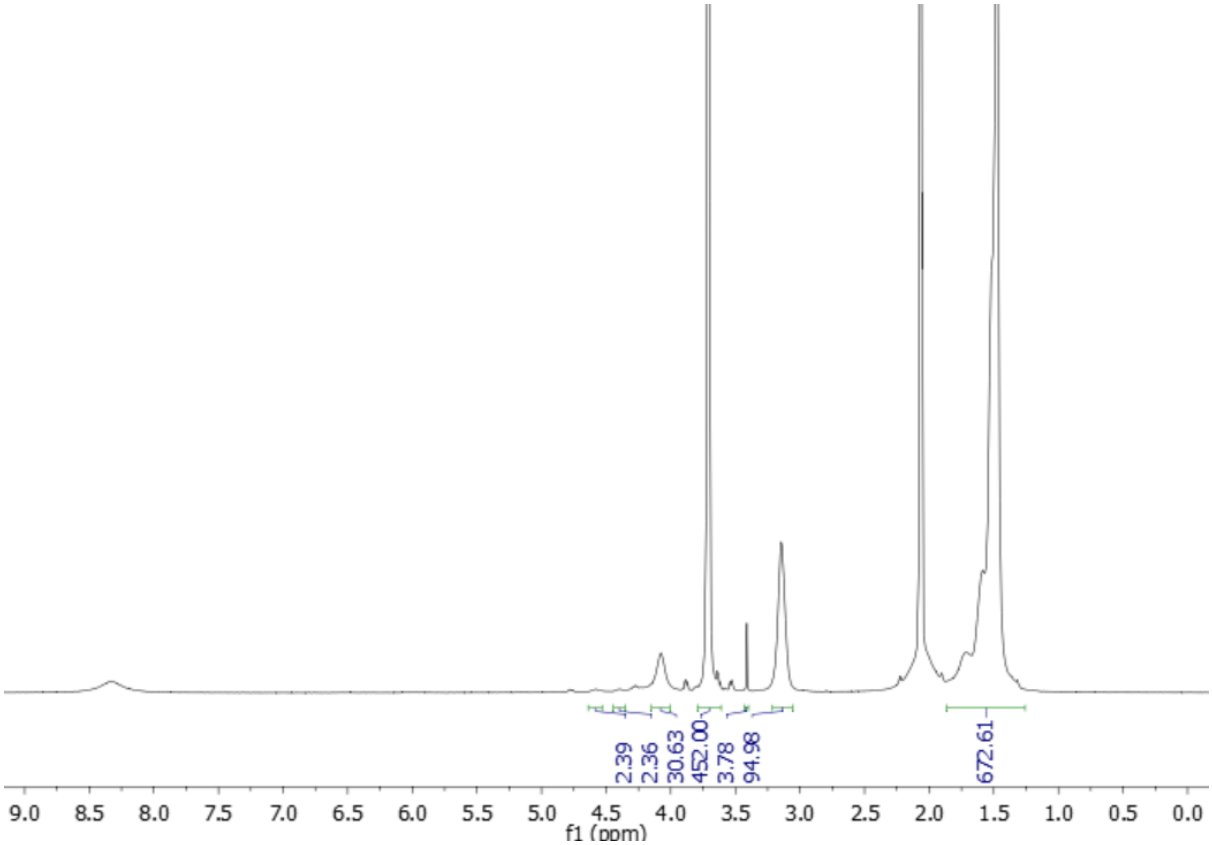

Figure A.5.1.15: ^{1}H NMR spectrum (500 MHz, DMSO-d_6) of **BC196**, mPEG-*b*-PLys(Boc).

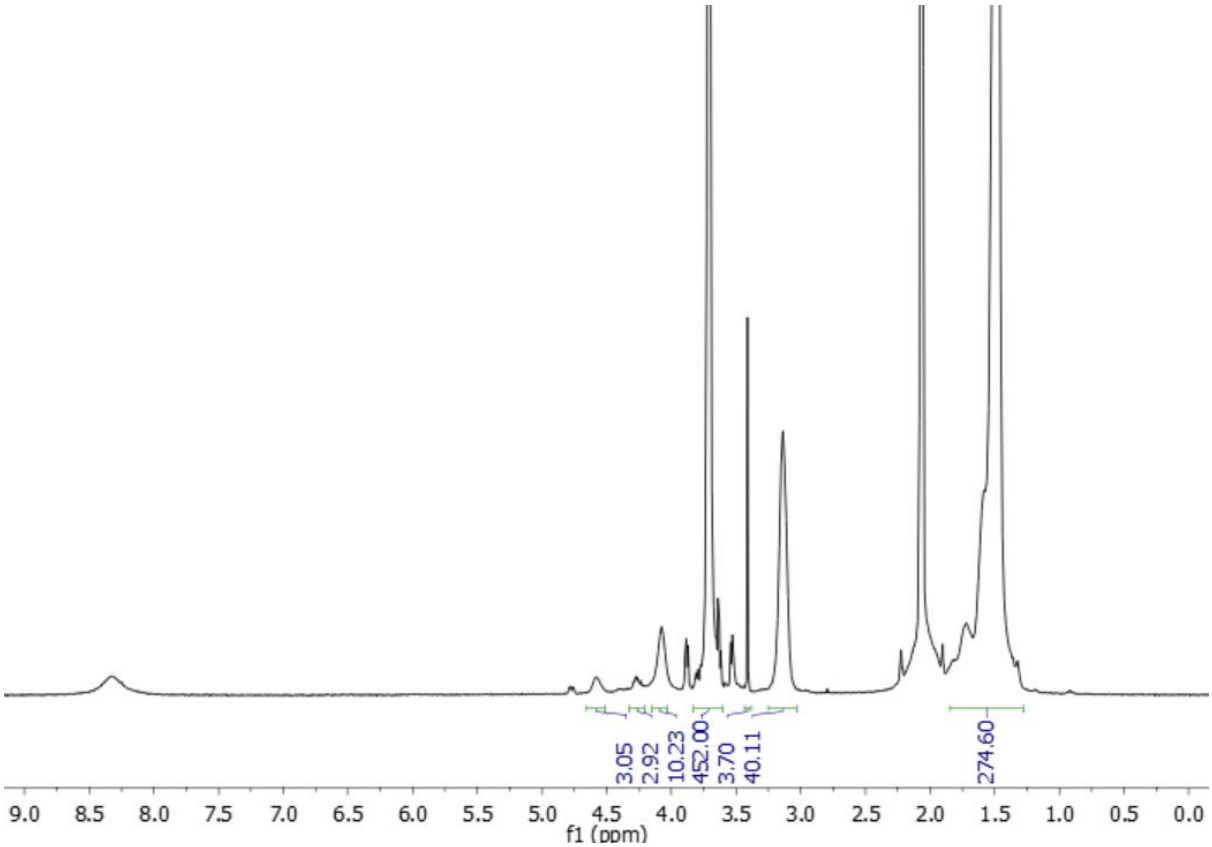

Figure A.5.1.16: ^{1}H NMR spectrum (500 MHz, DMSO-d_6) of **BC197**, mPEG-*b*-PLys(Boc).

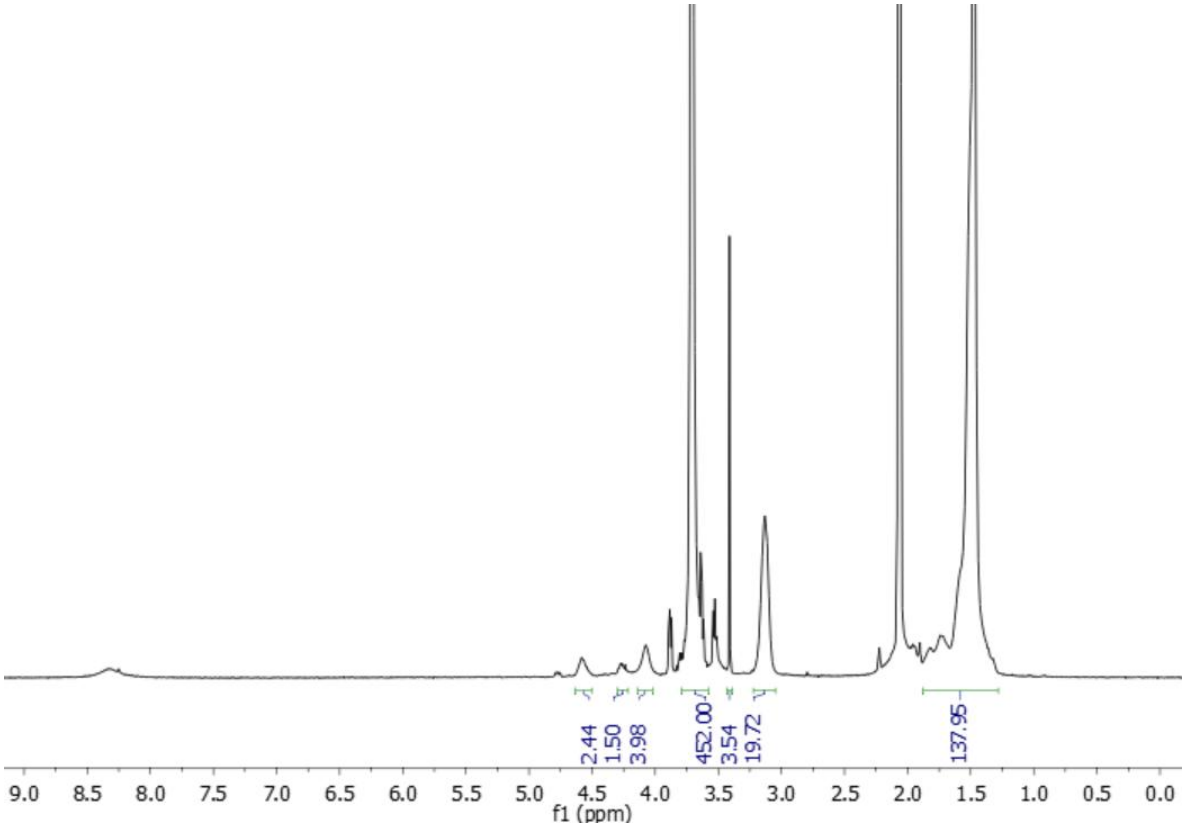

Figure A.5.1.17: ^{1}H NMR spectrum (500 MHz, DMSO-d_6) of **BC198**, mPEG-*b*-PLys(Boc).

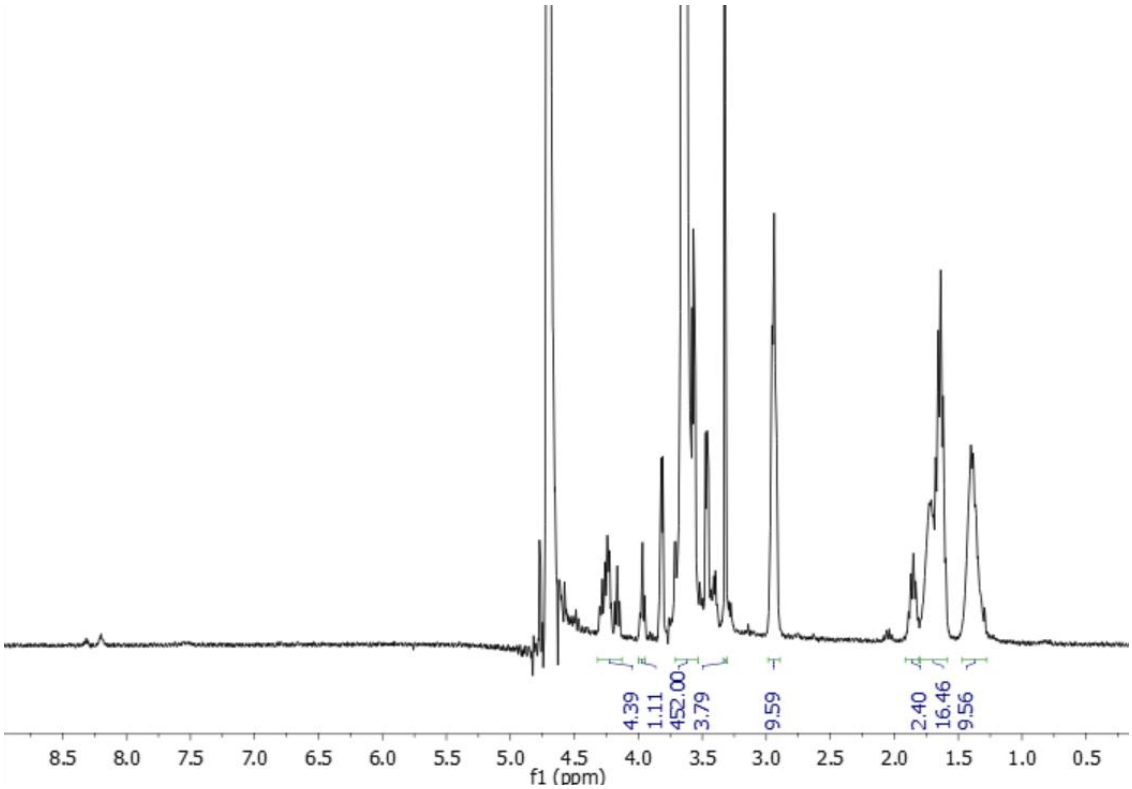

Figure A.5.1.18: ^{1}H NMR spectrum (500 MHz, DMSO-d_6) of **BC195D**, mPEG-*b*-PLys[NH_2.TFA].

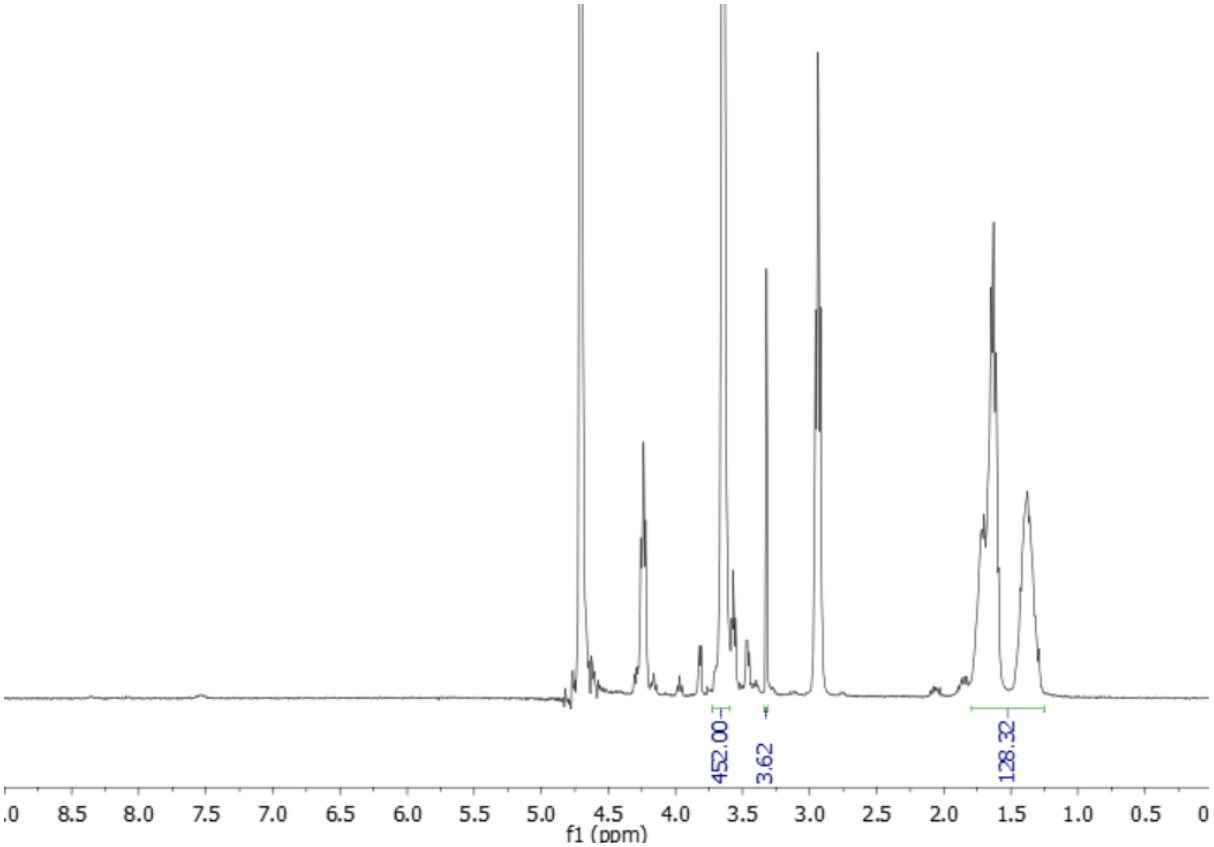

Figure A.5.1.18: ^{1}H NMR spectrum (500 MHz, DMSO-d_6) of **BC196D**, mPEG-*b*-PLys[NH_2.TFA].

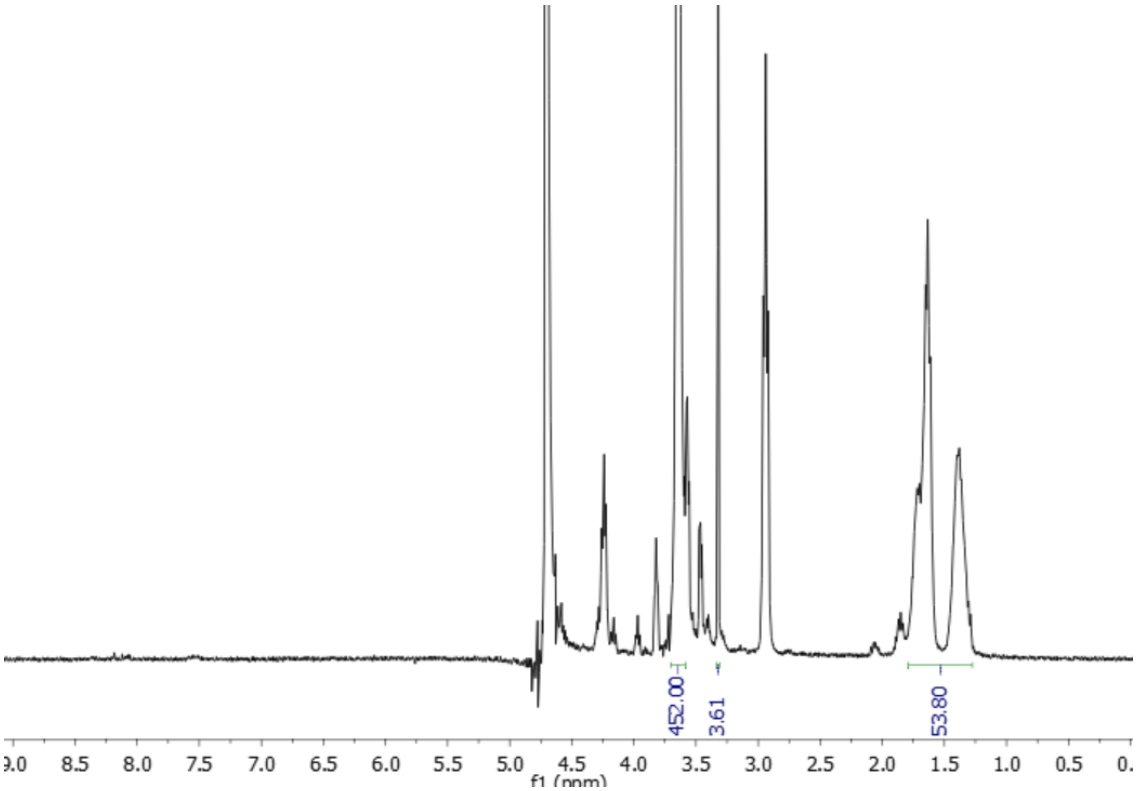

Figure A.5.1.19: ^{1}H NMR spectrum (500 MHz, DMSO-d_6) of **BC197D**, mPEG-*b*-PLys[NH_2.TFA].

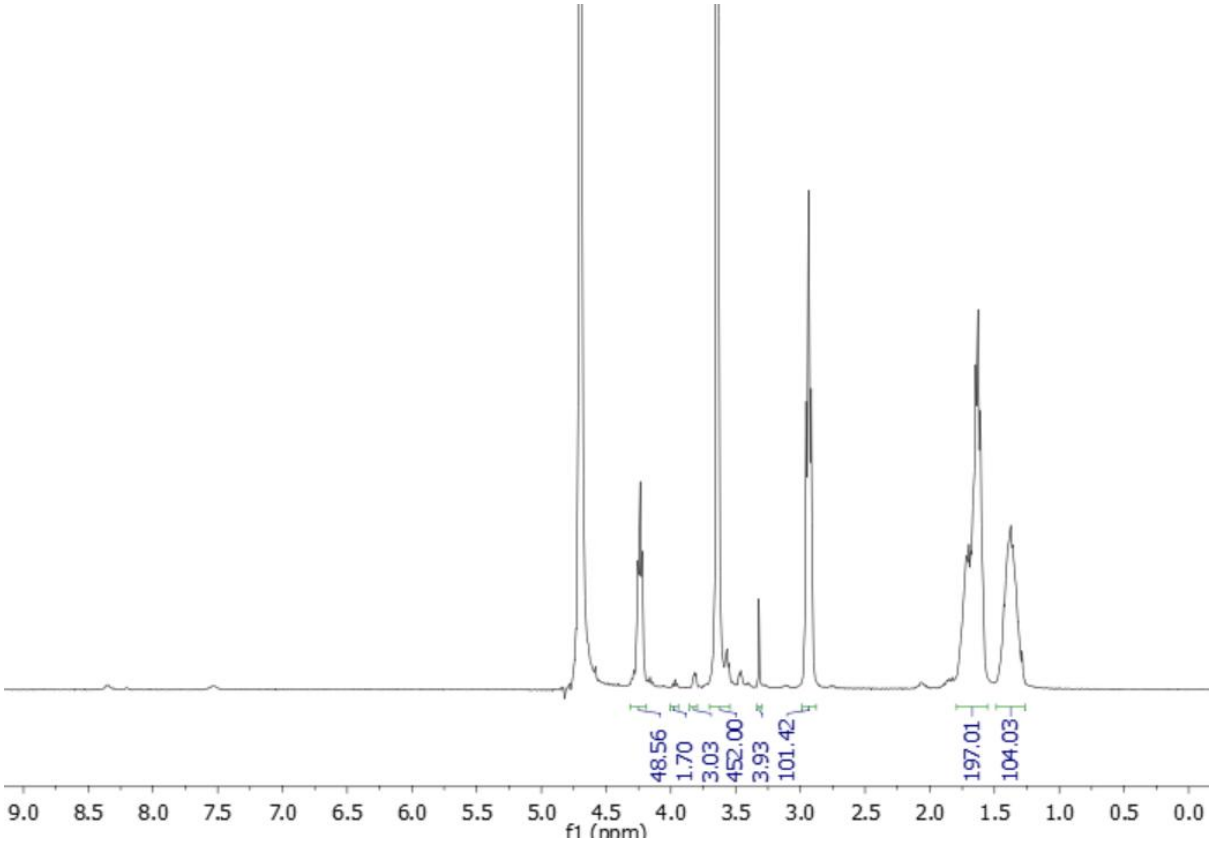

Figure A.5.1.20: ^{1}H NMR spectrum (500 MHz, DMSO-d_6) of **BC198D**, mPEG-*b*-PLys[NH_2.TFA].

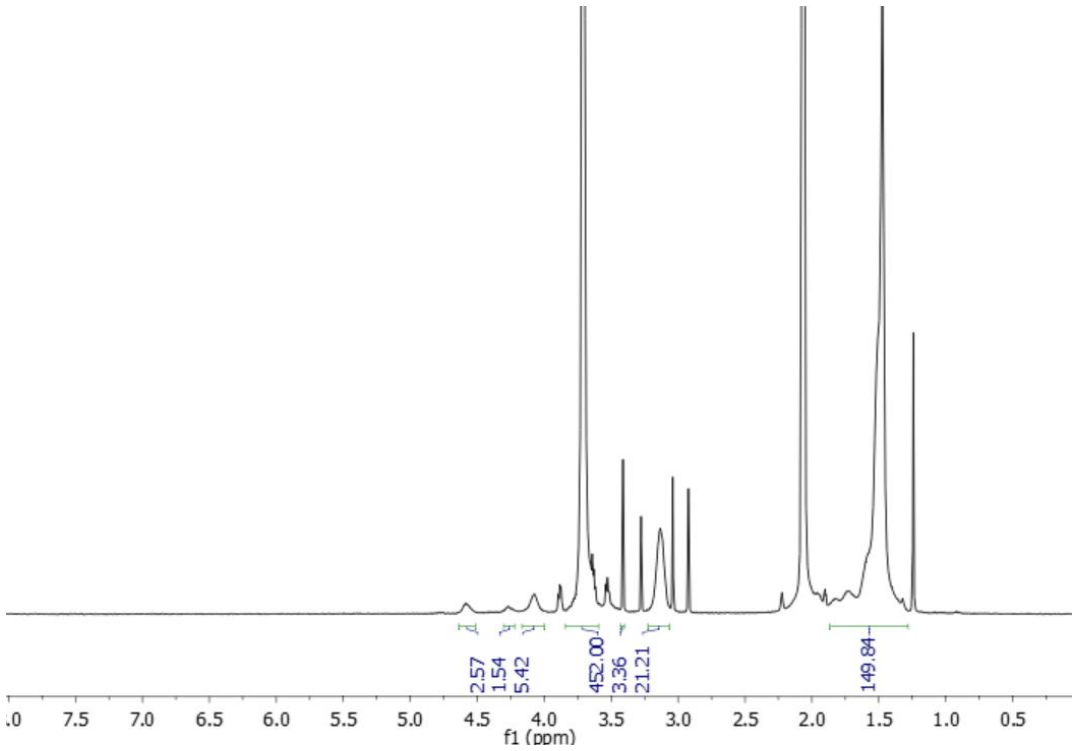

Figure A.5.1.21: ^{1}H NMR spectrum (500 MHz, DMSO-d_6) of **BC210**, mPEG-*b*-PLys(Boc).

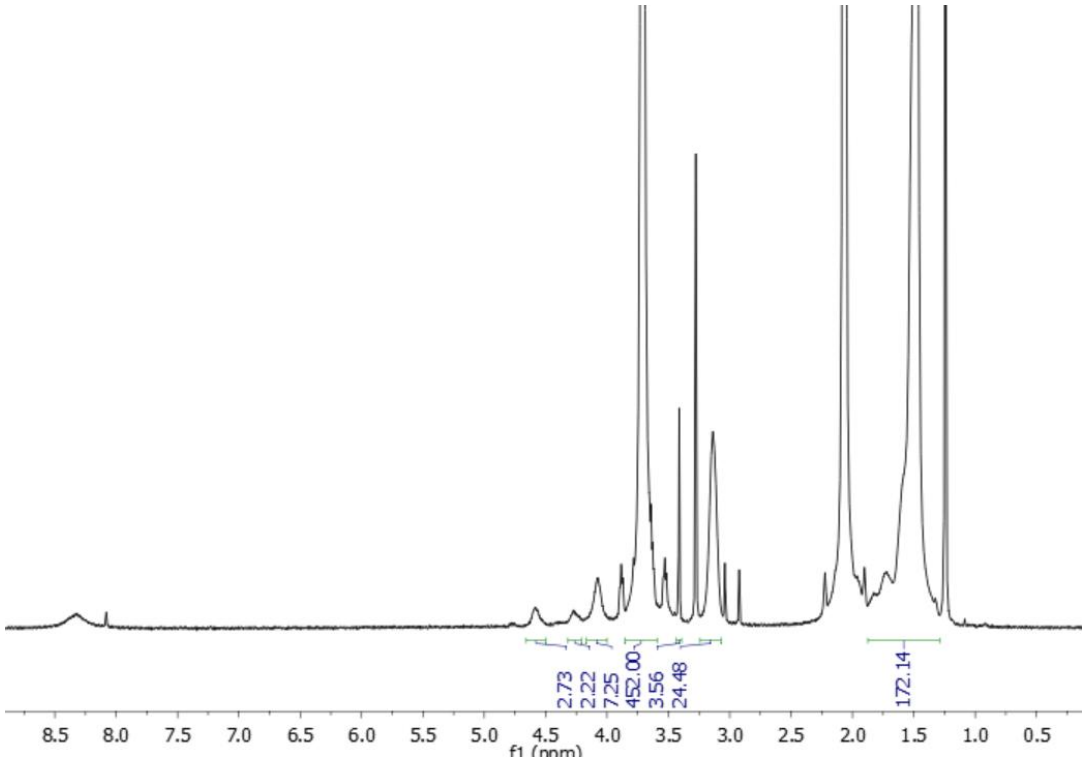

Figure A.5.1.22: ^{1}H NMR spectrum (500 MHz, DMSO-d_6) of **BC211**, mPEG-*b*-PLys(Boc).

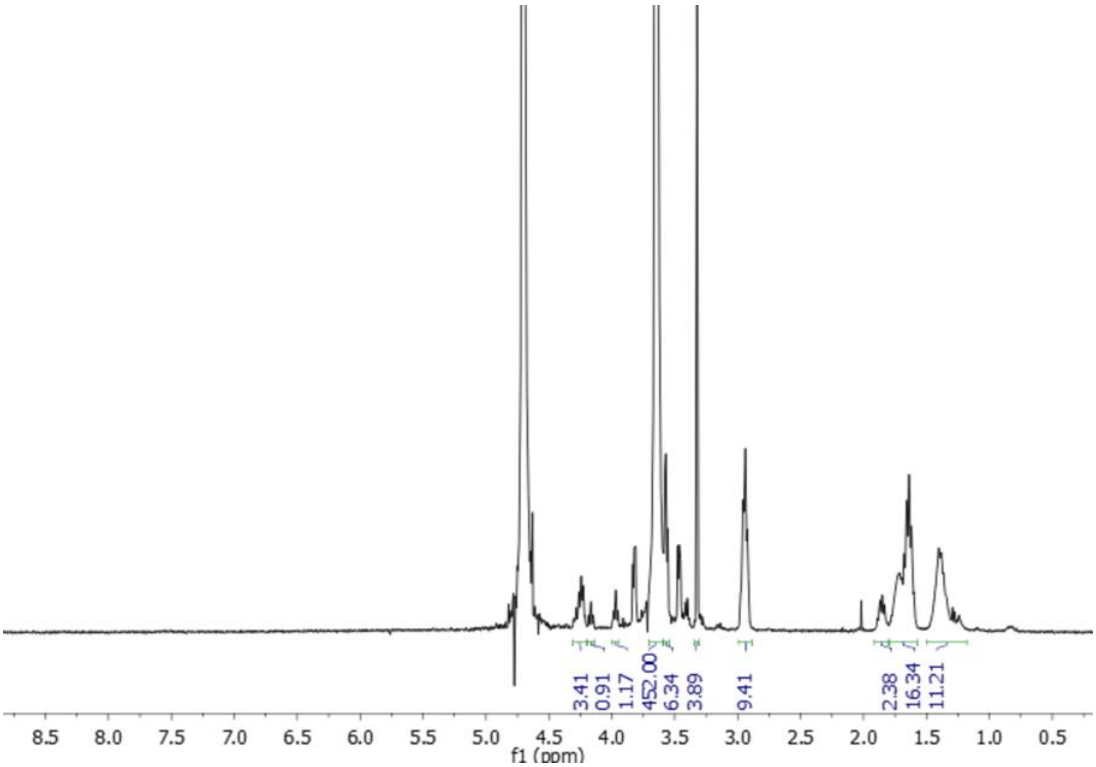

Figure A.5.1.23: ^{1}H NMR spectrum (500 MHz, DMSO-d_6) of **BC210D**, mPEG-*b*-PLys[NH_2.TFA].

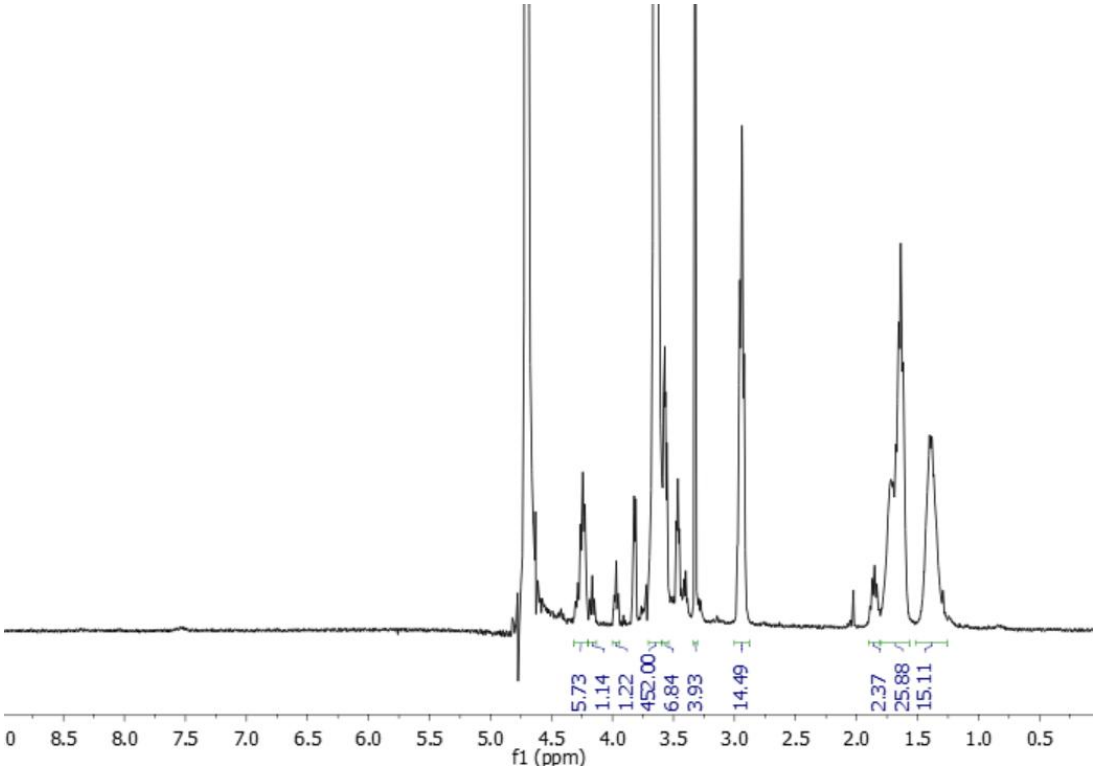

Figure A.5.1.24: ^{1}H NMR spectrum (500 MHz, DMSO-d_6) of **BC211D,** mPEG-*b*-PLys[NH_2.TFA].

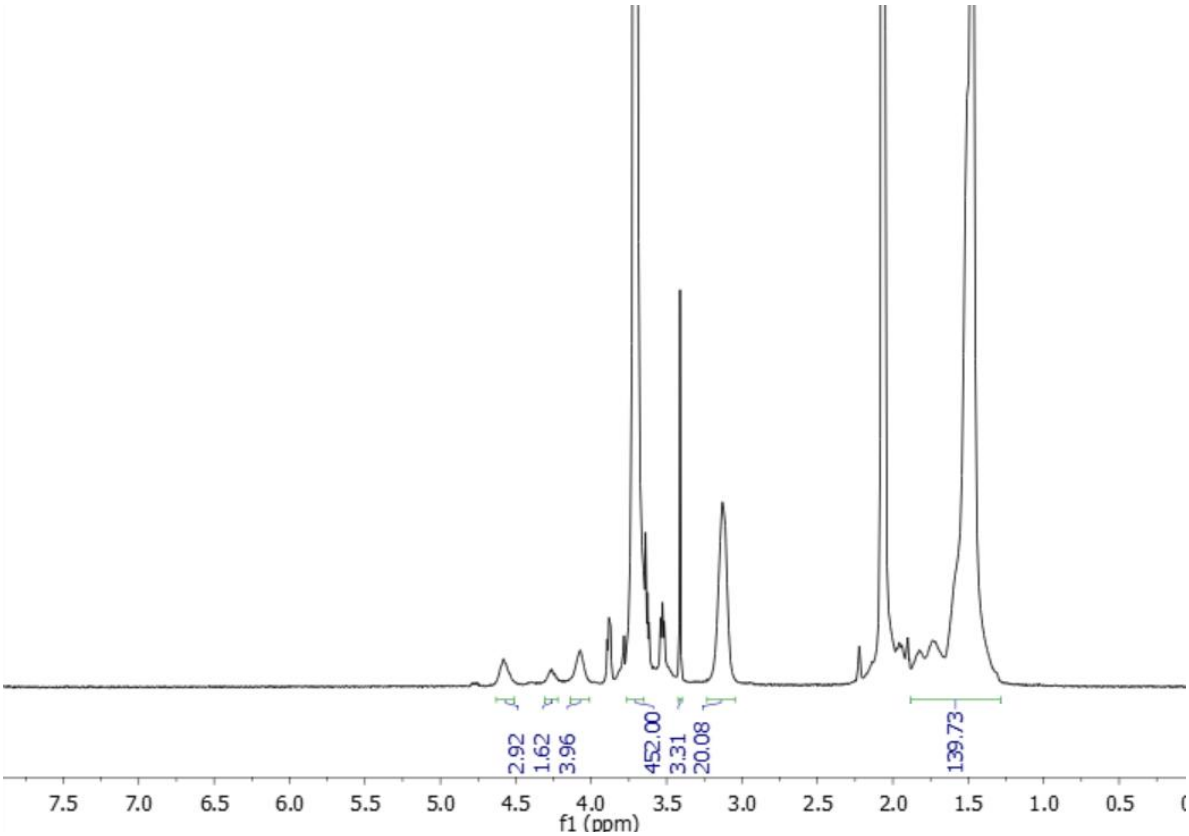

Figure A.5.1.25: ^{1}H NMR spectrum (500 MHz, DMSO-d_6) of **BC219,** mPEG-*b*-PLys(Boc).

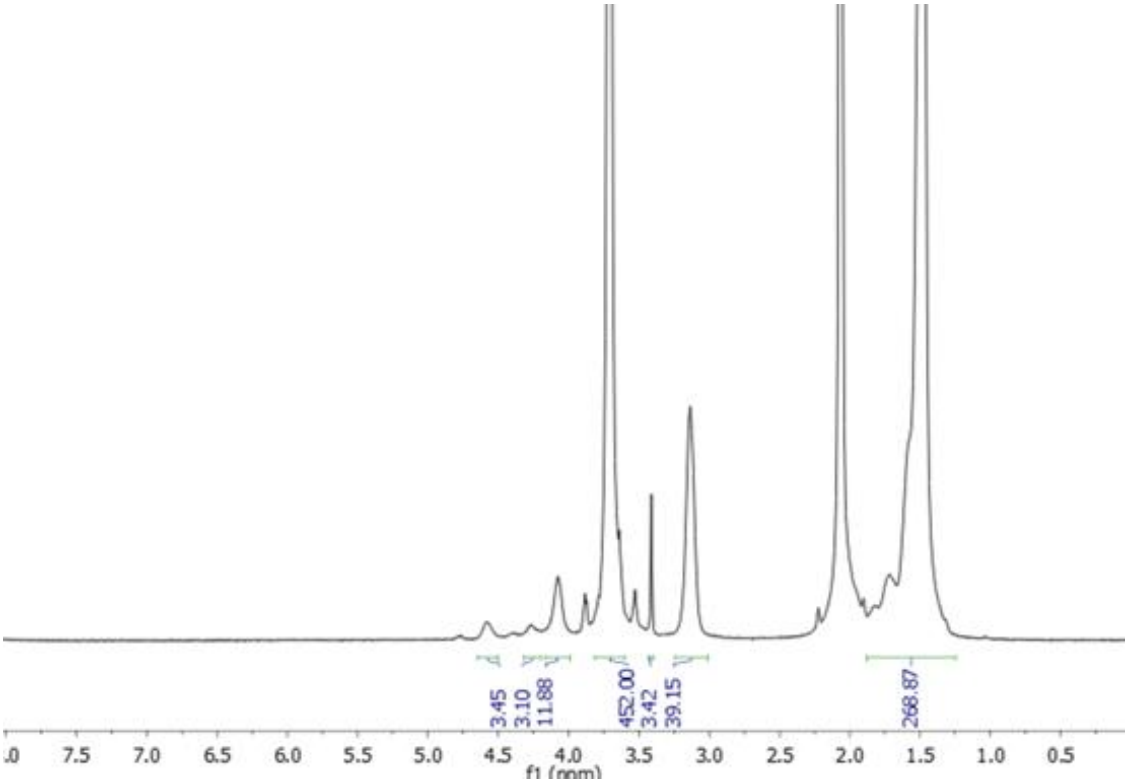

Figure A.5.1.26: ^{1}H NMR spectrum (500 MHz, DMSO-d_6) of **BC220**, mPEG-*b*-PLys(Boc).

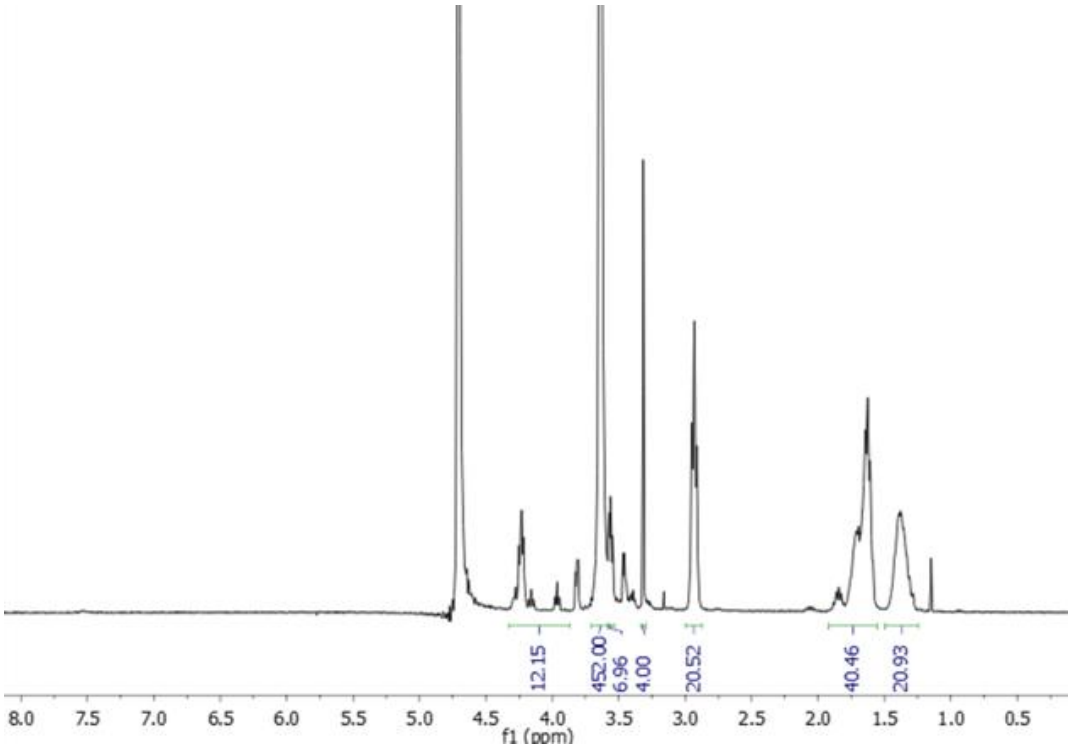

Figure A.5.1.26: ^{1}H NMR spectrum (500 MHz, DMSO-d_6) of **BC220D**, mPEG-*b*-PLys[NH_2.TFA].

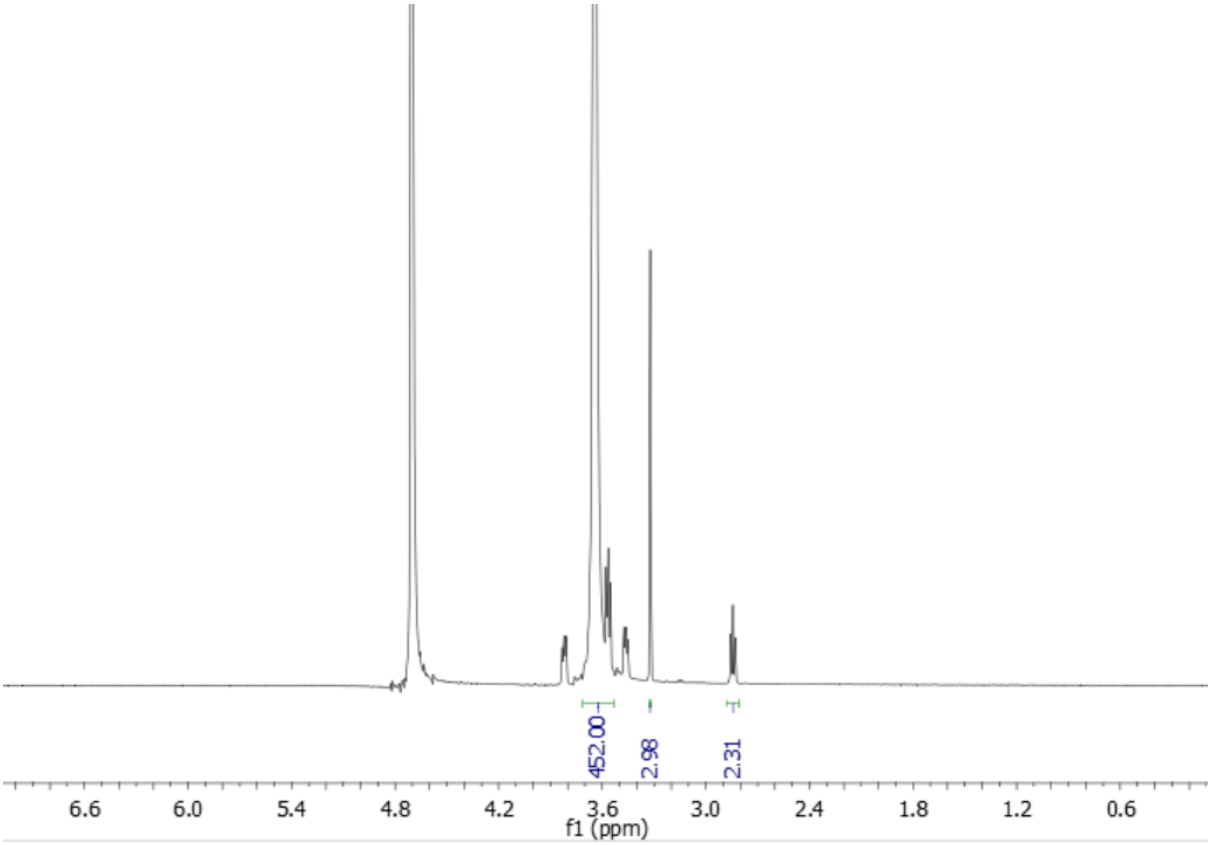

Figure A.5.1.27: ^{1}H NMR spectrum (500 MHz, DMSO-d_6) of mPEG-NH_2 (Iris Batch A)

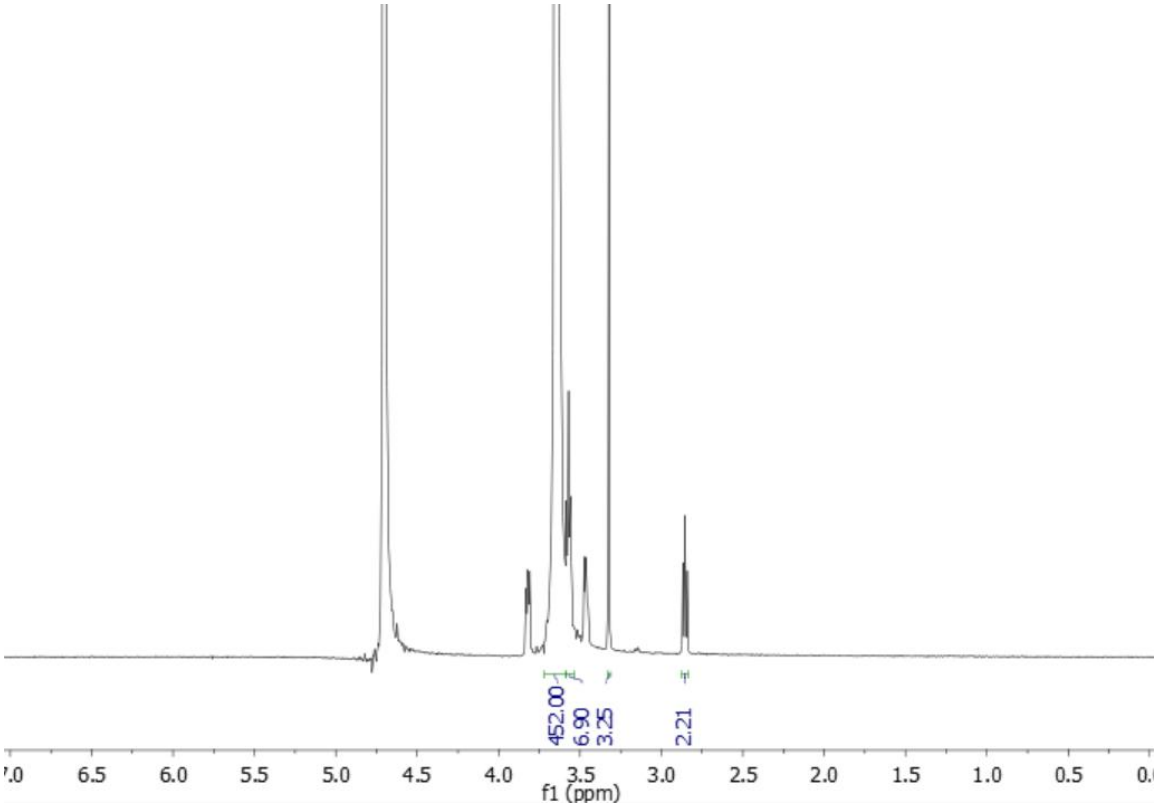

Figure A.5.1.28: ^{1}H NMR spectrum (500 MHz, DMSO-d_6) of mPEG-NH_2 (Iris Batch B)

A.5.2 FTIR Spectra

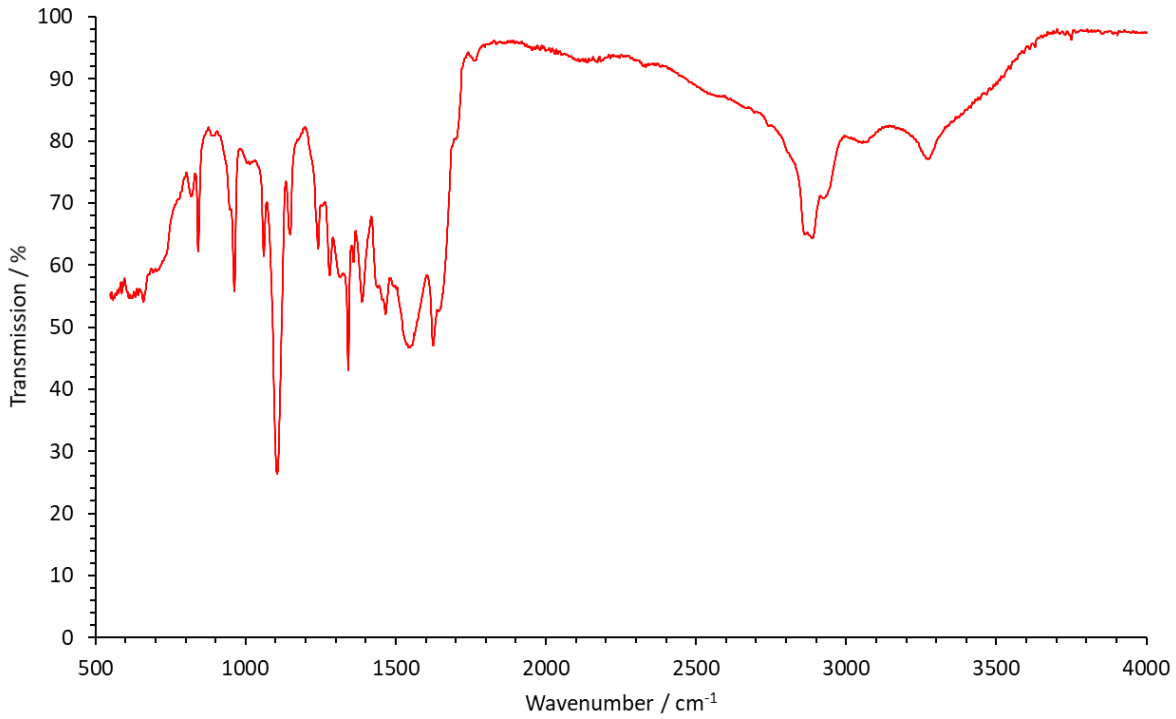

Figure A.5.2.1: FTIR spectrum of **BC54**, reported in **Section 5.3.1**.

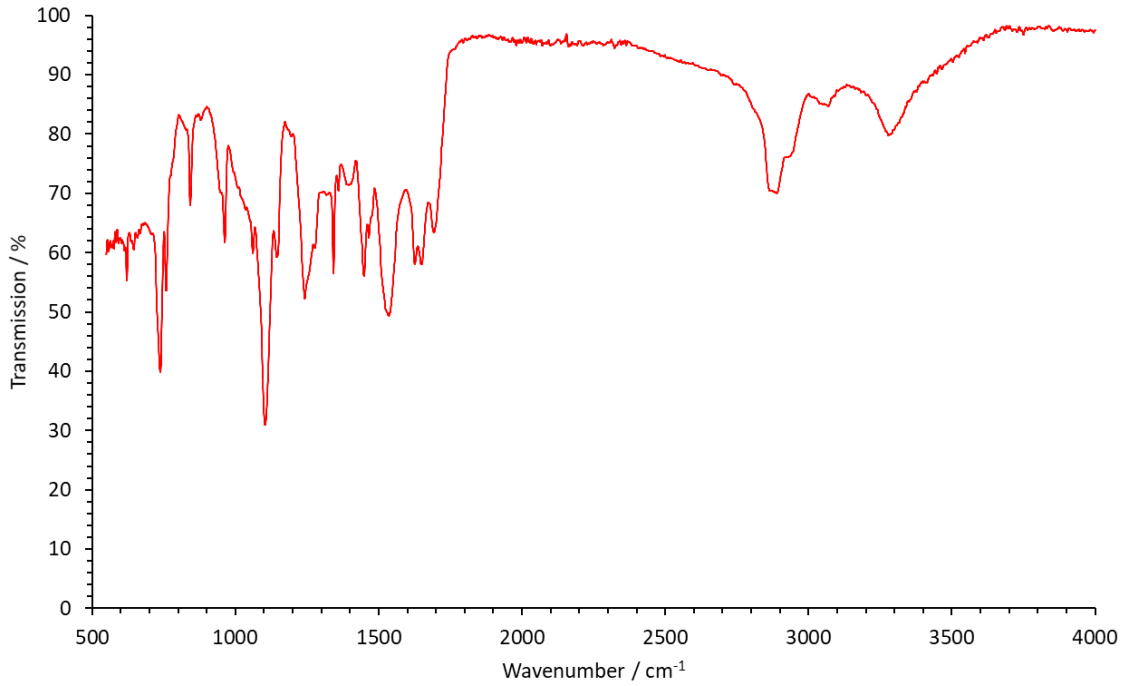

Figure A.5.2.2: FTIR spectrum of **BC56**, reported in **Section 5.3.1**.

Chapter 6: Post-polymerisation modification of mPEG-b-PLys protected block copolymers for conjugated drug transport and controlled release.

Abstract

The post-polymerisation modification of mPEG-*b*-PLys[NH_2.TFA]$_n$ block copolymers is reported here, investigating the impact of chain extension on SN38 conjugation, self-assembly and controlled drug release. ^{1}H NMR spectroscopy confirmed high grafting efficiencies (80 - 97 %) of single (O2O-Boc) and double (O2O-O2O-Boc) spacer units with SEC analysis showing correlated increases in molecular weight. For BCPs with longer PLys block lengths, Đ broadening and solubility issues were observed for O2O-O2O-Boc, indicating partial grafting and suggesting the need for tighter ROP control in future. TFA-mediated Boc-deprotection of the chain-extended products yielded stable amine-functionalised products with no evidence of chain degradation. MW and uniformity were maintained, confirming the robustness of the spacer molecules during sequential modification. Following this, an activated SN38 intermediate (10-O-(p-nitro phenyl carbonate)-SN38) was prepared in good yield and carbamate coupling of SN38 was performed, yielding distinct molecular weight increases and aromatic signatures, as confirmed by ^{1}H NMR spectroscopy. Comparative data confirmed improved conjugation efficiency for chain-extended systems, validating the steric relief hypothesis. Subsequently, all SN38-conjugated polymers were self-assembled *via* nanoprecipitation in PBS, with DLS analysis confirming uniform nanostructures. Controlled-release tests (AstraZeneca) showed sustained SN38 release under physiological conditions. Both linear and extended BCPs functioned as viable nano-carriers, with chain-extended samples showing enhanced release tunability. This work demonstrated a complete, modular framework for post-polymerisation modification of PEG-*b*-PLys toward SN38 drug conjugates, building upon existing research to develop a novel chain-extension strategy that improves conjugation yield and increases control of sustained-release. These products present a simpler alternative to complex dentrimeric architectures, enabling tuneable, sterically-flexible nanocarriers with significant translational potential.

6.1 Introduction

Whilst a significant portion of the literature revolves around the direct conjugation of PLys-containing systems to therapeutics, a growing body of research has focused on PPM-addition of short-chain spacer molecules, for enhanced functionality and control over conjugation and payload delivery.[1,2] These modifications allow for the installation of responsive linker technologies onto the pre-synthesised backbone through orthogonal or "click" reactions, enabling rapid diversification without resynthesising the backbone. One such example of this technology is in the work performed by Di Iorio *et al*., who outfitted PLys with oligo(ethylene glycol) (OEG) spacers, before furnishing these with click-handles such as dibenzocylcooctyne (DBCO) and tetrazine (Tz).[3] These click-handles were then capable of mild-condition, Diels-Alder click reaction chemistries to immobilise biomolecules onto their surfaces, with DNA used as an example. Another example is the work conducted by Shakiba *et al*., who utilized copper-catalysed azide-alkyne cycloaddition and thiol-ester Michael addition strategies to install immobilised ligands onto a PLL-modified, self-assembled monolayer (SAM) on a gold surfaces.[4] Such research will translate into the advancement of biosensory technologies and antifouling surfaces, exemplifying the scope of the impact that post-polymerisation modification of PLL can achieve.[5,6]

Post-polymerisation strategies utilising PLL have also been applied widely in targeted, controlled release scenarios, wherein bio-orthogonal conjugation introduces pH- and redox-sensitive motifs, capable of stimulus-triggered release. This was demonstrated by Zheng *et al*., who developed PLL-*g*-PEG nanoparticles to encapsulate bovine serum albumin (BSA).[7] The nanoparticles were crosslinked using 3,3'-dithiobis(sulfosuccinimidyl propionate) (DTSSP), a disulphide-containing cross-linker which remained stable under extracellular conditions, but was under reduction by glutathione (GSH) within the cytosol, thereby providing a model for intracellular protein delivery.

In parallel with these chemical advances, structural design has also evolved to exploit branched and dendritic architectures. Dendrimers and telodendrimers provide dense, multifunctional surfaces and highly solvated interiors, which substantially enhance non-covalent encapsulation efficiency and colloidal stability in comparison to linear analogues.[8,9]

The work of England *et al*. exemplifies this approach, whereby a series of PSar-*b*PLys hyper-branched telodendrimers were conjugated to fulvestrant *via* amide coupling, producing nanoparticles with drug loading efficiencies approaching 77 wt%, including non-covalent loading.[10] This strategy demonstrated the capability of lysine-based architectures to serve as both covalent carriers and non-covalent hosts, balancing near-quantitative drug content with robust stability under physiological conditions.

Whilst these dendritic systems represent an ideal platform for the delivery of therapeutics their synthetic complexity, requiring iterative coupling and deprotection steps across generations of branching, limits scalability and reproducibility.[11,12] A simpler, but comparably more tuneable route lies in side-chain engineering of polymers, through post-polymerisation modification. By grafting short, flexible spacers such as OEGs onto relative sites, the microenvironment around each conjugative pendant amine of PLL can be finely tuned to moderate steric accessibility and side-chain flexibility. In peptide and protein conjugation chemistry 2-(2-aminoethoxy)ethoxyacetic acid (AEEA) linkers are widely employed to increase the mobility and solvation of furnished moieties, improving reaction yields and bio-conjugate performance. This is exemplified by the work of Hnedzko *et al*., whose use of AEEA spacers to label peptide nucleic acid (PNA) with HiLyte Fuor 488 dye increased the local solvation of the PNA N-terminus as well as the conformational (rotational) freedom of the bound dye, which subsequently increased labelling yields to ca. 90 %.[13] Similarly, the work of Zaykov *et al*. highlights the use of OEG-type spacers as a recurring design motif that strongly influences solubility, steric presentation and receptor interaction/clearance in peptide/protein conjugation pharmacokinetics.[14] These AEEA spacers (herein referred to as O2O and O2O-O2O units for OEG_1 and OEG_2) offer a straightforward means to relieve steric crowding around lysine pendant amine groups and facilitate the conjugative yield of subsequent coupling reactions with sterically bulky, hydrophobic drugs.

This approach is pertinent to the conjugation of SN38 (7-ethyl-10-hydroxycamptothecin), a potent topoisomerase I inhibitor with poor physiological solubility and limited therapeutic applicability in its native form.

Previous studies have demonstrated that tethering SN38 to polymers *via* hydrolysable linkages significantly prolongs its circulation half-life, reduces clearance *via* nonspecific binding to proteins like albumin, and reduces premature inactivation by sterically occluding access of water to the unstable E-lactone ring.[15-18] These linkers remain stable under physiological conditions, but undergo cleavage under mildly acidic or enzymatic environments. These include the extracellular conditions of tumour microenvironments (pH 6.0 – 6.8), intracellular conditions of endosomes and lysosomes (pH 5.0 – 5.5) as well as exposure to carboxylesterases (CESs) that are abundant in blood plasma.[15,19,20] Reviews of carbamate-based drug conjugates highlight that their stability against burst release upon intravenous delivery is balanced by their sufficient lability under tumour-adjacent conditions to ensure therapeutic activation at the target site.[21,22]

Within this context, the investigation performed here explores the modification of mPEG-*b*-PLys BCPs (synthesised within **Chapter 5**) by post-polymerisation modification using OEG-type spacers to create chain-extended derivatives, capable of relieving steric hindrance during SN38 conjugation and subsequent self-assembly. Using an activated carbonate intermediate, 10-O-(p-nitro phenyl carbonate)-SN38, carbamate linkages are introduced to the terminal amines of these flexible spacers, producing a series of amphiphilic BCPs with varied spacer lengths and poly(L-lysine) block sizes. This sequential modification integrates established chemistries within a single synthetic platform. By systematically varying both degree of polymerisation (n = 5, 10, 20) and spacer length (OEG_1 vs. OEG_2), this work investigates how polymer architecture influences conjugation efficiency, polymer uniformity and subsequent self-assembly. In doing so, it aims to capture the advantages presented by dendritic and hyper-branched systems, such as high drug loading and structural stability, whilst maintaining the synthetic simplicity and reproducibility of a linear mPEG-*b*-PLys backbone. The resulting conjugates are evaluated in terms of coupling yield, dispersity, solubility and drug release behaviour, providing insight into the impact of increased side chain flexibility and hydrophilicity on both polymer-drug conjugation and subsequent release. Ultimately, the investigation seeks to establish a modular design framework for sterically optimised, controlled release polymer-drug conjugate based on the mPEG-*b*-PLys framework, to bridge the gap between complex polymer architectures and practical, scalable therapeutic synthesis.

6.2 Experimental

6.2.1 Boc-O2O-OH Grafting

All mPEG-NH_2 macroinitiators herein were sourced from Iris BioTech GmbH.

A generalised method for the grafting of Boc-O2O-OH to mPEG-*b*-PLys[NH_2.TFA]$_n$ is presented below. Specifics such as reagent masses and molar quantities are provided below in **Table 6.1**.

To a round-bottom flask under N_2 atmosphere, mPEG-*b*-PLys[NH_2.TFA]$_n$ (**Table 6.1**) was added and dissolved in anhydrous DMF (**Table 6.1**), followed by subsequent addition of DIPEA (**Table 6.1**). Benzotriazol-1-yloxytripyrrolidinophosphonium hexafluoro-phosphate (PyBOP) (**Table 6.1**) was dissolved in further anhydrous DMF (**Table 6.1**), before addition to the reaction mixture. In parallel, (2-(2-(t-Butyloxycarbonylamino)ethoxy)ethoxy)-acetic acid (Boc-O2O-OH) (**Table 6.1**) was dissolved in anhydrous DMF, before addition to the reaction mixture following PyBOP. The reaction was stirred for ca. 3 hours to ensure completion. Subsequently, DMF was removed *in vacuo* to yield the product as a translucent film and gummy solid. This material was the dissolved in MeOH (0.5 mL), and purified using a PD-10 column. The resultant product was again dried *in vacuo* to yield a transparent film layer, for which mass and yield values were determined. ^{1}H NMR spectra of the products can be found in **Section A.6.1**.

Table 6.1: Masses, molar quantities and solvent volumes for Boc-O2O-OH grafting reactions.

Experiment Title	mPEG-*b*-PLys[NH_2.TFA]$_n$		DIPEA		PyBOP		Boc-O2O-OH		Solvent
	Mass / mg	Moles / mmol	Mass / mg	Moles / mmol	Mass / mg	Moles / mmol	Mass / mg	Moles / mmol	Vol / mL
BC203 ($n = 5$)	80	0.013	39.62	0.305	79.33	0.152	40.14	0.152	4
BC224 ($n = 10$)	196	0.026	81.53	0.627	163.24	0.314	82.59	0.314	8
BC226 ($n = 20$)	135	0.014	148.88	1.146	298.09	0.573	150.82	0.573	8

BC203 - mPEG-*b*-PLys(O2O-Boc)$_5$-O2O-Boc

Yield: 77.4 mg, 79 %

^{1}H NMR (500 MHz, CD_3COOD, ppm): 4.47 – 4.63 (m, 4H, αC-H), 4.15 – 4.25 (3 x s, 3H, αC-H), 4.08 – 4.15 (m, 10H, CH_2 (Boc-O2O-OH)), 3.54 – 3.80 (m, 482H, PEG CH_2-CH_2 + CH_2-CH_2 (Boc-O2O-OH)), 3.56 (s, 3H, PEG-CH_3) 3.21 – 3.35 (m, 22H, Lys-CH_2 + CH_2 (Boc-O2O-OH)), 1.25 – 1.75 (m, 87H, Lys CH_2 + Boc $C(CH_3)_3$).

BC224 - mPEG-*b*-PLys(O2O-Boc)$_{10}$-O2O-Boc

Yield: 154.8 mg, 65 %

^{1}H NMR (500 MHz, D_2O, ppm): 4.10 – 4.35 (m, 6H, αC-H), 4.00 – 4.08 (m, 3H, αC-H), 3.8 – 4.0 (m, 16H, CH_2 (Boc-O2O-OH)), 3.40 – 3.75 (m, 518H, PEG CH_2-CH_2 + CH_2-CH_2 (Boc-O2O-OH)), 3.30 (s, 3H, PEG-CH_3) 3.12 – 3.29 (m, 30H, Lys-CH_2 + CH_2 (Boc-O2O-OH)), 0.9 – 2.1 (m, 138H, Lys CH_2 + Boc C(CH_3)$_3$).

BC225 - mPEG-*b*-PLys(O2O-Boc)$_{20}$-O2O-Boc

Yield: 199.1 mg, 70 %

^{1}H NMR (500 MHz, D_2O, ppm): 4.20 – 4.40 (m, 6H, αC-H), 4.11 (s, 3H, αC-H), 4.00 – 4.10 (m, 45H, CH_2 (Boc-O2O-OH)), 3.45 – 3.80 (m, 578H, PEG CH_2-CH_2 + CH_2-CH_2 (Boc-O2O-OH)), 3.40 (s, 3H, PEG-CH_3) 3.18 – 3.29 (m, 37H, Lys-CH_2 + CH_2 (Boc-O2O-OH)), 1.2 – 2.1 (m, 154H, Lys CH_2 + Boc C(CH_3)$_3$).

6.2.1.1 O2O-Boc Deprotection

The mPEG-*b*-PLys(O2O-Boc)$_n$-O2O-Boc copolymers synthesised in **Section 6.2.1** were subjected to deprotection *via* exposure to TFA. The generalised method for this process, as well as the workup and purification procedure for each polymer, is presented below.

mPEG-*b*-PLys(O2O-Boc)$_n$-O2O-Boc was added to a round-bottom flask, and dissolved in pure TFA (2 mL) The reaction mixture was stirred for 3-5 minutes at room temperature in air, to allow for the escape of eliminated gaseous by-products. Reaction was considered complete shortly after all material has dissolved into the TFA solution. The product was then collected *via* precipitation and centrifugation in TBME, before being dried, dissolved in deionised water, and submitted for lyophilisation. The pure product was then re-collected as either white, fluffy powder, or a thin, transparent film. ^{1}H NMR spectra of the products can be found in **Section A.6.1**.

BC203D - mPEG-*b*-Plys[O2O-NH_2.TFA]$_5$-O2O-NH_2.TFA

Yield: 77.3 mg, 85 %

^{1}H NMR (500 MHz, D_2O, ppm): 4.14 – 4.33 (m, 5H, αC-H), 3.95 – 4.13 (m, 10H, CH_2 (Boc-O2O-OH)), 3.55 – 3.75 (m, 482H, PEG CH_2-CH_2 + CH_2-CH_2 (Boc-O2O-OH)), 3.33 (s, 4H, PEG-CH_3) 3.15 – 3.23 (m, 20H, Lys-CH_2 + CH_2 (Boc-O2O-OH)), 1.25 – 1.75 (m, 26H, Lys CH_2 + Boc C(CH_3)$_3$).

BC224D - mPEG-*b*-Plys[O2O-NH_2.TFA]$_{10}$-O2O-NH_2.TFA

Yield: 80.2 mg, 91 %

^{1}H NMR (500 MHz, D_2O, ppm): 4.10 – 4.30 (m, 10H, αC-H), 3.95 – 4.10 (m, 20H, CH_2 (Boc-O2O-OH)), 3.47 – 3.75 (m, 518H, PEG CH_2-CH_2 + CH_2-CH_2 (Boc-O2O-OH)), 3.30 (s, 4H, PEG-CH_3) 3.12 – 3.29 (m, 37H, Lys-CH_2 + CH_2 (Boc-O2O-OH)), 0.9 – 2.1 (m, 65H, Lys CH_2 + Boc C(CH_3)$_3$).

BC225D - mPEG-*b*-Plys[O2O-NH_2.TFA]$_{20}$-O2O-NH_2.TFA

Yield: 80.2 mg, 91 %

^{1}H NMR (500 MHz, DMSO-*d6*, ppm): 4.10 – 4.30 (m, 10H, αC-H), 3.95 – 4.10 (m, 43H, CH_2 (Boc-O2O-OH)), 3.47 – 3.75 (m, 584H, PEG CH_2-CH_2 + CH_2-CH_2 (Boc-O2O-OH)), 3.30 (s, 3H, PEG-CH_3) 3.12 – 3.29 (m, 41H, Lys-CH_2 + CH_2 (Boc-O2O-OH)), 0.9 – 2.1 (m, 63H, Lys CH_2 + Boc C(CH_3)$_3$).

6.2.2 Boc-O2O-O2O-OH Grafting

A generalised method for the grafting of Boc-O2O-OH to mPEG-*b*-PLys[NH_2.TFA]$_n$ is presented below. Specifics such as reagent masses and molar quantities are provided below in **Table 6.2**.

To a round-bottom flask under N_2 atmosphere, mPEG-*b*-PLys[NH_2.TFA]$_n$ (**Table 6.2**) was added and dissolve in anhydrous DMF (**Table 6.2**), followed by subsequent addition of DIPEA (**Table 6.2**). Separately, benzotriazol-1-yloxytripyrrolidinophosphonium hexafluorophosphate (PyBOP) (**Table 6.2**) was added dissolved in further anhydrous DMF (**Table 6.2**), before addition to the reaction mixture. In parallel, 17-(t-Butyloxycarbonyl-amino)-9-aza-3,6,12,15-tetraoxa-10-on-heptadecanoic acid (Boc-O2O-O2O-OH) (**Table 6.2**) was dissolved in anhydrous DMF, before addition to the reaction mixture following PyBOP. The reaction was stirred for ca. 3 hours to ensure completion.

Subsequently, solvent DMF was removed *in vacuo* to yield the product as a translucent film and gummy solid. This material was the dissolved in meOH (0.5 mL), and purified using a PD-10 column. The resultant product was again dried *in vacuo* to yield a transparent film layer, for which mass and yield values were determined. ^{1}H NMR spectra of the products can be found in **Section A.6.1**.

Table 6.2: Masses, molar quantities and solvent volumes for Boc-O2O-O2O-OH grafting reactions.

Experiment Title	mPEG-*b*-PLys[NH_2.TFA]$_n$		DIPEA		PyBOP		Boc-O2O-O2O-OH		Solvent
	Mass / mg	Moles / mmol	Mass / mg	Moles / mmol	Mass / mg	Moles / mmol	Mass / mg	Moles / mmol	Vol / mL
BC215 ($n = 5$)	90	0.014	44.57	0.343	89.25	0.172	70.05	0.172	4
BC225 ($n = 10$)	199	0.027	82.78	0.637	165.74	0.318	130.09	0.318	8
BC227 ($n = 20$)	135	0.014	148.88	1.146	298.09	0.573	233.97	0.573	8

BC215 - mPEG-*b*-PLys(O2O-Boc)$_5$-O2O-O2O-Boc

Yield: 58.7 mg, 39 %

Due to low yield, all material was conserved for subsequent deprotection. Hence, ^{1}H NMR is not here presented. However, BC215D, the subsequent deprotection product of this material, has been analysed by SEC, which is presented in **Section 6.3.1.1**

BC226 - mPEG-*b*-PLys(O2O-Boc)$_{10}$-O2O-O2O-Boc

Yield: 80.2 mg, 45 %

Due to low yield, all material was conserved for subsequent deprotection. Hence, ^{1}H NMR is not here presented. Further characterisation has been performed on BC226D, the subsequent deprotection product.

BC227 - mPEG-*b*-PLys(O2O-Boc)$_{20}$-O2O-O2O-Boc

Yield: 120.0 mg, 54 %

Due to low yield, all material was conserved for subsequent deprotection. Hence, ^{1}H NMR is not here presented. Further characterisation has been performed on BC227D, the subsequent deprotection product.

6.2.2.1 O2O-O2O-Boc Deprotection

The mPEG-*b*-PLys(O2O-Boc)$_n$-O2O-Boc copolymers synthesised in **Section 6.2.2** were subjected to deprotection *via* exposure to TFA. The generalised method for this process, as well as the workup and purification procedure for each polymer, is presented below.

mPEG-*b*-PLys(O2O-Boc)$_n$-O2O-Boc was added to a round-bottom flask, and dissolved in pure TFA (2 mL) The reaction mixture was stirred for 3-5 minutes at room temperature in air, to allow for the escape of eliminated gaseous by-products. Reaction was considered complete shortly after all material has dissolved into the TFA solution.

The product was then collected *via* precipitation and centrifugation in TBME, before being dried, dissolved in deionised water, and submitted for lyophilisation. The pure product was then re-collected as either white, fluffy powder, or a thin, transparent film. ^{1}H NMR spectra of the products can be found in **Section A.6.1**.

BC215D - mPEG-*b*-Plys[O2O-NH$_2$.TFA]$_5$-O2O-NH$_2$.TFA

Yield: 31.9 mg, 70 %

Due to low mass, all material was conserved for subsequent conjugation and drug release analysis. Hence, ^{1}H NMR is not here presented. However, BC215D, the subsequent deprotection product of this material, has been analysed by SEC, which is presented in **Section 6.3.1.1**

BC226D - mPEG-*b*-Plys[O2O-NH$_2$.TFA]$_{10}$-O2O-NH$_2$.TFA

Yield: 68.3 mg, 88 %

^{1}H NMR (500 MHz, D_2O, ppm): 4.10 – 4.30z (m, 20H, αC-H), 3.95 – 4.10 (2x s, 40H, CH_2 (Boc-O2O-OH)), 3.47 – 3.75 (m, 578H, PEG CH_2-CH_2 + CH_2-CH_2 (Boc-O2O-OH)), 3.30 (s, 3H, PEG-CH_3) 3.12 – 3.29 (m, 77H, Lys-CH_2 + CH_2 (Boc-O2O-OH)), 0.9 – 2.1 (m, 125H, Lys CH_2 + Boc C(CH_3)$_3$).

BC227D - mPEG-*b*-Plys[O2O-NH$_2$.TFA]$_{20}$-O2O-NH$_2$.TFA

Yield: 68.3 mg, 88 %

^{1}H NMR (500 MHz, DMSO-*d6*, ppm): 4.10 – 4.30z (m, 20H, αC-H), 3.95 – 4.10 (2x s, 75H, CH_2 (Boc-O2O-OH)), 3.47 – 3.75 (m, 704H, PEG CH_2-CH_2 + CH_2-CH_2 (Boc-O2O-OH)), 3.30 (s, 3H, PEG-CH_3) 3.12 – 3.29 (m, 75H, Lys-CH_2 + CH_2 (Boc-O2O-OH)), 0.9 – 2.1 (m, 145H, Lys CH_2 + Boc $C(CH_3)_3$).

6.2.3 Preparation of 10-O-(p-nitrophenyl carbonate)-SN38

In a round-bottom flask under N_2 atmosphere, SN38 (150 mg, 0.382 mmol) was suspended in DMF (8 mL). DIPEA (0.2 mL, 1.147 mmol) was added in one aliquot, causing a change in hue from pale to bold yellow and the complete dissolution of SN38. Subsequently, di-nitrophenyl carbonate (581 mg, 1.91 mmol) solid was added in one amount and N_2 pressure was re-applied.

The reaction was monitored by LC-MS to determined full consumption of SN38 and synthesis of the product, before the reaction was halted. Excess DMF was removed *in vacuo*, and the product precipitated in TBME. Subsequent TBME washes were performed to remove *p*-nitrophenol by-product, and the final product dried *in vacuo*. ^{1}H NMR spectra of the products can be found in **Section A.6.1**.

Yield: 157.3 mg, 74 %

^{1}H NMR (500 MHz, DMSO-*d6*, ppm): 8.20 – 8.50 (m, 4H, phenyl aromatic C-H), 7.90 – 8.00 (m, 1H, SN38 aromatic C-H), 7.70 – 7.80 (m, 2H SN38 aromatic C-H), 7.25 – 7.40 (s, 1H, SN38 aromatic C-H) 5.20 – 5.55 (m, 4H, 2x SN38 aliphatic CH_2), 3.33 – 3.40 (m, 2H, ethyl CH_2) 1.80 – 1.90 (m, 2H, ethyl CH_2), 1.25 – 1.35 (m, 3H, ethyl CH_3 terminal), 0.95 – 1.05 (m, 3H, ethyl CH_3 terminal).

6.2.4 Syntheses of mPEG-*b*-PLys-*g*-SN38-carbamates

A generalised method for the syntheses of SN38-grafted, O2O-SN38-grafted and O2O-O2O-SN38-grafted mPEG-*b*-Plys is presented here. Masses, molar quantities and solvent volumes are presented in **Table 6.3**

mPEG-*b*-Plys polymers (**Table 6.3**) were added to a round-bottom flask under N_2 atmosphere, and dissolved in anhydrous DMF (3 mL). Separately, 10-O-(p-nitrophenyl carbonate)-SN38 was suspended in anhydrous DMF (**Table 6.3**), to which DIPEA (**Table 6.3**) was added in one aliquot. Once fully dissolved, this separate solution was then added in one aliquot to the reaction mixture, and the solution was stirred for 3 hours, to ensure reaction completion.

Once complete, the reaction products were precipitated in diethyl ether, and washed (5 x 15 mL) to ensure *p*-nitrophenol by-product had been removed. Solid materials were then dried *in vacuo*. ^{1}H NMR spectra of the products can be found in **Section A.6.1**.

Table 6.3: Masses, molar quantities and solvent volumes for mPEG-PLys-CO-SN38 conjugation reactions.

Reaction	mPEG-*b*-Plys		SN38-CO-pNPC		DIPEA		DMF
	Mass / mg	Moles / mmol	Mass / mg	Moles / mmol	Vol / µL	Moles / mmol	Vol / mL
BC234 - mPEG-b-PLys(CO-SN38)$_5$-CO-SN38	50.00	0.0079	26.56	0.0476	8.30	0.0476	6
BC235 - mPEG-b-PLys(CO-SN38)$_{10}$-CO-SN38	80.00	0.0096	59.13	0.1061	18.48	0.1061	6
BC236 - mPEG-b-PLys(CO-SN38)$_{20}$-CO-SN38	80.00	0.0077	89.97	0.1614	28.11	0.1614	6
BC237 - mPEG-b-P(Lys-O2O-CO-SN38)$_5$-O2O-CO-SN38	20.00	0.0028	9.34	0.0168	2.92	0.0168	6
BC238 - mPEG-b-P(Lys-O2O-CO-SN38)$_{10}$-O2O-CO-SN38	60.00	0.0067	40.86	0.0733	12.77	0.0733	6
BC239 - mPEG-b-P(Lys-O2O-CO-SN38)$_{20}$-O2O-CO-SN38	50.00	0.0039	46.11	0.0827	14.41	0.0827	6
BC240 - mPEG-b-P(Lys-O2O-O2O-CO-SN38)$_5$-O2O-O2O-CO-SN38	80.00	0.0100	33.33	0.0598	10.41	0.0598	6
BC241 - mPEG-b-P(Lys-O2O-O2O-CO-SN38)$_{10}$-O2O-O2O-CO-SN38	80.00	0.0075	46.28	0.0830	14.46	0.0830	6
BC242 - mPEG-b-P(Lys-O2O-O2O-CO-SN38)$_{20}$-O2O-O2O-CO-SN38	40.00	0.0025	29.75	0.0534	9.29	0.0534	6

BC234 - mPEG-*b*-PLys(SN38)$_5$-SN38

Yield: 52.2 mg, 80 %

^{1}H NMR (500 MHz, DMSO-*d6*, ppm): 7.20 – 8.40 (m, 31H, Aromatic C-H), 5.20 – 5.45 (m, 14H, Aliphatic Ring CH_2), 4.10 – 4.50 (m, 4H, αC-H), 3.35 – 3.60 (m, 452H, PEG CH_2-CH_2) 3.24 (m, 8H, ethyl CH_2), 3.00 – 3.20 (m, 8H, Lys-CH_2 + ethyl CH_2), 0.75 – 2.20 (m, 59H, Lys CH_2 + ethyl CH_2 + ethyl terminal CH_3).

BC235 - mPEG-*b*-PLys(SN38)$_{10}$-SN38

Yield: 78.2 mg, 74 %

^{1}H NMR (500 MHz, DMSO-*d6*, ppm): 7.20 – 8.40 (m, 101H, Aromatic C-H), 5.20 – 5.45 (m, 46H, Aliphatic Ring CH_2), 4.10 – 4.50 (m, 8H, αC-H), 3.35 – 3.60 (m, 452H, PEG CH_2-CH_2) 3.24 (m, 22H, ethyl CH_2), 3.00 – 3.20 (m, 33H, Lys-CH_2 + ethyl CH_2), 0.75 – 2.20 (m, 238H, Lys CH_2 + ethyl CH_2 + ethyl terminal CH_3).

BC236 - mPEG-*b*-PLys(SN38)$_{20}$-SN38

Yield: 87.1 mg, 69 %

^{1}H NMR (500 MHz, DMSO-*d6*, ppm): 7.20 – 8.40 (m, 106H, Aromatic C-H), 5.20 – 5.45 (m, 44H, Aliphatic Ring CH_2), 4.10 – 4.50 (m, 8H, αC-H), 3.35 – 3.60 (m, 452H, PEG CH_2-CH_2) 3.24 (m, 20H, ethyl CH_2), 3.00 – 3.20 (m, 35H, Lys-CH_2 + ethyl CH_2), 0.75 – 2.20 (m, 235H, Lys CH_2 + ethyl CH_2 + ethyl terminal CH_3).

BC237 - mPEG-*b*-P(Lys-O2O-SN38)$_5$-O2O-SN38

Yield: 15.5 mg, 61 %

^{1}H NMR (500 MHz, DMSO-*d6*, ppm): 7.20 – 8.40 (m, 35H, Aromatic C-H), 5.20 – 5.45 (m, 15H, Aliphatic Ring CH_2), 4.10 – 4.50 (m, 4H, αC-H), 3.80 – 4.00 (m, 10H, -CH_2CON-), 3.35 – 3.60 (m, 518H, PEG CH_2-CH_2) 3.24 (m, 10H, ethyl CH_2), 3.00 – 3.20 (m, 8H, Lys-CH_2 + ethyl CH_2), 0.75 – 2.20 (m, 67H, Lys CH_2 + ethyl CH_2 + ethyl terminal CH_3).

BC238 - mPEG-*b*-P(Lys-O2O-SN38)$_{10}$-O2O-SN38

Yield: 61.9 mg, 74 %

^{1}H NMR (500 MHz, DMSO-*d6*, ppm): 7.20 – 8.40 (m, 166H, Aromatic C-H), 5.20 – 5.45 (m, 22H, Aliphatic Ring CH_2), 4.10 – 4.50 (m, 11H, αC-H), 3.80 – 4.00 (m, 21H, -CH_2CON-), 3.35 – 3.60 (m, 518H, PEG CH_2-CH_2), 3.00 – 3.30 (m, 46H, Lys-CH_2 + ethyl CH_2), 0.75 – 2.20 (m, 113H, Lys CH_2 + ethyl CH_2 + ethyl terminal CH_3).

BC239 - mPEG-*b*-P(Lys-O2O-SN38)$_{20}$-O2O-SN38

Yield: 49.1 mg, 64 %

^{1}H NMR (500 MHz, DMSO-*d6*, ppm): 7.20 – 8.40 (m, 250H, Aromatic C-H), 5.20 – 5.45 (m, 60H, Aliphatic Ring CH_2), 4.10 – 4.50 (m, 9H, αC-H), 3.80 – 4.00 (m, 50H, -CH_2CON-), 3.35 – 3.60 (m, 578H, PEG CH_2-CH_2) 3.00 – 3.20 (m, 104H, Lys-CH_2 + ethyl CH_2), 0.75 – 2.20 (m, 204H, Lys CH_2 + ethyl CH_2 + ethyl terminal CH_3).

BC240 - mPEG-*b*-P(Lys-O2O-O2O-SN38)$_{5}$-O2O-O2O-SN38

Yield: 67.5 mg, 68 %

^{1}H NMR (500 MHz, DMSO-*d6*, ppm): 7.20 – 8.40 (m, 250H, Aromatic C-H), 5.20 – 5.45 (m, 70H, Aliphatic Ring CH_2), 4.10 – 4.50 (m, 3H, αC-H), 3.80 – 4.00 (m, 17H, -CH_2CON-), 3.35 – 3.60 (m, 524H, PEG CH_2-CH_2) 3.00 – 3.20 (m, 23H, Lys-CH_2 + ethyl CH_2), 0.75 – 2.20 (m, 62H, Lys CH_2 + ethyl CH_2 + ethyl terminal CH_3).

BC241 - mPEG-*b*-P(Lys-O2O-O2O-SN38)$_{10}$-O2O-O2O-SN38

Yield: 70.5 mg, 66 %

Due to poor solubility, samples could not be submitted for ^{1}H NMR analysis and so have not been reported. These solubility issues are discussed in greater detail in **Section 6.3.3**.

BC242 - mPEG(5000)NH2-b-P(Lys-O2O-O2O-SN38)20-O2O-O2O-SN38

Yield: 45.8 mg, 80 %

^{1}H NMR (500 MHz, DMSO-*d6*, ppm): 7.20 – 8.40 (m, 135H, Aromatic C-H), 5.20 – 5.45 (m, 60H, Aliphatic Ring CH_2), 4.10 – 4.50 (m, 9H, αC-H), 3.80 – 4.00 (m, 53H, -CH_2CON-), 3.35 – 3.60 (m, 704H, PEG CH_2-CH_2), 3.00 – 3.20 (m, 66H, Lys-CH_2 + ethyl CH_2), 0.75 – 2.20 (m, 199H, Lys CH_2 + ethyl CH_2 + ethyl terminal CH_3).

6.2.5 Formation of Nanoparticles

The generalised preparation of nanoparticle suspensions is here reported for the SN38-conjugated block copolymers synthesised in **Section 6.2.4**. Each SN38-conjugated block copolymer sample (2 mg) was dissolved in DMSO (50 µL). These dissolved samples were the pipetted in one aliquot into a 2 mL sample tube containing 950 µL of PBS solution without agitation, before being gently turned to ensure full mixture of the two solutions. Solubility of the resulting nanoparticle dispersion was observed, with any precipitated materials noted. Samples were then left to equilibrate for 1 hour before an additional examination for precipitates. Subsequently, samples were submitted for DLS analysis.

6.2.6 Drug Release Analysis

Nanoprecipitation and subsequent drug release analysis were performed externally by collaborators at AstraZeneca in Macclesfield, UK. Analysis was performed according to the methodology outlined in **Section 2.10**, which is summarised here:

A 10 mg/mL stock solution of the sample was prepared in DMSO, from which 25 µL was combined with 25 µL of 0.2 M NaOH in a 250 µL HPLC vial insert and mixed by pipetting. The mixture was incubated at room temperature for 1 h before quenching with 50 µL of a 10% acetic acid solution in acetonitrile. Samples were analyzed on a Waters Acquity UPLC system using a BEH Phenyl column (2.1 × 50 mm, 1.7 µm) with a 5-90% gradient of acetonitrile in water (0.1% TFA) over 5 min. SN-38 was detected at 360 nm and quantified against a calibration curve prepared from DMSO stock solutions of SN-38 diluted in acetonitrile.

6.3 Results and Discussion

6.3.1 Chain Extension of mPEG-*b*-PLys[NH_2.TFA]$_n$

Whilst it is possible to conjugate SN38 directly to the mPEG-*b*-PLys[NH_2.TFA]$_n$ block copolymers synthesised in **Section 5.3**, the size and steric hindrance of the SN38 molecule translates to a significant enthalpic penalty with increasing degree of conjugation.

As one lysine unit undergoes successful conjugation, adjacent pendant chains experience increased spatial crowding, raising the activation energy for subsequent conjugation.[23,24] This effect is compounded further for pendant chains sandwiched between two successfully conjugated units, an effect which significantly hinders reaction progress as polymers reach 100 % conjugation. To investigate whether this steric hindrance can be mitigated, spacer molecules have here been grafted to the main polymer chain to provide increased range of mobility and flexibility to the pendant-conjugate chain. This spacing affect has typically been achieved using polymer branching, as is demonstrated by England *et al*. in their use of lysine telodenrimers as sites for fulvestrant conjugation.[10] However, without further optimisation of the Lys-NCA ROP process, the poor chain uniformity observed throughout **Section 5.3.4** may have been compounded here during second or third generation branching, which would significantly impact both characterisation and analysis of the resultant BCPs, as well as the stability of their derived nanoparticles. Instead, small molecule chain extenders, with backbone functionality similar to that of PEG, have here been used. These molecules are illustrated in **Figure 6.1** below.

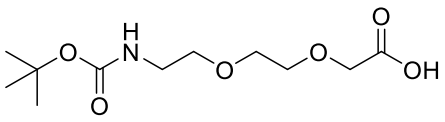

Boc-O2O-OH

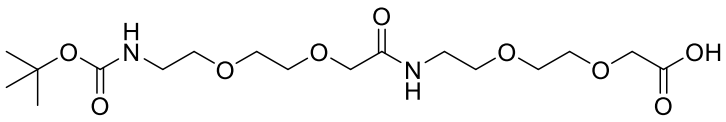

Boc-O2O-O2O-OH

Figure 6.1: Structure of two spacer molecules, grafted to the pLys block to increase the mobility and flexibility of its pendant chains.

The synthetic procedure for grafting extenders to the lysine pendant chain amines, as detailed in **Section 6.2**, was performed using PyBOP as a coupling intermediate, activating the small-molecule carboxylic acids prior to nucleophilic attack by the pendant chain amine.

DIPEA was utilised to both activate the carboxylic acid, and to neutralise the BCP-TFA salt, a remnant of prior deprotection reaction. This then enabled the amine side chain to act as a nucleophile and undergo an addition-elimination reaction, displacing the benzotriazole unit of the reactive intermediate to generate the product amide.[25,26]

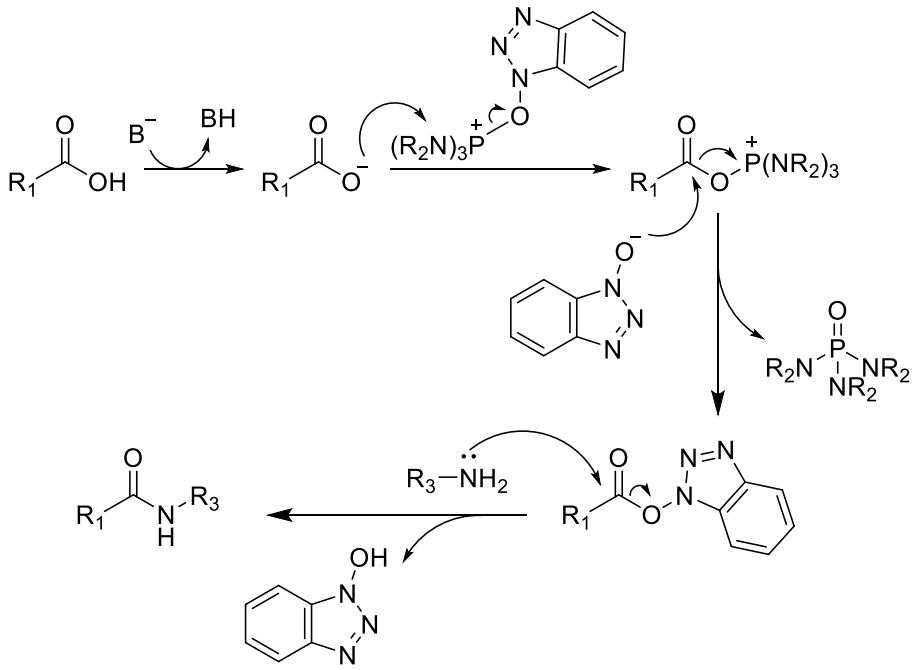

Figure 6.2: Mechanism of PyBOP coupling agent as part of amide coupling reaction.

It can be observed within **Figure 6.2** that the by-products generated include 1-hydroxy benzotriazole, tri(pyrrolidin-1-yl)phosphine oxide, and the PF_6^- spectator ion (here excluded). It was important to remove these agents prior to deprotection of the grafted polymer products, to avoid potential degradation reactions (specifically for tri(pyrrolidin-1-yl)phosphine oxide) in the presence of TFA.[27,28] As such, PD-10 Sephadex resin columns were used to separate the by-products *via* size-based chromatography, generating the purified product as fine white powders following lyophilisation. The successful grafting of the aforementioned small-molecule chain extenders is here verified for **BC224** and **225** *via* ^{1}H NMR spectroscopy, and for **BC224**, **225**, and **227** by SEC analysis. Due to the low yield achieved for **BC226**, this product was not evaluated at this stage, but was instead characterised following the mass-depletive deprotection stage, to ensure a sufficient mass of material for the following conjugation step.

This is also true for **BC227**, though SEC analysis was possible. The characterisation of the products has been detailed previously across **Sections 6.2.1** and **6.2.2**. However, for better evaluation of the attained product, visual representations of this characterisation for **BC224** and **BC225** have here been presented in **Figures 6.2** and **Figure 6.3**.

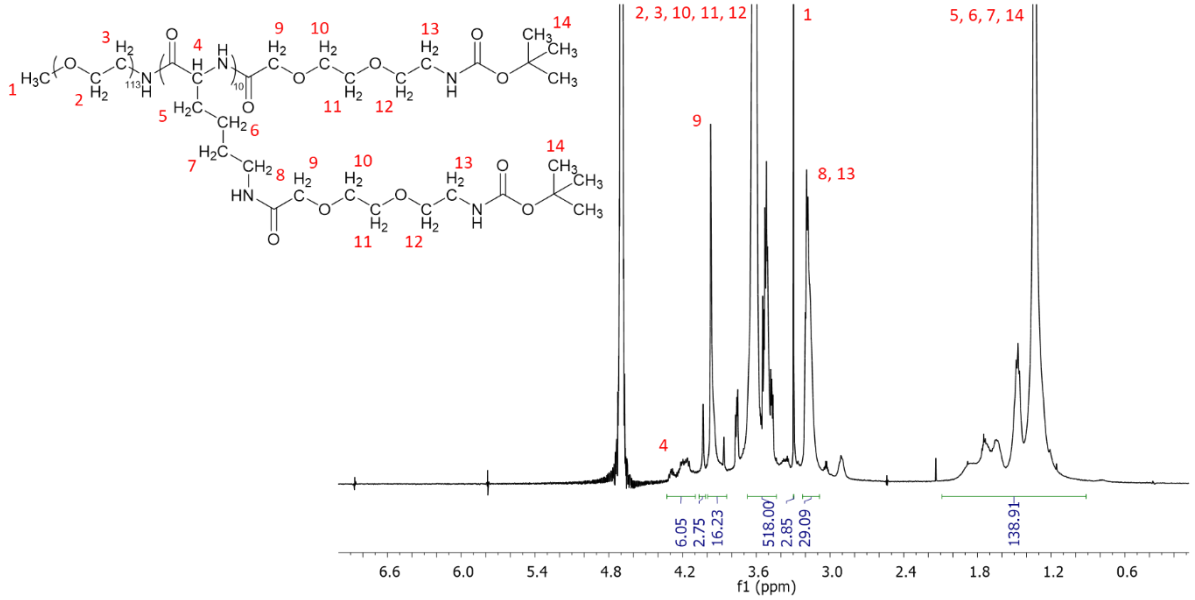

Figure 6.3: Visual ^{1}H NMR (500 MHz, D_2O) characterisation of BC224 – mPEG-*b*-PLys(O2O-Boc)$_{10}$-O2O-Boc, derived from BC219D.

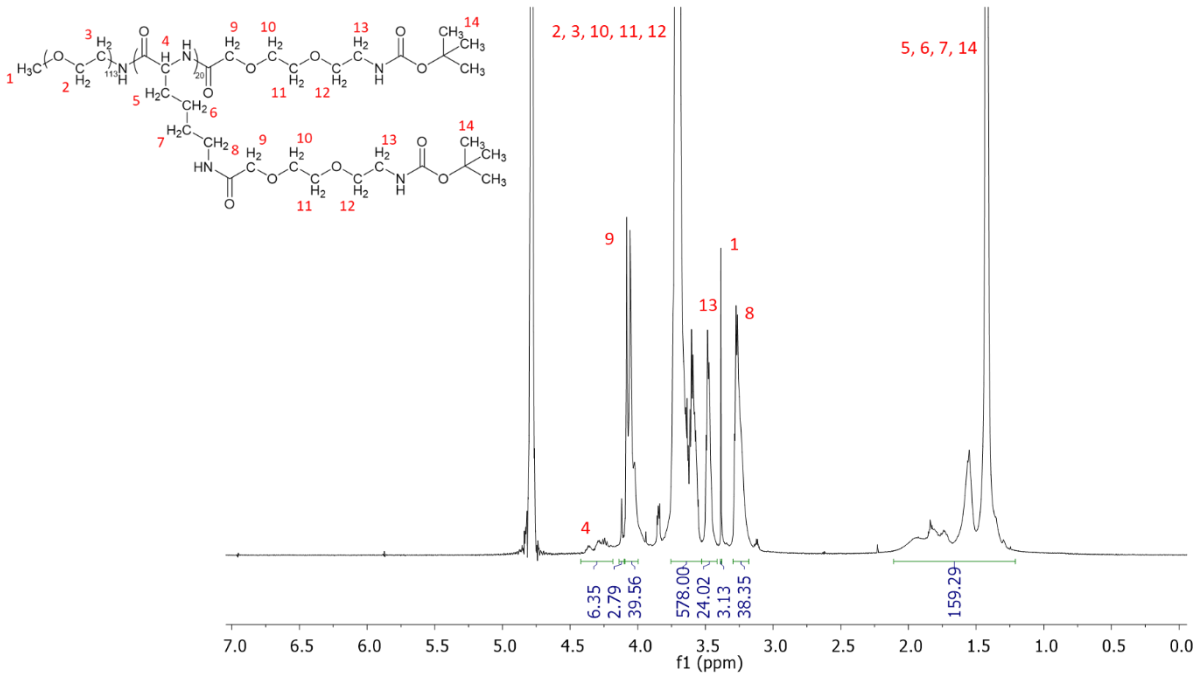

Figure 6.4: Visual ^{1}H NMR (500 MHz, D_2O) characterisation of BC225 – mPEG-*b*-PLys(O2O-Boc)$_{20}$-O2O-Boc, derived from BC220D

As is demonstrated within **Figure 6.3**, mPEG-*b*-PLys(O2O-Boc)$_{10}$-O2O-Boc has here been synthesised successfully. Notably, by using integral values within this spectrum corresponding to environments 9, 13 and 14, the average number of grafted O2O-Boc units per BCP can here be estimated as 8.8, suggesting that between 8 and 9 of the 11 available graft locations on the linear BCP have been occupied, corresponding to a grafting efficiency (GE) of 80 %. From this figure, the average number of grafted O2O-Boc units per BCP for **BC225** can be estimated as 19, 12, or as low as 4, dependent on which peak ranged is used to derive the figure. Nevertheless, this data does suggest that Boc-O2O-OH grafting to **BC219D** and **BC220D** (mPEG-*b*-PLys[NH_2.TFA]$_{10}$ and mPEG-*b*-PLys[NH_2.TFA]$_{20}$ respectively) has here been achieved to a degree.

SEC chromatograms (**Figures 6.5** and **Figure 6.6)** that compare the linear mPEG-*b*-PLys(Boc)$_n$ copolymers **BC196/7** to the products here obtained, explicitly show the relative change in molecular weights achieved by each reaction. Whilst it should be noted that **BC219/220**, the true linear precursors to **BC224/226**, were synthesised under reduced-temperature conditions, it was not possible to gather their SEC data in DMF eluent at the time of synthesis, making **BC196/197** the best comparison available.

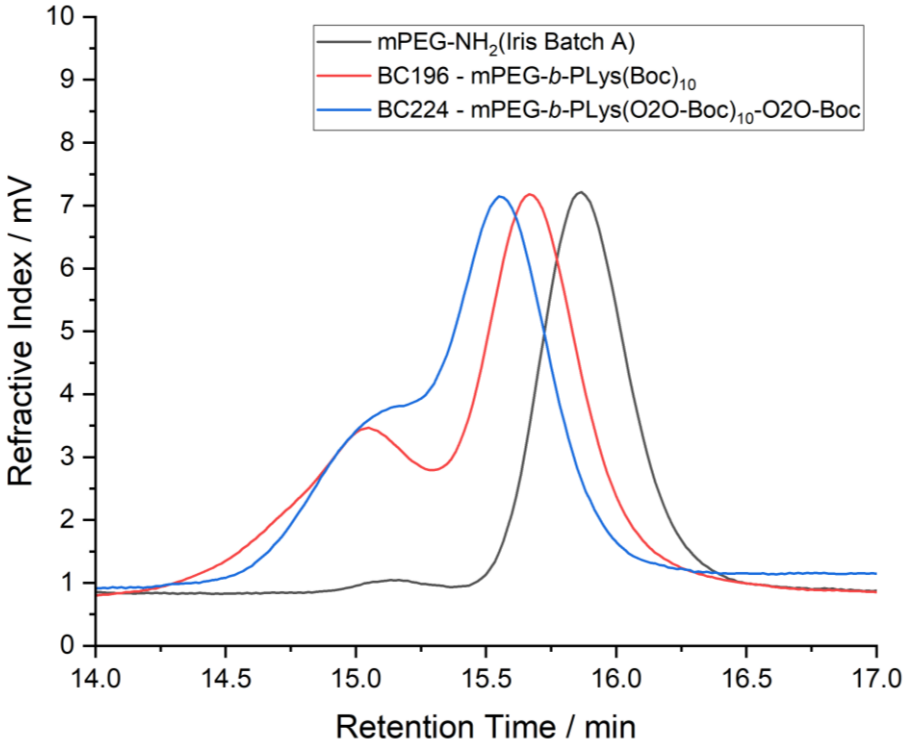

Figure 6.5: Comparative SEC analysis of mPEG-NH_2 (Iris Biotech), BC196 and BC224, to determine the increase in mass achieved by grafting the Boc-O2O-OH spacer unit.

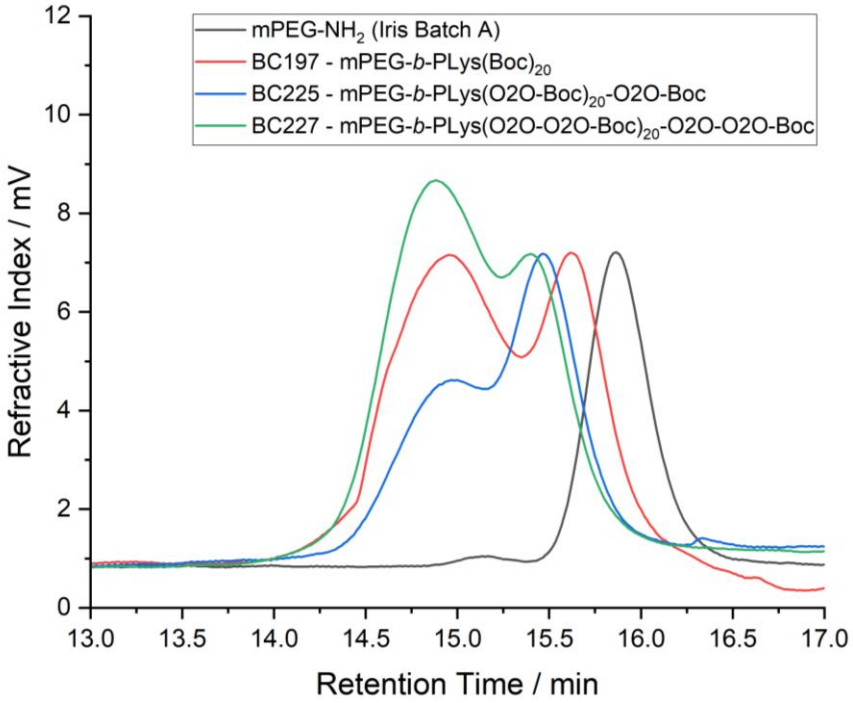

Figure 6.6: Comparative SEC analysis of mPEG-NH_2 (Iris Biotech), BC197, BC225 and BC227, to evaluate changing mass upon grafting the Boc-O2O-OH and Boc-O2O-O2O-OH spacer units.

The most notable observation from **Figure 6.5** is the clear increase in the relative position of the peaks for each distribution curve (M_p). Whilst values for M_n and M_w are not here reported for **BC196**, due to its non-uniform and multi-modal distribution, the consistent shift in M_p between the samples is strongly suggestive of a successful grafting procedure, and the increase in molecular weight of the polymer chains. In addition, though a clear shoulder is present on the left-hand slope of the **BC224** chromatogram, it can be seen that the reduced-temperature preparation of its **BC219** precursor, when compared with **BC196**, has produced subsequent polymers with a more controlled distribution of molecular weight and a smaller proportion of extremely-high-M.W. contaminants. This increase in polymer uniformity can also be evidenced the comparing the Đ values calculated for **BC224** and its precursor **BC219D**, versus the linear **BC196D**, for which molecular weight data was collected (albeit *via* an incomparable calibration system). The Đ value of mPEG-NH_2 (Iris Biotech) was 1.05, which was increased to 1.29 for **BC196D**. In contrast, **BC219D** and **224** have Đ values of 1.16 and 1.13, respectively, which quantify the significant improvement in their uniformity that was illustrated in **Figure 6.5** above. These data evidence qualitatively that a molecular weight increase has here been achieved over the non-extended, linear **BC196**.

Quantitative data here also evidences that an increase in uniformity has been achieved for the **BC219** line of products, and supports that progress has been made towards tighter control of NCA ROP side reactions. This suggests that further steps may be possible to eradicate the presence of these by-products altogether. **Figure 6.6** presents a more complex range of product chromatograms, owed principally to the diminished effect that reduced-temperature reaction conditions had on the uniformity of **BC220**. This can also be recalled from **Figure 5.18** in **Section 5.3.5.2**, wherein the significant multimodality of **BC220D**, whilst an improvement upon that of **BC197D**, left significant work to be done to achieve a uniform BCP product with greater than 10 polylysine repeat units. From initial observation between the chromatograms presented in **Figure 6.6**, it can again be noted that an upward trend in the retention time (and corresponding molecular weight) of the right-hand peak in each distribution correlates with the expected M.W. increase for each polymer product.

A significant shift exists between the macroinitiator and first linear BCP (**BC197**), corresponding to a jump from 5000 g mol^{-1} to 9844 g mol^{-1}, as well as between **BC196** and the grafted products (**BC225**/**227**), corresponding to jumps of 3188 g mol^{-1} and 6234 g mol^{-1}, respectively. A smaller shift is afforded by the increase in length of the spacer molecule (illustrated in **Figure 6.1**) resulting in the smaller shift between **BC225** and **BC227**, from 13,031 g mol^{-1} to 16,078 g mol^{-1}. This shift is also shortened in **Figure 6.6** due to the logarithmic nature of the x-axis, which compresses apparent shifts as molecular weight increases. Also of note for **Figure 6.6**, and more pronounced here than for the previous figure, is the behaviour of the left-hand peaks of each distribution. There is a clear decrease in size for the left hand peak between **BC197** and **BC225**, indicating that the reduced-temperature protocol, whilst unable to eliminate high-M.W. contaminants from the **BC220** precursor product, was still sufficient in mitigating the contributory side reaction within NCA ROP to some extent. An unexpected observation, however, is the apparent growth of this left-hand peak between **BC225** and **BC227**, indicating an increase in the proportion of high-M.W. material in the resultant **BC227** product. Though it is not possible to identify this high-M.W. material, it can be gleaned from the data that this increase in the relative area of its correlating peak was not a direct result of the grafting reaction, but more likely a symptom of the subsequent purification procedure *via* PD-10 size-based separation. However, this increase in the proportion of the left-hand peak of this distributions is not clearly reflected in a corresponding increase in M_w, and therefore appears to have no incidence upon the resulting Đ value for **BC227**. In fact, the value of Đ for each of these grafted materials (**BC225**/**227**) is 1.17, which is consistent with a value of 1.20 attained for **BC220D**. These values are significantly lower than that of **BC197D**, however, which again supports forward progress towards increased uniformity in these products.Importantly, these collected SEC chromatograms evidence a significant reduction in the retention times for each of the grafted products in comparison to the linear mPEG-*b*-PLys(Boc)$_n$ BCP, consistent with the expected increase in their molecular weight values as a result of the addition of small-molecule chain extenders. These data, coupled with the successfully characterisation of the ^{1}H NMR data above, are suggestive that this grafting procedure was achieved successfully, leading to the subsequent deprotection of these materials, as discussed in **Section 6.3.1.1** below.

6.3.1.1 Deprotection of Grafted Chain Extenders

Deprotection of products **BC203**, **BC215** and **BC224**-**227** was performed *via* the methodology described in **Sections 6.2.1.1** and **6.2.2.1**, in line with previous Boc-deprotection strategies employed throughout **Section 5**.

To evaluate first the derivatives of **BC195**: **BC203D** was successfully obtained in good yield (85 %) sufficient for characterisation *via* ^{1}H NMR and SEC techniques. **BC215D**, however, through a combination of a low-yielding amide coupling reaction (39 %) and the negative atom economy of the subsequent deprotection, was not here submitted for ^{1}H NMR analysis, with further characterisation delayed until completion of the drug conjugation step. Therefore, presented in **Figures 6.7** and **6.8** here are the fully characterised ^{1}H NMR spectrum of **BC203D**, as well as the SEC data for both **BC203D** and **BC215D**. Molecular weight data and dispersity values are provided inset within **Figure 6.8**.

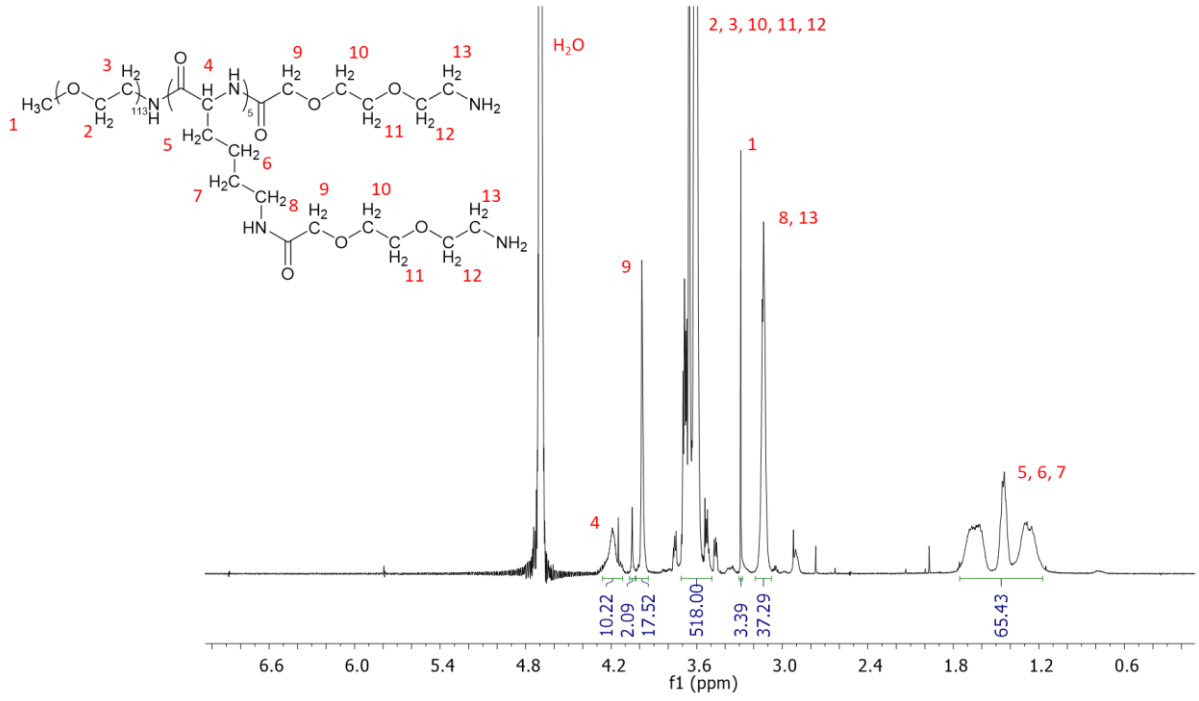

Figure 6.7: ^{1}H NMR characterisation (500 MHz, D_2O) of **BC203D** – mPEG-*b*-PLys[O2O-NH_2.TFA]$_5$-O2O-NH_2.TFA. For simplicity, the product is presented in neutral form, as opposed to the TFA salt.

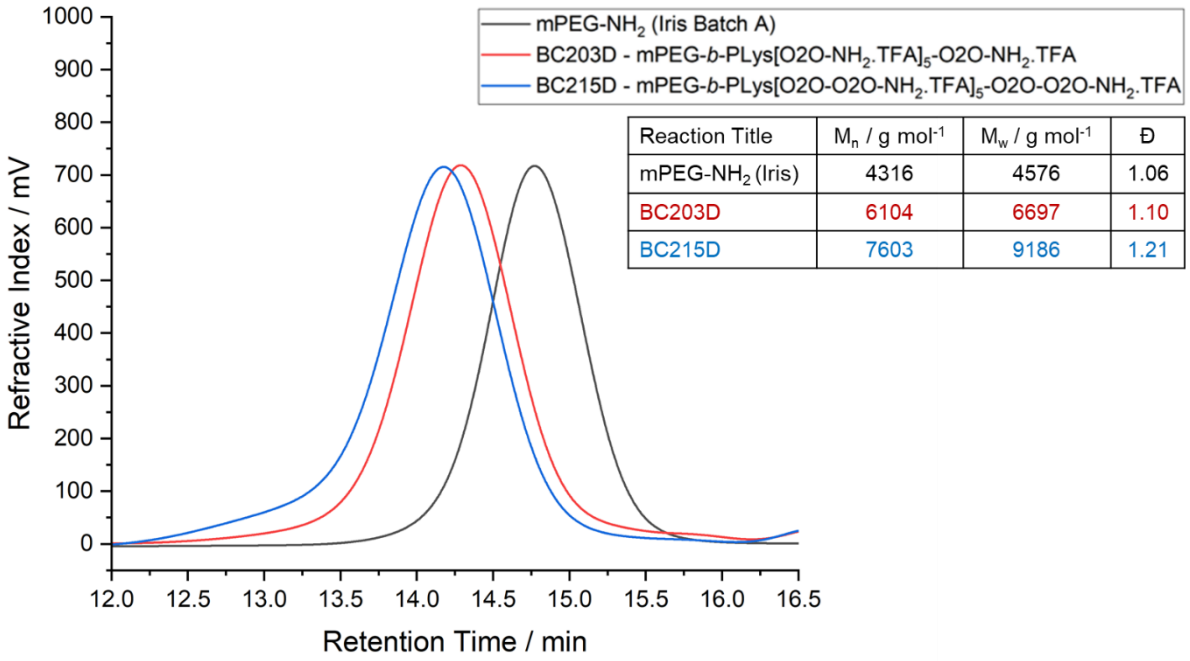

Figure 6.8: Comparative SEC analysis of mPEG-NH_2 (Iris Biotech), BC203D and BC215D, to determine the increased in mass of the two in comparison to the macroinitiator, as well as the increase in M.W. due to differing chain extender size.

Figure 6.7 clearly illustrates the successful deprotection of **BC203**, which has here been achieved without the presence of impurities. The relative integrals here are in good agreement with the previously estimated D.P. of the **BC195** polymer series (ca. 5 repeat units), revealing a very promising estimated grafting efficiency of 87 %. These data are further supported by SEC analysis (**Figure 6.8**) which illustrates a clear decrease in retention time and increase in associated M_n values for the deprotected graft BCPs above that of the macroinitiator. Furthermore, a slight increase between **BC203D** and **215D** can also be seen, which accounts for the increase in molecular weight corresponding to the larger linker (774 g mol^{-1}). In addition, whilst the M_n values for these materials do not appear to align with those derived *via* calculations from the constituent repeat units, the values obtained are downshifted to a similar extent as the M_n obtained for mPEG-NH_2. This downshift is likely due to the calibration setup of the SEC system, and it is promising that there appears to exist such a consistent disparity between the expected and reported values.

A final, important observation can be made of the Đ values reported for these products. The slight increases in Đ reported for each polymer (to 1.10 and 1.21, respectively), whilst acceptable parameters for this investigation, are somewhat unexpected. Both **BC203** and **215** are derived from **BC195D**, for which Đ was determined to be 1.05, meaning that throughout the grafting and deprotection process, there has been introduced some level of non-uniformity into the product. This could potentially be linked to an incomplete grafting procedure, as suggested by the estimated 87 % grafting efficiency (GE) derived within **Section 6.3.1**. With grafting being non-uniform across all polymer chains the distribution may be broadened, with low GE chains broadening the peaks to higher retention times and vice versa for high GE chains. This effect would then be compounded for **BC215D**, due to the greater M.W. of the Boc-O2O-O2O-OH chain extender molecule, which explains the greater increase in Đ for this chain. Nevertheless, these polymers represent a high standard of control for NCA-ROP and for the uniformity of the resultant products. These products currently represent the best candidates for future nanoprecipitation, encapsulation and subsequent release.

^{1}H NMR characterisation was performed for **BC224D**, and overlaid spectra are provided for **BC224D**/**226D** and **BC226D**/**227D**, across **Figures 6.8**, **6.9** and **6.10**. Overlaid spectra have been normalised by equilibrating the PEG-methoxy CH_3 peak for each product pair (▢).

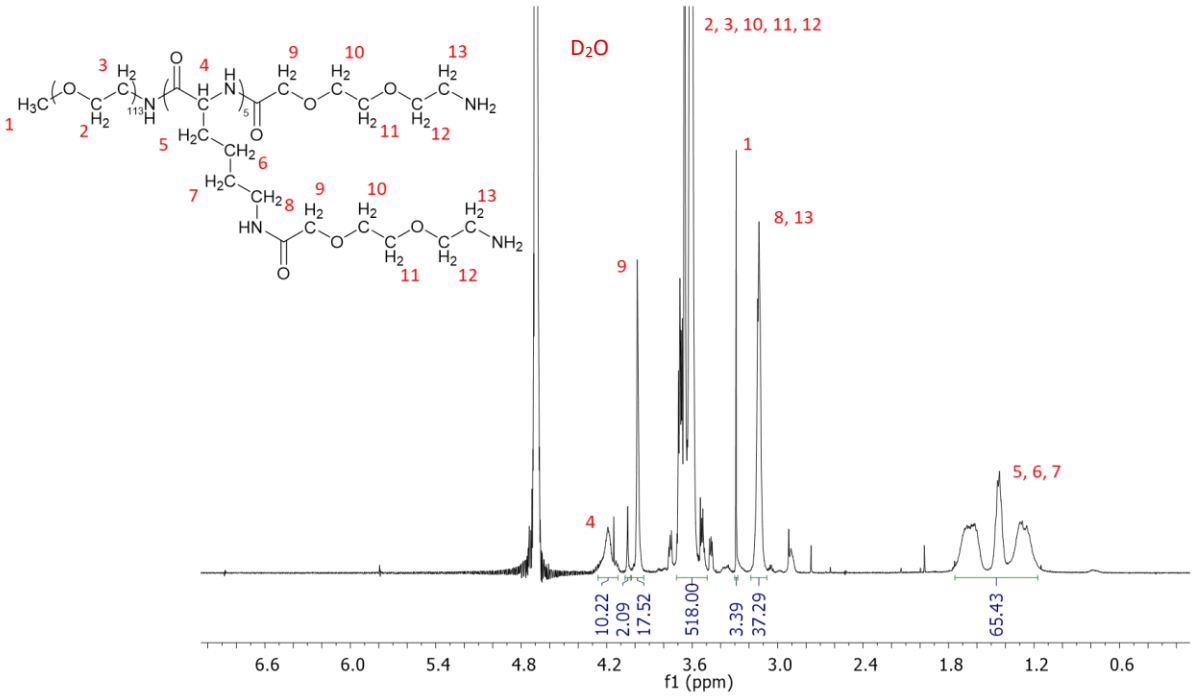

Figure 6.9: ^{1}H NMR characterisation (500 MHz, D_2O) of BC224D – mPEG-*b*-PLys[O2O-NH_2.TFA]$_{10}$-O2O-NH_2.TFA. For simplicity, the product is presented in neutral form, as opposed to the TFA salt.

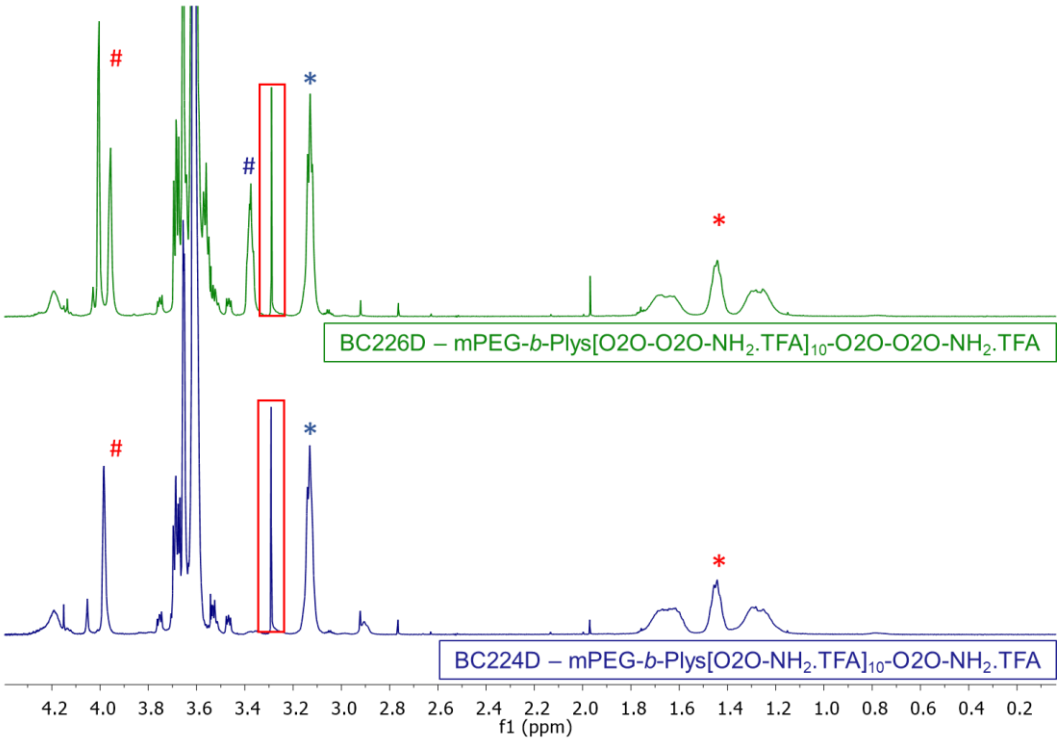

Figure 6.10: Overlaid ^{1}H NMR spectra (500 MHz, D_2O) of BC224D and BC226D highlighting the changes in relevant integral ranges in comparison to a normalised PEG-CH_3 integral (▢).

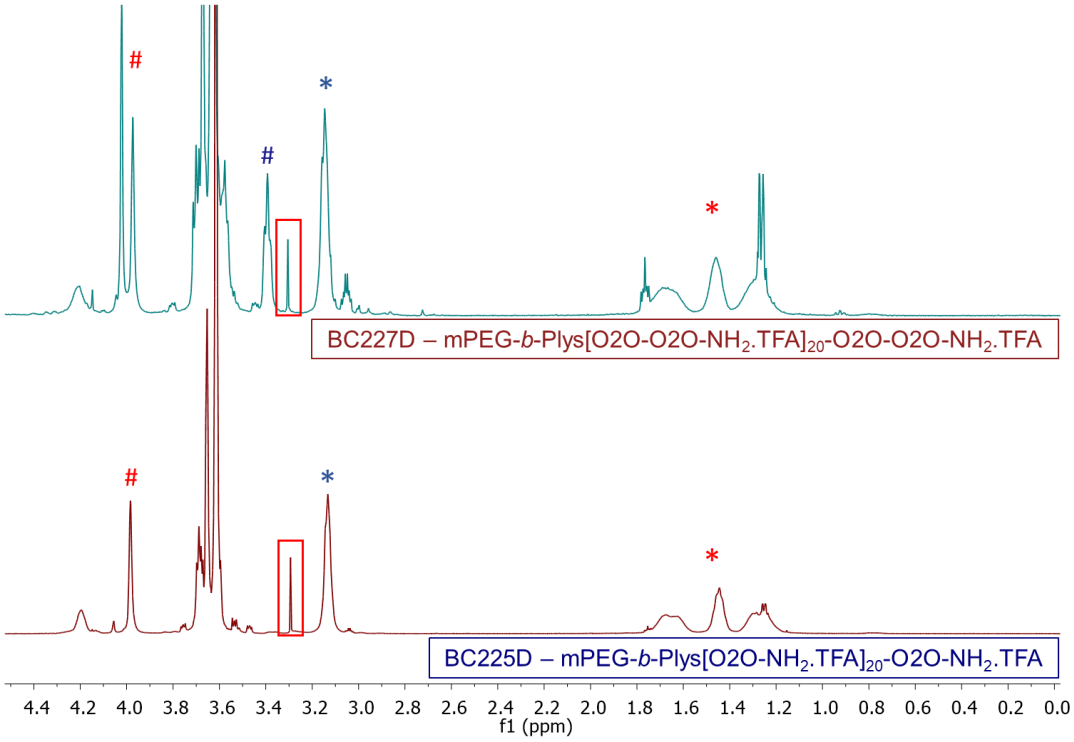

Figure 6.11: Overlaid ^{1}H NMR spectra (500 MHz, D_2O) of BC225D and BC227D highlighting the changes in relevant integral ranges in comparison to a normalised PEG-CH_3 integral (▢).

Figure 6.9 illustrates integral values that correspond with those expected for the intended D.P. of the PLys block (ca. 10 repeat units). Importantly, integral ranges representing the chain extender molecule are in good agreement with estimated grafting efficiency of **BC224,** with estimations of 89% (9) and 78% (13), compared to the previously derived average of 80 %. The significant integral decrease between 1.2 ppm – 1.8 ppm evidences that Boc-deprotection has been performed successfully. **Figure 6.10** clearly demonstrates that **BC226D** has been obtained in similarly high purity, and evidences the increased length of the grafted chain extender between the two samples. Between **BC224D** and **226D**, the addition of the second O2O-unit is visually represented both in the in the appearance of a second amide-adjacent ethyl peak (#) and an additional pseudo-glycol environment (#).

From the integral values recorded for **BC226D** (**Figure A.6.1.4)** grafting efficiency can here be estimated as 95 %. From **Figure 6.11,** similar observation of the lysine aliphatic integral range (*) and amide-adjacent ethyl ranges (#, #) demonstrate grafting efficiency values for **BC225D** and **BC227D** of 90 % and 97 %, respectively.

These data provide compelling evidence of the success of each grafting and deprotection reaction, from the perspective of product purity, targeted grafting efficiency and complete deprotection.

SEC analysis for **BC224D**, **225D**, and **226D** was performed, with comparative traces reported below across **Figures 6.11** and **6.12**. It should be noted prior that, due to a change in column, these data were collected in a format that does not allow for their comparison to either the macro initiator, or their linear precursors, **BC219D**/**220D**. As such, they have been presented in comparison to one another, highlighting the effect of increasing PLys block D.P. between **BC224D**/**225D**, and the effect of increasing chain extender M.W. between **BC224D**/**226D**.

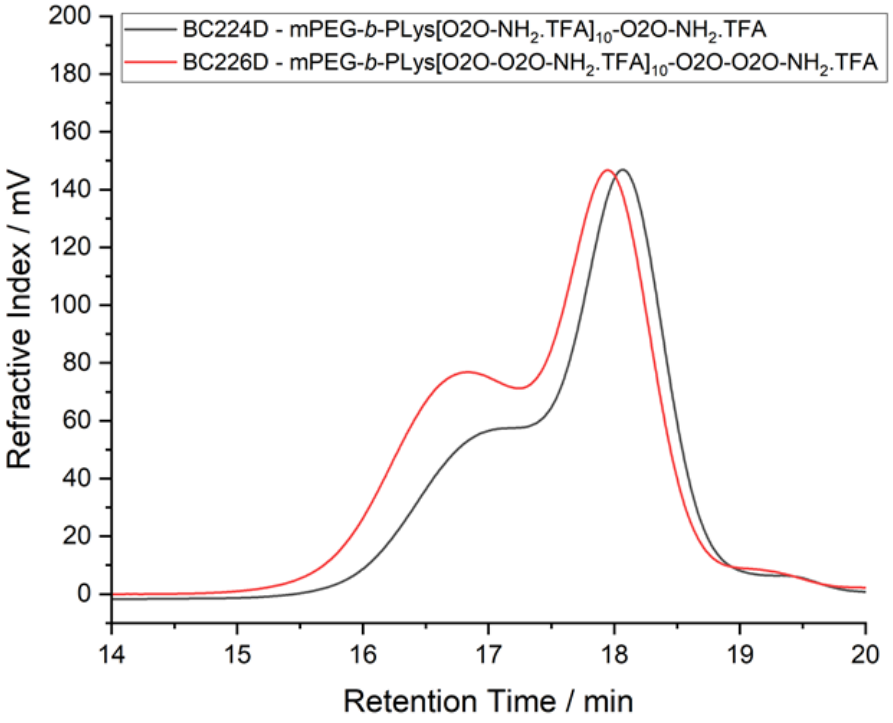

Figure 6.12: Comparative SEC analysis pairs of BC224D/226D.

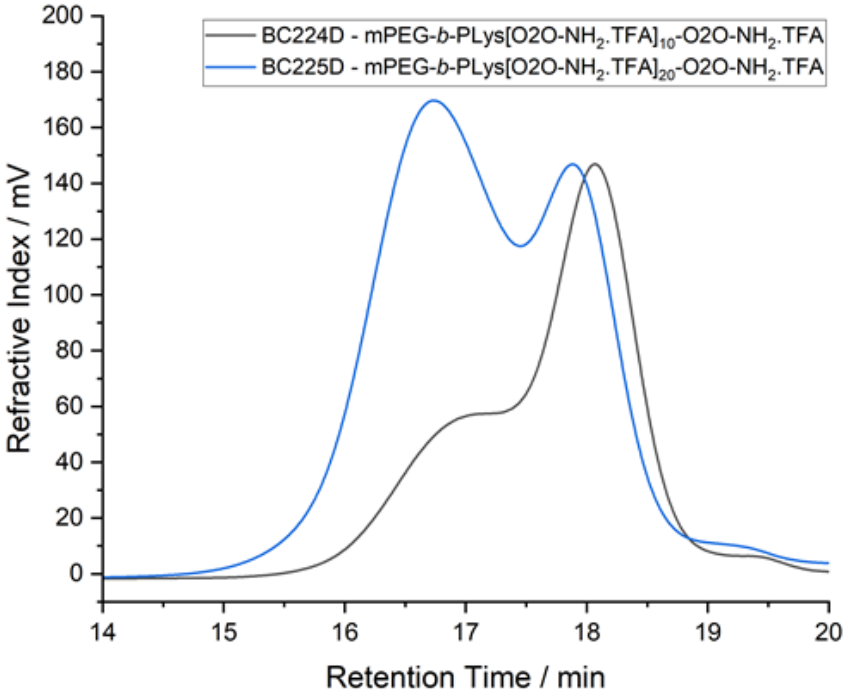

Figure 6.13: Comparative SEC analysis pairs of BC224D/225D.

Whilst it is clear from **Figure 6.12** that the shape of the M.W. distribution for the protected precursor remains relatively unchanged, the corresponding Đ value for**BC224D** is far higher than expected (1.38). This is likely a symptom of the calibration system which, thanks to the logarithmic dependence of M.W. on retention time, artificially inflates the M_w value of the polymer.[29,30] It is more pertinent to evaluate the qualitative shifts present between **BC224D** and **226D** here, such as the slight upward shift in retention time associated with the higher-M.W. chain extender molecules. This effect is consistent with that observed for **BC225** and **BC227** in **Figure 6.5**. In addition, it can be observed that, for **BC226D**, a similar M.W. distribution exists in comparison to both **BC224D**, and **BC219D**, illustrated in **Figure 6.4**. This suggests that chain uniformity has been conserved throughout grafting and deprotection. Furthermore, as the shifts in molecular weight are clearly conserved across the M.W. distribution for the polymer, it can be surmised that the high-M.W. contributor to the left-hand shoulder of these distributions is similarly capable of undergoing grafting and deprotection.

Upon evaluation of **Figure 6.13**, a qualitative comparison of **BC225D** can also be made here, against its protected counterpart from **Figure 6.5**. Unexpectedly, an inflation of the left-hand peak area within the bimodal distribution here has occurred, similar to that observed for **BC227** in the same figure. However, as there was no purification *via* PD-10 column for this reaction, nor any other size-based separative procedures performed upon the products, there is no clear argument for this shift in proportion. Nevertheless, *via* qualitative comparison to the chromatogram of **BC224D**, it is clear that an upward shift in retention time occurs between the right-hand peak of each trace's distribution, representative of the expected increase in molecular weight between polymers with PLys block of 10 and 20 repeat units. These data support the success of the deprotection step for these materials and the conservation of chain uniformity for the products, with only minor peak broadening observed for **BC215D**.

While more in-depth comparison could not be achieved here, the available data is sufficient to support the progression of each polymer product to the final stage of post-polymerisation modification – conjugation *via* cleavable linker to SN38.

6.3.2 Synthesis of 10-O-(p-nitrophenyl carbonate)-SN38

SN38 was conjugated to a *p*-nitrophenyl carbonate linker *via* the preparative procedure outlined in **Section 6.2.3**. Sequential sampling and LC-MS analyses were used to determine the end point of reaction by monitoring the depletion of SN38 over time, and to monitor the appearance of unwanted by-products. These included re-generated SN38, formed as a result of hydrolysis of the carbonate product, as well as SN38-carbonate dimer, formed through secondary reaction of SN38 with an already formed 10-O-(p-nitrophenyl carbonate)-SN38. To reduce the impact of the former and the likelihood of the latter, di-nitrophenyl carbonate was employed in 5-fold excess. The product was obtained in good yield (74 %) and was subject to characterisation *via* ^{1}H NMR spectroscopy (**Figure 6.14**).

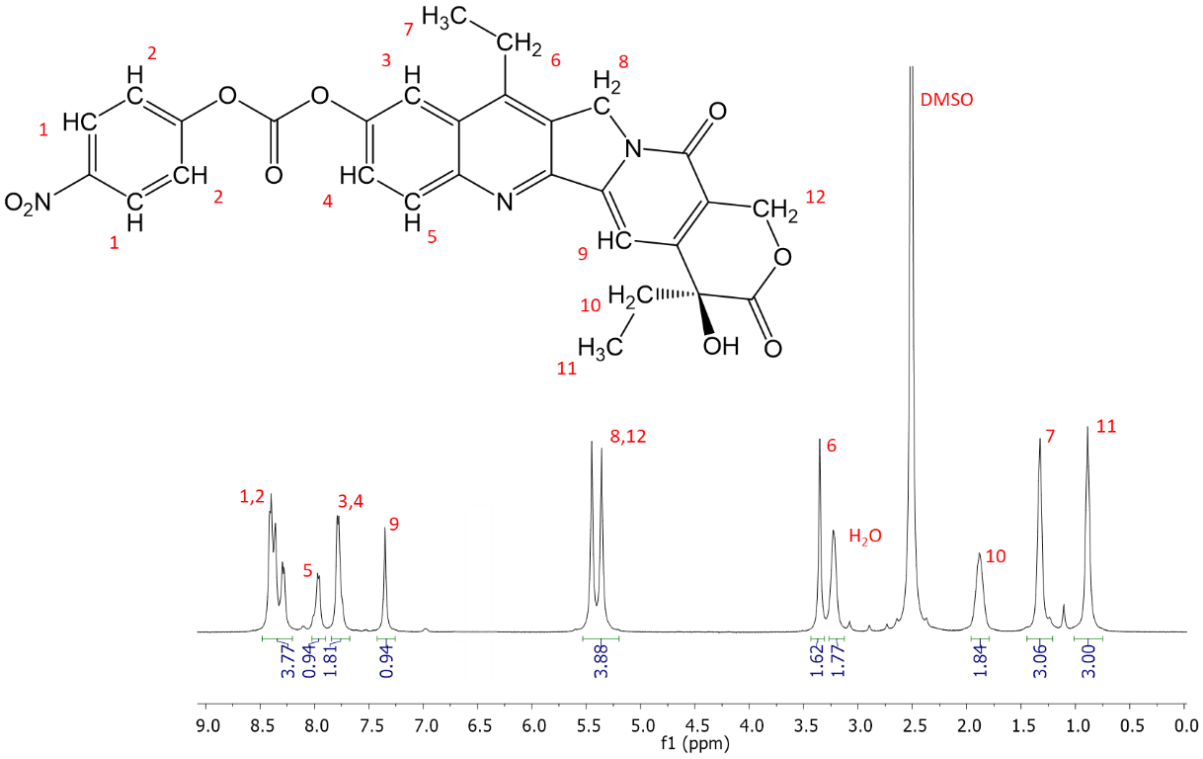

Figure 6.14: ^{1}H NMR spectrum (500 MHz, DMSO-d_6) of (10-O-(p-nitrophenyl carbonate)-SN38).

As observed in **Figure 6.14**, the product has been obtained without the presence of impurities. The positions and relative areas of the integrals, normalised against an aliphatic methyl proton environment of the SN38 molecule, are in good agreement with relevant literature.[31]

In addition, it appears that the purification procedure, specifically the removal of *p*-nitrophenol *via* TBME washes, has been successful in delivering a pure product.

As such, this intermediary was considered suitable for reaction with the nine available polymer platforms generated previously. These include non-extended, linear mPEG-*b*-PLys[NH_2.TFA]$_n$, where n = 5, 10 and 20, as well as two sets of three chain-extended equivalents (O2O-grafted and O2O-O2O-grafted), with corresponding PLys block lengths of 5, 10 and 20 repeat units.

6.3.3 Syntheses of mPEG-*b*-PLys[(O2O)$_n$-SN38]$_m$

Prior to evaluating the products obtained and analysed within this section, it is first pertinent to re-organise each of the precursor polymers and associate them with their subsequent conjugative product. **Table 6.4** clearly illustrates the groupings within which polymer products comparisons might be made, with products grouped by varying levels of chain extension (□) and colour-coded according to the targeted degree of polymerisation of their constituent lysine blocks, as reported in **Section 5.3.4**.

Table 6.4: Product table for SN38 conjugation products. Triplet groupings correspond to levels of chain extension for each product, whilst colour coding delineates different degrees of PLys polymerisation within the products.

Precursor Polymer	Conjugation Product	Expected Lysine Block D.P.	Conjugate Polymer Formula
BC195D	**BC234**	5	mPEG$_{113}$-*b*-PLys(CO-SN38)$_5$
BC219D	**BC235**	10	mPEG$_{113}$-*b*-PLys(CO-SN38)$_{20}$
BC220D	**BC236**	20	mPEG$_{113}$-*b*-PLys(CO-SN38)$_{20}$
BC203D	**BC237**	5	mPEG$_{113}$-*b*-PLys(O2O-CO-SN38)$_5$
BC224D	**BC238**	10	mPEG$_{113}$-*b*-PLys(O2O-CO-SN38)$_{10}$
BC225D	**BC239**	20	mPEG$_{113}$-*b*-PLys(O2O-CO-SN38)$_{20}$
BC215D	**BC240**	5	mPEG$_{113}$-*b*-PLys(O2O-O2O-CO-SN38)$_5$
BC226D	**BC241**	10	mPEG$_{113}$-*b*-PLys(O2O-O2O-CO-SN38)$_{10}$
BC227D	**BC242**	20	mPEG$_{113}$-*b*-PLys(O2O-O2O-CO-SN38)$_{20}$

These yields are reported across **Section 6.2**, and the quantities used are available within **Table 6.3**. Due to this, the yielded quantities of conjugative products also varied significantly, with **BC237** being a clear example. Due to the low yield of **BC237**, SEC data was not collected, and this product was not continued forward for drug release testing.

^{1}H NMR data was collected for this sample, however. Furthermore, it should be noted that purification was made significantly more complicated for this procedure, due to the difficulty of separating SN38-conjugated polymer from impurities such as SN38-dimer, generated *via* the secondary reaction discussed in **Section 6.3.2**, and non-conjugated SN38, which either remained unreacted from the previous preparatory procedure, or was generated *in situ* from the hydrolysis of the 10-O-(p-nitrophenyl carbonate)-SN38 intermediate or the dimer.[32] These materials share similar solubility to the conjugated chain, making their separation challenging. It was therefore considered more appropriate not to attempt purification following the conjugation therefore, and instead to expect an increased initial presence of these excess SN38-like materials during the drug release process.

The increased presence of these impurities was also taken into account during ^{1}H NMR analysis of the products. It was expected that SN38-corresponding peak ranges (aromatic ring C-H, aliphatic ethyl and methyl C-H) would experience some inflation, in comparison to the PEG-CH_2 ethyl peaks typically presented at ca. 3.5 ppm. This is exemplified throughout **Figures A.6.1.9-A.6.1.16** within appendix **Section A.6.1** for each of the conjugated products, and can be seen illustrated clearly in **Figure 6.15** below, which illustrates the ^{1}H NMR spectrum of product **BC235**.

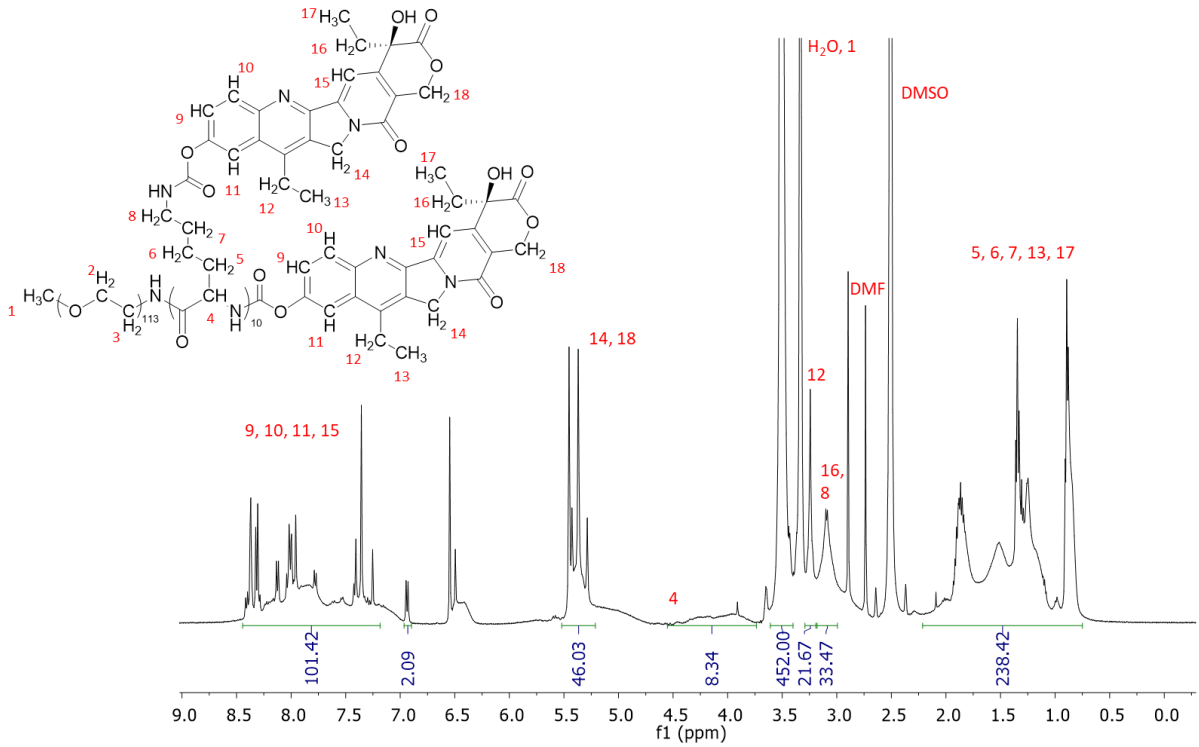

Figure 6.15: Visually characterised ^{1}H NMR spectrum (500 MHz, DMSO-d_6) for BC235.

For this product, it is possible to clearly identify the expected proton domains identified for its precursors, including SN38 aromatic ring protons between 7.0 and 8.5 ppm, ring aliphatic protons at 5.5 ppm, linear aliphatic protons across 1.0 – 2.0 ppm and even the O2O-linker pseudo-PEG ethyl proton ranges at 3.10 and 3.25 ppm. However, the integral ranges for these are indeed inflated above the values expected for them. For instance, with 10 repeat units and one terminal, it could be estimated that the aromatic group integral contribution (7.0 – 8.5 ppm) would be 44, reflecting eleven sets of four individual proton environments. However, the integral is *ca.* 100, coupled with the presence of sharp, tall peaks, which likely correspond to low-molecular weight species such as the impurities discussed. This is reflected in integral ranges across this spectrum and those of the other product species, compounded by the presence of additional DMF impurity. As such, whilst characterisation of the ^{1}H NMR spectroscopy was possible, it appears that estimation of the number of conjugated units, and subsequent calculation of conjugation efficiency, has here been made inaccurate. Instead, further examination of the products was left to GPC analysis, for comparative evaluation of the relative M.W. values for each product.

GPC data was collected for several of the product polymers, excluding **BC237**, for which product quantity was too low, as well as products **BC240** and **BC241**. These latter products exhibited extremely poor solubility in the DMF/LiBr eluent system, even in the presence of additional heat and perturbation, and as such were unable to be analysed. Qualitative comparisons to elucidate trends between products with related precursor chains have been made. Quantitative analyses were not possible due to the vast chemical difference between the polymers generated and GPC calibrant (PMMA). The first of these qualitative comparisons is illustrated in **Figure 6.16**, between **BC234**-**236**, the linear SN38-conjugated products derived from **BC195D**, **BC219D** and **BC220D**.

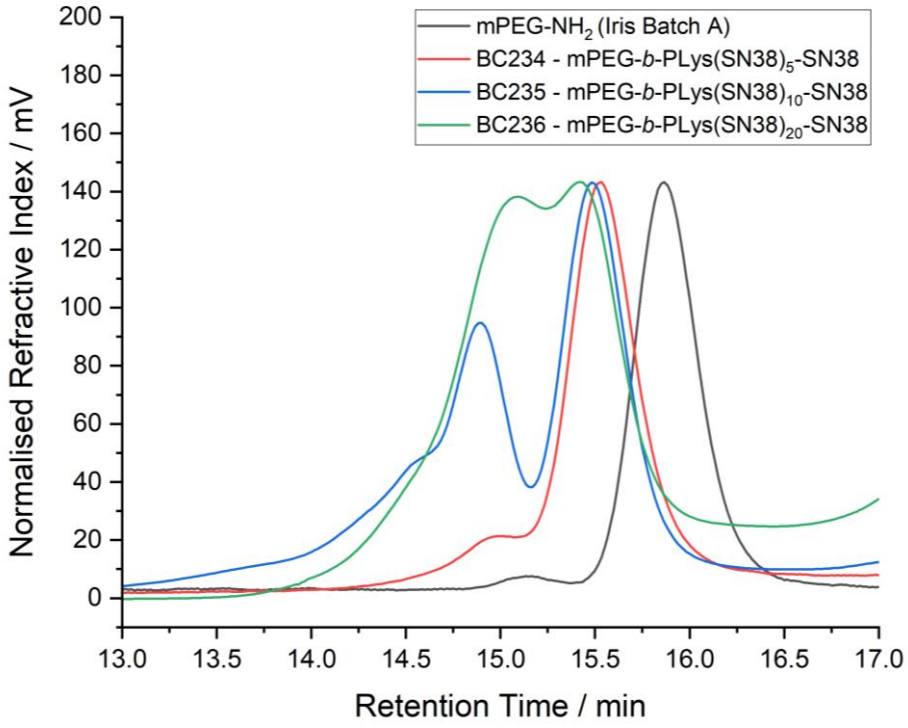

Figure 6.16: Overlaid GPC Chromatograms for mPEG-NH_2 macroinitiator, BC234, BC235 and BC236. Samples were obtained in DMF-LiBr eluent.

There is a clear trend of increasing molecular weight between the samples displayed in **Figure 6.16**, consistent with the expected increasing target D.P. of the linear polymers from which each product is derived. This is more pronounced between **BC235** and **BC236** than for **BC234** and **235**, due to the greater increase of PLys repeat units between their respective precursors, increasing from 5 to 10 to 20 from **BC234** to **235** to **236**.

This suggests that the linear precursor chains have been maintained from initial NCA-ROP reaction, throughout subsequent deprotection and conjugation. The M_n value for **BC234** was here determined to be 18,500 g mol^{-1}, which exceeds the maximum expected M.W. for mPEG-*b*-PLys(SN38)$_5$-SN38 by over 10,000 g mol^{-1}. Whilst this excess might be expected for samples with bimodal distributions, such as those derived from **BC219D** and **BC220D**, **BC234** and its precursors are uniform and well-defined, suggesting a methodological inaccuracy as opposed to a vast, unexpected M.W. increase. It can be noted that between these conjugated polymer species and their linear precursor species (**BC219D/20D**, illustrated in **Figure 5.18 in Section 5.3.5.2**) that there is an additional, unexpected increase in area for these high-M.W. impurities.

This is less clear between **BC219D** and **BC235**, for which the apparent increase may be related to an improvement in resolution between aqueous and organic eluents. However, between **BC220D** and **BC236**, it is clear that a proportional increase of the left-hand peak does occur in the conjugated product surpasses that of the precursor. Whilst a similar proportional shift has been observed previously, between **BC220D** and **BC227**, this was as a result of purification measures which were not applied here. An alternate explanation for this shift occurring following SN38 conjugation can instead be linked to the possibility of a bi-functional PEG macroinitiator, which has been discussed frequently within prior sections of this report. Such an initiator would undergo a more prolific NCA-ROP reaction, bearing more lysine units than the mono-functional equivalent and, hence, would bear a greater number of conjugated lysine units following this stage of reaction. During the subsequent diethyl-ether washing procedures, it is possible that the more heavily-conjugated species experienced poorer ether solubility, meaning that a smaller proportion was removed. Comparison of **BC235** and **BC238** is presented in **Figure 6.17** below, which allows investigation of the effects of O2O chain extension on the conjugated mPEG-*b*-PLys$_{10}$ framework.

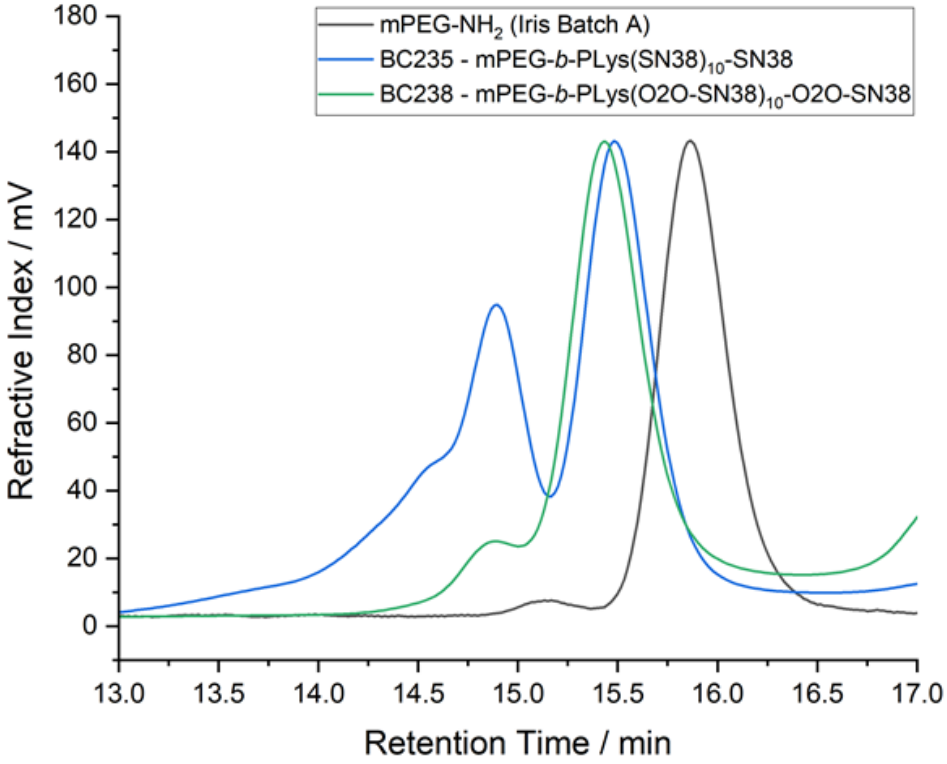

Figure 6.17: Overlaid GPC Chromatograms for mPEG-NH_2 macroinitiator, **BC235** and **BC238**. Samples were obtained in DMF-LiBr eluent.

From initial comparison of the right-hand peaks from each distribution, in keeping with the methodology for previous comparisons of these multi-modal distributions, it can again be seen that a slight increase occurs between **BC235** and **BC238**, in line with the molecular weight increase provided by the O2O chain extender. For a more clear representation of the successful conjugation of **BC238**, **Figure 6.18** is presented below, comparing its chromatogram with that of the Boc-protected precursor, **BC224**.

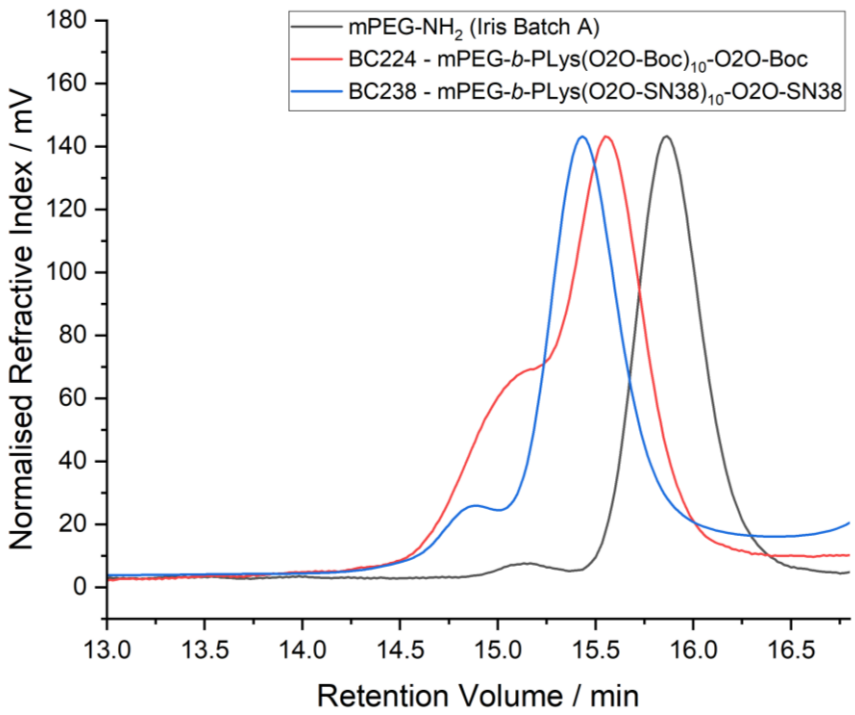

Figure 6.18: Overlaid GPC Chromatograms for mPEG-NH_2 macroinitiator, **BC224** and **BC238**. Samples were obtained in DMF-LiBr eluent.

From **Figure 6.18**, it can be clearly observed that a significant shift in retention time has occurred between the right-most peaks of **BC224** and **BC238**. This aligns with the expected molecular weight increase of 3400 g mol^{-1}, afforded by the substitution of ten Boc groups for ten SN38-carbamate groups and suggests that both Boc-deprotection of the chain extended copolymer, as well as subsequent conjugation to the drug-linker system has here been achieved successfully. Comparison to Boc-protected precursors has not been possible for **BC234-6**, due to the lack of SEC facilities at the time of synthesis for the **BC215**, **BC219** and **BC220** precursors. For **BC239** and **BC242**, however, such comparison has been possible, and is presented in **Figures 6.19** and **6.20** below.

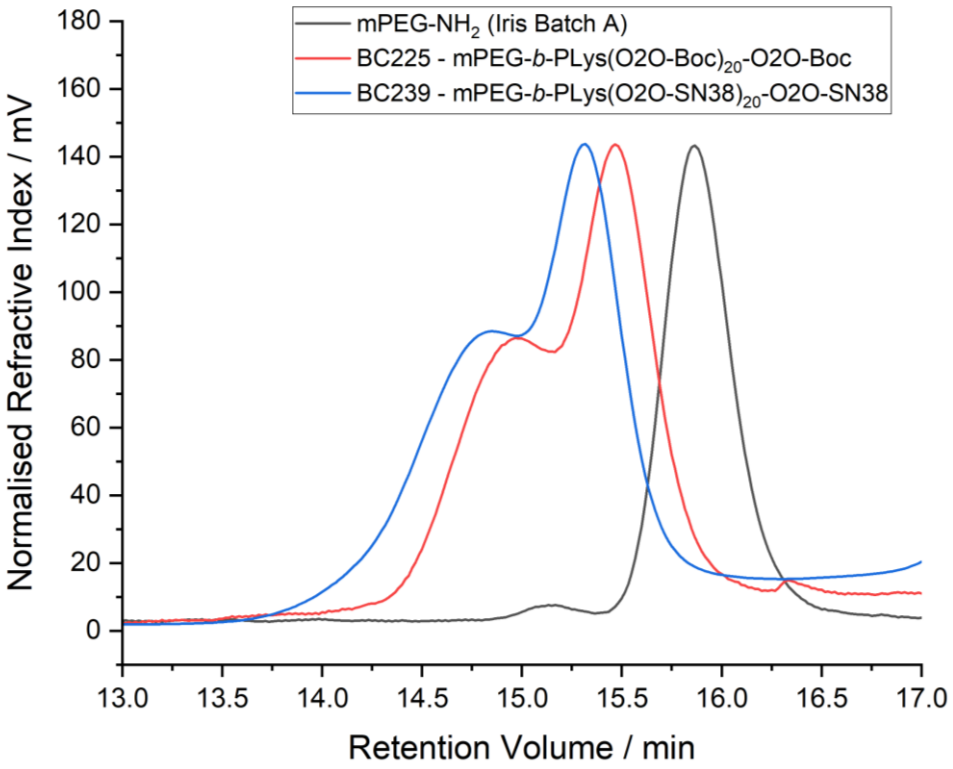

Figure 6.19: Overlaid GPC Chromatograms for mPEG-NH_2 macroinitiator, **BC225** and **BC239**. Samples were obtained in DMF-LiBr eluent.

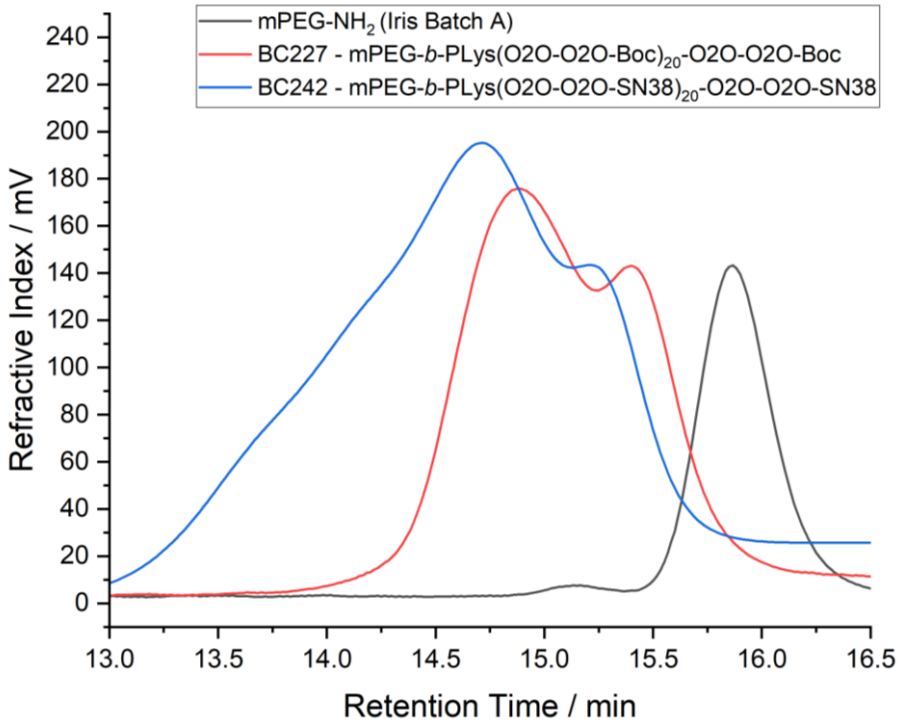

Figure 6.20: Overlaid GPC Chromatograms for mPEG-NH_2 macroinitiator, **BC227** and **BC242**. Samples were obtained in DMF-LiBr eluent.

It can be seen for **BC239**/**BC225** and **BC242**/**BC227** that a downward shift in retention time has occurred compared to the precursors, again consistent with the expected molecular weight increases associated with each SN38 conjugation reaction (6400 g mol^{-1}). It can therefore be inferred that conjugation has been achieved successfully in each case. For **BC239**, minimal changes are observed in the uniformity of the chromatogram relative to **BC225**. In contrast, **BC242** shows a clear increase in the relative area of the left-hand distribution compared to **BC227**. One potential explanation for this increase in peak area, is the decreasing solubility of these species in the **DMF/LiBr** mobile phase used for SEC. In particular, for the SN38-conjugated species, poor solubility in the mobile phase may lead to aggregation or even self-assembly of the amphiphilic block copolymers into ill-defined nanostructures, which are then misrepresented as false high-molecular-weight species in the chromatogram.[33] Although **LiBr** has been included to screen hydrogen bonding and limit chain aggregation, it does not effectively screen hydrophobic π-π stacking interactions between the highly aromatic drug moieties, and therefore likely does little to prevent such aggregation or self-assembly.[34] Furthermore, interactions between the polymers and the stationary phase may still occur, particularly in the case of **BC242**, which may not have been previously accounted for. If a self-assembled **BC242** aggregate species approached or exceed the exclusion limit of the pores in the stationary phase (100 Å), they may be excluded from entering and hence elute earlier than expected.[35] If the aggregates are close in size to the stationary pore maxima, or are flexible enough to experience deformation under the shear forces within the column, they may experience inconsistent or partial partitioning, wherein aggregates explore different portions of the pore volume. This leads to peak broadening, which may explain the significant breadth of the left-hand distribution shown in the chromatogram of **BC242.** To counter this, multi-angle light scattering (MALS) and DLS-SEC would be an effective combined analytical approach to determine aggregate retention. Furthermore, alternative SEC solvents such as HFIP or TFA might be used to better solubilise and disaggregate the polymers.[34]

While less likely, non-specific interactions between solvated polymers and the stationary phase may also contribute to the observations made. As detailed in **Section 2.6**, the stationary phase used here is a Novema Max PSS column, composed of a highly crosslinked poly(styrene-divinylbenzene) (PS-DVB) copolymer which is rigid, chemically stable, and highly hydrophobic.

Although surface modifications are likely employed to reduce Van der Waals' forces, electrostatics, and hydrogen bonding, these do little to suppress hydrophobic interactions, notably π–π stacking between SN38 moieties and the styrene backbone of the stationary phase.[35] Such interactions may contribute to peak broadening or dragging, as seen in **BC242**. MALDI-TOF mass spectrometry would more accurately determine the distribution of molecular weights, without the requirement sample solubility. There would be no need for a calibrant, as molecular weight would be determined directly from time of flight. However, for high-M.W. species, this would invite the additional labour of optimising the matrix and the sample preparation procedure to ensure effective ionisation and avoid chain fragmentation. Nevertheless, there are clear avenues for future projects to improve upon the clarity and accuracy of these data.

Figure 6.21 allows clear comparison of the traces for **BC236**, **239** and **242**. Through this, the success of single-O2O and double-O2O chain extension for the mPEG-*b*-PLys$_{20}$ conjugates can be evaluated.

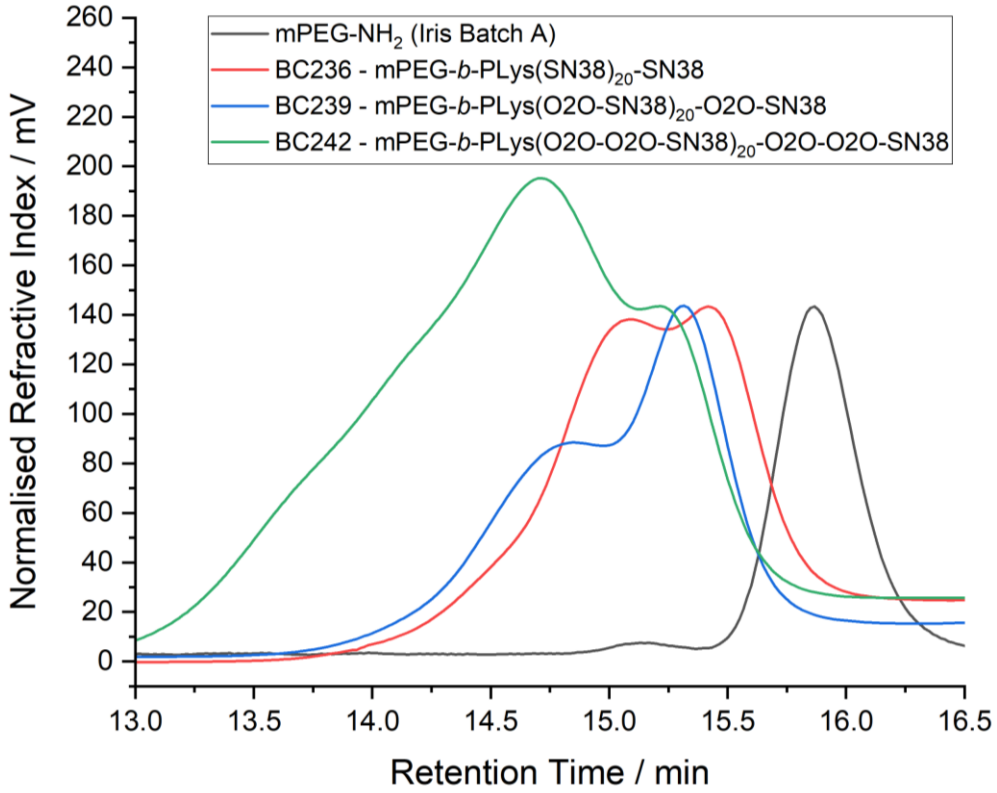

Figure 6.21: Overlaid GPC Chromatograms for mPEG-NH_2 macroinitiator, **BC236**, **BC239**, and **BC242**. Samples were obtained in DMF-LiBr eluent.

It can be observed that grafting of each of the chain extenders to both **BC239** and **BC242** has here been successful. Consistent jumps in the peaks' retention times (ca. 6 seconds) can be seen between each chromatogram, reflecting a consistent increase in molecular weight between non-extended **B236** (16,400 g mol^{-1}), single-O2O extended **BC239** (19500 g mol^{-1}) and double-O2O extended **BC242** (22,500 g mol^{-1}). From these data, as well as the chromatograms presented in **Figures 6.15** and **6.16**, it can be inferred that the conjugative syntheses of **BC234-6**, **BC238**, **BC239** and **BC240** have here been achieved successfully, as evidenced by the comparatively decreased retention times of their right-hand M.W. distributions. The products underwent self-assembly in preparation for analysis *via* DLS. This analysis would act both to evidence the capacity of the conjugated BCPs to self-assemble for delivery applications, and to determine to what extent their stability was affected by the uniformity of their constituent polymers' molecular weight distributions. This would in turn provide insights into the relative stability of these nanoparticles during administration and circulation, prior to delivery of their therapeutic payload.

6.3.4 Formation of Nanoparticles

6.3.4.1 Dynamic Light Scattering Analysis

Figure 6.22 demonstrates that all eight samples submitted for DLS analysis were capable of self-assembly, forming nanoparticles in PBS buffer solution at a concentration of 2 mg mL^{-1}. Particle size and polydispersity data (PDI) for these are presented in **Table 6.5**, further below.

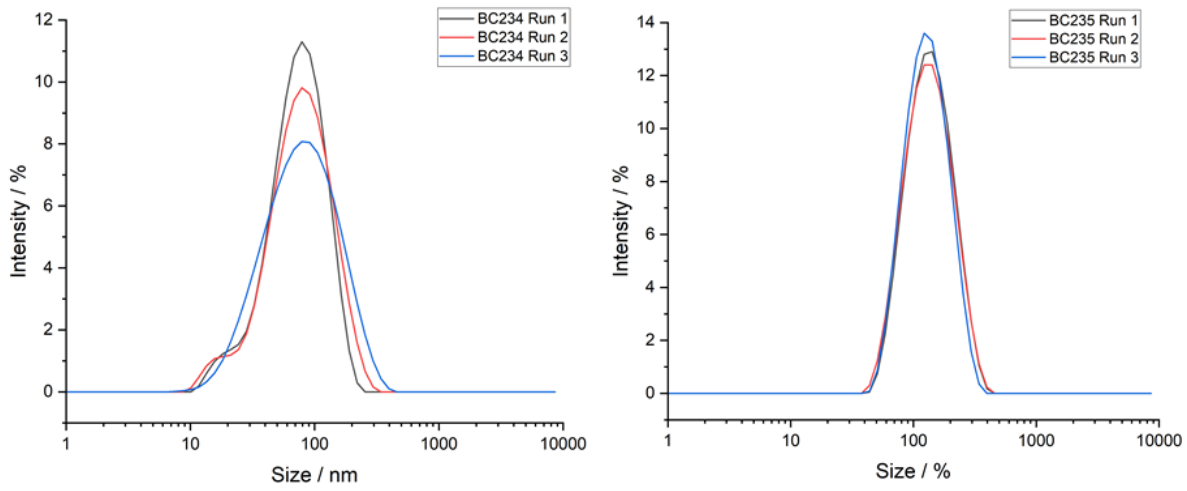

Figure 6.22: DLS traces, taken in triplicate, of 2 mg mL^{-1} nanoparticle dispersions of **BC234-BC242**, excluding **BC237,** in PBS buffer solution.

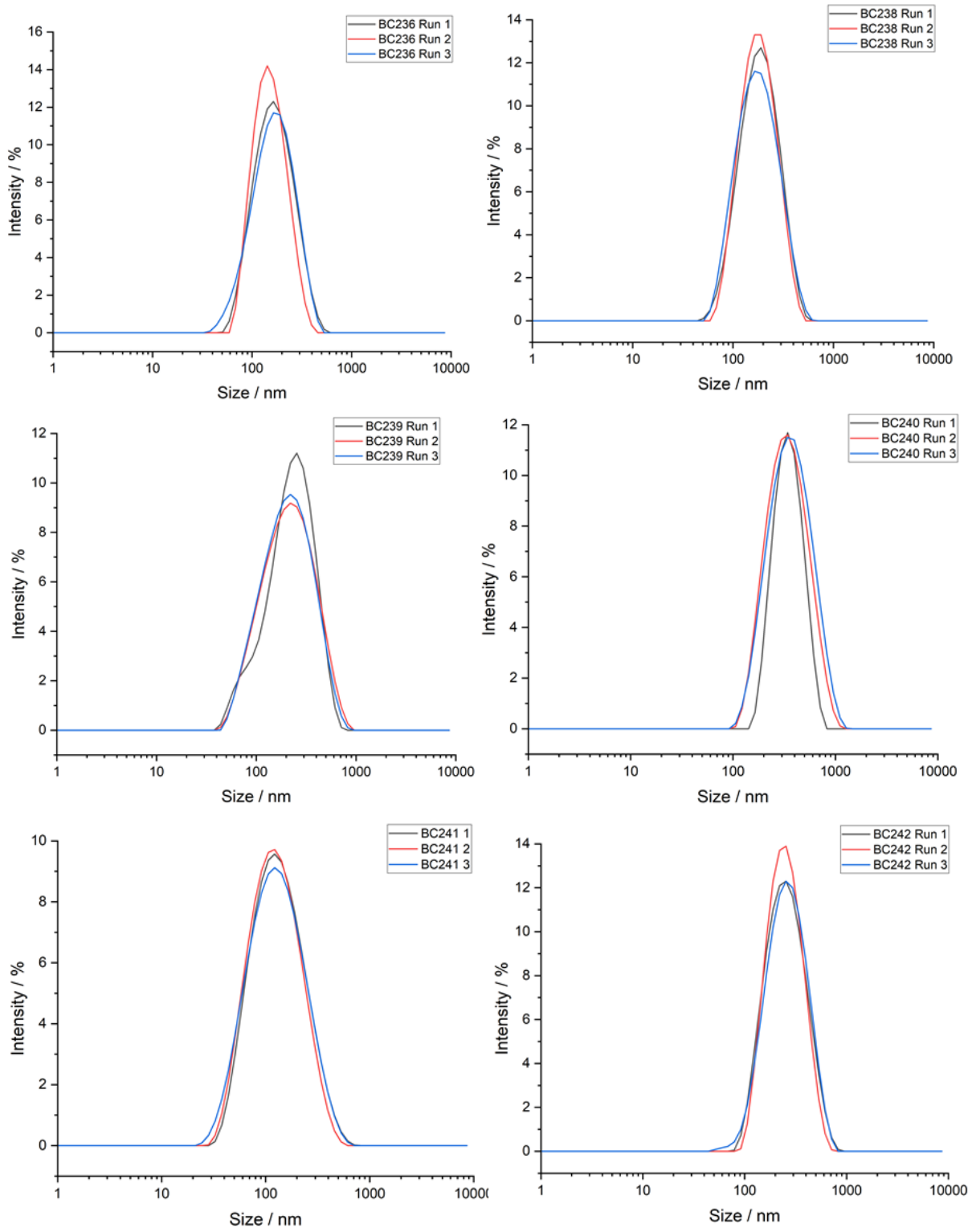

Figure 6.22 (continued): DLS traces, taken in triplicate, of 2 mg mL^{-1} nanoparticle dispersions of **BC234**-**BC242**, excluding **BC237,** in PBS buffer solution.

Table 6.5: Tabulated particle size and PDI data for polymers presented in **Figure 6.22**. Values represent the mean ± standard error of triplicate measurements.

Sample	Formula	Mean Particle Size (d.nm)	PDI
BC234	mPEG-*b*-PLys(CO-SN38)$_5$	68 ± 1.4	0.313 ± 0.010
BC235	mPEG-*b*-PLys(CO-SN38)$_{10}$	120 ± 1.7	0.147 ± 0.005
BC236	mPEG-*b*-PLys(CO-SN38)$_{20}$	149 ± 2.4	0.185 ± 0.006
BC238	mPEG-*b*-P(Lys-O2O-CO-SN38)$_{10}$	161 ± 0.8	0.157 ± 0.007
BC239	mPEG-*b*-P(Lys-O2O-CO-SN38)$_{20}$	179 ± 2.6	0.231 ± 0.003
BC240	mPEG-*b*-P(Lys-O2O-O2O-CO-SN38)$_5$	317 ± 7.3	0.308 ± 0.024
BC241	mPEG-*b*-P(Lys-O2O-O2O-CO-SN38)$_{10}$	108 ± 1.6	0.255 ± 0.004
BC242	mPEG-*b*-P(Lys-O2O-O2O-CO-SN38)$_{20}$	230 ± 0.7	0.177 ± 0.006

For samples other than **BC240**, good agreement is shown between measurements of particle size and PDI values, as demonstrated by standard error values presented in **Table 6.5**. This increased error for **BC240**, coupled with its high mean particle diameter (317 nm) and PDI (0.308) in comparison to other polymer-drug conjugate nanoparticles, suggests that the formed nanoparticles are poorly uniform in their size distribution and unlikely to be stable for storage and extended circulation.[36,37] Another outlier is **BC234**. With a mean particle diameter of only 68 nm this product is by far the most applicable for therapeutic administration, capable of crossing the blood-brain barrier (**Section 4.3.2**, **Table 4.4**). However, with a high PDI value (0.313), there is a question of the stability of the nanoparticles and their ability to store and circulate over long periods of time, as is required of long-circulating neuro-therapeutic carriers. To further assess the uniformity of **BC234** nanoparticles, a sample has been further visualised *via* transmission electron microscopy (TEM) in **Section 6.3.4.2**. For all other samples, PDI values remain below 0.3 which suggests that their stability is suitable for long-term storage. Furthermore, for samples other than **BC242**, mean particle sizes below 200 nm indicate applicability for intravenous administration and long-circulation to tumour sites.[38] These results suggest that this novel chain extension and conjugation of mPEG-*b*-PLys polymers has here been achieved in a controlled manner, and self-assembly into stable nanoparticles has here been verified. This is an encouraging finding for this report, and these data will be further corroborated by subsequent drug-release data, reported in **Section 6.3.5**.

6.3.4.2 TEM Analysis

To further investigate the self-assembly of drug-conjugated nanoparticles from samples generated within this report, samples **BC234**, **BC237** and **BC240** were submitted for TEM analysis, utilising the methodology outlined in **Section 2.9.** For both **BC237** and **BC240**, it was not possible to successfully image nanoparticles. However, it was possible to visualise **BC234**, which has been presented in **Figure 6.23** below.

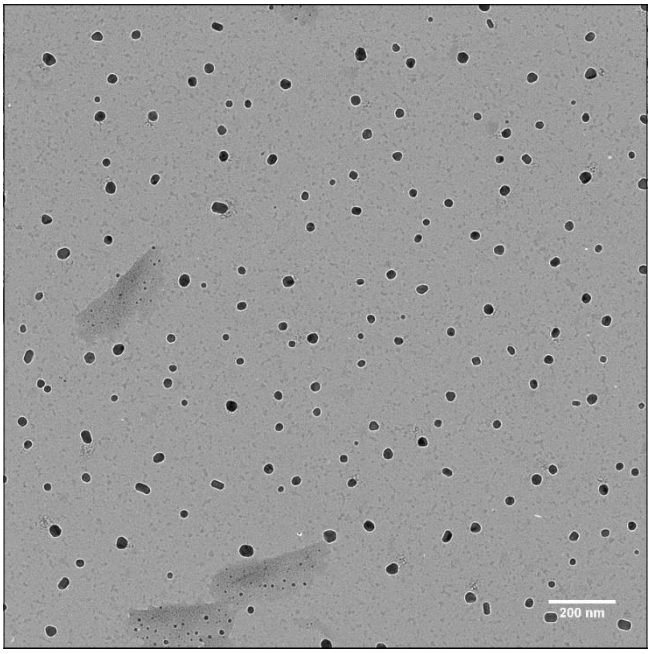

Figure 6.23: Transmission electron microscopy images depicting nanoparticles of **BC234**, mPEG-*b*-PLys(CO-SN38)$_5$, showing qualitative comparison of shape and size.

The diameters of the nanoparticles shown in **Figure 6.23** were measured using ImageJ to obtain an average particle size and polydispersity value, to enable comparison and validation of the data obtained *via* DLS analysis. For this sample, 145 particles were measured. The polydispersity values from these data were calculated as follows:

$$\mathrm{PDI} = \frac{\sigma^2}{{d_{av}}^2}$$

Where σ = standard deviation of nanoparticle diameter and d_{av} = mean nanoparticle diameter. The results of these calculations, alongside those obtained for **BC234** from *via* DLS, are shown in **Table 6.6** below.

Table 6.6: Mean particle size and polydispersity values for **BC234**. Values were obtained by DLS and TEM analyses, respectively.

Sample	Formula	DLS Measurements		TEM Measurements	
		Mean Particle Size (d.nm)	PDI	Mean Particle Size (d.nm)	PDI
BC234	mPEG-*b*-PLys(CO-SN38)$_5$	68	0.313	28	0.0309

Here, mean particle size values provided from DLS and TEM analyses show reasonable agreement, with only a slight decrease between the two respective figures. This reduction in size can be explained by the difference in measurements taken by each process. DLS measures the hydrodynamic diameter of nanoparticles in dispersion – in this case, in PBS buffer. In addition to the diameter of the particle core, this includes the hydrophilic PEG corona of the nanoparticle, as well as the water molecules that make up the surrounding hydration layer.[39] In contrast, TEM provides a measure of the electron-dense core of the dry nanoparticle. The samples are analysed under high vacuum, removing the layer of solvation, and the lower electron density of the corona provides poorer contrast and is hence not visualised. For this reason, it is typical for TEM-measured nanoparticle diameter values to be smaller than their DLS counterparts.[40] For the associated PDI values, this discrepancy can be explained by difference in methods used to calculate each value. The pseudo-PDI value determined above for TEM is more accurately described as the squared coefficient of variation (CV^2), which measures only the relative spread in the size values collected. This differs from the true PDI value as determined using DLS, which is calculated from the cumulants expansion of the correlation function, shown below:

$$\text{polydispersity} = \frac{\mu_2}{\Gamma^2}$$

Where Γ represents the first cumulant (the average decay rate, linked to average diffusion coefficient/particle size) and μ_2 the second cumulant, which represents the variance of decay rates. In summation, this PDI value is the relative variance of the distribution of decay rates, as opposed to a statistical spread of particle size values. Furthermore, this explains the increased PDI value associated with DLS, shown in **Table 6.5**. Because decay rate (Γ) is proportional to diffusion coefficient via a nonlinear, *inverse* relationship to size, the spread of

particle sizes produces an amplified spread in decay rates which leads to an *amplified* PDI value for DLS. This is better described here as a relatively *suppressed* CV^2 value, determined *via* TEM analysis. Nevertheless, imaging has here been achieved for **BC234**, with consistent size values to those determined *via* DLS analysis. From here, each sample that had successfully been imaged using DLS was taken forward for drug release study, conducted externally at AstraZeneca facilities in Macclesfield, UK.

6.3.5 Drug Release Analysis

Typical intravenous administration of SN38 leads to a spike in plasma concentration (C_{max}) that causes dose-limiting toxicities (DLT) (gastrointestinal damage, myelosuppression) as well as promoting rapid glucoronidation, which expedites removal of drug from the plasma. [15,16,41] Controlled release formulations reduce peak-related toxicity and prolong effective concentration of the drug circulation, widening the therapeutic window. To evaluate the controlled release efficacy of the polymer-drug conjugated samples synthesised above, nanoprecipitation and subsequent drug release analysis were performed externally by collaborators at AstraZeneca in Macclesfield, UK. This analysis was performed according to the methodology outlined in **Section 2.10**, which is summarised in **Section 6.2.6**. Nanoparticle samples were prepared from polymers **BC234**, **5**, **6**, **8** and **9**, as well as **BC240** and **BC242**. The release profile for each was recorded, and UPLC analysis was performed to determine SN38 content. It should be noted here that residual SN38 linker and other impurities were also detected within the samples, artificially inflating the final values.[42] As discussed in **Section 6.3.2**, impurities likely include re-generated SN38, from hydrolysis of the carbonate linker prior to conjugation, as well as the SN38–carbonate dimer formed through secondary reaction with 10-O-(p-nitrophenyl carbonate)-SN38. Although a 5-fold excess of di-nitrophenyl carbonate was used to limit their formation, they could not be fully avoided. The release data allows for qualitative comparison SN38 release kinetics under hydrolytic conditions, as well as quantitative evaluation of both the released quantity of SN38 and the calculated drug loading for each sample. For future publication, formal kinetic fitting would strengthen analysis considerably. Fitting to a first-order model would allow comparison of rate constants between samples, consistent with the first-order hydrolysis of carbamate linkages. Alternatively, application of the Korsmeyer-Peppas power law model would provide

mechanistic insight into whether release is limited by either diffusion or hydrolysis. This can be expected to vary across samples, given the differences in core packing and solubility discussed herein. Whilst NaOH here acts as a base-catalysed hydrolytic trigger to simulate controlled release over a shorter timeframe, the *in vivo* process is non-selective and instead relies on slow, spontaneous hydrolysis. It is therefore important here to identify any instances of "burst release" that may result in an unexpected spike in drug concentration C_{max}.[43] Release profiles of the polymer-drug-conjugates are presented in **Figure 6.24**. **Table 6.7** reports the release data for each sample, including SN38 concentrations calculated at 10 h of release and at the experimental end point. Drug loading (%) is calculated from final release concentrations and is compared to theoretical drug loading (%), determined using relative molecular weight values.

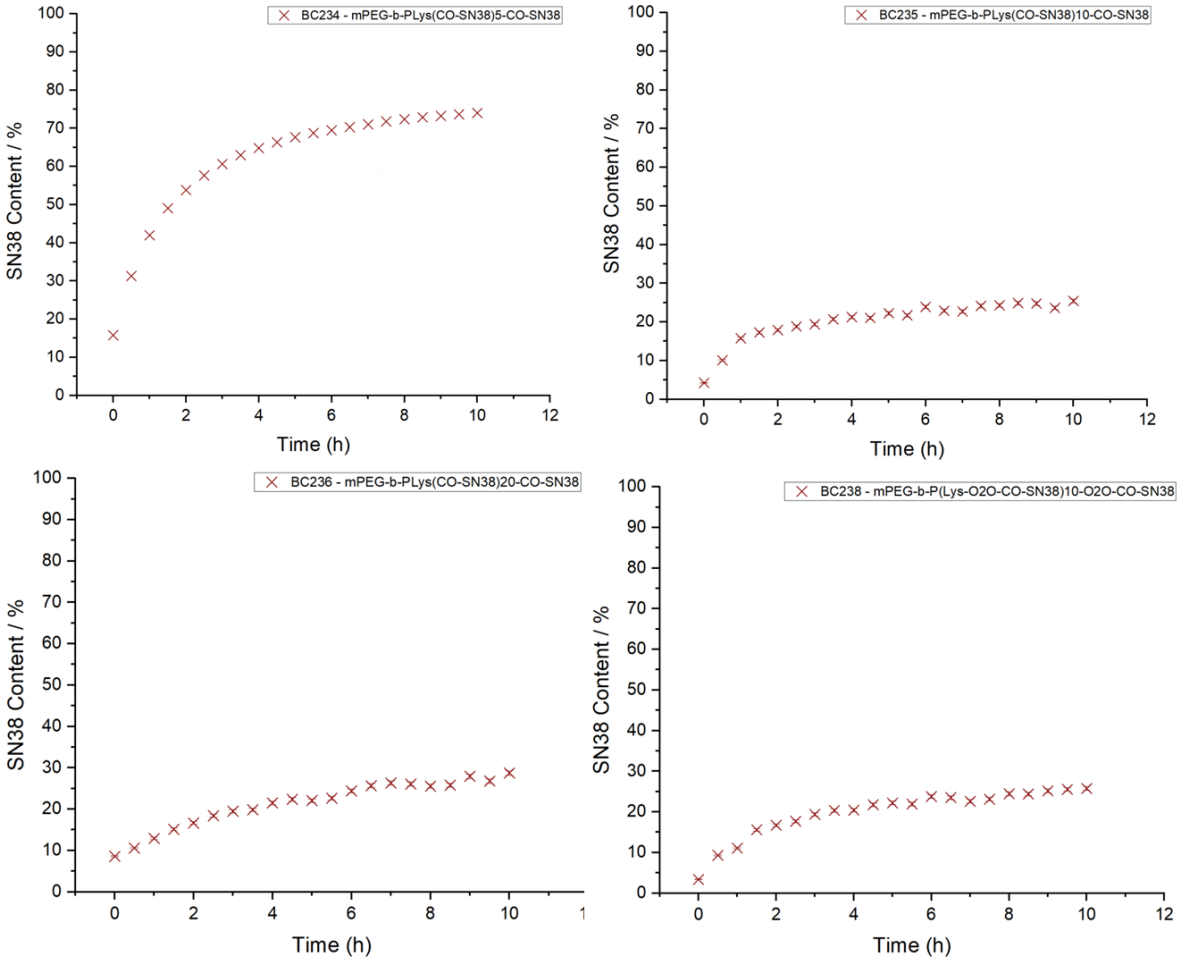

Figure 6.24: Drug release profiles for samples of mPEG-*b*-PLys-co-SN38 grafted copolymers, taken over 10.5 h of incubation.

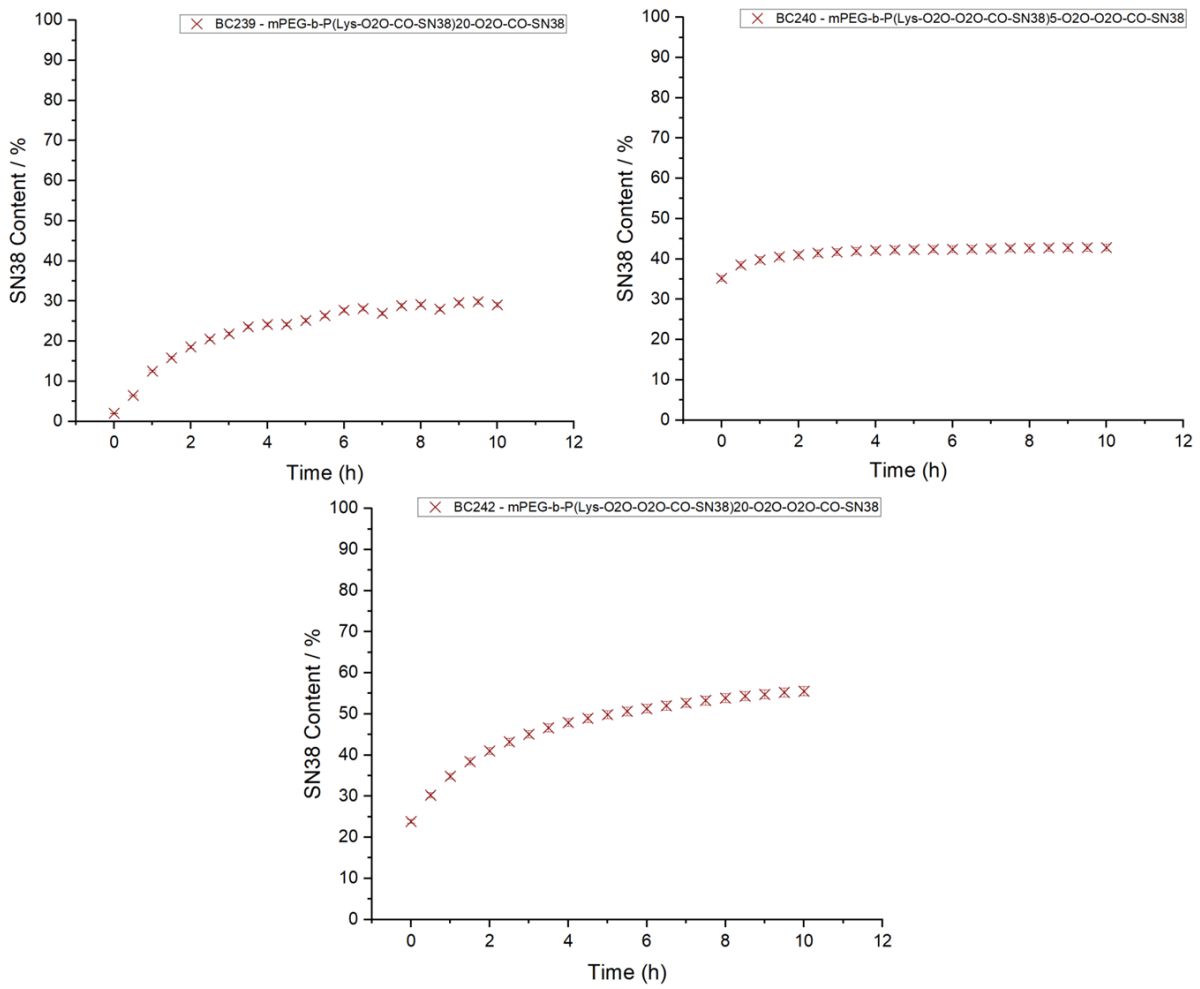

Figure 6.24 (continued): Drug release profiles for samples of mPEG-*b*-PLys-co-SN38 grafted copolymers, taken over 10.5 h of incubation.

Table 6.7: Total SN38 content for each sample, alongside theoretical drug loading percentages determined from relative molecular weights.

Sample Name	Total Drug Release (10 h) / mg/mL	Total Drug Release (Final) / mg/mL	Actual Drug Loading / %	Theoretical Drug Loading / %
BC234	0.33	0.48	19.98	28.63
BC235	0.08	0.36	14.41	39.40
BC236	0.12	0.54	21.88	50.18
BC238	0.06	0.27	11.04	34.39
BC239	0.11	0.39	15.51	42.32
BC240	0.04	0.36	15.42	23.63
BC242	0.15	0.36	14.89	36.59

For **Figure 6.24**, SN38 content (y-axis) was calculated by taking SN38 concentration at a time point as a percentage of total release by the experimental end point. From this and **Table 6.7**, it can be observed that controlled release of SN38 was successfully achieved across all samples, with burst release avoided in all cases. Whilst initial SN38 concentration in solution has here been eliminated from resultant release and drug loading calculations, their impact on sample solubility and their reflection of drug loading efficiency are still here discussed. The most rapid release was recorded for **BC234**, which deposited ca. 58 % of its payload within the first ten hours of release, contrasting with only 22 % from **BC235** and 21 % from **BC236**. This rapid release of payload can be attributed to the short (5 repeat unit) hydrophobic tail of **BC234** which, with fewer π-π stacking interactions between conjugated SN38 molecules, adopts a looser and less uniform conformation, allowing faster ingress of aqueous NaOH solution during analysis. This is corroborated by the DLS data presented in **Section 6.3.4.1**, wherein nanoparticle uniformity (PDI) is significantly higher than for other samples. Whilst **BC235** and **BC236** are larger in hydrophobic tail length than **BC234**, comparison of their release data is more complex. Theoretically, total SN38 release would be expected to increase proportionally with increasing *theoretical* drug loading values, described in the right-most column of **Table 6.7**. However, drug loading has not been achieved ideally here, as demonstrated *via* translation of the SN38 release data into the *actual* drug loading values presented adjacent to the theoretical. Opportunities for reduced drug loading could have arisen from incomplete reaction during NCA-ROP, deprotection, chain extension or conjugation. Within the timeframe of this research, it was not feasible to further investigate, nor perform repeats. In comparing the total concentration of SN38 released from **BC234**, **5** and **6** by the experimental end-point, as well as the corresponding actual drug loading percentages, it can be observed that all values fell below the theoretical maximum, with ratios of 0.70, 0.37 and 0.44 respectively. The relative increase for **BC234** can be attributed to complications observed during NCA-ROP of **BC235**/**6**, as demonstrated by the multi-modality and increased Đ of the precursor products **BC219** and **BC220** in **Figure 5.19**. It is possible that the achieved degree of polymerisation for each product was below what was expected and, with the occurrence of possible side reactions as suggested in **Section 5.3.3**, the proportion of available free-amine moieties on the final polymer may have been decreased.

For this reason, or perhaps due to sub-optimal stock of the reactive 10-O-(*p*-nitrophenyl carbonate)-SN38 intermediate, the conjugation of the polymer system to CO-SN38 may also have been impaired. Comparing **BC235** and **BC236**, release ratios remain similar, and a clear increase can be observed in the total released SN38 concentration for **BC236**. This aligns with prediction, due to the larger lysine block length of the product, allowing for a greater proportion of the molecular weight to comprise conjugated SN38 molecules. In addition, payload release within the 10 h window remains somewhat similar for each product, which is explained by the less stabilised hydrophobic core of **BC235**, which released a greater proportion of its total payload within the earlier time frame.

Evaluating differences hydrophobic chain length between chain-extended products, **Figure 6.24** demonstrates a 10 h payload release of 22 % for **BC238** and 28 % for **BC239**, with similar actual-to-theoretical drug loading ratios of 0.32 and 0.37, respectively. This increased rate of release for the product with a larger hydrophobic domain is initially curious, as it does not align with the trend observed between the release rates of **BC235** and **BC236**. However, it should be noted here that **BC238,** despite showing a similar actual-to-theoretical drug loading ratio versus **BC239**, demonstrated the lowest drug loading of all samples recorded, at only 11 %, representing the lowest total concentration of conjugated SN38 by a significant margin. As the process of hydrolysis under aqueous conditions is first order with respect to this concentration, it is reasonable to assume that such a decrease in the quantity of active carbamate linkages would adversely impact the rate of SN38 generation during this process.

Comparing **BC240** and **BC242**, the ratios of actual-to-theoretical drug loading align closely with those observed for **BC234** and **BC236**, at 0.65 and 0.40 respectively. In addition, the release profile of **BC242** aligns with other samples as well, with 31 % of the SN38 payload released within the first 10 h. **BC240**, however, strays significantly from previous trends, releasing only 9 % of its total conjugated payload within the first 10 h of reaction. This does not agree with the previously asserted logic that, due to a shorter hydrophobic domain, the nanoparticle core would be swiftly penetrated by aqueous solution, exposing a greater proportion of the conjugated material more quickly and resulting in a faster overall rate of hydrolysis. It is possible that the inclusion of the chain extender species may have impacted this rate of release, but this will be discussed in greater detail below.

As can be observed in **Figure 6.24**, the initial concentrations of SN38 present within samples **BC240** and **BC242** were 35 % and 24 % of the total quantity found at their respective experimental endpoints. All other samples evaluated showed an initial percentage of below 10%, the only exception being **BC234** at 15 %. While the identity of the non-conjugated SN38 impurities have been previously discussed above, it is important to identify the contributing factors that lead to their increased presence. There was no access to LC-MS analysis of the resultant product, meaning that it was not possible to determine the purity of the intermediate prior to conjugation. This has allowed a significant increase in the presence of SN38 impurities. The most significant impact of these increased initial concentrations was on the solubility of the resultant sample during nanoparticle preparation. For **BC240** and **BC242**, the solubility of the samples was extremely poor, with **BC241** so insoluble that it was not taken forward for analysis. With only partial dissolution in DMSO at the outset of analysis and potential aggregation upon the introduction of aqueous solution, only the surface-exposed fraction of carbamate linkers were accessible for hydrolysis, reducing their effective concentration significantly and resulting in the lag in reactivity here exhibited. This effect would only be exacerbated by the presence of the SN38 impurities within the sample, which would likely have acted as nucleation sites for aggregation and flocculation of the polymer chains, specifically attracting the SN38 conjugates and their associated carbamate linkages. The observed release profiles demonstrate successful controlled release of conjugated SN38 from the polymer-drug system in each case.

It was also pertinent to evaluate the observable trends between polymer-drug conjugates of equal hydrophobic block length, to better understand the impact of chain extension upon release and drug loading for these polymer architectures. Comparing **BC234** and **BC240**, for which actual-to-theoretical drug loading ratios are 0.70 and 0.65 respectively, the clear disparity in release can be attributed to the poor solubility of the **BC240**. However, it should also be noted that, similarly to **BC234**, the nanoparticles of **BC240** formed during DLS analysis in **Section 6.3.4.1** were also poorly uniform, with PDI 0.308 ± 0.024, higher than any other samples by a significant margin. It is sensible that this can also be attributed to the short hydrophobic block length of the two samples, which prohibits formation of a tightly packed hydrophobic core.

It is plausible that, for **BC240** with increasing steric bulk in the hydrophobic domain brought on by the inclusion of chain extenders, stable core formation was hindered to the point that polymer-drug conjugates instead adopting loosely associated polymer aggregates, encouraged by SN38 impurities acting as nucleation sites. As a general consideration, with the successful conjugation of these polymer samples lying below the theoretical expectation, it should be considered that a number of potential reaction sites along the hydrophobic chain will still bear an unreacted amine group. These nucleophilic groups, positioned within the hydrophobic core, will have acted to further destabilise core formation upon nanoprecipitation. For this example, assuming that degree of polymerisation matched predictions and all deprotection was complete, 4 out of 6 reactive sites were linked to SN38, suggesting that 2 free amine groups remained.

Between **BC235** and **BC238** actual-to-theoretical loading values are similar at 0.32 and 0.37, meaning 4 out of 11 possible amine sites were successfully conjugated (assuming targeted D.P. was achieved). Furthermore, it can be observed that the rate of release within the first 10 h for each polymers was the same, releasing 22 % of the payload. The similarities continue when evaluating DLS data which, between the samples, shows a predictable increase in nanoparticle diameter with the inclusion of chain extenders, with only a slight increase in PDI. With such consistent performance from each nanoparticle, it calls into question what impacts the inclusion of such extenders has not had upon the polymer-drug conjugate. For **BC238**, it is reasonable to expect that the increase in steric bulk of the chain extenders would act to increase the size of the hydrophobic core as observed. However, despite there being no increase in the number of SN38 groups within that expanded core, the stability of the nanoparticle appears unchanged, especially when considering the hydrophilicity introduced by the PEG-like O2O extender. While this observed behaviour could be attributed to the structural influence of the chain extenders, where their flexibility enables efficient packing of the hydrophobic core and positions hydrophilic domains at the core-shell interface, it is more likely that the low concentration of conjugated SN38 was the primary factor responsible the reduced apparent release rate. As the hydrolysis of the carbamate linkage follows first-order kinetics with respect to the concentration of active conjugates, a lower initial drug loading would directly reduce the rate of SN38 release.[44]

Comparing **BC236**, **239** and **242**, with actual-to-theoretical drug loading ratios of 0.44, 0.37 and 0.40 respectively, the estimated number of conjugated amine sites for each polymer falls between 7 and 9 out of 21. This demonstrates that between each grouping of samples, the inclusion of chain extenders has not impacted the conjugative success of the final product, an encouraging observation within the scope of this investigation.[10] Instead, unsuccessful conjugation may be attributed to as-yet unidentified complications during NCA ROP, given that each of the samples other than **BC234** has achieved a similar ratio of conjugation.

Alternatively, the steric occlusion of conjugated SN38 groups may have hindered further conjugation reactions at neighbouring sites, though it is unusual then that increases in chain extension did not relieve hindrance and increase conjugation for **BC239** and **BC242**. Recalling earlier observations, percentage release for these three samples after 10 h was determined to be 21 %, 28 % and 31 %, respectively. It is also important to recognise that this trend does not align with that observed for **BC235** and **BC238** despite the fact that, similarly, the initial concentrations for each of these samples does decrease, with the highest observed in **BC236**. It can inferred that, for these samples, increasing chain extension was the primary contributor to increased initial release rate. These effects are likely more pronounced across samples also, due to the increased degree of polymerisation of their hydrophobic blocks, versus their hydrophilic PEG blocks. Given that 2 in 3 of the pendant amine groups of this hydrophobic block were left unconjugated, their inherent polarity and hydrophilicity will likely have acted to destabilise core formation during self-assembly.

Furthermore, whilst chain extenders had been added here with the intention of increasing conjugate linker flexibility and stabilising the core, they too are made-up of a hydrophilic, PEG-like backbone.[49] Whilst the SN38 content of the core remained unchanged between successive samples, the proportion of hydrophilic material present in the core was increased, sterically hindering and ultimately disrupting the hydrophobic π-π stacking interactions that associated the SN38 molecules. This is corroborated by the DLS data, which shows an increase in particle diameter between samples, indicating swelling and poor cohesion within the core.

With a greater proportion of conjugated repeat units, achieved through a more robust methodologies for NCA-ROP, carbamate conjugation and product purification, it is possible

that the core might better compensate for this increased steric bulk and destabilisation, pushing hydrophilic environments to the core-shell interface and reducing permeability.

For each of the polymer-drug conjugates evaluated, controlled release of SN38 was successfully achieved without any instances of burst release. This demonstrates that the linker chemistry and nanoparticle formulation strategy applied throughout this work were effective in the creation of a platform for the controlled and sustained release of SN38. Whilst variations in release rate and overall drug loading were observed between samples, these were each rationalised by contributions of SN38 concentration, sample solubility and aggregation behaviour, rather than any intrinsic instability of the designed polymer-drug conjugate system itself. Slower apparent rate of release, recorded for samples **BC240** and **BC242**, were attributed to reduced solubility arising from SN38-related impurities and correspondingly low SN38 concentrations within the nanoparticles. As the rate of hydrolysis in these instances was first-order with respect to the active carbamate linkages, their reduced effective concentration will have directly slowed the rate of SN38 liberation. These observations support that inter-sample differences in release rate and drug loading can be attributed to individual changes in morphology and composition, rather than implicit limitations of the polymer architectures or conjugation chemistries utilised.

It is also significant that the inclusion of chain extenders within the hydrophobic domain did not appear to impact conjugation efficiency. Across both extended and non-extended polymer series, actual-to-theoretical drug loading ratios remained consistent, indicating that the increased steric bulk and PEG-like character of the extenders neither hindered carbamate formation nor restricted access to reactive amine sites. While subtle differences in nanoparticle size and early-stage release behaviour were evident between samples, those were reasonably attributed to local effects on core packing and solvation, rather than systemic limitation introduced by the chain extenders themselves. Taken together, these results confirm that each of the polymer-drug conjugates investigated here is capable of mediating controlled SN38 release, robust against both the presence of impurities and unintended structural variability.

The platform described here represents a promising framework for the controlled delivery of SN38, with the potential to reduce peak-related toxicities associated with high C_{max}

administration of the free drug to maintain effective therapeutic concentrations over extended periods. With optimisation of purification and analytical procedures, this system could provide a reproducible and clinically relevant route for SN38 administration.

6.4 Conclusions and Future Work

In conclusion, this chapter has investigated the post-polymerisation modification of the mPEG-*b*-PLys[NH_2.TFA]$_n$ copolymers for enhanced SN38 conjugation and release. Chain-extended copolymers were successfully synthesised, achieving high grafting efficiencies (between 80 – 97 %). TFA-mediated deprotection was then performed successfully, yielding the desired amine-functionalised product, confirming that structures remained robust throughout multi-stage modification. Grafting efficiency was retained, showing the chemical fidelity of the spacers. SN38 was then conjugated to both linear and chain-extended mPEG-*b*-PLys$_n$ derivatives through carbamate linkages to yield a series of drug-loaded BCPs. Comparisons across products indicated that the inclusion of extenders into the side chains of the PLys$_n$ block improved the conjugation yield. All conjugated polymers then underwent

successful self-assembly, confirming amphiphilic behaviour. This self-assembly was validated *via* DLS analysis and TEM imaging confirmed the formation of near-spherical micelles for **BC234**. Controlled-release experiments, verified that SN38 was successfully released under simulated physiological conditions for each polymer-drug conjugate, without burst release.

This represents a significant success for the platform, building upon existing research by Sadat *et al.* and Matsumura *et al*. in the pursuit of SN38-conjugated BCP nanoparticles by exploiting novel assembly of well-known linker technologies to extend the spatial separation of active amine side-chains and reduce steric occlusion.[45,46] In addition, the system provides more effective control over final polymer architecture than comparable hyperbranched systems, whilst reducing the synthetic complexity of high-generation dendrimer comparisons.[47-49] This creates the potential to reduce labour and resource costs for the industrial manufacture of prodrug therapeutics, whilst delivering control and specificity comparable to high-cost solutions on the market.

As confirmed by DLS analysis, the polymer-drug conjugates synthesised throughout this research are of a size and stability suitable for long-carrying circulation. This makes them suitable for the treatment of cancers such as pancreatic adenocarcinoma and metastatic colorectal cancer, for which survivability is considerably low versus localised disease, and for which irinotecan/SN38 is commonly applied.[50,51] By reducing systemic DLTs such as diarrhoea and neutropenia, this delivery platform could extend the therapeutic window for conditions and allow patients to receive higher relative doses, improving both treatment efficacy and quality of life for those most vulnerable.[52]

To improve upon the products synthesised here, in addition to the improvements discussed within **Chapter 5**, it is most important to ensure accurate *in situ* monitoring of 10-O-(p-nitrophenyl carbonate)-SN38 *via* LC-MS, to eliminate the potential for contamination with by products as observed above. In addition, a more thorough purification strategy for the conjugated polymers must be researched, to ensure removal of any non-conjugated SN38-containing impurities that might affect characterisation, release analysis or future therapeutic applications. The most appropriate strategy for this is likely dialysis in a suitable solvent, such as DMF, utilising a robust tubing material such as PTFE or PAN. To bolster data presented within this chapter, future analysis should be conducted towards completion of a full suite of

TEM analysis, to better evaluate the size and shape of the self-assembled nanoparticles here characterised by DLS (**Section 6.3.4.1**). In correlation, the kinetics of nanoprecipitation should be evaluated by For future research, alternative spacer and linker chemistries could be explored to impart alternative release triggers, such as a cystamine-PABC system that enable redox-sensitive release of free SN38, *via* self-immolative 1,6-elimination of the linker following disulphide cleavage.[53,54]

To progress the existing system to real-world applications, it is necessary to further evaluate SN38 release using more representative physiological buffers and serum-containing cell-culture media, to accurately determine kinetic control and cytotoxic response. From this, a staged testing pathway would explore *in-vitro* cell-based evaluation on relevant cell lines (PANC-1, AsPC-1, HCT116, DLD-1) against a non-malignant control and irinotecan, to evaluate cell viability, uptake and apoptosis. Provided success is indicated (comparable or lower IC_{50}, selective toxicity), subsequent *in-vivo* studies would then allow accurate comparison of bio-distribution, circulation half-life, tumour growth inhibition and, crucially, overall survival. The system synthesised and characterised within this report shows promising potential at a successful journey through this pathway.

6.5 References

1. A. P. Mackiewicz, J. M. Sobczak, A. P. Korzuch, P. Chmielewski and H. Padlewska, *Pharmaceutics*, **2023**, 15, 1308.
2. A. Li, S. Wang, Z. Zhang, N. Xu, G. Ling and P. Zhang, *J. Mater. Chem. B*, **2022**, 10, 5191–5202.
3. D. Di Iorio, A. Marti, S. Koeman and J. Huskens, RSC Adv., **2019**, 9, 21186–21194.
4. A. Shakiba, A. C. Jamison and T. R. Lee, *Langmuir*, **2015**, *31*, 6154–6164.
5. P. Akkahat, W. Mekboonsonglarp, S. Kiatkamjornwong and V. P. Hoven, Langmuir, **2012**, 28, 5302–5311.
6. Z. M. Zheng, P. Wang, Y. Gong and X. Y. Liu, *J. Mater. Chem. B*, **2020**, *8*, 5337–5371.J. L. Dalsin, B.-H. Hu, B. P. Lee and P. B. Messersmith, J. Am. Chem. Soc., **2003**, 125, 4253–4258.

7. D. Zhu, H. Zhang, Y. Huang, B. Lian, C. Ma, L. Han, Y. Chen, S. Wu, N. Li and W. Zhang, Pharmaceutics, **2021**, 13, 1092.
8. C. Ma, D. Zhu, W. Lin, Y. Li, Y. Huang, H. Zhu, M. Ye, Y. Wang, L. Peng and X. Liu, Chem. Commun., **2022**, 58, 4168–4171.
9. England, R. M.; Yu, Q.; Gunnarsson, A.; Luxenhofer, R.; Treacher, K.; Ashford, M. B., *Macromolecules*, **2022**, *55*, 401–412.
10. M. Ficker, V. Paolucci and J. B. Christensen, Can. J. Chem., **2017**, 95, 954–964.
11. R. Sharma, A. Sharma, S. P. Kambhampati, R. R. Reddy, Z. Zhang, J. L. Cleland, S. Kannan and R. M. Kannan, Bioeng. Transl. Med., **2018**, 3, 87–101.
12. D. Hnedzko, D. W. McGee and E. Rozners, *Bioorg. Med. Chem.*, **2016**, *24*, 4199–4205.
13. A. N. Zaykov, V. M. Gelfanov, T. M. Tagmose, D. Demozay, V. Manfè, R. Rohlfs, M. Rivir, D. Perez-Tilve, B. Finan and R. D. DiMarchi, *RSC Chem. Biol.*, **2024**, *5*, 763–775.
14. D. V. Santi, S. D. Fontaine, Y. Wang, et al., J. Med. Chem., **2014**, 57, 4979–4989.
15. M. Haaz, L. P. Rivory, J. Robert, et al., Cancer Chemother. Pharmacol., **1997**, 40, 135–141.
16. A. Pal, S. Khan, Y.-F. Wang, et al., Anticancer Res., **2005**, 25, 331–342.
17. A. Swami, R. Duncan, R. K. Jain, et al., Cancer Res., **2013**, 73, 2700–2709.
18. Meyer-Losic, F.; Nicolazzi, C.; De Coupade, C.; et al., Clin. Cancer Res., **2008**, 14, 2145–2153.
19. Alas, M.; Sun, X.; Sun, Y.; et al., J. Med. Chem., **2020**, 63, 1351–1373.
20. Santi, D. V.; McCabe, A.; Chen, E. K., J. Med. Chem., **2014**, 57, 2303–2314.
21. Liu, L.; Zhang, Y.; Li, H., J. Control. Release, **2021**, 331, 1–10.
22. H. Gao and K. Matyjaszewski, J. Am. Chem. Soc., **2007**, 129, 11828–11834.
23. A. C. Engler, J. M. Chan, S. J. Chan, C. P. C. Ng, P. L. Stayton and J. A. Hubbell, Biomacromolecules, **2009**, 10, 2156–2164.
24. P. W. M. Freeman, S. G. Yeates, J. R. Warren and W. J. Feast, *Polym. Chem.*, **2015**, *6*, 5693–5704.
25. N. Weigand, A. L. Hook, C. M. Holownia, J. R. Howse, D. G. Fernig and M. M. Stevens, *Chem. Sci.*, **2020**, *11*, 10981–10990.

26. Bejder, B. S.; et al. *Nat. Commun.* **2024**, *15*, 11297923.
27. Lai, W. W. P.; et al. *Environ. Sci. Water Res. Technol.* **2024**, *10*, 3349–3357.
28. J. B. Matson, A. Q. Steele, J. D. Mase and M. D. Schulz, *Polym. Chem.*, **2024**, *15*, 3050–3067
29. Moro, S.; Rovigatti, L.; Camponeschi, A.; et al., *ACS Nano*, **2024**, *18*, 14440–14451.
30. Guo, N.; Jiang, D.; Wang, L.; You, X.; Teng, Y.-O.; Yu, P. *Molecules* **2015**, *20*, 9393–9404.
31. Cheetham, A. G.; Zhang, P.; Lin, Y.-A.; Lock, L. L.; Tang, J., *Chem. Commun.*, **2014**, *50*, 6039–6042.
32. Imamura, R.; Imai, Y.; Shirahama, H., *ACS Omega*, **2019**, *4*, 19068–19076.
33. Mendichi, R.; Giordano, C.; Gabriele, B., *J. Chromatogr. A*, **2004**, *1057*, 39–45; Waters App Note (2022).
34. Popov, A. S.; Anisimova, O.; Shvets, V., *J. Chromatogr. A*, **2021**, *1651*, 462327.
35. Danaei, M.; et al., *Pharmaceutics*, **2018**, *10*, 57.
36. Shi, R.; et al., *Nano Research*, **2024**, *17*, 5871–5887.
37. Teja, S. P. S.; et al., *Acta Biomater.*, **2023**, *157*, 479–497.
38. D. R. Baer, M. H. Engelhard, G. E. Johnson, S. L. Laskin, S. A. Nelin, D. J. Qian, P. S. Shutthanandan and L. Wang, *J. Vac. Sci. Technol. A*, **2013**, *31*, 050820.
39. D. R. Baer, S. Thevuthasan and P. Nachimuthu, *Surf. Interface Anal.*, **2010**, *42*, 751–759.
40. Castellanos-Rubio, I.; Rodrigo, I.; Olazagoitia-Garmendia, A.; Arriortua, O.; Gil de Muro, I.; Garitaonandia, J. S.; Bilbao, J. R.; Fdez-Gubieda, M. L.; Plazaola, F.; Orue, I.; Castellanos-Rubio, A.; Insausti, M. ACS Appl. Mater. Interfaces **2020**, 12, 27917–27929.
41. Farahani, T. Z.; et al., *Sci. Rep.*, **2024**, *14*, 15371.
42. Fan, W.; et al., *Int. J. Pharm.*, **2014**, *471*, 358–367.
43. Koseki, Y.; et al., *J. Colloid Interface Sci.*, **2021**, *599*, 366–374.
44. I. Ekladious, H. M. Colson and M. W. Grinstaff, *Chem. Rev.*, **2019**, *119*, 123–168
45. S. M. A. Sadat, M. A. T. et al., *Pharmaceutics*, **2020**, *12*, 507.
46. Y. Matsumura, K. Kataoka et al., *Adv. Drug Deliv. Rev.*, **2011**, *63*, 170–179
47. L. Y. Qiu and Y. H. Bae, *Pharm. Res.*, **2006**, *23*, 1–30.

48. R. Rodríguez Schmidt, J. G. Hernández Cifre and J. García de la Torre, *Polymers*, **2015**, *7*, 610–628.
49. B. Halford, *Chem. Eng. News*, **2005**, *83*(24), 30–35.
50. T. Conroy, F. Desseigne, M. Ychou *et al.*, *N. Engl. J. Med.*, **2011**, *364*, 1817–1825.
51. J.-Y. Douillard, D. Cunningham, A. D. Roth *et al.*, *Lancet*, **2000**, *355*, 1041–1047.
52. Y. Huang, L. Wang, Z. Cheng *et al.*, *J. Control. Release*, **2021**, *339*, 297–306.
53. H. Wang, X. Li, J. Li, Y. Wang, Y. Li and C. Shen, *Biomater. Sci.*, **2016**, *4*, 1032–1041.
54. J. M. Choi, S. W. Lee and T. H. Kim, *Polym. Chem.*, **2018**, *9*, 2873–2883.

Appendices

A.6.1 ^{1}H NMR Spectra

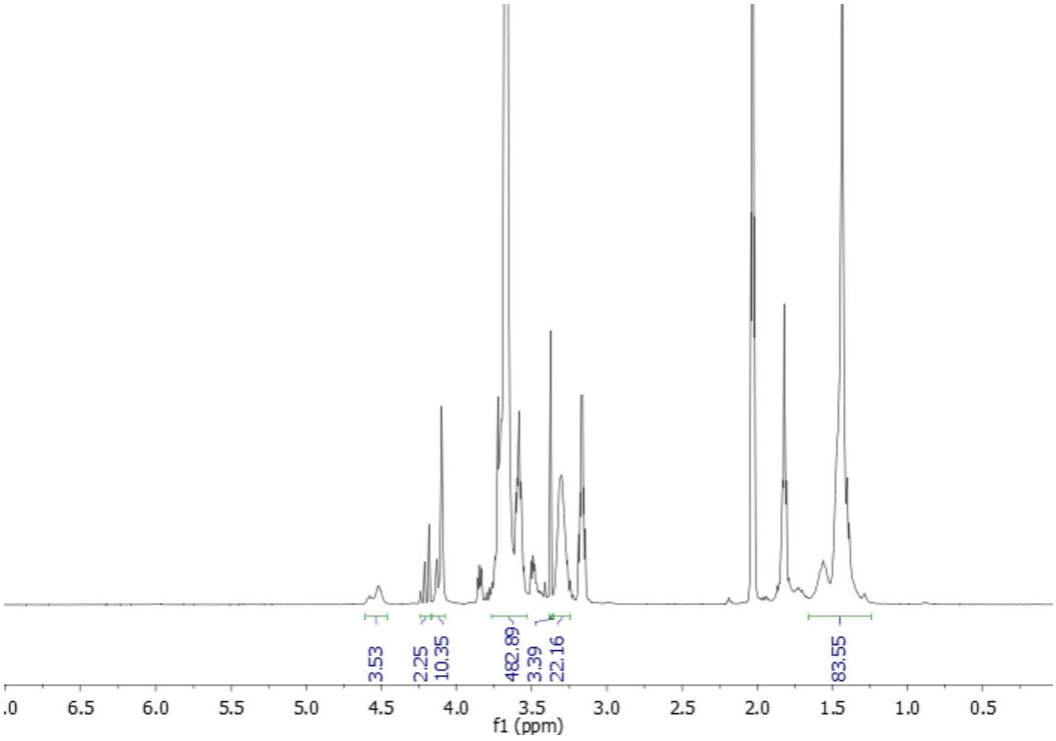

Figure A.6.1.1: ^{1}H NMR spectrum (500 MHz, DMSO-d_6) of **BC203**, mPEG$_{113}$-*b*-PLys(O2O-Boc)$_5$.

Figure A.6.1.2: ^{1}H NMR spectrum (500 MHz, D_2O) of **BC224**, mPEG$_{113}$-*b*-PLys(O2O-Boc)$_{10}$.

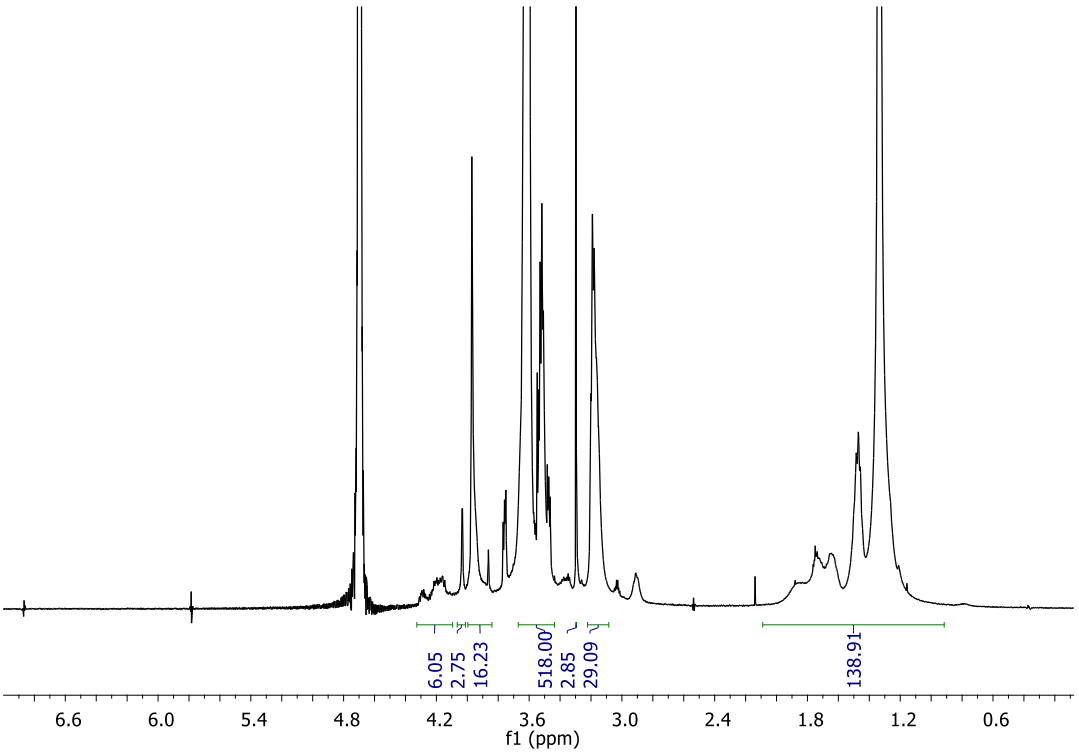

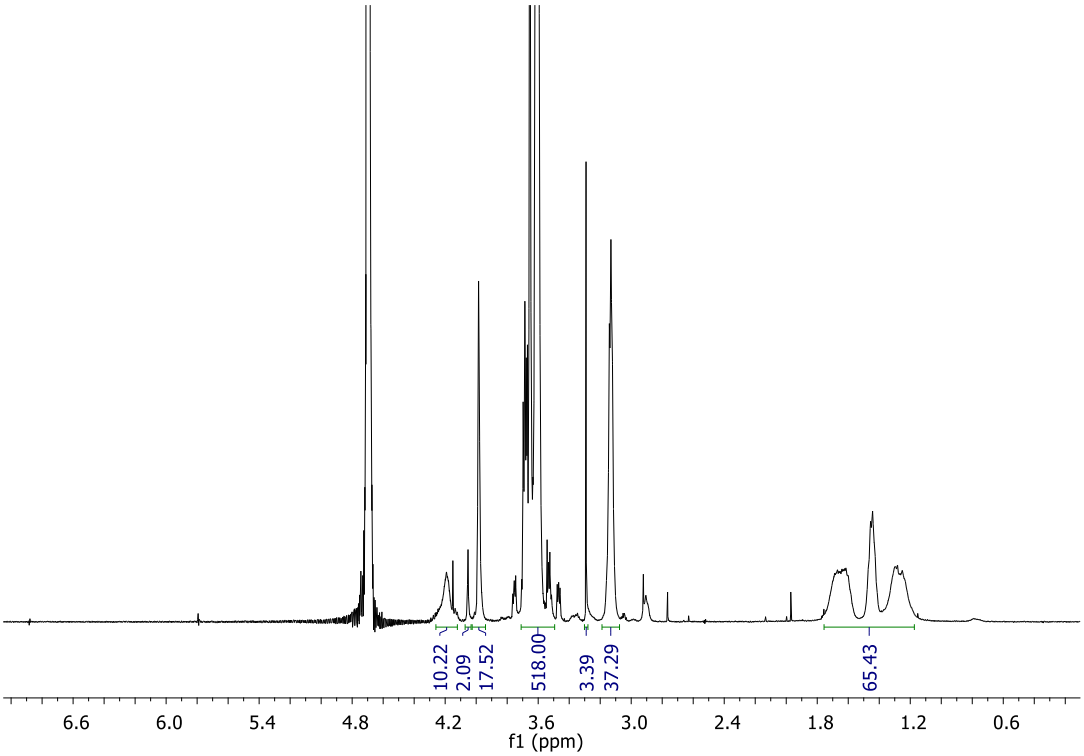

Figure A.6.1.3: ^{1}H NMR spectrum (500 MHz, D_2O) of **BC224D**, $mPEG_{113}$-*b*-PLys[O2O-NH_2.TFA]$_{10}$.

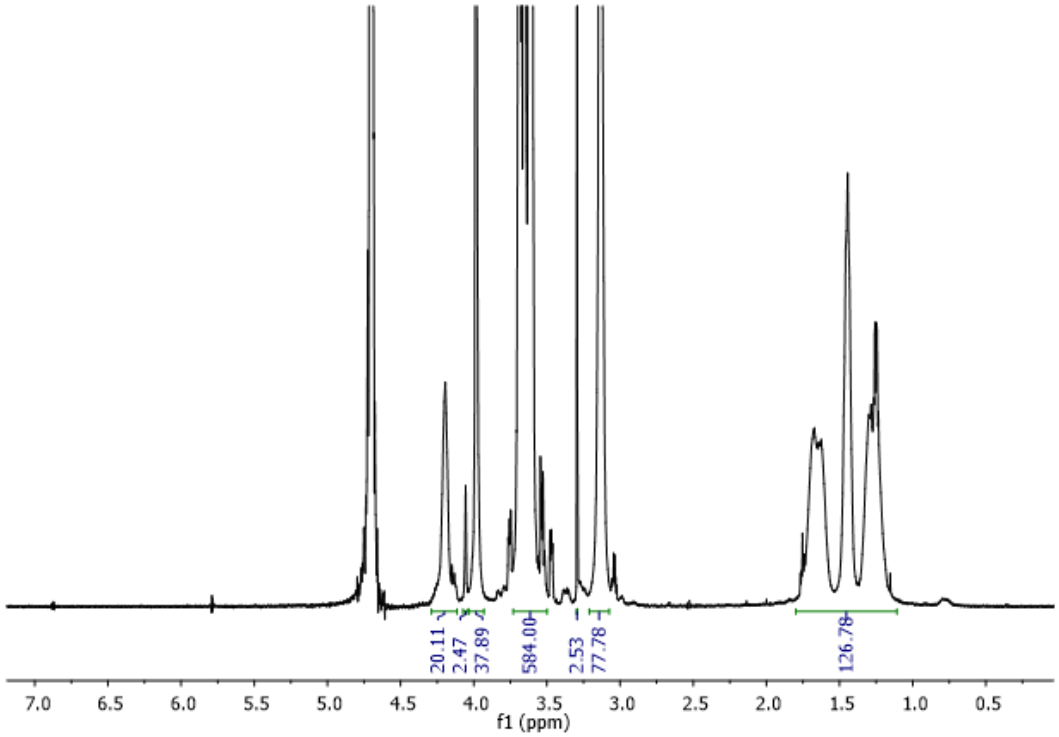

Figure A.6.1.4: ^{1}H NMR spectrum (500 MHz, D_2O) of **BC226D**, $mPEG_{113}$-*b*-PLys[O2O-O2O-NH_2.TFA]$_{10}$.

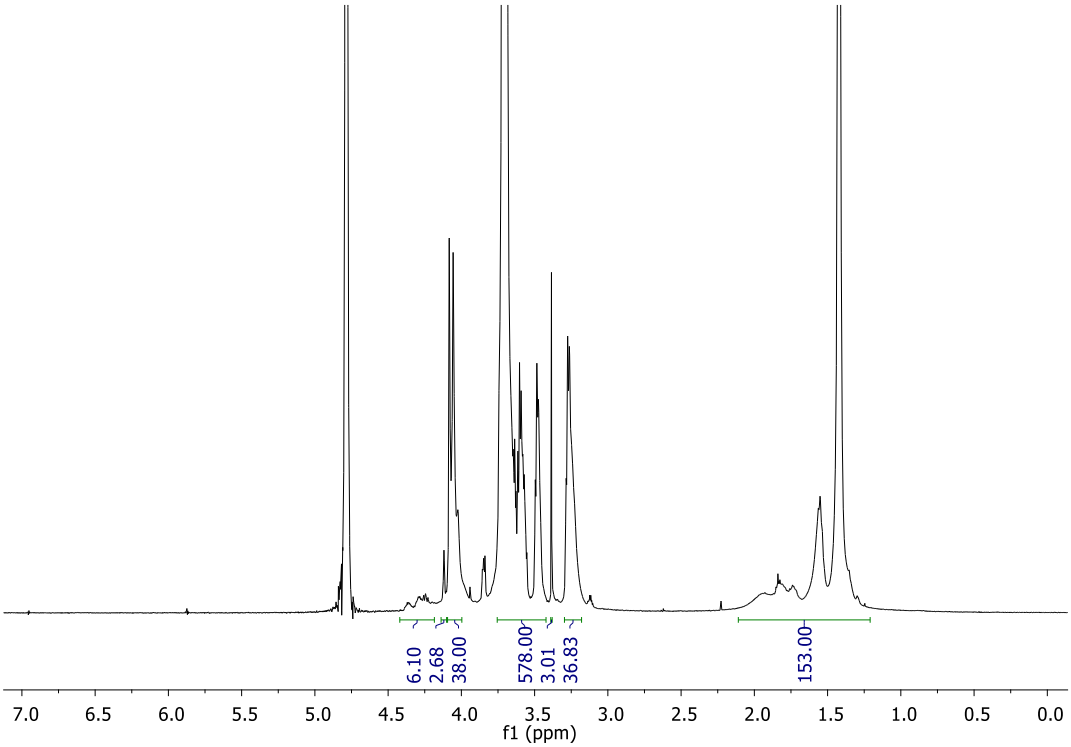

Figure A.6.1.5: ^{1}H NMR spectrum (500 MHz, D_2O) of **BC225**, mPEG$_{113}$-*b*-PLys(O2O-Boc)$_{20}$.

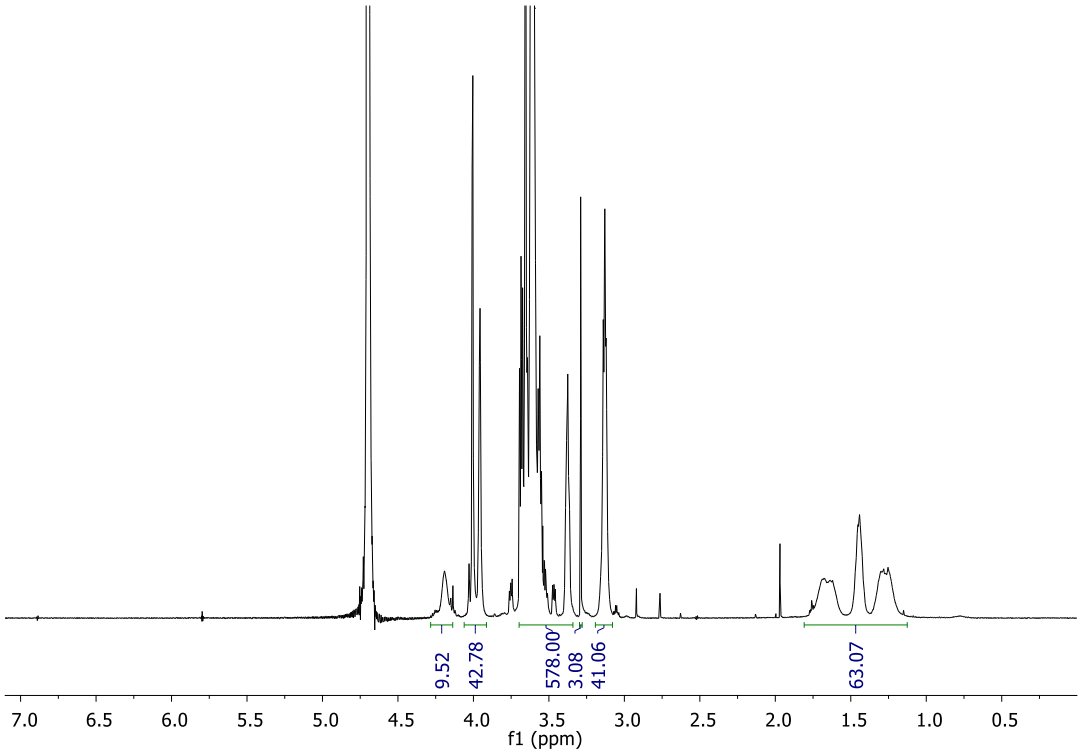

Figure A.6.1.6: ^{1}H NMR spectrum (500 MHz, D_2O) of **BC225D**, mPEG$_{113}$-*b*-PLys[O2O-NH_2.TFA]$_{20}$.

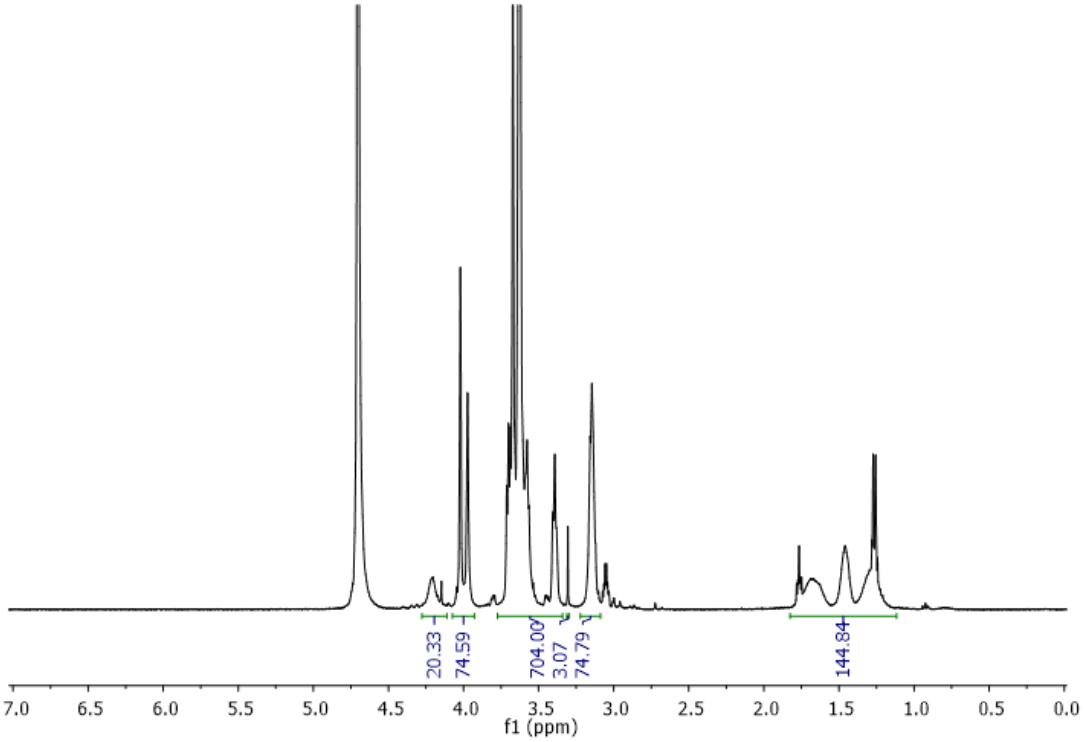

Figure A.6.1.7: ^{1}H NMR spectrum (500 MHz, D_2O) of **BC227D**, mPEG$_{113}$-*b*-PLys[O2O-O2O-NH_2.TFA]$_{20}$.

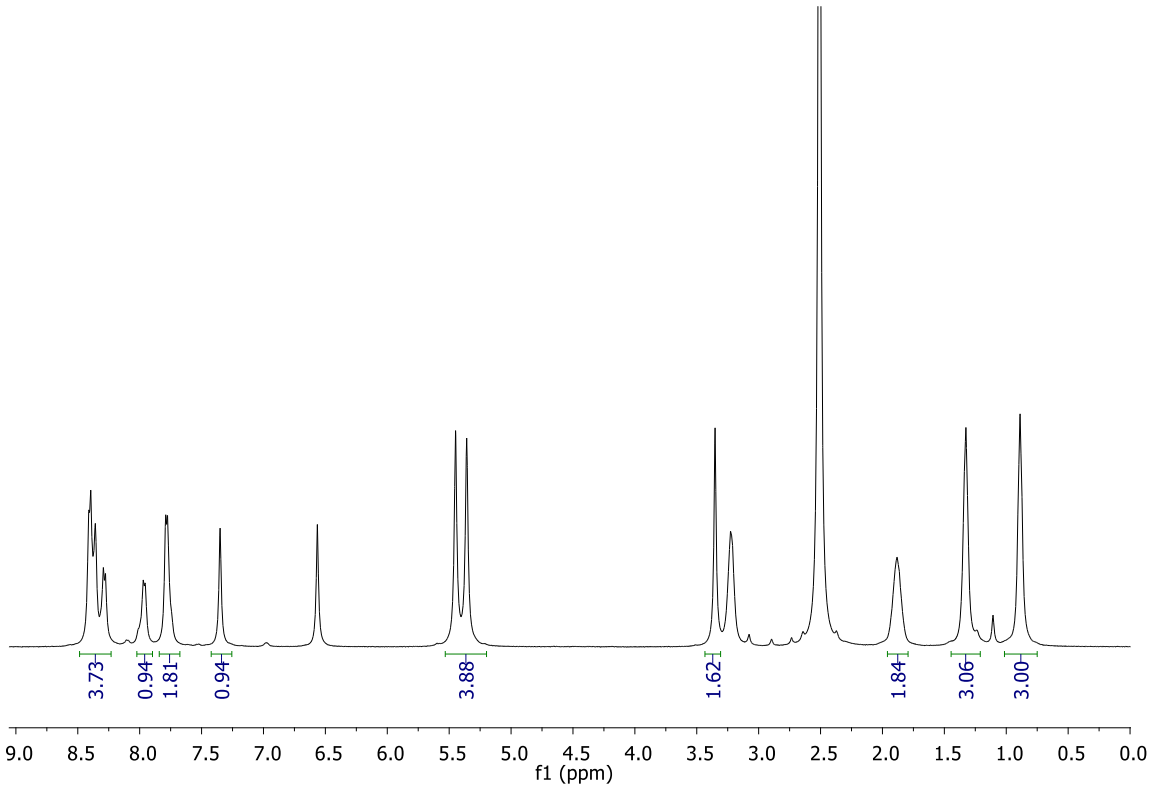

Figure A.6.1.8: ^{1}H NMR spectrum of 10-O-(p-nitrophenyl carbonate)-SN38.

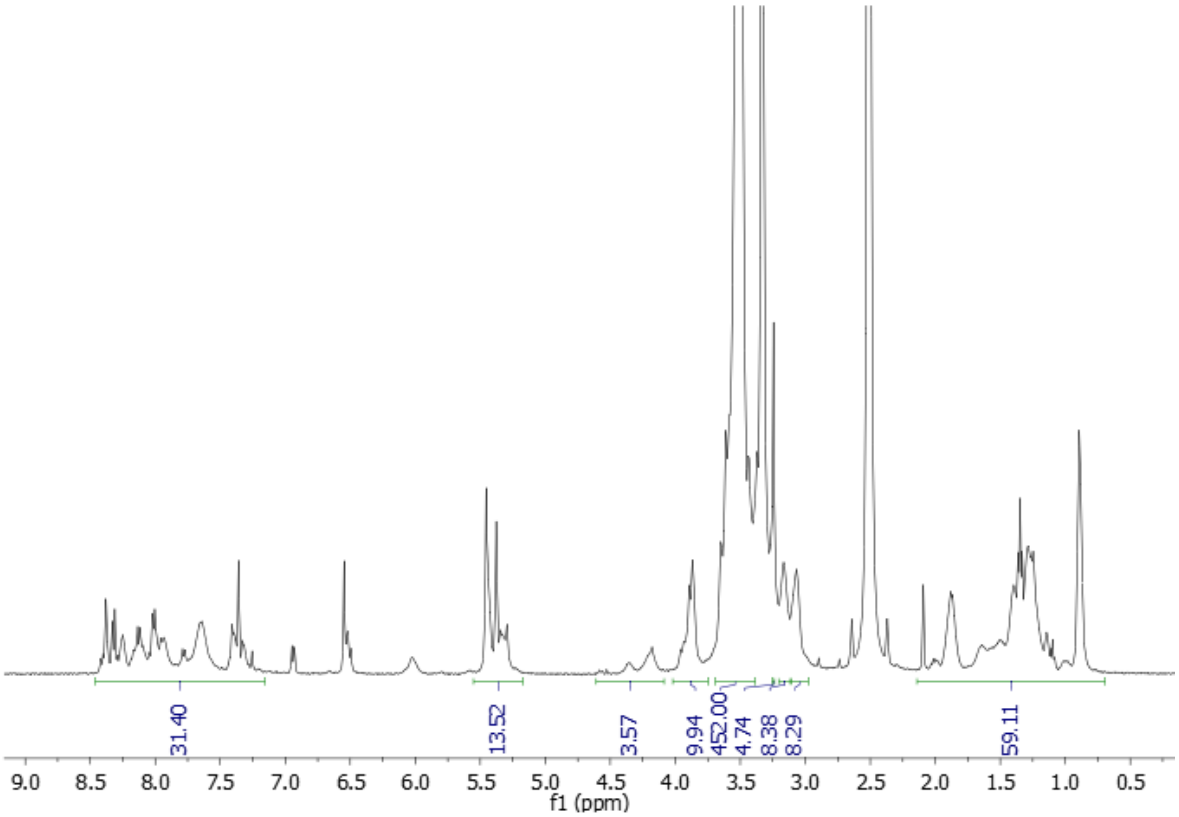

Figure A.6.1.9: ^{1}H NMR spectrum (500 MHz, DMSO-d_6) of **BC234,** mPEG$_{113}$-*b*-PLys(CO-SN38)$_5$.

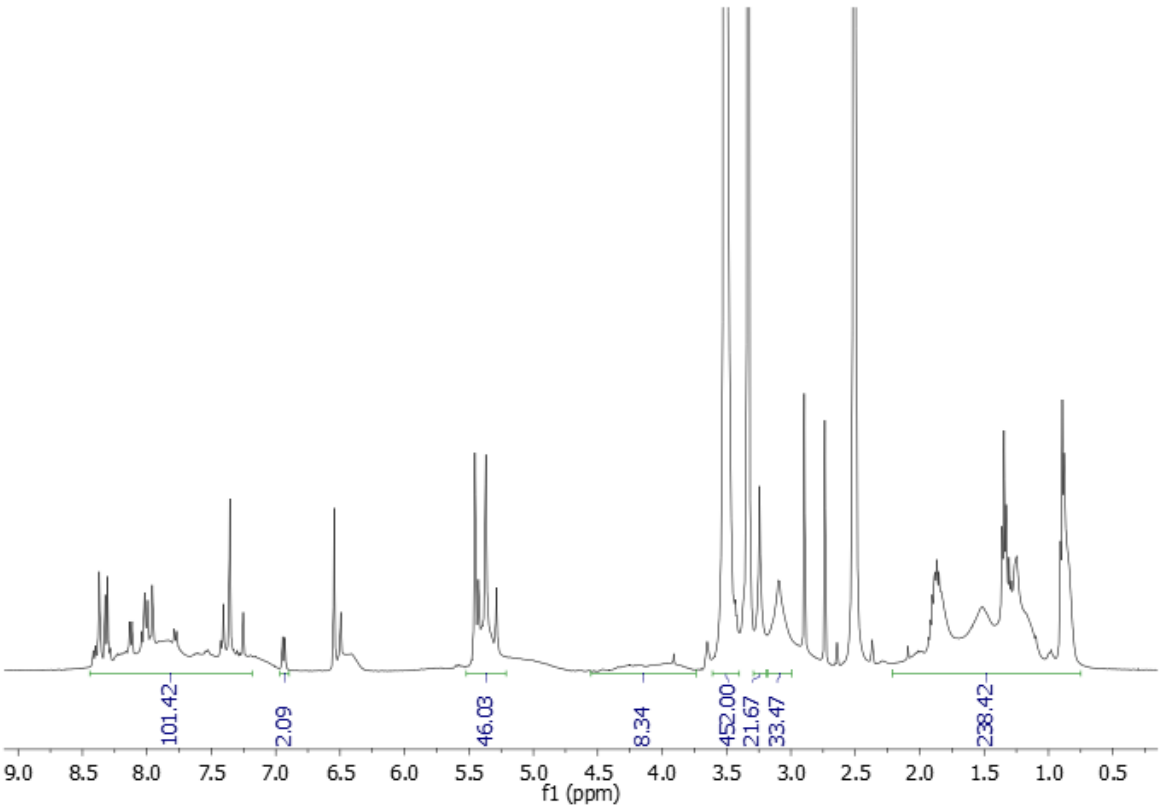

Figure A.6.1.10: ^{1}H NMR spectrum (500 MHz, DMSO-d_6) of **BC235**, mPEG$_{113}$-*b*-PLys(CO-SN38)$_{20}$.

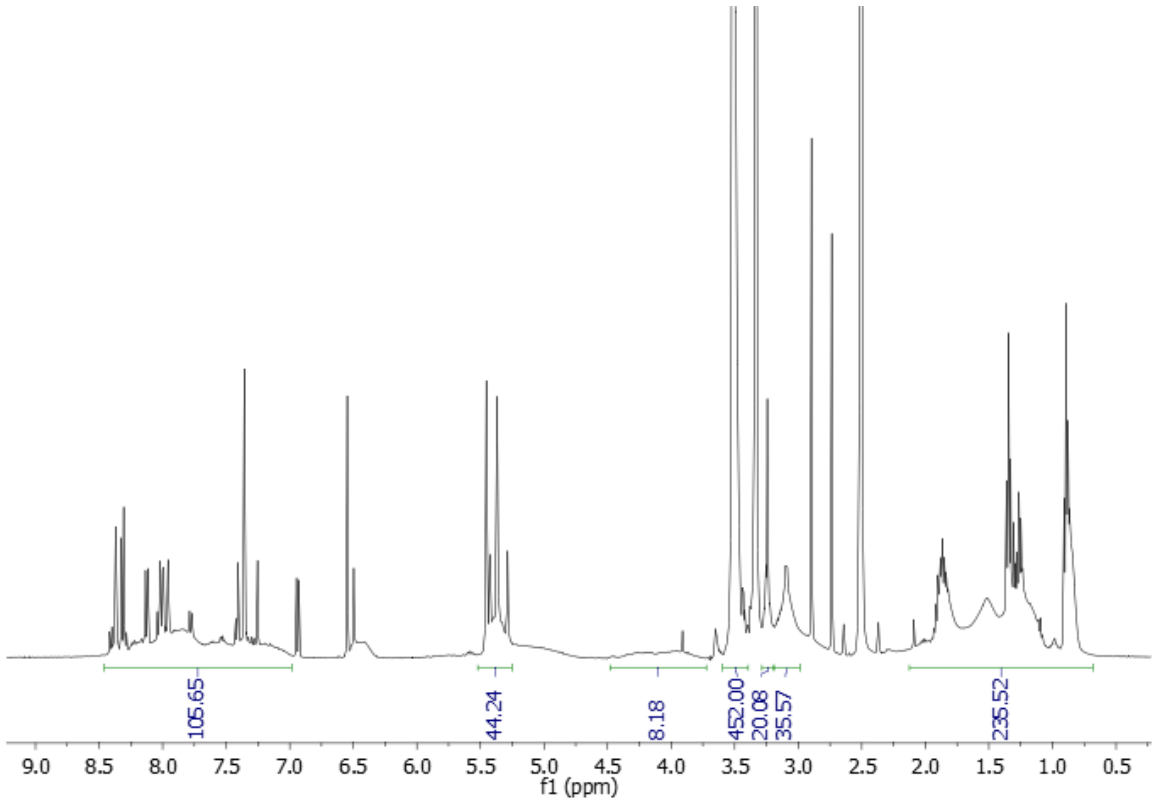

Figure A.6.1.11: ^{1}H NMR spectrum (500 MHz, DMSO-d_6) of **BC236**, mPEG$_{113}$-*b*-PLys(CO-SN38)$_{20}$.

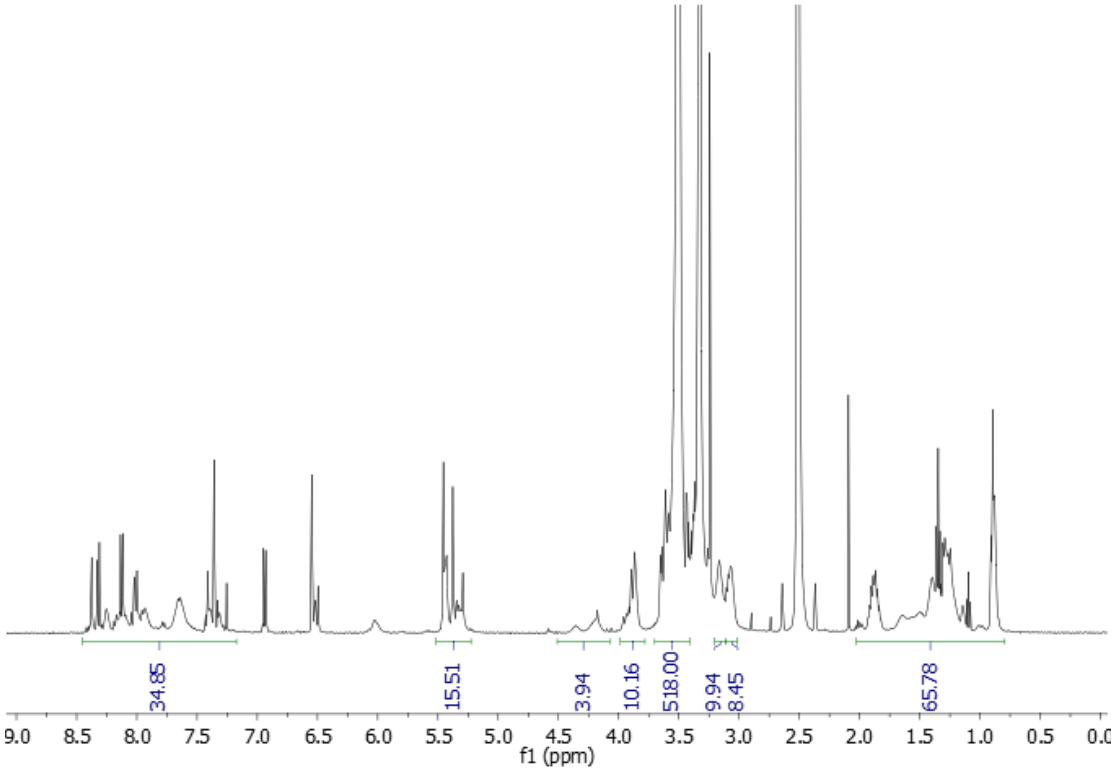

Figure A.6.1.12: ^{1}H NMR spectrum (500 MHz, DMSO-d_6) of **BC237**, mPEG$_{113}$-*b*-PLys(O2O-CO-SN38)$_5$

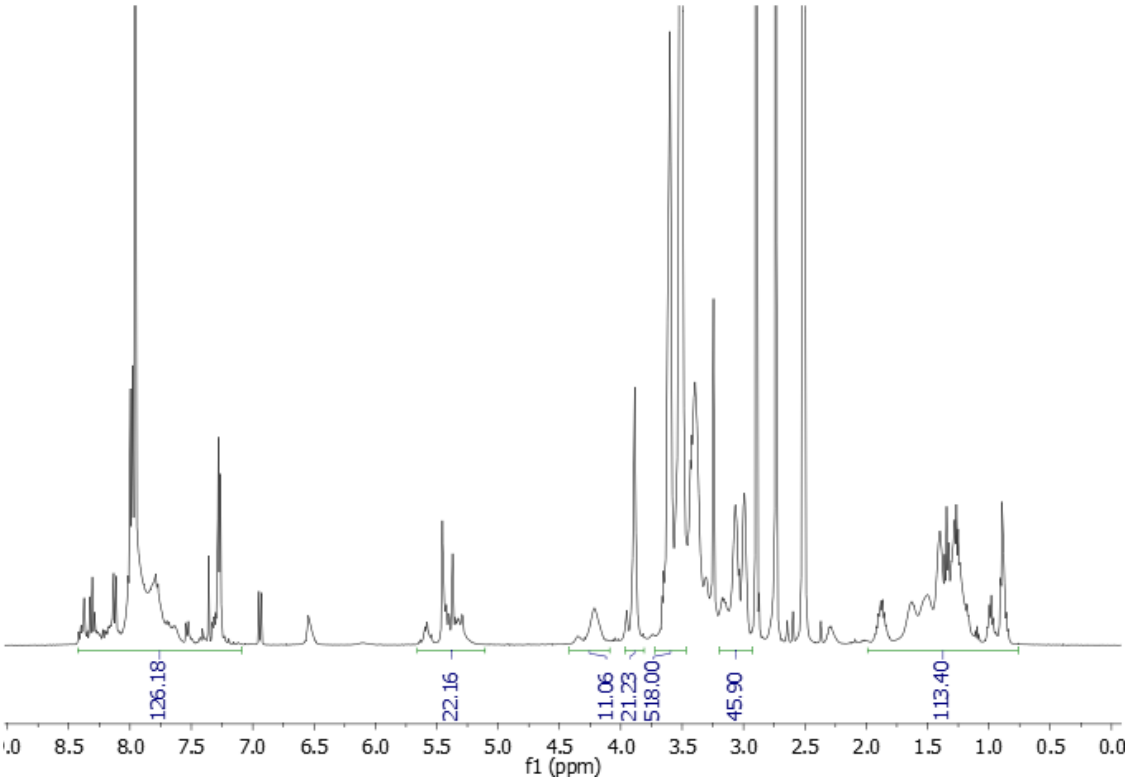

Figure A.6.1.13: ^{1}H NMR spectrum (500 MHz, DMSO-d_6) of **BC238**, mPEG$_{113}$-*b*-PLys(O2O-CO-SN38)$_{10}$.

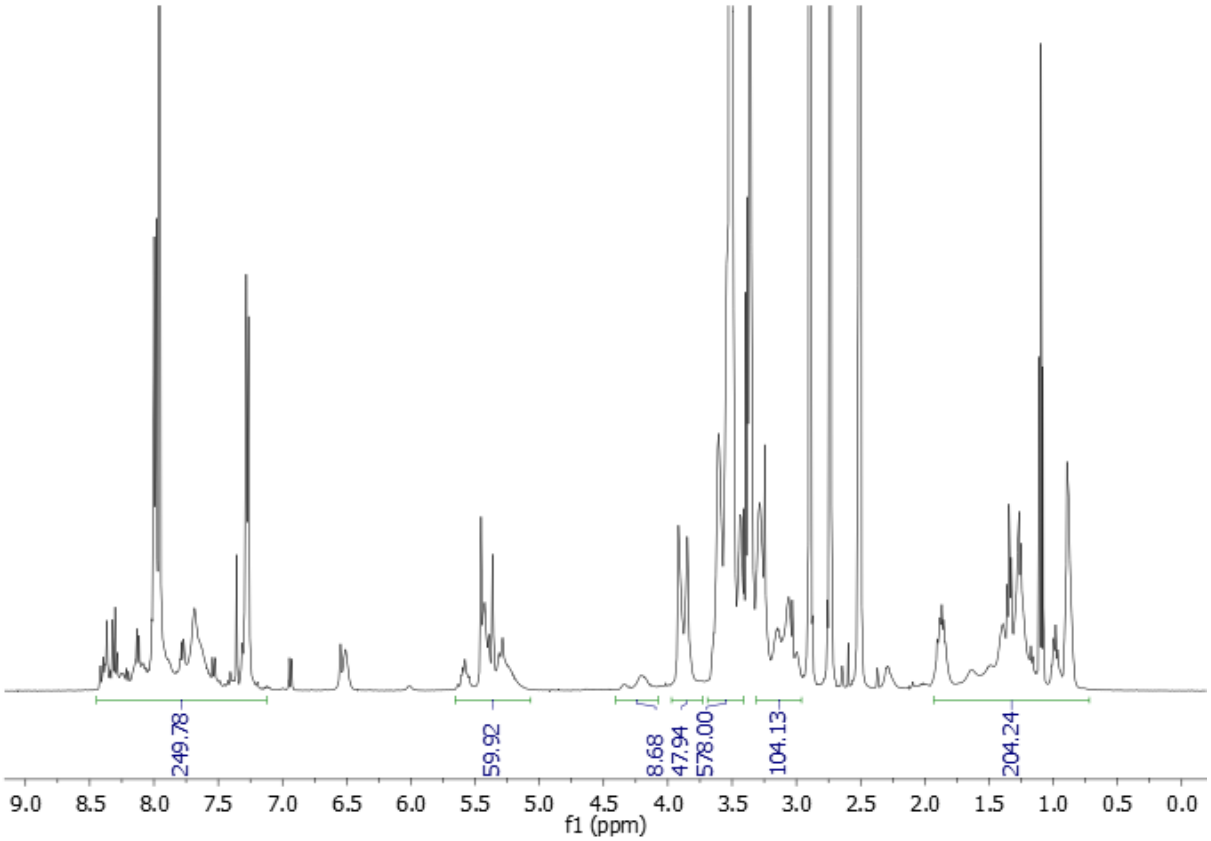

Figure A.6.1.14: ^{1}H NMR spectrum (500 MHz, DMSO-d_6) of **BC239**, mPEG$_{113}$-*b*-PLys(O2O-CO-SN38)$_{20}$.

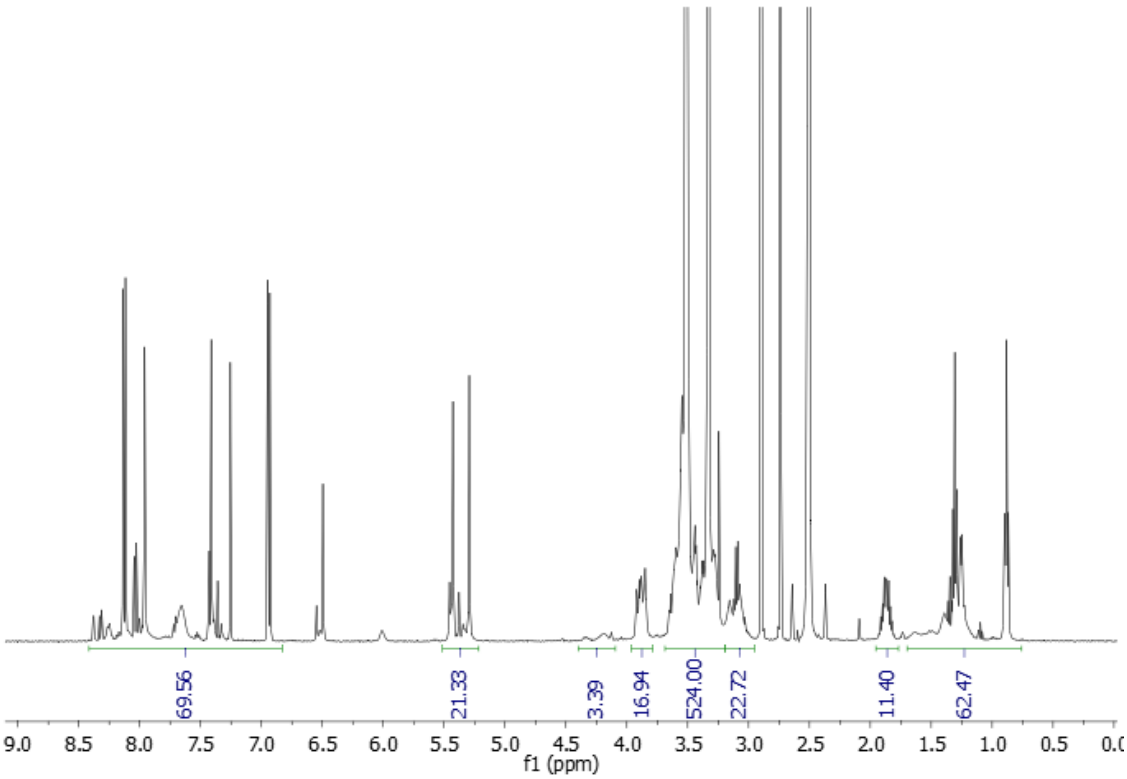

Figure A.6.1.15: ^{1}H NMR spectrum (500 MHz, DMSO-d_6) of **BC240**, mPEG$_{113}$-*b*-PLys(O2O-O2O-CO-SN38)$_5$

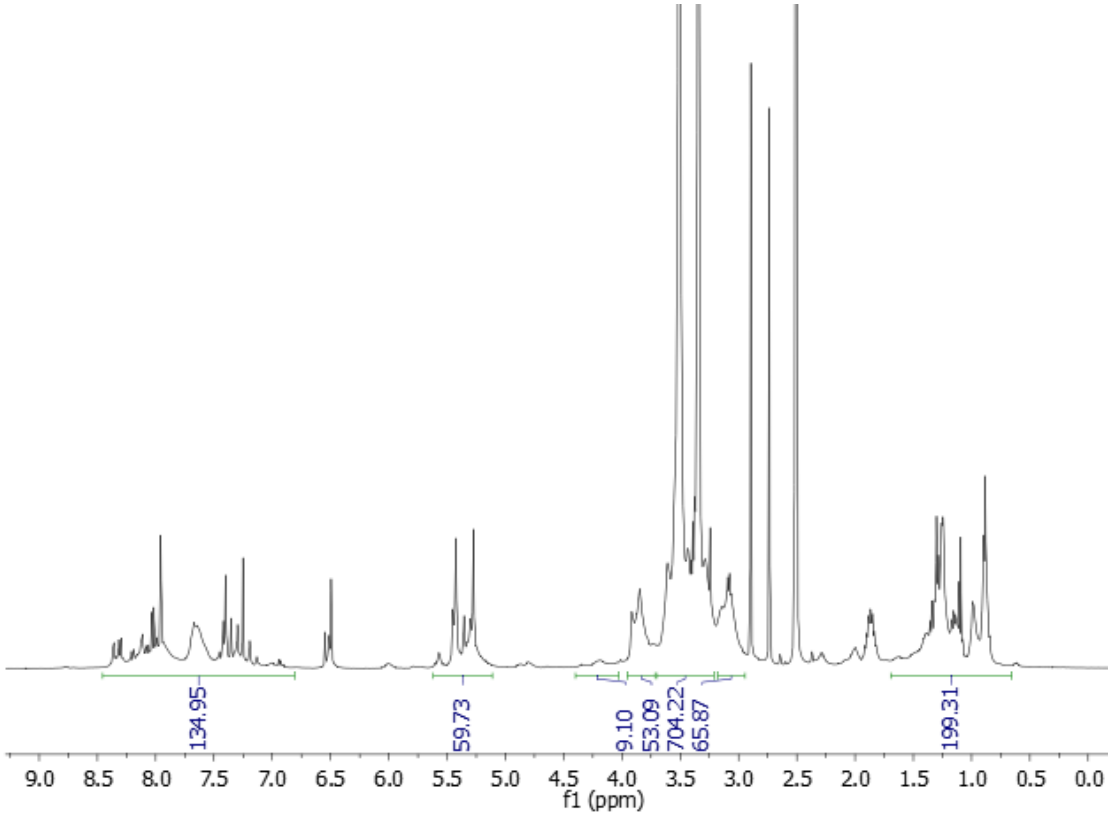

Figure A.6.1.16: ^{1}H NMR spectrum (500 MHz, DMSO-d_6) of **BC242**, mPEG$_{113}$-*b*-PLys(O2O-O2O-CO-SN38)$_{10}$

Chapter 7. Thesis Conclusions and Future Work

This thesis investigated the synthesis and optimisation of two amphiphilic block copolymer platforms, mPEG-*b*-poly(mandelic acid) and mPEG-*b*-poly(L-lysine) for the encapsulation and conjugation of chemotherapeutic agents, with self-assembly and release behaviour characterised under stimulus-responsive and controlled-release conditions. The work has addressed challenges in monomer synthesis, polymerisation control, nanoparticle assembly, and drug loading, establishing reproducible synthetic routes to functional delivery vehicles.

The foundation of both polymer systems was established through the preparation of a library of NCA and OCA monomers, including Fmoc-, Z- and Boc-protected lysine NCAs and mandelic acid OCA. Traditional phosgene-activated synthetic strategies were evaluated alongside modern phosgene-free alternatives, which were found to offer meaningful improvements in operational safety and product purity, whilst remaining robust against side reactions.

In Chapter 4, Man-OCA was polymerised from mPEG-OH (5000 g mol^{-1}, Fluorochem) via OCA ROP under systematically varied conditions, yielding a series of novel mPEG-*b*-PMA block copolymers with narrow Đ. Whilst the DP achieved for the products were consistently below target values, attributed primarily to long reaction times and high temperatures necessitatated by the low nucleophilicity of the macroinitiator, products were obtained in good yield and demonstrated increased DP through elevated temperature, establishing a clear avenue for further optimisation. Each polymer self-assembled into nanoparticles below 200 nm with low PDI values, suitable for intravenous administration and long-circulating tumour delivery. For Polymer 1, Dox encapsulation efficiency was high at 87 ± 3 wt%, comparing favourably with literature values for poly(amino acid)-based systems. Polymer 1 also demonstrated resistance to hydrolysis and leakage under physiological conditions (pH 7.4), whilst enabling accelerated, acid-triggered release under simulated endosomal conditions (pH 5.0), with burst release avoided in both cases. These results establish mPEG-*b*-PMA as a viable and reproducible platform for pH-sensitive encapsulative drug delivery.

In Chapter 5, optimisation of Lys(Boc)-NCA ROP from mPEG-NH_2 (5000 g mol^{-1}, Iris Biotech GmbH) was undertaken, employing *in situ* FTIR monitoring alongside SEC and ^{1}H NMR characterisation to evaluate the effect of reaction conditions on polymerisation control.

Early investigations using Fmoc- and Z-protected NCA systems revealed fundamental incompatibilities, including catalyst-mediated *in situ* Fmoc deprotection and incomplete deprotection of Z-groups that precluded their use in downstream applications. Lys(Boc)-NCA ROP was subsequently investigated, with multimodal molecular weight distributions observed for target block lengths of n > 5. Through systematic investigation, these distributions were attributed to the presence of high-molecular weight impurities within the polymerisation, rather than analytical artefact, and were successfully suppressed by conducting ROP at reduced temperature (10 °C) in THF. This approach yielded well-defined mPEG-*b*-PLys[NH_2·TFA]$_n$ products (n = 5, 10, 20) with markedly improved dispersity and narrower molecular weight distributions, providing a controlled and reproducible route to deprotected PLys block copolymers amenable to post-polymerisation modification.

In Chapter 6, these mPEG-*b*-PLys[NH_2·TFA]$_n$ copolymers were subjected to post-polymerisation modification through the grafting of OEG chain extenders to the pendant lysine amines via amide coupling. This strategy was designed to relieve steric congestion around the reactive amine groups, improving their accessibility for subsequent conjugation. High grafting efficiencies were achieved across all samples (80 – 97 %), and TFA-mediated Boc-deprotection was performed successfully without loss of grafted material, confirming the chemical robustness of the modified architecture. Carbamate conjugation of SN38 to both linear and chain-extended mPEG-*b*-PLys derivatives was then accomplished, with chain-extended products demonstrating improved conjugation yields consistent with the intended reduction in steric occlusion. The resulting polymer-drug conjugates successfully self-assembled into stable nanoparticles, the majority below 200 nm with PDI values below 0.3, suitable for long-circulating intravenous administration. Controlled release of SN38 under hydrolytic conditions was demonstrated for all samples without burst release, with release rate shown to be tuneable through hydrophobic block length and chain extender architecture. This represents a significant step forward in the development of prodrug nanocarrier platforms for the treatment of SN38-relevant malignancies, including pancreatic adenocarcinoma and metastatic colorectal cancer, for which reduction of systemic dose-limiting toxicities remains a critical clinical need.

Looking ahead, several priorities have been identified for future development of both platforms. For the mPEG-*b*-PMA system, further optimisation of both DP control and nanoparticle self-assembly procedure would improve the reproducibility and tunability of particle size, expanding the range of accessible administration routes. This could be achieved through a reapplication of *in situ* reaction monitoring, combined with more representative analytical follow-up (DOSY NMR, SEC-MALS). For the mPEG-*b*-PLys system, exploration of alternative NCA ROP solvent systems (DMAc and cyrene) alongside improved SEC characterisation methodologies such as HFIP eluent and MALDI-TOF mass spectrometry, would allow more accurate assessment of molecular weight and more robust suppression of high-MW impurities. In the context of SN38 conjugation specifically, rigorous LC-MS monitoring of the reactive carbonate intermediate and development of a more thorough purification strategy for the conjugated polymers would eliminate the impurity contributions that complicated release data in the present work. Most critically, progression of the mPEG-*b*-PLys-SN38 platform toward biological evaluation, encompassing *in vitro* cytotoxicity assessment on relevant cancer cell lines and *in vivo* biodistribution, circulation half-life and tumour growth inhibition studies, represents the natural and necessary next step in establishing the clinical translational potential of these materials.